

STUDY OF THE KINETICS OF CONDENSATION AND EVAPORATION OF WATER VAPOR OVER ATMOSPHERICALLY RELEVANT PURE AND DOPED ICE FILMS: A MULTIPLE DIAGNOSTIC APPROACH

THÈSE N° 3159 (2005)

PRÉSENTÉE À LA FACULTÉ ENVIRONNEMENT NATUREL, ARCHITECTURAL ET CONSTRUIT

Institut des sciences et technologies de l'environnement

SECTION DES SCIENCES ET INGÉNIERIE DE L'ENVIRONNEMENT

ÉCOLE POLYTECHNIQUE FÉDÉRALE DE LAUSANNE

POUR L'OBTENTION DU GRADE DE DOCTEUR ÈS SCIENCES

PAR

Christophe DELVAL

DEA en acousto-opto-électronique et Mécanique des structures, Université de Franche-Comté, Besançon, France
et de nationalité française

acceptée sur proposition du jury:

Dr M. Rossi, directeur de thèse
Dr P. Hoffmann, rapporteur
Prof. L. Schriver, rapporteur
Prof. U. Schurath, rapporteur
Prof. H. van den Bergh, rapporteur

Lausanne, EPFL
2005

A la Louise passée, à la présente, à toutes les petites Louise futures...

A Delphine...

A tout ce qui est Rouge et Noir...

NDM

Abstract

This thesis presents the different steps in the development of a multiple diagnostic experimental setup and the results concerning the kinetics of condensation and evaporation of water over pure ice, as well as ice films doped with a known amount of atmospheric trace gases. The goal of this project is to obtain reliable data concerning the evaporative flux, J_{ev} [molec cm⁻² s⁻¹], and the concomitant rate of condensation, k_{cond} [s⁻¹], of H₂O molecules in the presence of an ice film. A further aim of this work is the detailed investigation of the impact on the aforementioned kinetic processes of the deposition of atmospherically relevant trace gases such as hydrogen chloride (HCl), hydrogen bromide and nitric acid (HNO₃) under well defined conditions including those that are representative of the atmosphere. The new experimental apparatus consisting of a stainless steel reactor may be used under three different regimes, namely *static*, *stirred flow* and *dynamic* condition which correspond to equilibrium, low rate of pumping and molecular flow, respectively. The separation of the kinetics into individual processes is principally afforded by the application of these 3 regimes.

First, using a combination of the first two regimes, we have measured J_{ev} and γ of H₂O in the case of pure as well as HCl- or HBr-doped ice in the range 190-240 K. The resulting Arrhenius expressions for pure ice are:

$$J_{\text{ev}}=1.6 \cdot 10^{28 \pm 1} \cdot \exp\left(\frac{-10.3 \pm 1.2}{\mathcal{R}} \times \frac{1000}{T}\right) \text{ molec cm}^{-2} \text{ s}^{-1}, k_{\text{cond}}=1.7 \cdot 10^{-2 \pm 1} \cdot \exp\left(\frac{\pm 1.6 \pm 1.5}{\mathcal{R}} \times \frac{1000}{T}\right) \text{ s}^{-1},$$

in the presence of an average mole fraction of HCl, χ_{HCl} , in the range $3.2 \cdot 10^{-5}$ to $6.4 \cdot 10^{-3}$ we have found:

$$J_{\text{ev}}=6.4 \cdot 10^{26 \pm 1} \cdot \exp\left(\frac{-9.7 \pm 1.2}{\mathcal{R}} \times \frac{1000}{T}\right) \text{ molec cm}^{-2} \text{ s}^{-1}, k_{\text{cond}}=2.8 \cdot 10^{-2 \pm 1} \cdot \exp\left(\frac{\pm 1.5 \pm 1.6}{\mathcal{R}} \times \frac{1000}{T}\right) \text{ s}^{-1},$$

and for χ_{HBr} at a HBr mole fraction smaller than $6.4 \cdot 10^{-3}$

$$J_{\text{ev}}=7.4 \cdot 10^{25 \pm 1} \cdot \exp\left(\frac{-9.1 \pm 1.2}{\mathcal{R}} \times \frac{1000}{T}\right) \text{ molec cm}^{-2} \text{ s}^{-1}, k_{\text{cond}}=7.1 \cdot 10^{-5 \pm 1} \cdot \exp\left(\frac{\pm 2.6 \pm 1.5}{\mathcal{R}} \times \frac{1000}{T}\right) \text{ s}^{-1}$$

was found, where $\mathcal{R}=1.987 \text{ cal mol}^{-1} \text{ K}^{-1}$. Owing to the rate separation, γ applies to an individual rate process and should be called an accommodation rather than an uptake coefficient.

Of utmost importance is the fact that during most of the ice film evaporation the vapor pressure remained that of pure ice even in the presence of small amounts of HCl or HBr on the order of a fraction to several formal monolayers. This is consistent with the enthalpies of sublimation that may be derived following the relation $\Delta H_{\text{subl}}^0 = E_{\text{cond}} - E_{\text{ev}}$. It leads to different thermochemical parameters A (pre-exponential factor) and E values (energy of activation) for the three cases that are identical within experimental uncertainty. In addition, FTIR spectroscopy of the ice films involved in these experiments in transmission have revealed that different species such as amorphous HCl·H₂O mixtures or the crystalline

HCl·6H₂O hexahydrate are formed depending on the doping protocol. These two species significantly affect the temporal change of J_{ev} each in a different manner.

For the sake of precision and accuracy of the kinetic results, a quartz crystal microbalance (QCM) was subsequently added to the experimental apparatus and used as a substrate for ice film growth. The development of a QCM-based device for the investigation of the kinetic processes of ice films at atmospherically relevant temperatures was a challenge we have successfully surmounted whereas previously published attempt had given barely convincing results. The Arrhenius representation of the zero order evaporative flux J_{ev} (molec cm⁻² s⁻¹) of H₂O from pure ice displays a discontinuity at 193±2 K that could be observed owing to the accuracy and precision of the QCM measurements. It leads to:

$$\begin{aligned} \text{for } 223 > T > 193 \text{ K, } J_{\text{ev}} &= (1.6 \pm 0.7) \cdot 10^{28} \times \exp\left(\frac{-10.2 \pm 0.5}{R} \times \frac{1000}{T}\right) \text{ molec cm}^{-2} \text{ s}^{-1} \\ \text{for } 173 < T < 193 \text{ K, } J_{\text{ev}} &= (2.2 \pm 0.9) \cdot 10^{30} \times \exp\left(\frac{-12.0 \pm 0.5}{R} \times \frac{1000}{T}\right) \text{ molec cm}^{-2} \text{ s}^{-1} \end{aligned}$$

In addition, γ of H₂O onto ice was found to be lower than 0.5 for temperatures below 240 K in contrast to the value of 1.0 which is often encountered in the literature.

Subsequently, the deposited ice films have been doped with HNO₃ using different protocols depending on parameters such as temperature, rate of deposition of HNO₃ onto ice as well as number of HNO₃ molecules deposited. The reproducible and quantitative dosing of the doping gas was key to the quality of the results. This study has shed light on a complex interplay between several of these parameters that affect the continuous decrease of J_{ev} during ice evaporation. Using atmospherically relevant conditions in the doping of ice by HNO₃ we have observed crystalline α -NAT being most likely the first species that forms in/on ice films. During most of the evaporation of the ice film doped with known amounts of HNO₃ we have checked that the vapor pressure over the ice film remains that of pure ice.

Finally, HCl-doped ice films have been investigated in experiments that are complementary to the first set in order to verify that HCl doping has a similar impact on the change of J_{ev} of H₂O in the presence of small albeit known amounts of HCl. The doping protocol is a fundamental parameter determining the decrease of J_{ev} with H₂O evaporation time of doped ice films.

In summary, we have developed from scratch a new experimental apparatus that allows the separation of the kinetic processes of condensation and evaporation of pure as well as doped ice films using multiple diagnostics under the same experimental conditions which was heretofore not attainable. The main result for pure ice films is that the uptake coefficient, γ of H₂O on ice is always lower than approximately 0.5 for atmospherically relevant temperatures. Its negative temperature dependence has been confirmed. An accurate control of the doping protocol has allowed us to observe that for a fraction to a few monolayers of the doping gases, HCl, HBr and HNO₃, the nature of the aforementioned protocol is the predominant factor influencing the continuous temporal decrease of J_{ev} and γ during doped ice film evaporation. Of utmost importance is the fact that the vapor pressure over the doped ice films remains that of pure water ice during almost all of the evaporation process.

These results may be of importance in atmospheric modelling for determining the lifetime of ice particles involved in clouds in regions that are undersaturated in the vapor pressure of H₂O over ice. In this way the physical process of evaporation affects the importance of heterogeneous chemistry of atmospheric trace gases on ice substrates representative of Cirrus clouds, aviation induced Cirrus clouds and contrails as well as type II PSC's.

Version Abrégée

Cette thèse présente les différentes étapes du développement d'un dispositif expérimental à diagnostics multiples permettant la mesure des cinétiques de condensation et d'évaporation de la vapeur d'eau en présence de films de glace pure ou contaminée par des quantités bien définies de gaz-traces, impliqués dans la chimie atmosphérique. Le principal but de ce travail est d'obtenir des données fiables concernant le flux d'évaporation, J_{ev} [$\text{molec cm}^{-2} \text{s}^{-1}$], ainsi que le taux de condensation, k_{cond} [s^{-1}], des molécules d'eau sur les films de glace. De plus, notre intérêt s'est focalisé sur l'impact de la déposition de gaz-traces présents dans l'atmosphère tels l'acide chlorhydrique (HCl), l'acide bromohydrique (HBr) et l'acide nitrique (HNO_3) sur les processus cinétiques précédemment cités. Le dispositif expérimental consiste en un réacteur en acier inoxydable qui peut être utilisé suivant trois régimes distincts, nommément *statique*, *stirred flow* (bien mélangé) et *dynamique* qui correspondent respectivement à des conditions d'équilibre, de taux de pompage faible et de flux moléculaire. La séparation des processus sus-cités repose principalement sur la combinaison de ces trois régimes.

Dans un premier temps, en utilisant une combinaison des deux premiers régimes, nous avons mesuré J_{ev} et γ pour H_2O dans le cas de films de glace pure ainsi que dopée avec HCl ou HBr dans la gamme de température 190-240 K. Les expressions Arrhénius correspondantes pour la glace pure sont les suivantes:

$$J_{ev}=1.6 \cdot 10^{28 \pm 1} \cdot \exp\left(\frac{-10.3 \pm 1.2}{\mathcal{R}} \times \frac{1000}{T}\right) \text{ molec cm}^{-2} \text{ s}^{-1}, k_{cond}=1.7 \cdot 10^{-2 \pm 1} \cdot \exp\left(\frac{+1.6 \pm 1.5}{\mathcal{R}} \times \frac{1000}{T}\right) \text{ s}^{-1},$$

en présence d'une fraction molaire moyenne de HCl, χ_{HCl} , comprise entre $3.2 \cdot 10^{-5}$ et $6.4 \cdot 10^{-3}$, nous avons déterminé que:

$$J_{ev}=6.4 \cdot 10^{26 \pm 1} \cdot \exp\left(\frac{-9.7 \pm 1.2}{\mathcal{R}} \times \frac{1000}{T}\right) \text{ molec cm}^{-2} \text{ s}^{-1}, k_{cond}=2.8 \cdot 10^{-2 \pm 1} \cdot \exp\left(\frac{+1.5 \pm 1.6}{\mathcal{R}} \times \frac{1000}{T}\right) \text{ s}^{-1},$$

et pour χ_{HBr} inférieure à $6.4 \cdot 10^{-3}$

$$J_{ev}=7.4 \cdot 10^{25 \pm 1} \cdot \exp\left(\frac{-9.1 \pm 1.2}{\mathcal{R}} \times \frac{1000}{T}\right) \text{ molec cm}^{-2} \text{ s}^{-1}, k_{cond}=7.1 \cdot 10^{-5 \pm 1} \cdot \exp\left(\frac{+2.6 \pm 1.5}{\mathcal{R}} \times \frac{1000}{T}\right) \text{ s}^{-1}$$

a été déterminé, en considérant $\mathcal{R}=1.987 \text{ cal mol}^{-1} \text{ K}^{-1}$. On notera que grâce à la séparation des différents taux, γ correspond à un processus élémentaire et devrait être appelé plutôt taux d'accommodation que coefficient de capture.

Un des résultats les plus importants de ces expériences est la constance de la pression de vapeur saturante de H_2O en présence des films de glace, même lorsque ceux-ci sont dopés avec des quantités de HCl ou HBr comprises entre une fraction et quelques monocouches formelles. Ceci reste cohérent avec les enthalpies de sublimation que l'on peut déduire selon la relation $\Delta H_{\text{subl}} = E_{\text{cond}} - E_{\text{ev}}$. Les facteurs pré-exponentiels des expressions d'Arrhénius diffèrent alors que les énergies

d'activation restent identiques, dans la limite des incertitudes expérimentales, pour les trois cas de figure. En complément, l'étude simultanée par spectroscopie FTIR des films de glace, dont il est question ici, a révélé la présence de différentes espèces chimiques à la surface ou dans la glace telles que l'hexahydrate cristallin de HCl ou sa structure amorphe $\text{HCl}\cdot\text{H}_2\text{O}$. Nous avons pu constater que ces deux espèces ont un impact différent quant à l'évolution au cours du temps de J_{ev} .

Par la suite, et par soucis de précision et d'exactitude, une microbalance à quartz piézo-électrique a été introduite dans le dispositif expérimental et utilisée comme substrat pour la croissance de films de glace. Le développement d'un dispositif de mesure basé sur une microbalance, utilisable dans nos conditions expérimentales, fut une gageure couronnée de succès, là où les tentatives publiées dans la littérature scientifiques n'étaient qu'à peine convaincantes.

Les représentations d'Arrhénius de J_{ev} ($\text{molec cm}^{-2} \text{ s}^{-1}$) de H_2O ont fait apparaître cette fois, et ce, grâce à la grande précision et à l'exactitude de la microbalance, une discontinuité à 193 ± 2 K.

$$\text{Pour } 223 > T > 193 \text{ K, } J_{\text{ev}} = (1.6 \pm 0.7) \cdot 10^{28} \times \exp\left(\frac{-10.2 \pm 0.5}{R} \times \frac{1000}{T}\right) \text{ molec cm}^{-2} \text{ s}^{-1}$$

et

$$\text{pour } 173 < T < 193 \text{ K, } J_{\text{ev}} = (2.2 \pm 0.9) \cdot 10^{30} \times \exp\left(\frac{-12.0 \pm 0.5}{R} \times \frac{1000}{T}\right) \text{ molec cm}^{-2} \text{ s}^{-1}$$

ont été déterminées avec \mathcal{R} valant $1.987 \text{ cal mol}^{-1} \text{ K}^{-1}$.

En complément, des films ont été dopés avec HNO_3 selon différents protocoles, correspondant à différents taux de déposition ainsi qu'à différentes quantités de HNO_3 déposées. La reproductibilité et l'aspect quantitatif des méthodes de dosage ont été la clef de la qualité des résultats obtenus. Cette étude a montré qu'une interaction complexe entre la température de déposition et les deux paramètres précédemment cités conduit à un impact différent sur la façon dont J_{ev} évolue avec le temps dans le cas d'un dopage avec HNO_3 . En se plaçant dans des conditions de dopage réalistes par rapport à l'atmosphère, nous avons pu observer que la forme de HNO_3 la plus probable sur la glace correspond au NAT cristallin, sous sa forme α -NAT. Comme pour le cas de HCl, cité auparavant, nous avons pu constater que pour la plus grande part de l'évaporation du film de glace, la pression de vapeur, même en cas de dopage, reste celle au-dessus de la glace pure.

Finalement, quelques expériences complémentaires sur la contamination de films de glace par de petites quantités bien déterminées de HCl nous ont conduits à des conclusions similaires: le protocole de déposition du dopant est fondamental dans la détermination de l'évolution de J_{ev} .

Ces résultats pourraient être à prendre en considération, dans la modélisation atmosphérique, pour déterminer la durée de vie des particules de glace impliquées dans des systèmes nuageux lors de passages dans des régions sous-saturées d'un point de vue pression de vapeur d'eau au-dessus de la glace. En ce sens, les processus physiques invoqués précédemment affectent la chimie atmosphérique des gaz-traces sur les particules de glace représentatives des Cirrus naturels, des Cirrus induits par l'aviation et des traces de condensations dues à l'aviation, ainsi que sur les PSCs.

Table of Contents

1	Introduction	1
1.1	The impact of anthropogenic activities	5
1.2	Motivation and plan of the thesis	12
	Bibliography	15
2	Experimental Setup: Global view	19
2.1	Main elements of the experiment	19
2.2	Origin and design of the cryogenic support	30
2.3	Three regimes of operation	36
2.4	Corrections of the measured total gas pressure	37
2.5	Mass spectrometry: calibrations and measurements	40
2.6	HeNe interferometry	44
2.7	FTIR calibrations	46
2.8	Aspects of data acquisition	51
2.8.1	Homemade inexpensive but efficient thermocouple noise-reducer/amplifier	51
2.8.2	Data acquisition	53
2.9	Appendix: cryostat Mark II dimensions	53
	Bibliography	58
3	Kinetics of water condensation and evaporation from ice substrates in the presence of HCl and HBr.	61
3.1	Supplementary information on the experimental apparatus	62
3.2	Experimental Results	70
3.2.1	Gas phase study of the kinetics of condensation and evaporation of H ₂ O from pure and HX-doped ice	70
3.2.2	HeNe monitoring of the change of thickness of the ice film	79
3.2.3	FTIR spectroscopic study in transmission of the condensed phase	84

3.3	Discussion and atmospheric implications	90
3.4	Appendix: Infrared absorption cross-sections at characteristic wavelengths for crystalline hexahydrate $\text{HCl}\cdot 6\text{H}_2\text{O}$	97
	Bibliography	102
4	The kinetics of condensation and evaporation of H_2O from pure ice in the range 173 to 223 K: a quartz crystal microbalance study.	105
4.1	Experimental section	108
4.1.1	Apparatus	108
4.1.2	Quartz Crystal Microbalance Calibration	113
4.1.3	The residual gas mass spectrometer	120
4.1.4	Check of the ice sample temperature	121
4.2	Experiments and Results	121
4.2.1	Kinetics of evaporation and condensation based on the measurement of water vapor in the gas phase	121
4.2.2	Kinetics of condensation of H_2O on pure ice: approach to pressure equilibrium	125
4.2.3	Use of the QCM to measure the kinetics of evaporation and condensation of water over ice	127
4.3	Discussion	138
4.4	Appendix : Kinetics of condensation of H_2O on pure ice from QCM measurements	144
4.5	Appendix : QCM temperature control device	145
4.6	Appendix : Surface roughness of the gold coating of the QCM sensing element and its probable impact on J_{ev} for pure ice films	148
	Bibliography	155
5	The influence of monolayer amounts of HNO_3 on the evaporation rates of H_2O over ice in the range 179 to 208 K: a QCM study.	159
5.1	Supplementary information on the experimental apparatus	161
5.2	Experimental Strategy	172
5.3	Systematic Results and Discussion	184
	Bibliography	200
6	The influence of monolayer amounts of HCl on the evaporation rates of H_2O over ice in the range 188 to 210 K: a QCM study.	203
6.1	Experiments and Results	204
6.2	Discussion	211

7 Outlook: Fourier transform infrared reflection-absorption spectroscopy of pure and doped ice films condensed on a QCM sensor	217
Bibliography	222
8 General Appendix	223
8.1 Ideal Gas Law: numerical values and justification	223
Bibliography	230

List of Figures

1.1	Schematic of the atmosphere showing the different layers.	2
1.2	The Earth's annual and global mean energy balance.	5
1.3	Global annual mean radiative forcing due to a number of agents.	8
1.4	Persistent contrail coverage (in % area cover) for the 1992 aviation fleet.	10
1.5	Global distribution of the net radiative forcing at the top of the atmosphere. . .	11
1.6	Radiative effect at the top of the atmosphere for a 50 % increase in climate parameters.	13
2.1	Global view of the experimental setup.	20
2.2	Schematic drawing of the reactor.	21
2.3	Top view of the apparatus.	22
2.4	Schematic drawing of the experimental apparatus.	23
2.5	Schematic drawing of the gas inlet line.	25
2.6	The doping gas injection line.	26
2.7	NaCl infrared transmission spectrum.	27
2.8	Top view of the dosing tubes (schematic).	29
2.9	The cryostat Mark I.	31
2.10	Si infrared transmission spectrum.	33
2.11	The cryostat Mark II.	35
2.12	Schematic drawing of the cryostat Mark II.	36
2.13	Dose and rate of deposition of the doping gas	43
2.14	Optical paths	45
2.15	Dependence of optical densities with thickness at low T.	47
2.16	FTIR spectrum of amorphous ice exhibiting the dangling bond	48
2.17	FTIR spectrum of I_h ice.	51
2.18	Inexpensive, homemade thermocouple noise-reducer and amplifier.	52
2.19	Schematic cross-sectional drawing of the cryostat Mark II	54

3.1	Typical calibrations for HCl.	64
3.2	Raw MS signal for HCl at $m/z=36$	68
3.3	Typical interferometric signal of evaporating pure and doped ice.	74
3.4	Arrhenius plot of the evaporative flux of H_2O (J_{ev}) from pure and HX doped ice films.	75
3.5	Temperature dependence of the uptake coefficient γ of H_2O from pure and HX-doped ice films.	76
3.6	Dependence of J_{ev} on the number of HCl molecules adsorbed at 210 K.	77
3.7	Dependence of J_{ev} on the number of HBr molecules adsorbed at 210 K.	78
3.8	Cartoon of the fate of a HCl-doped ice film upon evaporation of H_2O	83
3.9	FTIR absorption spectrum of pure and HCl-doped ice (case 1).	86
3.10	FTIR absorption spectrum of pure and HCl-doped ice (case 2).	87
3.11	FTIR absorption spectrum of pure and HBr-doped ice.	91
3.12	Phase diagram of the HCl/ H_2O system constructed by Molina and coworkers.	94
3.13	Infrared absorbance in transmission at different wavenumbers of interest for the characterization of the crystalline $HCl \cdot 6H_2O$ hexahydrate.	97
3.14	Infrared absorbance in transmission at two wavenumbers of interest for the characterization of the crystalline $HCl \cdot 6H_2O$ hexahydrate.	100
4.1	Schematic drawing of the experimental apparatus equipped with QCM.	109
4.2	Quartz crystal microbalance (QCM) support housed in its tightly fitted Delrin insulation.	113
4.3	Horizontal cut (view from the top) through dosing tubes and IR beam transmitted across the Si window attached to the cryostat.	115
4.4	Complete recording of an exchange sequence (mass transfer) between the optical cryostat and the QCM.	116
4.5	FTIR spectra in transmission of the ice film on the Si window at the beginning and the end of a mass transfer sequence.	118
4.6	Synopsis of experimental results on the evaporative flux J_{ev} of H_2O from pure ice using either the cryostat or the QCMB as substrate for deposition.	123
4.7	Synopsis of results on the uptake coefficient from pure ice as a function of temperature.	124
4.8	Approach to equilibrium of the partial pressure of H_2O	127
4.9	Realtime change of the raw QCM signal S_{QCM}^{DYN}	129
4.10	Temporal change of several experimental observables of importance.	134
4.11	Experimental results on the evaporative flux J_{ev} of H_2O from ice.	137

4.12 Synopsis of results on the flux of evaporation J_{ev} from pure ice as a function of temperature.	139
4.13 Arrhenius representation of k_{cond} of H_2O showing a change of slope.	142
4.14 QCM temperature control device.	146
4.15 Schematic drawing of the temperature controlling device.	147
4.16 Investigation of the morphology of the gold coating of the piezoelectric crystal using Atomic Force Microscopy.	149
4.17 3D view corresponding to set C of Figure 4.16.	151
4.18 Change of the equivalent pit volume V_v as a function of height H	152
4.19 Cross-section of the scanned sample area presented in Panel C2 of Figure 4.16.	154
5.1 Horizontal cut (view from the top) containing the HNO_3 dosing tube.	162
5.2 Schematic drawing of the gas admission line.	166
5.3 Typical MS signals for $m/z=30$ during directed HNO_3 admission onto the quartz sensor of the QCM.	168
5.4 Typical MS signal at $m/z=30$ during evaporation of an ice film.	171
5.5 Typical experimental protocol of the evaporation at 189 K of a 1.2 μm thick ice film doped with approximately 5 monolayers of HNO_3	174
5.6 Profile of the change of the average relative concentration of HNO_3 at 189 K, χ_{HNO_3} , in the ice film treated in Figure 5.5 during water evaporation.	179
5.7 Change of the evaporative flux of H_2O , J_{ev} , with the average relative concentration, χ_{HNO_3}	180
5.8 Typical transmission FTIR spectra recorded during experiments to evaluate the impact of the deposition of HNO_3 on the vapor pressure of H_2O upon ice.	182
5.9 Change in $P_{\text{H}_2\text{O}}$ in the presence of HNO_3 -doped ice.	183
5.10 Change of evaporative flux, J_{ev} , of H_2O with the average relative concentration, χ_{HNO_3} : Range 1	185
5.11 Change of evaporative flux, J_{ev} , of H_2O with the average relative concentration, χ_{HNO_3} : Range 2	186
5.12 Change of evaporative flux, J_{ev} , of H_2O with the average relative concentration, χ_{HNO_3} : Range 3	187
5.13 Synopsis of the dependence of $r^{\text{b/e}}$ on the rate of deposition R_{HNO_3} of HNO_3	190
5.14 Synopsis of the dependence of $r^{\text{b/e}}$ on the adsorbed number of HNO_3 , $N_{\text{HNO}_3}(t_{\text{dyn}})$	191
5.15 Synopsis of the dependence of d_D on the rate of deposition R_{HNO_3} of HNO_3	194
5.16 Synopsis of the dependence of d_D on the adsorbed number of HNO_3 , $N_{\text{HNO}_3}(t_{\text{dyn}})$	195

6.1	Change of the evaporative flux J_{ev} of H_2O with the average relative concentration, χ_{HCl}	209
6.2	Synopsis of the dependence of $r^{\text{b/e}}$ on the rate of deposition R_{HCl}	210
6.3	Synopsis of the dependence of $r^{\text{b/e}}$ on the number of adsorbed HCl.	211
6.4	Synopsis of the dependence of d_{D} on the rate of deposition R_{HCl}	212
6.5	Synopsis of the dependence of d_{D} on the number of adsorbed HCl.	213
7.1	Overview of the grazing incidence QCM.	219
7.2	FTIR RAIR spectrum under grazing incidence of 68° of pure ice deposited on a QCM gold-coated piezoelectric sensor.	220

List of Tables

1.1	Main components of dry air and their average lifetime in the atmosphere [3, 4].	3
1.2	Main greenhouse gases in the atmosphere taken from [3] and [4].	4
3.1	Data on two different experimental hardware configurations and results of the calibrations.	63
3.2	HCl mass balance for 6 typical experiments.	69
3.3	Experimental observations of the HeNe interferogram during the evaporation of a 1 μm thick pure, as well as HCl-doped, ice film.	82
3.4	FTIR spectral observations of a 1 μm thick ice film doped with HCl using different dosing protocols at 190 K.	85
3.5	Infrared absorbance in transmission at different wavelengths of interest for the characterization of the crystalline HCl \cdot 6H ₂ O hexahydrate.	98
4.1	Hardware parameters of both cryogenic sample support.	110
4.2	Representative results for J_{ev} and k_{cond} for H ₂ O vapor in the presence of ice in the range 181-223 K.	135
4.2	<i>Continued...</i>	136
5.1	Hardware parameters of both cryogenic sample supports for the kinetic study of HNO ₃ -doped ice.	163
5.2	Representative experimental results for the kinetics of H ₂ O evaporation in the presence of HNO ₃ for three temperature ranges.	170
5.3	Partial pressure of HNO ₃ required to result in the measured rate of HNO ₃ deposition, R_{HNO_3} , listed in column 4 and also given in column 5 in Table 5.2.	188
6.1	Hardware parameters of both cryogenic sample supports for the kinetic study of HCl-doped ice.	205

- 6.2 Representative experimental results for the kinetics of H₂O evaporation in the presence of HCl for different temperatures, rates of deposition and doses of HCl. 207

Chapter 1

Introduction

From

"Tout est pour le mieux dans le meilleur des mondes possibles"

(inspired by Candide of Voltaire)

to

"La conduite humaine est incorrigible dans son éternelle folie dangereuse..."

(A.E. van Vogt)

Of all the planets that are well known up to today, Earth seems to be only one that provides the necessary conditions for the existence of life, as defined by the human race. Its dimensions (polar radius, 6356 km; equatorial radius, 6377 km; volume, $1.083 \cdot 10^{12} \text{ m}^3$) and average density (5.517 g cm^{-3}) have allowed the emergence of an atmosphere and its position relative to the Sun ($150 \cdot 10^6 \text{ km}$) has permitted the presence and persistence of liquid water that is indispensable to the appearance of life. In addition, the presence of a magnetic field acts as a protective barrier against high energy particles originating from the Sun, the solar wind [1].

The terrestrial atmosphere which is relatively thin (approximately 100 km) compared to the diameter of the planet is commonly divided into different layers that are presented in Figure 1.1.

The troposphere, our living space, extends from the surface of the Earth to altitudes between 8 and 17 km depending on latitude.

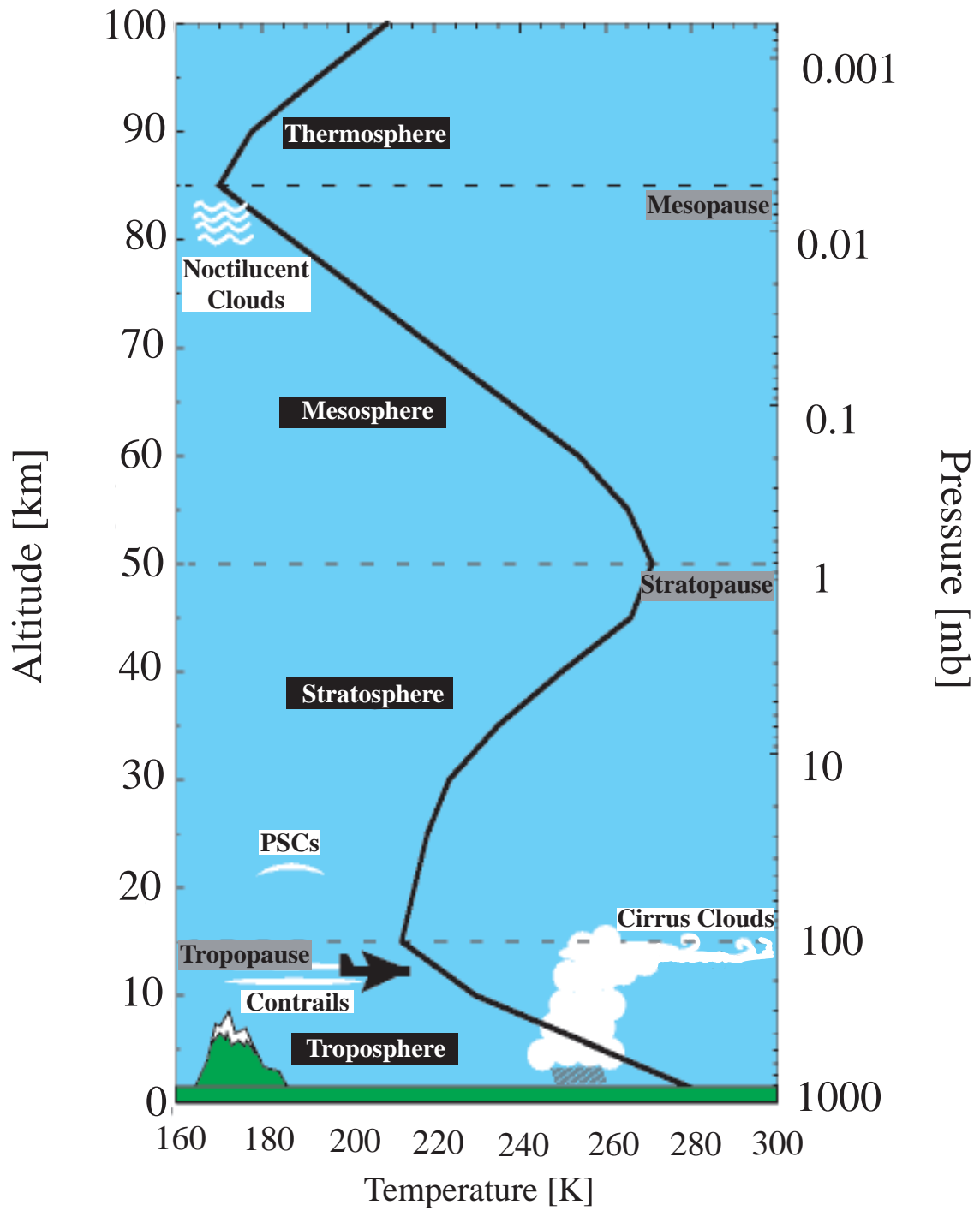


Figure 1.1: Schematic of the atmosphere showing the different layers as well as the location of atmospheric ice particles. The temperature profile of the atmosphere is shown by the solid black line (adapted from Zondlo et al. [2]).

Gas	Formula	volumetric percentage	Average lifetime
Nitrogen	N ₂	78.08	1.6·10 ⁷ yr
Oxygen	O ₂	20.94	1.0·10 ⁴ yr
Argon	Ar	0.934	-
Carbon Dioxyde	CO ₂	0.035	5 yr
Neon	Ne	0.0018	-
Helium	He	0.00052	-
Methane	CH ₄	0.00017	8 yr
Ozone	O ₃	0.000001-0.000004	100 d

Table 1.1: Main components of dry air and their average lifetime in the atmosphere [3, 4].

Most of the weather (clouds, rain, snow) or meteorological phenomena occur in this region. The tropopause is the thin region that separates the troposphere from the next atmospheric layer, the stratosphere, which extends up to an average altitude of 45 km and is the location where important atmospheric events such as the ozone hole occur.

The mean composition of the atmosphere presented in Table 1.1 points to the predominance of nitrogen and oxygen, which together with argon, represent more than 99.9 % of the total mass of atmospheric gases.

This composition atmospheric composition is the result of biological, microbiological, chemical and physical processes that are not only of natural origin but -as it is now commonly admitted- also depends on anthropogenic perturbation of natural cycles that have begun at the same time as the beginning of the industrialized era around 1850.

In addition to protecting us from some harmful effects of high energy ultraviolet radiation, the absorbance of solar radiation by the atmosphere leads to an increase of the temperature at the surface of the Earth. Indeed, by considering the Earth in a simple model as an ideal black body radiator the incoming solar radiation should lead to a globally averaged temperature of 5.5 °C at the surface of the Earth according to the Stefan-Boltzmann law. If we now take into account that the Earth is not a black body in the visible and has an average albedo of 0.3 the estimated surface temperature decreases to -18.3 °C. A more complex model, taking into account partial absorption and multidirectional emission of the atmosphere considered as a grey

Gas	Formula	concentration	Average lifetime
Carbon Dioxide	CO ₂	350 ppm	5 yr
Methane	CH ₄	1.7 ppm	8 yr
Nitrous Oxide	NO ₂	310 ppb	120 yr
Chlorofluorocarbons	CFC	100 ppt-1 ppb	> 100 d
Ozone	O ₃	10-40 ppb (unpolluted troposphere) 10 ppm (stratosphere, 25-30 km)	100 d
Water	H ₂ O	Variable	10 d

Table 1.2: Main greenhouse gases in the atmosphere taken from [3] and [4].

body as well as non-radiative energy transfer processes such as evapotranspiration, leads to the balance presented in Equation 1.1 [5]:

$$S_r \times \frac{(2 - f)(1 - A - a_{sw}) + a_{sw}}{2 - a_{lw}} = \sigma T_{\text{Earth}}^4 \quad (1.1)$$

with S_r the total incoming solar radiation to the Earth, f the fraction of the energy that is transferred from the planetary surface to the atmosphere mainly by evapotranspiration, A the global mean planetary albedo, a_{sw} the short-wave light absorption of the atmosphere, a_{lw} the infrared absorbance of the atmosphere and T_{Earth} the temperature of the terrestrial surface. From Equation 1.1 we obtain a global mean temperature of the Earth of $T_{\text{Earth}}=15$ °C using $f=30$ %, $a_{sw}=1$ % and $a_{lw}=97$ %. In addition, the higher the absorption by the atmosphere the more important is T_{Earth} . This phenomenon is known as the "greenhouse effect". Figure 1.2 lists the Earth's annual and global mean energy balance and illustrates the different energy exchange processes that occur between the Earth and its atmosphere. The main greenhouse gases are summarized in Table 1.2.

All these gases have both natural and anthropogenic sources, except for CFCs, and Equation 1.1 reveals that an increase of the sources, mainly due to anthropogenic activities, may induce an increased greenhouse effect. In contrast, increasing amounts of atmospheric aerosols and clouds may induce a decrease of the globally average temperature called whitehouse effect [6] due to scattering of radiation.

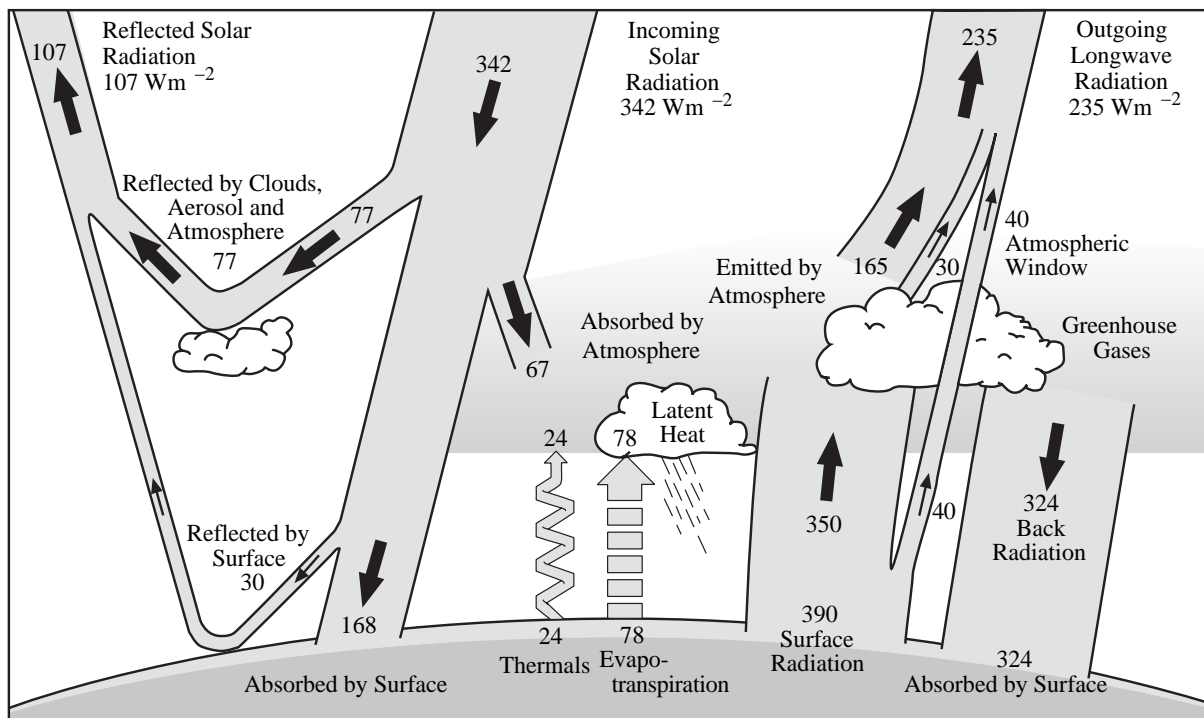


Figure 1.2: The Earth's annual and global mean energy balance [4]. Of the incoming solar radiation, 49 % (168 W m^{-2}) is absorbed by the surface. That heat is returned to the atmosphere as sensible heat, as evapotranspiration (latent heat) and as thermal infrared radiation. Most of this radiation is absorbed by the atmosphere, which in turns emits radiation both up and down. The radiation lost to space originates at cloud tops and atmospheric regions much colder than the planetary surface. This causes a greenhouse effect. Original source: Kiehl and Trenberth, 1997: Earth's Annual Global Mean Energy Budget, Bull. Am. Met. Soc.78, 197-208.

1.1 The impact of anthropogenic activities

Since 1850 and the beginning of the industrialized era the environment is under an increasing anthropogenic pressure that perturbs the natural cycles.

The most striking recent long-term atmospheric impact of human activities on the atmosphere is the phenomenon known as "the ozone hole". Ozone is a naturally produced species present in the atmosphere and consists of three bound oxygen atoms. It is present in both the stratosphere (90 % of the total of O_3) and the troposphere. In the stratosphere ozone protects the Earth by absorbing ultraviolet light, and consequently all forms of life as well as the environ-

ment, from this radiation. Its relative concentration is significant across an altitude range of 10 to 70 km and reaches a relative maximum of 8 ppmv at 30 km whereas its absolute stratospheric concentration maximum is measured at 20 km. The ozone concentration is maintained by the equilibria that were evoked in the 1930's by Chapman and consists of four basic equations that are known as the *Chapman Mechanism*. However, this mechanism is not sufficiently complete and fails to explain the natural ozone atmospheric concentration by overestimating it by a factor of two. The mechanism was completed in the 1970's following the work of Crutzen [7] on the catalytic cycles produced by the reactions of nitrogen oxides, NO_x , with O_3 .

Since the early 1950's the British Antarctic Survey had measured a steady decrease of stratospheric ozone using a Dobson spectrometer. In 1974, Lovelock [8] shed new light on the atmospheric fate of anthropogenic species such as chlorofluorocarbons (CFC's) invented in 1928 and been largely used since the 40's. Their high chemical stability allowed them to diffuse through the troposphere and to reach the stratosphere where they undergo photolysis. At the same time, Molina and Rowland [9] showed that the chlorine atoms released during the photodissociation of CFC's react with ozone to initiate a catalytic cycle that allows the destruction of approximately 100 000 molecules of O_3 per chlorine atom before chain reaction termination. Molina and Rowland thus predicted a reduction of up to 13 % of the stratospheric ozone concentration. In 1985, Farman et al. [10] of the British Antarctic Survey showed that ozone had decreased down to unprecedented levels during the Southern Hemisphere spring period and the trend of the decrease was confirmed year after year. This phenomenon is now better known as "the Antarctic ozone hole". In the Antarctic area, the specific meteorological conditions, namely the temperatures that may be lower than 190 K due to the yearly formation of a Vortex that isolates the high altitude air mass from the global atmosphere, favors the formation of ice particles condensed from the water vapor commonly known as Polar Stratospheric Clouds (PSC's). One may distinguish three different classes of PSC's, namely type Ia, Ib and II. Type Ia is believed to consist mainly of nitric acid trihydrate (NAT) [11]. It is thought that type Ib consists of supercooled ternary $\text{H}_2\text{SO}_4/\text{HNO}_3/\text{H}_2\text{O}$ solution droplets generated from sulfate aerosols [12],

whereas type II forms when the temperature decreases below 188 K and is likely to be a pure water ice particle [13]. Nowadays, the heterogeneous reactions occurring on the surfaces of these PSC's are known to play an important role in controlling the abundance of O₃ in the polar stratosphere by converting hydrogen halide reservoir species such as HX (X=Cl, Br) into photolytically active halogens [14, 15, 16, 17]. Whereas the international community has been periodically warned by scientists since the 1970's, more than 10 years were necessary for the Vienna convention in 1985 to establish an international framework for action and two additional years before the Montreal Protocol in 1987 officially took into account the impact of anthropogenic activities on the stratospheric ozone layer. It requires the developing and industrialized countries to stop the production of ozone depleting species such as CFCs. Based on this protocol and on the lifetime of these substances an increase in the ozone layer is not expected before 2050 [17] or at least 2020 [18].

In addition to the heterogeneous reactions occurring on the PSC particles, recent studies indicate that Cirrus cloud ice particles formed near the tropopause (see Figure 1.1) may act as substrates for heterogeneous reactions akin to PSC's with a similarly high efficiency [19, 20]. Contrary to the polar stratosphere where the persistence of PSC's is sufficient for complete heterogeneous processing of halogen containing reservoir molecules, the situation in the midlatitude upper troposphere is quite different. Cirrus clouds have a limited lifetime during which heterogeneous processing may occur. Borrmann et al. [19] have assumed an average cloud lifetime of only 20 min which nevertheless led to a significant predicted impact on atmospheric chemistry. This may explain the global ozone depletion of approximately 5 % that is observed at midlatitude between 30 and 70 ° over the past two decades. Therefore, the evaporative lifetime of Cirrus ice particles and the impact of atmospheric trace gas adsorbates such as HX on this lifetime are important parameters controlling the extent of heterogeneous processes.

In addition to these chemical considerations, the evaporative lifetime of water ice particles, pure or doped with atmospheric trace gases, is of importance regarding the radiative forcing of the climate system. Going back to the previously cited greenhouse effect we may consider the

case of H_2O vapor. Water vapor is the most important greenhouse gas in the atmosphere and ice clouds occurring in the upper troposphere, both as natural Cirrus clouds as well as aviation contrails, have garnered the interest of the global change community because of their large contribution to the radiative balance of the atmosphere. Figure 1.3 illustrates the importance of the global mean radiative forcing (W m^{-2}) of the climate system for the year 2000 relative to 1750 [4]. A positive radiative forcing tends to contribute to the increase of the averaged global temperature and a negative one tends to contribute to its decrease. As shown in Figure 1.3, the radiative forcing of natural Cirrus and contrails is not well understood as indicated by VL in the axis level of scientific understanding (LOSU: H, high; M, medium; L, low; VL, very low).

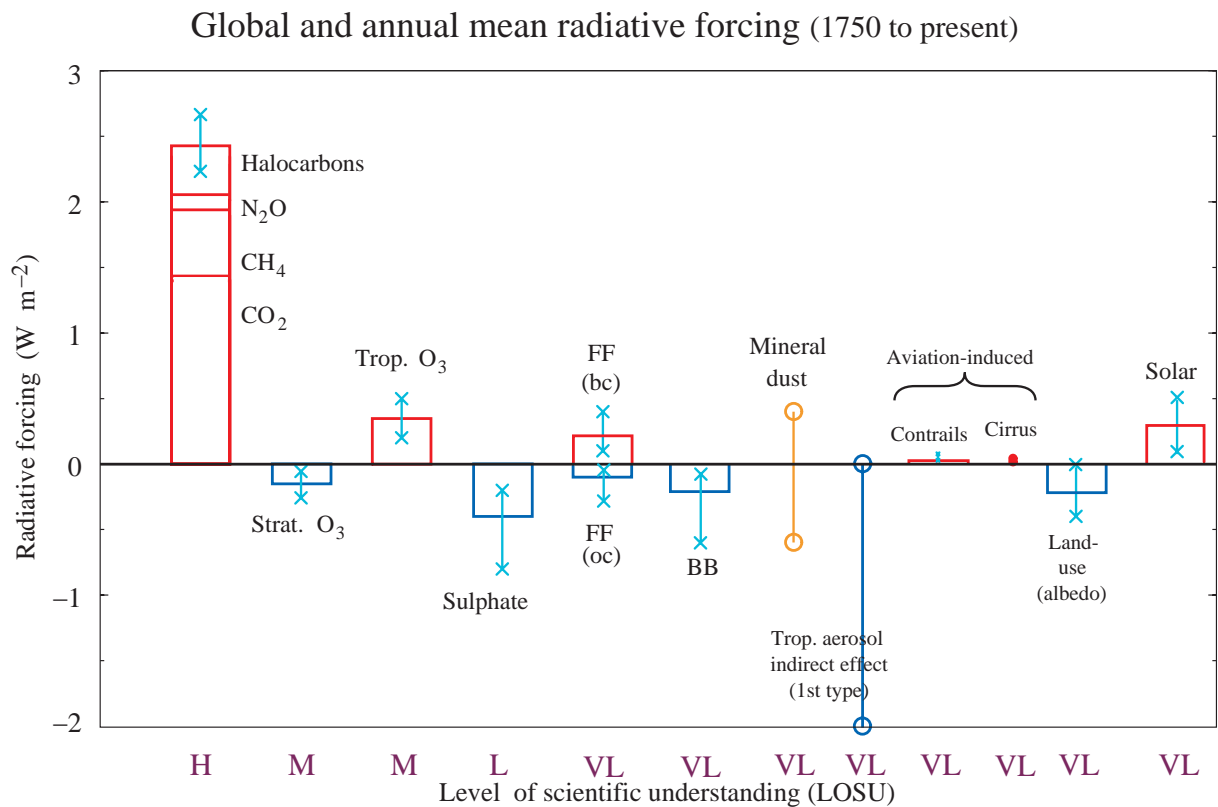


Figure 1.3: Global annual mean radiative forcing due to a number of factors for the period from pre-industrial 1750 to present [4].

Cirrus clouds are the most common form of high-level clouds forming in the vicinity of the

tropopause. In the tropics, their formation is mainly triggered by deep convection [21] while over northern midlatitudes they are associated with large ice supersaturated areas in the upper troposphere [22]. Cirrus cloud formation strongly depends on the existence of small particles that provide nuclei for ice crystal formation [23]. Cirrus clouds may have both positive and negative contribution to radiative forcing depending on their thickness. Thin Cirrus clouds produce a positive radiative forcing at the top of the atmosphere while thick Cirrus clouds may cause cooling [24, 25, 26].

Aviation induced condensation trails (contrails) are visible clouds that form at the exhaust of the aircrafts when liquid droplets may form on cloud condensation nuclei and freeze to ice particles [27]. In [28], Schumann described the parameters leading to contrail formation and persistence. Contrails quickly evaporate when the ambient air is dry or persist for hours when the ambient air is supersaturated with respect to ice [29] which is common in the upper troposphere at northern midlatitudes [30, 31]. Contrails present a similar trend as natural Cirrus clouds do in the case of thin Cirrus cover.

It is clear that the radiative forcing properties of natural Cirrus clouds or contrails are intimately linked to the kinetic processes, namely condensation and evaporation, that occur at the surface of ice particles, as their lifetime and thus their coverage depends on these kinetic parameters. Recently, an interesting example of the effect of civil aviation on contrail coverage over much of the North American continent was afforded by the events of September 11th 2001 in the aftermath of which commercial air traffic was completely grounded for three days. The data pointed to the conclusion of the possible direct climatic impact of aviation contrails [32, 33] as did statistical and modeling studies performed in the recent past [34, 35].

In addition, the conversion of contrails into Cirrus clouds is a recent field of interest that generally points to the significant potential of contrails to convert into Cirrus clouds thus changing the cloud cover over a region that is the subject of a high density of commercial air traffic [30, 36, 37, 38, 39, 40].

Figures 1.4 and 1.5 illustrate the importance of contrails in terms of the coverage and the

global annual contribution to the net radiative forcing for 1992 and as a prediction for 2050, respectively [4].

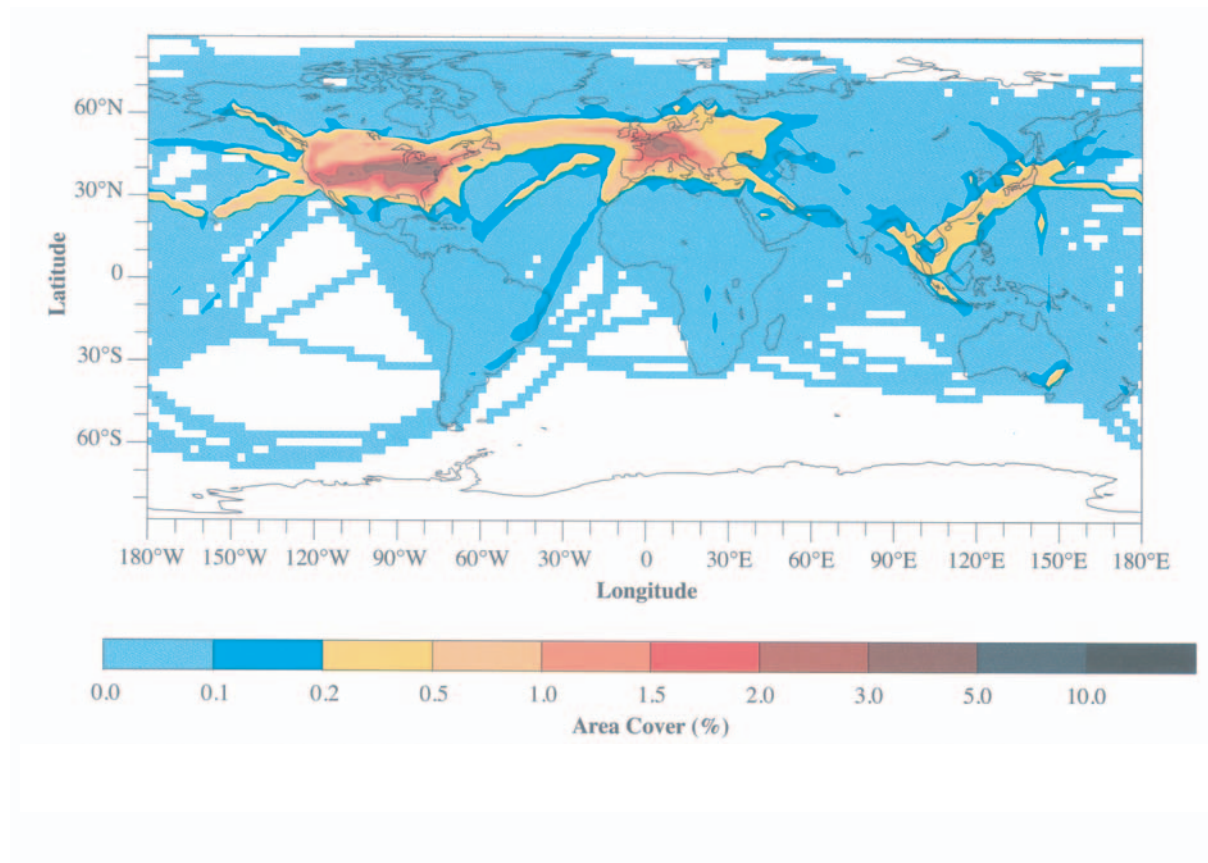


Figure 1.4: Persistent contrail coverage (in % area cover) for the 1992 aviation fleet, assuming a linear dependence on fuel consumption and overall efficiency of propulsion of 0.3. The global mean cover is 0.1 %. Taken from [4] with the original data of [40].

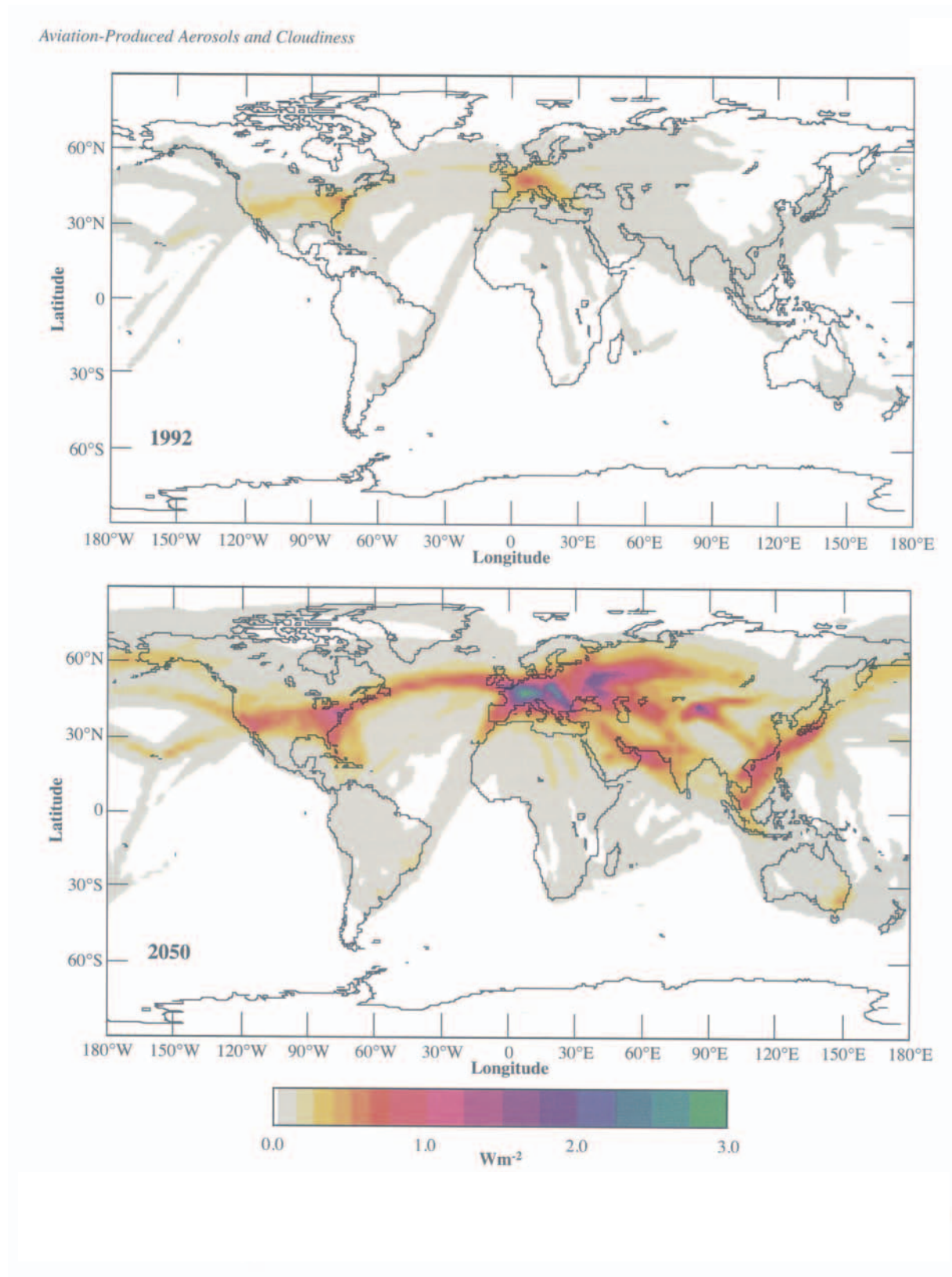


Figure 1.5: Global distribution of the net radiative forcing at the top of the atmosphere in daily and annual averages for contrails with $0.55 \mu\text{m}$ optical depth of 0.3, for 1992 and 2050 scenario.

One may notice that in the case of the 2050 scenario large areas over the European continent are covered with contrails that should lead to a net radiative forcing in the range 1 to 3 W m⁻² as displayed by the figure color bar legend. This value should be compared to the 1.5 W m⁻² of global annual radiative forcing due to accumulation of CO₂, for example (see Figure 1.3). In addition, Figure 1.6 taken from the CERES report * illustrates the importance of the significant 50 % increase of clouds, as well as other species as CO₂, on the radiative effect at the top of the atmosphere. It clearly shows the large impact of clouds compared to CO₂ both in terms of the positive and negative radiative forcing. It thus makes the case of the importance of improving the knowledge on the Cirrus clouds regarding the kinetics of evaporation and condensation of the ice particles.

1.2 Motivation and plan of the thesis

Atmospheric sciences consist of three major axes:

- Field measurement
- Laboratory studies
- Numerical modelling

The present work belongs to the second category and is meant to increase the knowledge in kinetic data, namely the rates of condensation and evaporation, of water vapor in the presence of ice particles that may be used as surrogates for ices characteristic of the atmosphere, namely the

*NASA's Earth Observing System (EOS) is part of an international program for studying the Earth from space using a multiple-instrument, multiple-satellite approach. This EOS program is critical for improving our scientific understanding of ongoing natural and human-induced global climate change and providing a sound scientific basis for developing global environmental policies. The Clouds and the Earth's Radiant Energy System (CERES) experiment is one of the highest priority scientific satellite instruments developed for EOS. CERES products include both solar-reflected and Earth-emitted radiation from the top of the atmosphere to the Earth's surface. Cloud properties are determined using simultaneous measurements by other EOS instruments such as the Moderate Resolution Imaging Spectroradiometer (MODIS). Analyses of the CERES data, which build upon the foundation laid by previous missions such as the Earth Radiation Budget Experiment (ERBE), will lead to a better understanding of the role of clouds and the energy cycle in global climate change. For further detail: "http://asd-www.larc.nasa.gov/ceres/".

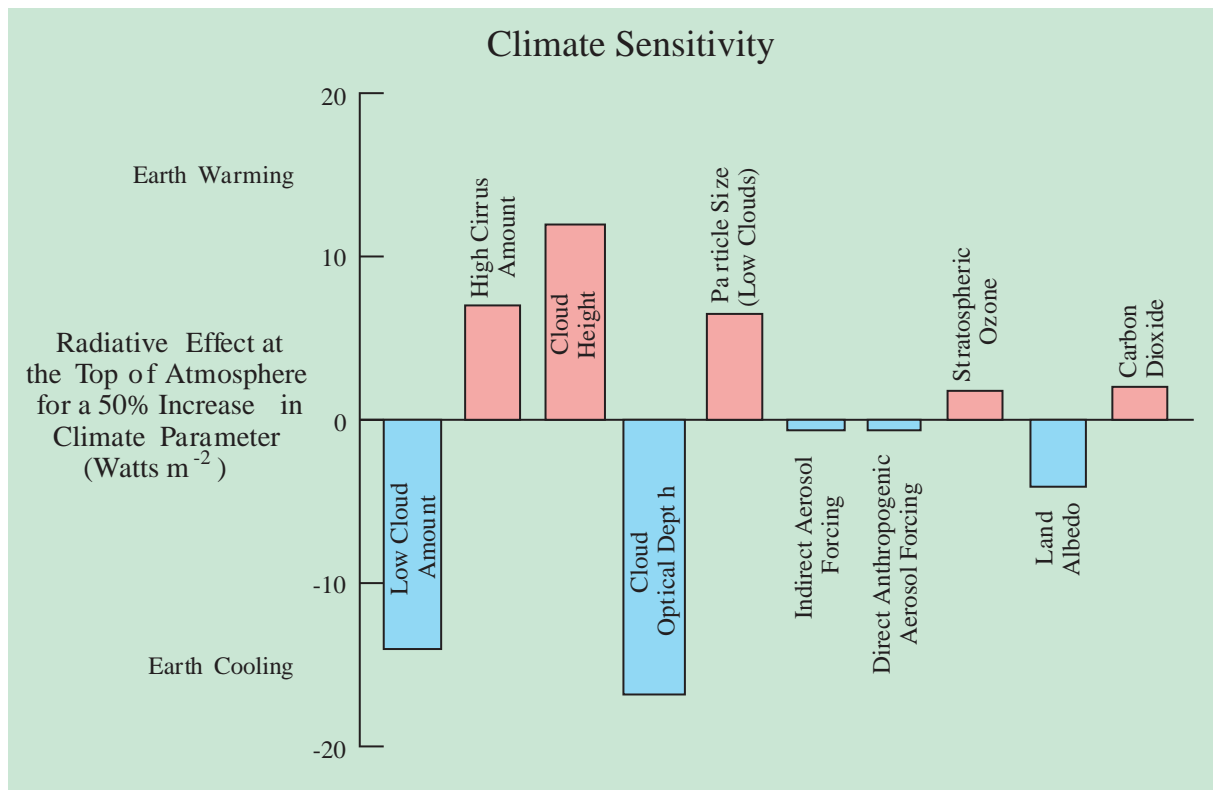


Figure 1.6: Radiative effect at the top of the atmosphere for a 50 % increase in climate parameters (source in the text).

ones constituting the PSC's and the Cirrus clouds. Such data may be used in cloud modelling mainly in the region that are undersaturated with respect to the vapor pressure of water in the presence of ice.

The progress of this work follows the development of an experimental apparatus which permits experimental conditions that largely cover the temperature range necessary to imitate atmospheric temperatures and pressures regarding water and the trace gases used and that may be encountered in the PSC's and Cirrus clouds regions.

Chapter Two provides an overview of the experimental setup which has constantly evolved during the course of this work and presents the basic measurement techniques. In Chapter Three, a method is presented that allows the measurements of the kinetics of both condensation and

evaporation of H_2O vapor in the presence of a pure or HX-doped ($\text{X}=\text{Cl}$ and Br) ice film. Based on a multiple diagnostic approach the experiments also afford the knowledge of some infrared characterization of the species involved in the kinetic change due to the doping. Chapter Four introduces a new method that involves a quartz crystal microbalance whose piezoelectric sensor is used to measure the kinetics of condensation and evaporation of pure ice films after suitable calibrations. Chapter Five and Six exploit the setup presented in Chapter Four for ice that have been doped with atmospherically relevant amounts of HNO_3 and HCl , respectively. Once more the perturbation of the kinetics of condensation and evaporation of H_2O in the presence of an ice film are presented. Finally, Chapter Seven affords an overview of the future evolution of the multiple diagnostics experimental setup.

Atmospheric implications are discussed in each part regarding the results.

Last but not least, one should remark that in the course of this thesis, the term evaporation is commonly used whenever a water molecule leaves the ice surface, whereas desorption is commonly used. The fact is that even at temperatures as low as 190 K some studies invoke the presence of a quasi-liquid layer sitting on top of the bulk ice substrates. As a result we will call henceforth the process of "desorption" of H_2O into the gas phase "evaporation".

Bibliography

- [1] J. Lacroux, *De la terre aux étoiles*, Bordas, 1986.
- [2] M. A. Zondlo, P. K. Hudson, A. J. Prenni, and M. A. Tolbert, *Annual Review of Physical Chemistry*, 2000, **51**, 473–499.
- [3] P. Hobbs, *Introduction to Atmospheric Chemistry*, Cambridge University Press, 1998.
- [4] J. T. Houghton and I. P. on Climate Change. Working Group I., *Climate change 2001 : the scientific basis : contribution of Working Group I to the third assessment report of the Intergovernmental Panel on Climate Change*, Cambridge University Press, Cambridge, UK ; New York, 2001.
- [5] R. M. Harrison and R. E. van Grieken, *Atmospheric Particles*, John Wiley and Sons, Ltd, New York, 1998.
- [6] S. E. Schwartz, *Journal of Aerosols Science*, 1996, **27**, 359–382.
- [7] P. J. Crutzen, *Journal of Geophysical Research*, 1971, **76**(30), 7311.
- [8] J. E. Lovelock, *Nature*, 1974, **252**(5481), 292–294.
- [9] M. J. Molina and F. S. Rowland, *Nature*, 1974, **249**(5460), 810–812.
- [10] J. C. Farman, B. G. Gardiner, and J. D. Shanklin, *Nature*, 1985, **315**(6016), 207–210.
- [11] D. Hanson and K. Mauersberger, *Geophysical Research Letters*, 1988, **15**(8), 855–858.
- [12] K. S. Carslaw, B. P. Luo, S. L. Clegg, T. Peter, P. Brimblecombe, and P. J. Crutzen, *Geophysical Research Letters*, 1994, **21**(23), 2479–2482.
- [13] O. B. Toon, R. P. Turco, J. Jordan, J. Goodman, and G. Ferry, *Journal of Geophysical Research-Atmospheres*, 1989, **94**(D9), 11359–11380.
- [14] S. Solomon, R. R. Garcia, F. S. Rowland, and D. J. Wuebbles, *Nature*, 1986, **321**(6072), 755–758.
- [15] M. A. Tolbert, M. J. Rossi, R. Malhotra, and D. M. Golden, *Science*, 1987, **238**(4831), 1258–1260.
- [16] P. O. Wennberg, J. W. Brault, T. F. Hanisco, R. J. Salawitch, and G. H. Mount, *Journal of Geophysical Research-Atmospheres*, 1997, **102**(D7), 8887–8898.
- [17] U. S. N. Oceanic, A. Administration., U. S. N. Aeronautics, and S. Administration., Scientific assessment of ozone depletion: 2002, global ozone research and monitoring project - report 47, 2002.
- [18] B. M. Knudsen, N. R. P. Harris, S. B. Andersen, B. Christiansen, N. Larsen, M. Rex, and B. Naujokat, *Atmospheric Chemistry and Physics*, 2004, **4**, 1849–1856.

- [19] S. Borrmann, S. Solomon, J. E. Dye, and B. P. Luo, *Geophysical Research Letters*, 1996, **23**(16), 2133–2136.
- [20] S. Solomon, S. Borrmann, R. R. Garcia, R. Portmann, L. Thomason, L. R. Poole, D. Winker, and M. P. McCormick, *Journal of Geophysical Research-Atmospheres*, 1997, **102**(D17), 21411–21429.
- [21] E. J. Jensen, O. B. Toon, H. B. Selkirk, J. D. Spinhirne, and M. R. Schoeberl, *Journal of Geophysical Research-Atmospheres*, 1996, **101**(D16), 21361–21375.
- [22] K. Gierens, U. Schumann, M. Helten, H. Smit, and P. H. Wang, *Journal of Geophysical Research-Atmospheres*, 2000, **105**(D18), 22743–22753.
- [23] E. J. Jensen and O. B. Toon, *Geophysical Research Letters*, 1997, **24**(3), 249–252.
- [24] G. L. Stephens and P. J. Webster, *Journal of the Atmospheric Sciences*, 1981, **38**(2), 235–247.
- [25] Q. Fu and K. N. Liou, *Journal of the Atmospheric Sciences*, 1993, **50**(13), 2008–2025.
- [26] J. E. Penner, I. P. on Climate Change. Working Group I., and I. P. on Climate Change. Working Group III., *Aviation and the global atmosphere : a special report of IPCC Working Groups I and III in collaboration with the Scientific Assessment Panel to the Montreal Protocol on Substances that Deplete the Ozone Layer*, Cambridge University Press, Cambridge, 1999.
- [27] D. K. Lynch, *Cirrus*, Oxford University Press, Cambridge ; New York, 2002.
- [28] M. Ponater, S. Brinkop, R. Sausen, and U. Schumann, *Annales Geophysicae-Atmospheres Hydrospheres and Space Sciences*, 1996, **14**(9), 941–960.
- [29] E. J. Jensen, O. B. Toon, S. Kinne, G. W. Sachse, B. E. Anderson, K. R. Chan, C. H. Twohy, B. Gandrud, A. Heymsfield, and R. C. Mialke-Lye, *Journal of Geophysical Research-Atmospheres*, 1998, **103**(D4), 3929–3936.
- [30] K. Gierens, U. Schumann, M. Helten, H. Smit, and A. Marenco, *Annales Geophysicae-Atmospheres Hydrospheres and Space Sciences*, 1999, **17**(9), 1218–1226.
- [31] E. J. Jensen, O. B. Toon, S. A. Vay, J. Ovarlez, R. May, T. P. Bui, C. H. Twohy, B. W. Gandrud, R. F. Pueschel, and U. Schumann, *Journal of Geophysical Research-Atmospheres*, 2001, **106**(D15), 17253–17266.
- [32] D. J. Travis, A. M. Carleton, and R. G. Lauritsen, *Nature*, 2002, **418**(6898), 601–601.
- [33] O. Boucher, *Nature*, 1999, **397**(6714), 30–31.
- [34] L. Strom and K. Gierens, *Journal of Geophysical Research-Atmospheres*, 2002, **107**(D18).
- [35] C. S. Zerefos, K. Eleftheratos, D. S. Balis, P. Zanis, G. Tselioudis, and C. Meleti, *Atmospheric Chemistry and Physics*, 2003, **3**, 1633–1644.

-
- [36] P. Minnis, D. F. Young, D. P. Garber, L. Nguyen, W. L. Smith, and R. Palikonda, *Geophysical Research Letters*, 1998, **25**(8), 1157–1160.
- [37] D. P. Duda, P. Minnis, L. Nguyen, and R. Palikonda, *Journal of the Atmospheric Sciences*, 2004, **61**(10), 1132–1146.
- [38] F. Stordal, G. Myhre, W. Arlander, T. Svendby, E. J. G. Stordal, W. B. Rossow, and D. S. Lee, *Atmospheric Chemistry and Physics Discussions*, 2004, **4**, 6473–6501.
- [39] S. A. Changnon, *Journal of Applied Meteorology*, 1981, **20**(5), 496–508.
- [40] R. Sausen, K. Gierens, M. Ponater, and U. Schumann, *Theoretical and Applied Climatology*, 1999, **63**, 1–9.

Chapter 2

Experimental Setup: Global view

In this work we present the different steps in the evolution of a multiple diagnostics experiment especially designed for the investigation of the kinetics of condensation and evaporation of H₂O from pure and doped-ice films at atmospherically relevant temperatures as well as some pertinent experiments.

This chapter is particularly devoted to the description of the elements that are constituting the skeleton of the setup. The evolving parts, that is the different cryogenic supports that have been used during the course of this work for example, as well as the change in the measurement techniques will be presented each at the time of their presentation.

2.1 Main elements of the experiment

The present experiment consists of a stirred flow reactor equipped with multiple diagnostics that will be described full detail below. Figure 2.1 gives a global view of the main elements of the experimental setup.

The apparatus itself is a stainless steel "cylindrical" reactor of volume $V_r^i=2812 \text{ cm}^3$. All along this work the effective volume V_r of the reactor chamber may change drastically due to the excluded volume owing to the presence of additional elements in the reactor such as

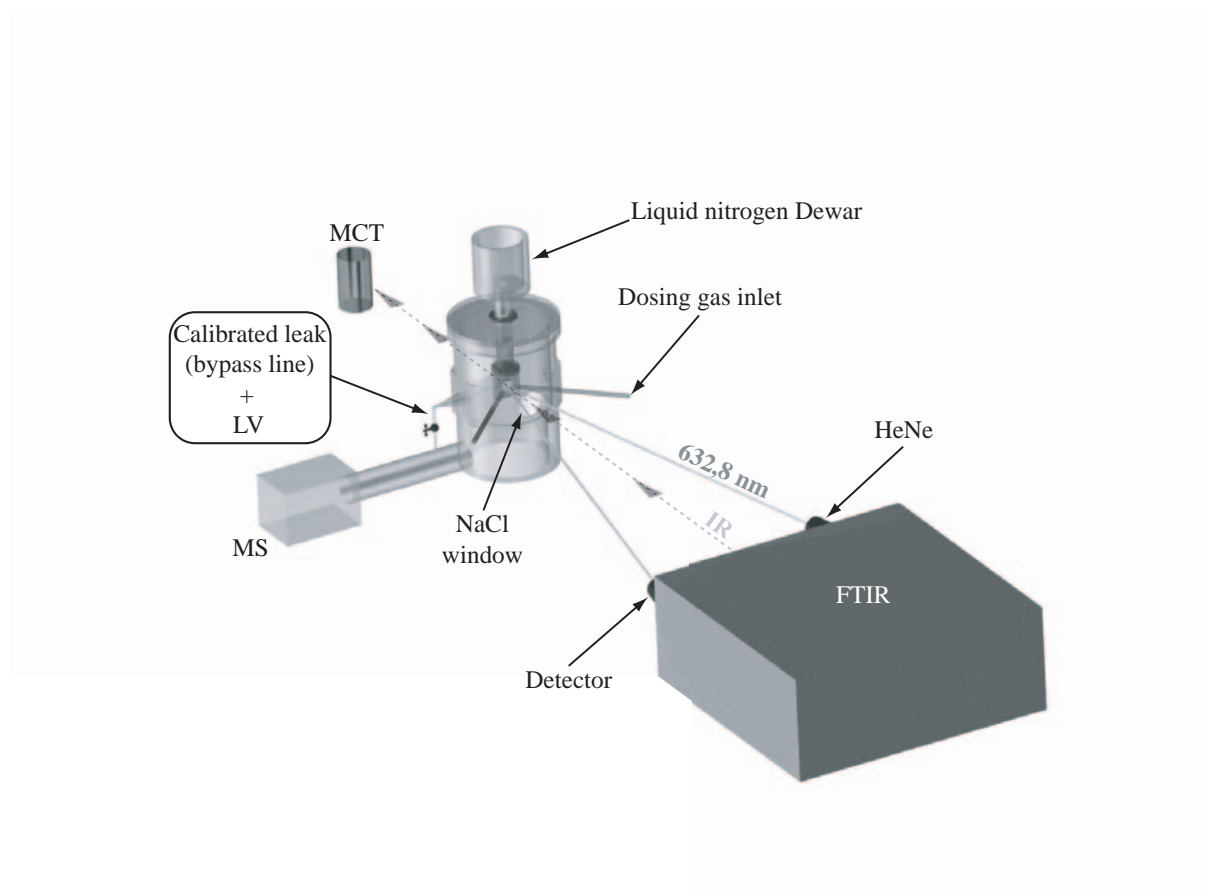


Figure 2.1: Global view of the experimental setup.

different cryogenic supports which led to a volume range of between 1750 and 2450 cm³. Indeed, whereas V_r^1 was calculated from approximate geometric data (see Figure 2.2), V_r was measured for each configuration of the setup using the isothermal expansion of a known quantity of N₂ of approximately 100 Torr contained in a 4500 cm³ Pyrex vessel into the upper chamber (UC) of the apparatus which was previously pumped out to lower than 1.0·10⁻³ Torr. Under these conditions V_r may be calculated using the ideal gas law with all the elements at room temperature:

$$V_r = \left(\frac{P_i}{P_f} - 1 \right) \times V_b \quad (2.1)$$

with V_b being the volume of the storage vessel, P_i and P_f the initial and final pressure in the vessel, respectively, and the initial pressure in UC considered as negligible.

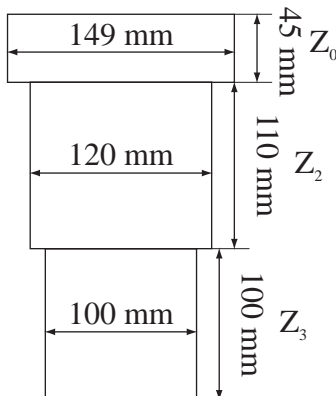


Figure 2.2: Schematic drawing of the reactor. Z_0 , Z_2 and Z_3 indicate the three zones of the apparatus of distinct inner diameters.

The reactor is pumped at the bottom by a turbomolecular pump (VARIAN Turbo-300VHT, $250 \text{ l s}^{-1} \text{ N}_2$) through a 6" diameter gate valve (GV, see Figure 2.3) that can be opened or closed during experiments. When it is closed GV isolates the upper (UC) from the lower (LC) Chamber. UC corresponds, strictly speaking, to the reactor or the measurement chamber whose measured volume is V_r .

A second connection exists between UC and LC and consists of a bypass line (see Figure 2.1) equipped with an ON/OFF valve (LV in Figure 2.4).

This calibrated leak (item 4 including LV, Figure 2.4) allows the effusion of residual gas from the upper to the lower chamber, when LV is open and GV is closed, at a rate constant of effusion, k_{esc} , that depends on the gas of interest and on the setup configuration. These kinetic constants as well as other characteristic experimental parameters will be summarized at the beginning of each chapter. The values of $k_{\text{esc}}(\text{H}_2\text{O})$, $k_{\text{esc}}(\text{HCl})$, $k_{\text{esc}}(\text{HBr})$ and $k_{\text{esc}}(\text{HNO}_3)$ are obtained from

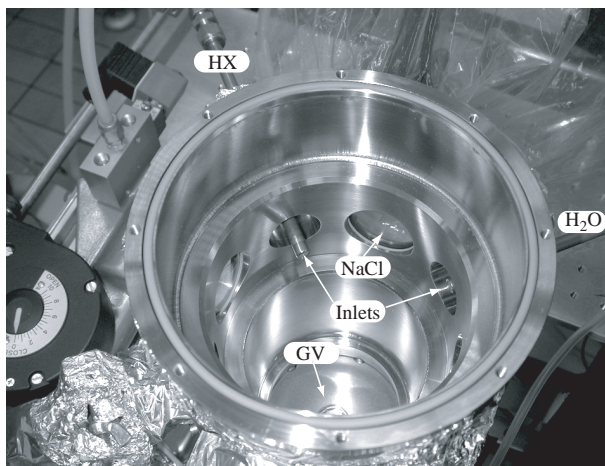


Figure 2.3: Top view of the apparatus. GV: 6" gate valve. Both the inlets used for the injection of H_2O and the dopant that is HCl , HBr or HNO_3 into the reactor are indicated. The zone corresponding to Z_2 in Figure 2.2 also includes two 2" diameter NaCl windows (only one visible here) and the connection to the Baratron absolute pressure gauge.

the exponential decrease of the total pressure in the upper chamber measured using a 1 mbar full scale absolute pressure gauge (MKS Baratron pressure transducer Type 220AHS) when the system is set from *static* (GV and LV closed) to *stirred flow* (GV closed, LV opened) condition by opening the calibrated leak valve after the upper chamber has been filled with the gas of interest. Further explanations of the terms *static*, *stirred flow* as well as *dynamic* (GV open) condition will be given in Section 2.3. In addition, the measured rate constants for effusion have been compared for each setup configuration to gases that are known not to stick to stainless steel, in contrast to all the gases used in this study. In the case of ideal gases it is established from gas kinetic theory that the average gas-wall collision frequency for a given molecule and per cm^2 of the surface, commonly referred to as Z_1 , is given by

$$Z_1 = \frac{\bar{c}}{4V} = 100 \times \sqrt{\frac{8\mathcal{R}T}{\pi M}} \times \frac{1}{4V} \quad (2.2)$$

where Z_1 is the collision frequency in $\text{collision molec}^{-1} \text{ cm}^{-2} \text{ s}^{-1}$, \mathcal{R} the ideal gas constant in $\text{J mol}^{-1} \text{ K}^{-1}$, M the molar mass in kg mol^{-1} , V and T the volume in cm^3 and the wall

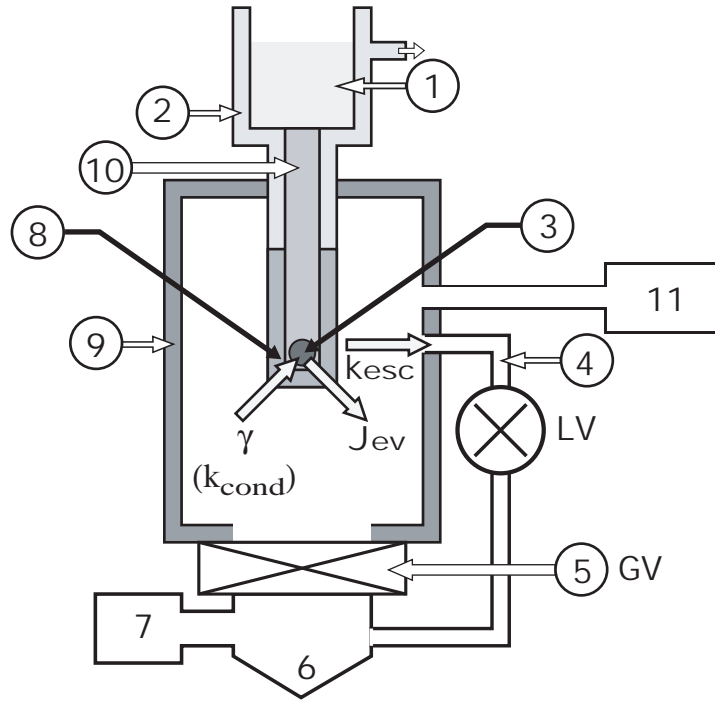


Figure 2.4: Schematic drawing of the experimental apparatus: **1** Liquid nitrogen reservoir, **2** Evacuated Dewar vessel, **3** Silicon window of 0.78 cm^2 area used as a substrate for H_2O deposition, **4** Calibrated leak equipped with valve LV allowing *Static* (valve and **5** closed) and *Stirred flow or Low pumping rate* (valve open and **5** closed) experiments, **5** 6" diameter gate valve GV allowing *Dynamic or High pumping rate* experiments when opened, **6** Flange for Turbo Pump, **7** Quadrupole Mass spectrometer, **8** PTFE thermal insulation isolating the whole cryostat but the Si window, **9** Reactor chamber, **10** Solid copper finger with cartridge heaters for control of the temperature of the Si Substrate, **11** Absolute pressure gauge (Baratron, MKS 220-AHS). Several type T thermocouples (not shown here) are located throughout the vacuum side of the cryostat in order to measure the temperature in different areas (Si window, PTFE Insulation, Reactor and Calibrated Leak walls, etc). In addition, two 2" diameter NaCl windows allow the FTIR monitoring of the condensed phase, and two inlet tubes allow the injection of H_2O as well as the trace gas into the reactor. The hollow arrows (γ , J_{ev} and k_{esc}) describe the important kinetic processes taking place, such as adsorption, desorption and effusion of H_2O vapor.

temperature of the reactor in K, respectively, and \bar{c} the mean velocity of a molecule in cm s^{-1} .

It follows that the theoretical k_{esc} for ideal gas is:

$$k_{\text{esc}} = A_{\text{esc}} \times Z_1 = A_{\text{esc}} \times \frac{\bar{c}}{4V} = 100 \times \sqrt{\frac{8RT}{\pi M}} \times \frac{A_{\text{esc}}}{4V} \quad (2.3)$$

with A_{esc} being the surface area of the effusion orifice. Under given experimental conditions Equation 2.3 leads to a linear dependence of k_{esc} with $\sqrt{\frac{1}{M}}$. As will be shown in some examples in the following chapters this linearity is well observed for the calibration gases, namely N_2 , Ar, Ne, SF_6 and even He. But for the gases of interest in this work a certain discrepancy may appear between semi-empirical (linear dependence, Equation 2.3) and experimental (exponential pressure decrease) data. We conclude that the most relevant value is the measured one considering that the worst case, that is the largest discrepancy, is observed for HNO_3 and is of the order of 30%, the measured value being smaller than the theoretically expected one.

The high pumping speed of the turbomolecular pump (item 6, Figure 2.4) leads to an ultimate pressure as low as $5.0 \cdot 10^{-8}$ Torr enabling the operation of a residual gas mass spectrometer (Balzers Prisma QMS 200, item 7, Figure 2.4) in the lower chamber (LC). Once calibrated, the quadrupole mass spectrometer (MS) allows the measurement of the partial pressure of the residual gas in the reactor and also enables the study of the rate of deposition, R , as well as the dose, N , of the doping gas molecules (HCl , HBr and HNO_3) dispensed on the ice surfaces. MS calibrations and determinations of R and N will be presented in detail in section 2.5.

Before effusing across the calibrated leak the molecules have to flow into the reactor which is the reason for the presence of two gas injection lines whose inlets going across the reactor wall are visible in Figure 2.3. The one on the right is made of stainless steel or glass depending on the specific experiment configuration and is used for the injection of H_2O into the reactor. The dosing tube is connected to a microvalve which is connected on the other side to a Teflon PFA-coated calibrated volume ($\text{CV}(\text{H}_2\text{O})$) of $V_{\text{CV}(\text{H}_2\text{O})} = 44 \text{ cm}^3$. The vernier handle equipped microvalve has been used to set the rate of deposition of H_2O molecules onto the different cryogenic supports used for the growth of ice film in this work. A given H_2O pressure in $\text{CV}(\text{H}_2\text{O})$ and a defined aperture of the microvalve always corresponds to the same rate of effusion of H_2O molecules from $\text{CV}(\text{H}_2\text{O})$ into the reactor. The pressure was chosen to be approximately 30 Torr in most of the cases, and was imposed by the pressure over liquid pure bidistilled-water in a trap that was used as a reservoir to fill $\text{CV}(\text{H}_2\text{O})$. One must notice that

both injection lines can be pumped using a primary pump protected by a liquid-nitrogen cooled trap thus allowing an ultimate pressure lower than 1 mTorr in the dosing lines. Before each ice film growth the liquid water was cooled to form ice at approximately 253 K in order to perform freeze-pump-thaw cycles. Subsequently, the whole H_2O inlet line was evacuated, and once steady-state pressure is reached the frozen water contained in the trap was heated to a temperature around 300 K ensuring that the calibrated volume contained only pure water vapor. Subsequently, the microvalve was opened to allow the effusion of H_2O into the reactor. The aperture of the microvalve was chosen to impose a rate of growth of the ice films at 190 K that was in the range between $5.0 \cdot 10^{16}$ and $1.0 \cdot 10^{17}$ molec $\text{cm}^{-2} \text{s}^{-1}$ under static conditions, whatever the cryogenic support. Such ice films should consist in thermodynamically stable hexagonal polycrystalline I_h ice [1, 2] which was verified during this study and which will be presented in the next chapter.

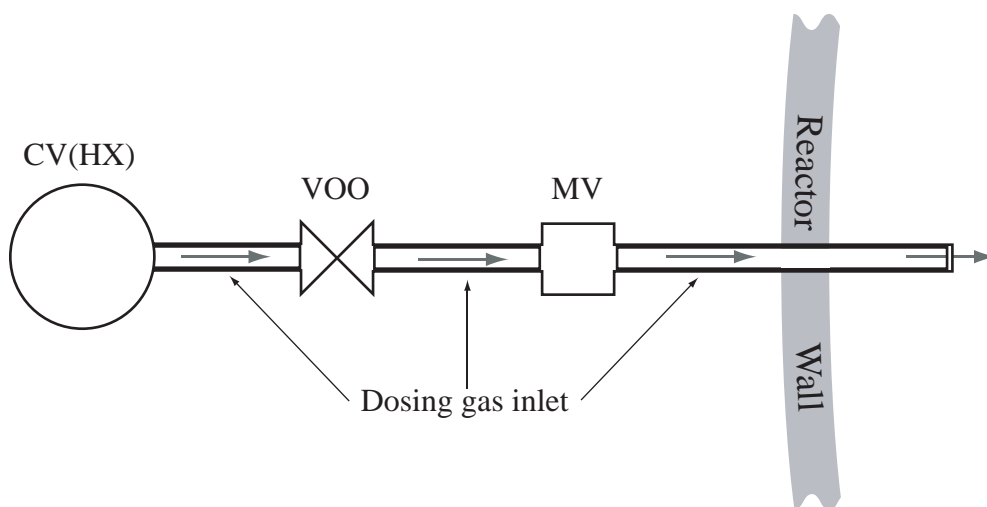


Figure 2.5: Schematic drawing of the gas inlet line: VOO allows the effusion of the trace gas (HX) from the $V_{\text{CV(HX)}}=60 \text{ cm}^3$ Teflon-coated calibrated volume (CV(HX)) through the dosing tube and across the metering valve MV into the reactor.

Figures 2.5 and 2.6 give a glimpse on the doping gas injection line. For the doping gas, labelled for the sake of clarity as HX, even for HNO_3 , the reservoir is a 60 cm^3 Teflon-coated

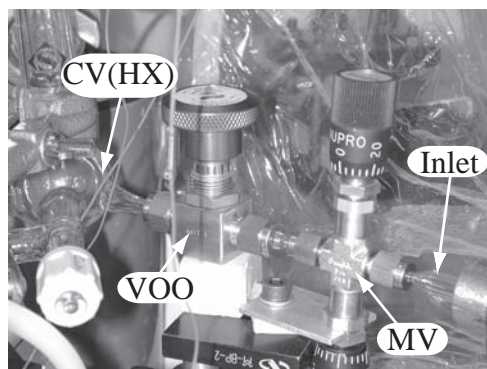


Figure 2.6: The doping gas injection line. Explanations and caption given in the text and Figure 2.5.

calibrated volume (CV(HX)) that is filled to a pressure between 1 and 2 Torr of HX depending on the experiment. The pressure in CV(HX) is measured using a 2000 mTorr full scale absolute pressure gauge MKS Baratron. As was the case for the injection line of H₂O, the micrometer dosing valve MV (Swagelok double pattern low pressure metering valve with vernier handle of type SS-SS2-D-TVVH, valves noted V₁ and V₂) aperture can be calibrated to reach well defined conditions of deposition of HX on the ice substrate. These calibrations will be described in more detail in Section 2.5. The protocol for injection was always the following. First, the injection line is evacuated to the base pressure, then V₁ and V₂ are fixed to the desired values. Subsequently, CV(HX) is filled with HX and the ON/OFF valve, VOO, located upstream of MV is opened to enable the effusion of HX from CV(HX) across MV and the glass tubing into the reactor. As in the case of the injection of H₂O vapor stainless steel and glass tubing have been tested. In Figure 2.3 both inlets are clearly made of stainless steel for example. However, in the case of corrosive gases as used in this study rather than stainless steel it seems that the material of choice is glass when working with dosing lines in the high pressure, which is approximately 2 Torrs, region.

The dosing gas inlets are retractable and allow either the directed injection on the different substrates used for ice deposition or the deposition by backfilling of the reactor. As will be

shown below, both methods have their advantages and disadvantages.

In addition to the gas inlets, the zone labelled Z_2 in Figure 2.2 is equipped with optical feedthroughs such as the two 2" diameter NaCl windows, one of which is visible in Figure 2.3. An adaptor for 1" windows has also been developed. These two windows are used for their good transparency in the mid-infrared region as displayed in Figure 2.7 that is taken from reference [3].

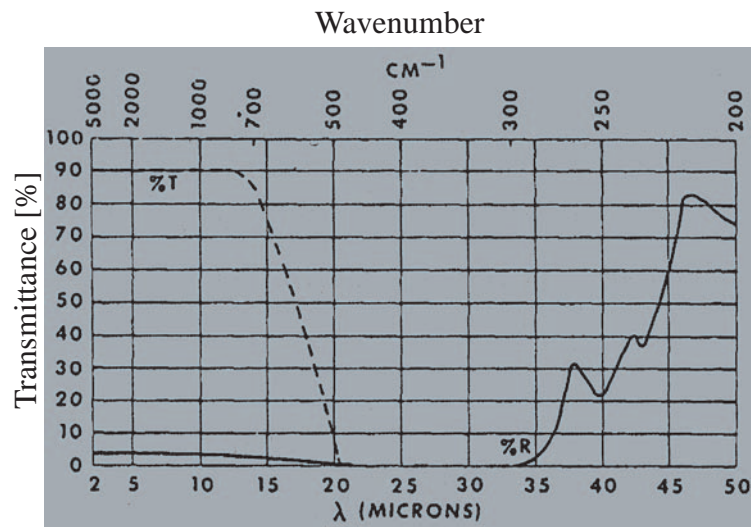


Figure 2.7: Infrared transmission spectrum from reference [3] for a 5 mm thick NaCl window.

Most of the time in this study the spectrum of interest extends from 700 to 4000 cm^{-1} corresponding to wavelength between 2.5 and 14 μm . The ice films that are characterized by Fourier Transform Infrared Spectrometry (BIORAD FTS-575C equipped with a cryogenic HgCdTe detector) are deposited on an infrared optical window of 1" diameter. Initially, a sodium chloride window was installed that was quickly replaced with Silicon for the remainder of this work. This window is held in place by a cryogenic support that is temperature controlled between 100 and 250 K and is housed in the upper chamber. In reality, there have been several different cryostats that have been developed during this work, and they will be presented in more detail in Section 2.2. Their common characteristics are the following:

- They are temperature controlled between approximately 100 and 250 K.
- The support consists of a copper finger that is externally cooled using liquid nitrogen which is contained in a reservoir located at the top of the reactor (see Figure 2.4). The counterheating is afforded by electrical heaters whose type and location has changed several times during the exploratory phase of this work.
- The optical window used for the deposition of the ice substrate has the normal to its surface aligned with the optical path of the FTIR beam and is centered on this beam as displayed in Figure 2.8. The IR beam is contained in the plane defined by both the tubes used for the gas injection into the reactor and allows the spectroscopic investigation of the deposit in transmission.
- Last but not least, the optical window held by the support is the only cold part of the cryostat that is exposed to the gas phase thanks to a tightly fitted PTFE insulation.

This last point has been checked in numerous experiments by correlating the loss of H₂O vapor by monitoring the pressure change in the Teflon-coated calibrated volume ($CV(H_2O)$) used as a reservoir for injection of H₂O vapor into the reactor with the number of molecules deposited on the optical window. It has been monitored using the optical density of the deposited ice film in the IR spectral region as will be described in Section 2.7 and correlated with the integrated MS signal at $m/z=18$ resulting from evaporation under stirred flow conditions (GV closed, LV open), as will be discussed in more detail in Section 2.5. The resulting mass balance usually agrees to within better than 15 %. In addition, the temperature of the PTFE sleeve used as an insulation is permanently recorded as close as possible to the optical window and it never reaches temperatures lower than 250 to 260 K depending on the cryostat, implying in itself the absence of a cold spot elsewhere as the region around the optical window should be the coldest part of the PTFE assembly by design.

An additional diagnostic technique is based on HeNe interferometry at 632.8 nm used to monitor the change of thickness of the ice deposit with time. The laser and the detector are

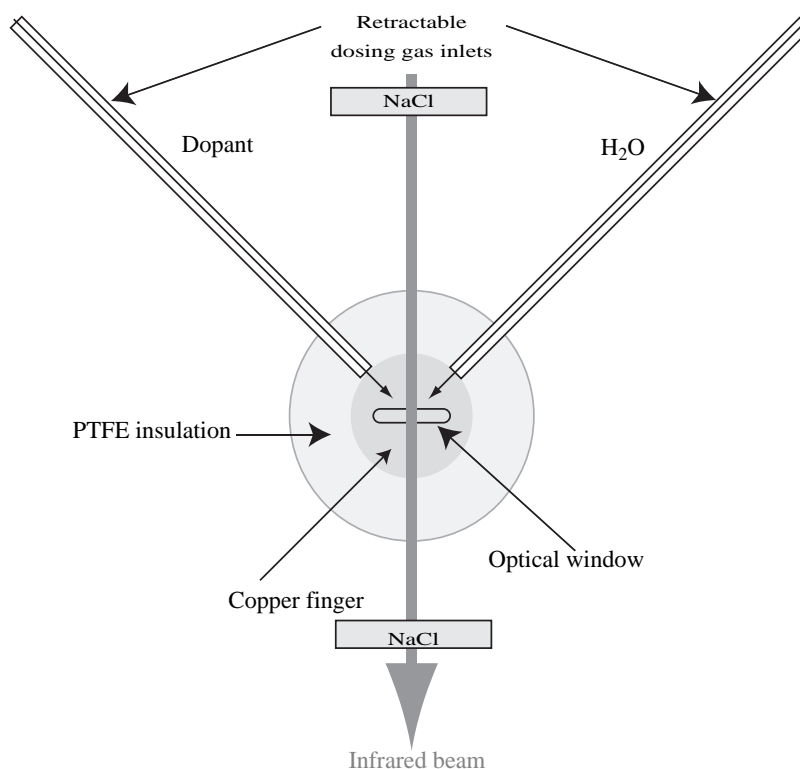


Figure 2.8: Horizontal cut (view from the top) through dosing tubes and IR beam transmitted across the optical window attached to the cryostat. The PTFE-insulated cryostat is perpendicular to the reference (paper) plane. Both the dosing inlets are retractable allowing either direct injection of the gas onto the cryostat or deposition on the cryostat window by backfilling of the chamber.

visible in Figure 2.1 and the beam crosses the NaCl window presented in Figure 2.3. The measurement of the thickness using HeNe interferometry is described in detail in Section 2.6 and may be used for the calibration of the FTIR signal in transmission thus allowing the determination of the absorption cross-section of H₂O at a given IR wavelength for example.

Before ending the general presentation of the different elements constituting the essence of this new experimental setup, we want to say some words about the electrical feedthroughs that allow the measurement of the temperature at several points inside the reactor. The temperatures are measured using Type T thermocouples in different locations allowing a measurement range that is larger than needed and with an accuracy smaller than 0.5 K according to the

manufacturer's data. But as the temperature measurement using thermocouples is based on the measurement of a voltage of the order of a μV and as the signals are highly subject to noise, we have decided to develop a homemade thermocouple noise-reducer/amplifier which is presented in Section 2.8.1. Finally, the temperature of the wall of the reactor as well as the by-pass line have also been equipped with such thermocouples and their temperature have been fixed for all the experiments presented in this work to a temperature between 300 and 340 K.

2.2 Origin and design of the cryogenic support

As previously stated the cryogenic support is used to afford temperature control of the optical window that served as the substrate for ice deposition. It has been the subject of several modifications from its initial to the final version.

Figure 2.9 presents some pictures of the initial homemade assembly that was used as a cryostat for the deposition of ice.

The cooling device (CD) consisted of a stainless steel evacuated vessel used as a reservoir for liquid nitrogen (Figure 2.9, part **1**, LND) that was brazed at its bottom to a copper finger (CF) thus enabling the cooling of the window holder made of copper. Item D in Panel **1** indicates the part of the Dewar (LND) that penetrates into the upper chamber of the experiment. To prevent the cooling of the O-ring joint between the cryostat and the top of the reactor this region was pumped to approximately 1 mTorr together with the Dewar storage vessel. This also prevented the presence of cold spots inside the reactor close to this area. At the outset the whole cooling device was totally devoid of any shielding. However, it became quickly evident that the presence of regions colder than the window used for deposition of ice hindered the performance of kinetics experiments. To surmount this obstacle the whole cold device was insulated from the gas phase using a tightly fitted PTFE sleeve that corresponds to the white elements in Figure 2.9. This cover was intended to be as close as possible to CD, in order to prevent the flow of residual gas between the copper body and the PTFE shielding, but without being in contact as much

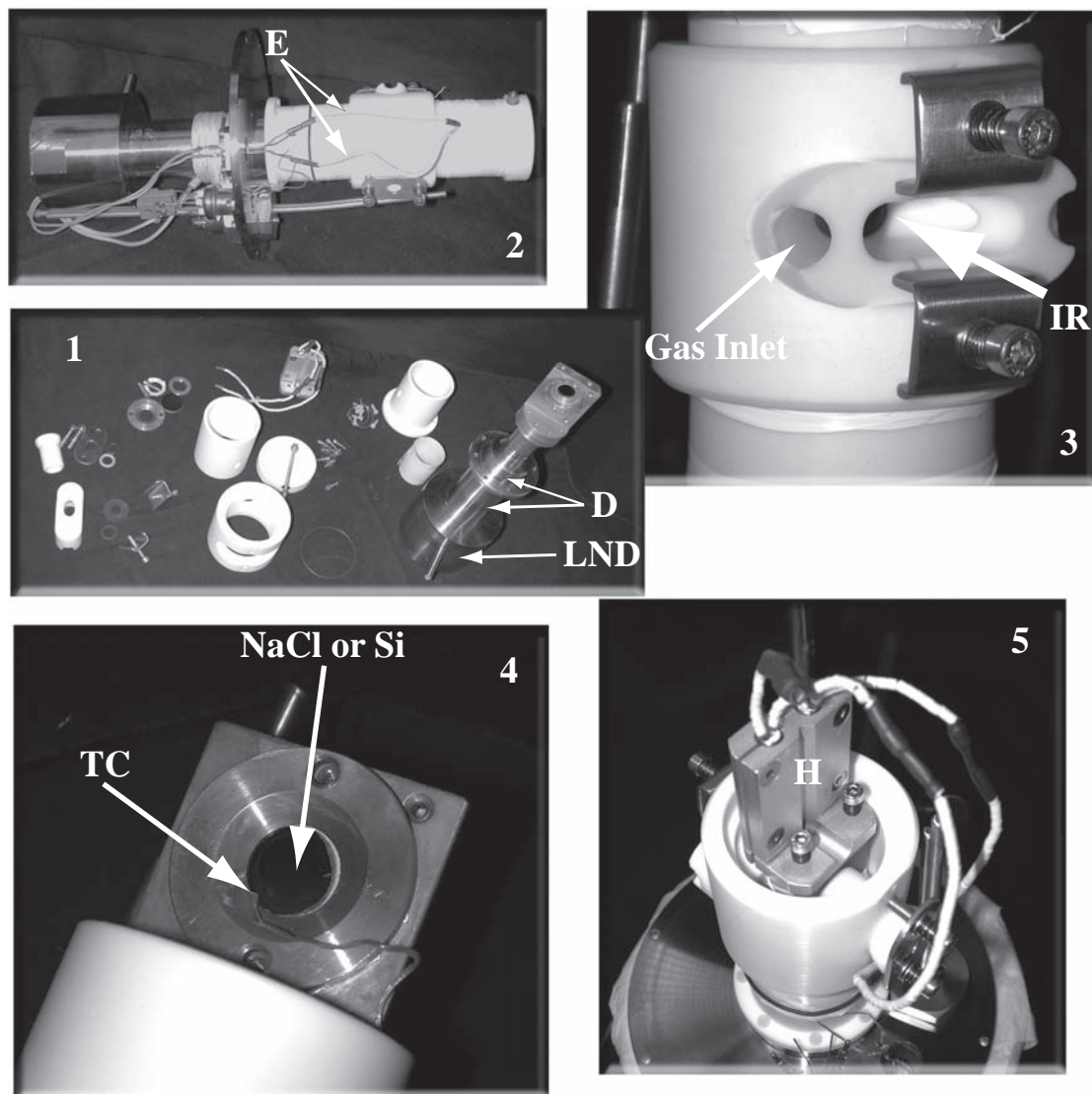


Figure 2.9: The cryostat Mark I. **1**: general view of all the elements of the assembly with the white PTFE elements and on the right the single bloc Dewar(LND)/copper-finger/holder device, **2**: mounted assembly with E the electrical power line for the heating cartridges, **3**: blow-up of the protected window holder region with indication for the dosing gas inlets and the IR beam, **4**: focus on the window holder with the Type T thermocouple TC wedge between the thin Indium foil and the window of NaCl or Si, **5**: view from the bottom of the cryostat revealing the *in situ* heating device H.

as possible in order to prevent the heat exchange by thermal conduction between copper and PTFE. When the contact was unavoidable the poor thermal conductivity of PTFE which is

around $2.3 \text{ W m}^{-1} \text{ K}^{-1}$ according to data of the manufacturer worked as a barrier to thermal exchange. It may be compared to the conductivity of the other materials that were used to build CD taken from reference [4]:

- Copper: from 483 to $398 \text{ W m}^{-1} \text{ K}^{-1}$ in the range 100 - 300 K,
- Indium: approximately $84 \text{ W m}^{-1} \text{ K}^{-1}$,
- Silicon: larger than $168 \text{ W m}^{-1} \text{ K}^{-1}$ at 300 K,
- NaCl: from 30 to $8 \text{ W m}^{-1} \text{ K}^{-1}$ in the range 100 - 300 K.

For crystalline Ih ice, extrapolation of data of Andersson et al. [5] results in values for the thermal conductivity of ice larger than $5 \text{ W m}^{-1} \text{ K}^{-1}$. Dillard and Timmerhaus obtain an approximate value of $4 \text{ W m}^{-1} \text{ K}^{-1}$ [6]. Even though our ice films are polycrystalline and not single crystals they are sufficiently thin (approximately $1 \mu\text{m}$) that the gradient of temperature between the surface of ice and the surface of the window is most probably negligible compared to the gradient between the contact surface of the PTFE with the copper body and the PTFE surface exposed to the gas phase as the PTFE part is generally thicker than 1 mm.

Several experiments have confirmed that the temperature of the PTFE sleeve measured using thermocouples never reached temperatures lower than 250 K in the areas that were the coldest by design. Another advantage of using PTFE is that it was totally inert for most of the gases that were used during our investigations. Panel **3** of Figure 2.9 shows both the passageways pierced into the PTFE for the dosing tubes as well as the passage allowing the FTIR investigation of the deposit on the window surface. At the end of the passages one may see the optical window whose effective surface is 0.78 cm^2 that is available for ice deposition. Panel **4** of Figure 2.9 is a blow-up of the copper window holder. It shows the window (NaCl or Si) that is well fitted in the holder and the type T thermocouple (TC) used to measure its temperature. The thermocouple was wedged between the optical window and the Indium foil that ensured the thermal contact between the window and the copper holder. In the beginning, we have used NaCl windows as

a substrate to grow ice because of its good optical transparency in the spectral range 700 - 4000 cm^{-1} which is the region of interest for ice. But some experiments have shown that NaCl has a finite solubility in ice at low temperature that may affect the results of our experiments. A manifestation of this problem was that the smooth window surface became rough after a few experiments. Moreover, a redox reaction that still remains unexplained occurred between NaCl, Indium, H_2O and HCl that led to the formation of a yellow coating on the surface of the window in some experiments once water had totally evaporated. When we took into account these problems as well as the relatively poor thermal conductivity of NaCl we have decided to switch to a Silicon window which presented the advantages of being inert to the gases used in this work, having a thermal conductivity a least 20 times larger than NaCl and presenting good, as far as we are interested, optical properties in the mid-infrared region as shown in Figure 2.10.

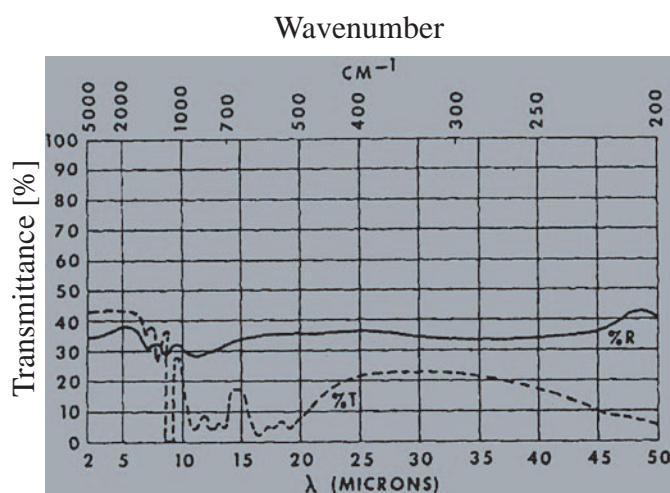


Figure 2.10: Infrared transmission spectrum from reference [3] for a 1 cm thick Si window.

After these modifications the cryostat seemed quite appropriate for the kinetics experiments we wanted to perform, however, the sporadic appearance of water in the reactor observed using mass spectrometry as well as an unexpected deposition of H_2O on the Si window observed by FTIR spectroscopy caught our attention. The cause was identified when the heating device (H in Figure 2.9, Panel 5) inside the reactor was put into operation. Indeed, the ceramics used to

build the heating cartridges used as a heating source are highly porous and it seemed that they released gases, mainly water, in an unpredictable way, even if they were heated *in situ* under vacuum before the low temperature experiment. As the presence of a counterheating device inside the reactor seemed a bad idea despite its frequent use we have decided to design a new cryostat with the intention to put the heating device outside the reactor, thereby taking the opportunity to reduce the dimensions of the cryostat. The old design was too voluminous as may be seen in Figure 2.9, Panel **2** where dimensions may be compared with the small diagram in Figure 2.2.

With this goal in mind we have developed a new cooling device that is presented in Figure 2.11. Panel **1** presents the bare cooling finger and the few PTFE elements constituting the housing and Panel **2** presents the mounted assembly. One may observe that the evacuated Dewar vessel used as a liquid nitrogen reservoir is now larger with an effective volume of approximately 5 l thereby affording a larger autonomy of the cooler.

The dimensions of the cooling finger made of stainless steel and copper brazed together have been calculated using a very simple thermal transfer model explained in Appendix 2.9 of this chapter. Panels **1** and **5** show the clearance holes in the copper body used as passageways for the dosing gas inlets (P) and protected from the gas phase using PTFE tubing. Owing to the high contrast of the image these inlets are difficult to see in Panel **3** but their position is given by the two arrows. As before the doubled-wall of the cryostat is pumped in the region where it fits the reactor chamber (D) in order to prevent the cooling of the O-ring joint and the generation of a cold spot in the upper chamber. Panel **4** shows the silicon window together with its thermocouple that is fixed using the same method as used for the first version of the cryostat. In Panel **2** one may see the new external counterheating device (H). It consists of an aluminium block housing two electrical heating cartridges and clamped onto the copper portion of the cooling finger. Figure 2.12 gives a schematic cross-section of the cooling finger from the reservoir (left) to the Si window holder (right).

This version of the cryostat has satisfied all tests we have performed during many experiments

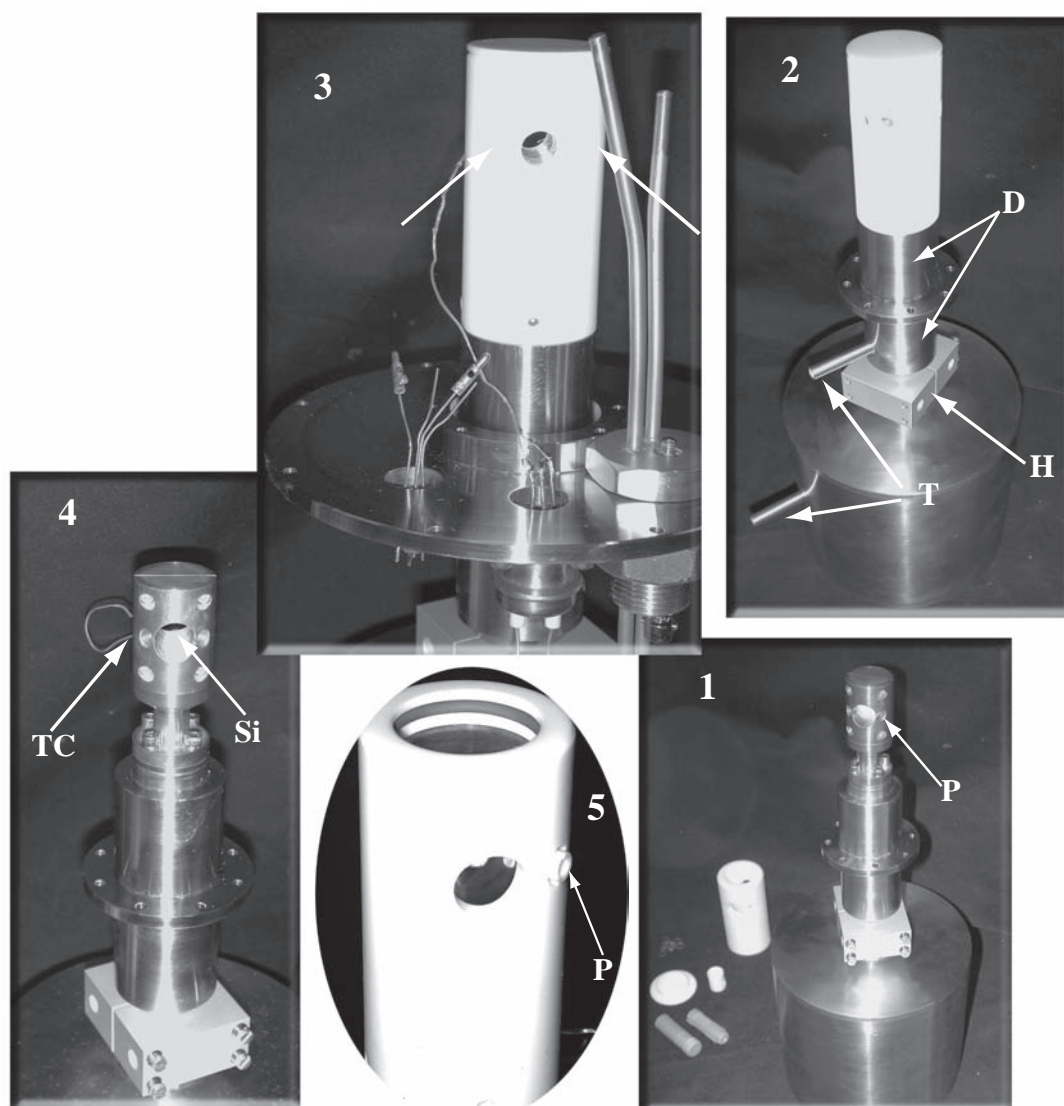


Figure 2.11: The cryostat Mark II. **1**:bare cooling device and its PTFE elements, **2**: mounted assembly with T the tubing ends connected to pump, **3**: arrows illustrating the positions of the passageways for the dosing gas tubes, **4**: the tightly fitted Si window in the holder and its thermocouple, **5**: small PTFE tubing insulating the copper element with the clearance holes (P) to butt against dosing tubes.

in the course of this work. The mass balance has been checked several times, as explained in section 2.1. No cold spot has been detected and the temperature measured on several points of the cryostat has never revealed temperatures lower than 250 K except on the Si window even

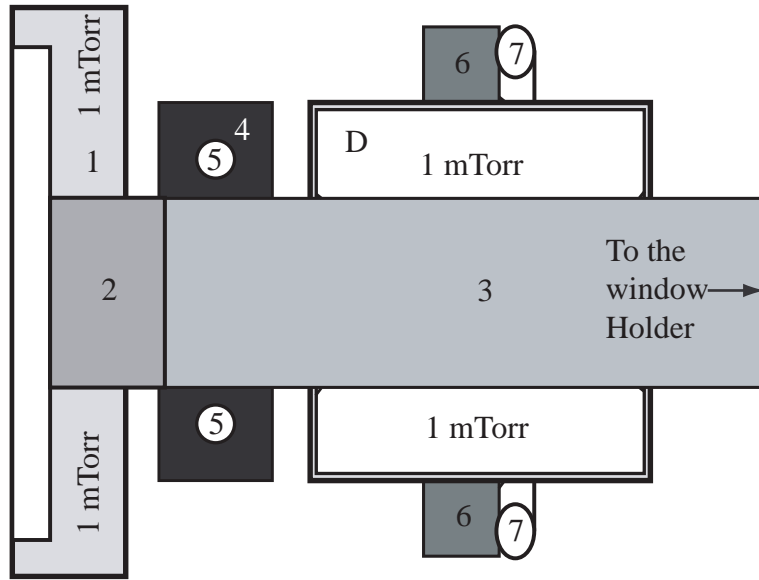


Figure 2.12: Schematic cross-sectional drawing of the cryostat Mark II. **1**: evacuated stainless steel Dewar vessel used as a liquid nitrogen reservoir, **2**: Stainless steel cylindrical element (length: 2 cm, radius: 1.5 cm), **3**: copper finger (length: 15 cm, radius: 1.5 cm), **4**: aluminium block with heating cartridges, **5**: two electrical heating cartridges, **6**: flange used to mount the cryostat on top of the upper chamber, **7**: O-ring joint. D has the same significance as in Figure 2.11. The thickness of the stainless steel wall of D is approximately 1 mm in the region where it is brazed to the copper finger.

for experiments lasting more than an hour. In this configuration the Si window has an effective surface area of 0.78 cm^2 on one face. The volume of the cryostat in the upper chamber was also reduced by a factor larger than two leading to an effective volume of the reactor $V_r=2450 \text{ cm}^3$. The temperature is accurately controlled in the range $100 \leq T \leq 250 (\pm 1) \text{ K}$.

2.3 Three regimes of operation

Section 2.1 alludes to the possibility that the experimental setup may be used in three different configurations. Indeed, by opening or closing either the 6" gate valve (GV) at the bottom of the reactor or the calibrated leak valve (LV), three regimes of operation are available:

- *Static* operation: GV and LV closed. This leads to equilibrium conditions within the reactor. This configuration has often been used during work that is presented in Chapter 3.
- *Stirred flow* operation: GV closed and LV open. This leads to a typical (stirred flow) residence time of H₂O in the upper chamber of the reactor that ranges between 5 and 18 s depending on the calibrated leak, that has also been changed during the course of this work. This configuration has been used all along this work and is necessary for calibrations of the MS signal as will be described in Section 2.5.
- *Dynamic* operation: GV open. Mainly used in Chapters 4, 5 and 6. This corresponds without ambiguity to molecular flow conditions whose estimated gas phase residence time for H₂O is approximately 1 ms and the partial pressure always smaller than $1.0 \cdot 10^{-4}$ Torr.

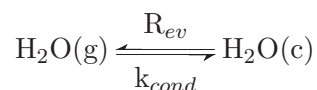
Thanks to these configurations the apparatus may be operated from the free molecular flow regime to the pressure transition region up to 760 mTorr or so of total pressure. However, some corrections should and will probably be applied as the pressure increases depending on the agreement of H₂O vapor behavior with ideal gas law. In this study we have limited our investigations to pressures lower than 200 mTorr and under these conditions corrections are not necessary as justified in the General Appendix, Section 8.1, page 223 of this work. Nevertheless, some corrections due to the difference of temperature between the ice film and the reactor walls have to be taken into account and that is the goal of the next section to accurately explain these corrections.

2.4 Corrections of the measured total gas pressure

The difference in the temperature between the ice surface (T_{ice}) and the wall of the reactor (T_r) necessitates a correction of the measured pressure as the factory-calibrated Baratron absolute pressure gauge is at the same temperature as the chamber. This phenomenon uses the same formalism as the one sometimes called thermal transpiration [7].

In this section we will anticipate certain data that will be presented in Chapter 3.

A. The partial pressure of H_2O over ice, $P_{\text{H}_2\text{O}}$, at typically 200 K measured in a static vessel of the same temperature T_r is identical to the equilibrium vapor pressure of H_2O , $P_{\text{H}_2\text{O}}^{\text{eq}}$. In such a system a single temperature, namely the temperature of the condensed phase as well as of the reactor walls, controls $P_{\text{H}_2\text{O}}^{\text{eq}}$. The corresponding H_2O concentration, $[\text{H}_2\text{O}]$, is equal to the molecular density given by Equations 2.4 and 2.5 when either the rate (R_{ev}) or the flux (J_{ev}) of condensation and evaporation of H_2O in the presence of ice, respectively, are expressed in terms of true chemical equilibrium between water vapor and the condensed phase, namely



$$R_{\text{ev}} = \gamma\omega[\text{H}_2\text{O}] \quad (2.4)$$

$$\omega = \bar{c} \frac{A_s}{4V_r}$$

$$J_{\text{ev}} = \gamma \frac{\bar{c}}{4} [\text{H}_2\text{O}] \quad (2.5)$$

$$R_{\text{ev}} = J_{\text{ev}} \frac{A_s}{V_r} \quad (2.6)$$

where γ , ω , \bar{c} , A_s and V_r are the uptake coefficient, the gas-surface collision frequency, the mean molecular velocity, the geometrical area of the substrate and the volume of the reactor, respectively.

B. In practice, however, $P_{\text{H}_2\text{O}}$ and $[\text{H}_2\text{O}]$ are measured in an experimental system where the condensed phase is at low temperature and whose walls are at ambient temperature. In this case the condense phase at low temperature ($T_L=T_{\text{ice}}$ in the present study) and the chamber walls at high temperature ($T_H=T_r$) both control $P_{\text{H}_2\text{O}}$ and $[\text{H}_2\text{O}]$, both of which do not correspond to the equilibrium vapor pressure $P_{\text{H}_2\text{O}}^{\text{eq}}$ and the equilibrium concentration, $[\text{H}_2\text{O}]^{\text{eq}}$, respectively. The former situation **A** corresponds to true equilibrium between the cold target and the cold

chamber walls without ambiguity, except that it is a hypothetical situation rarely encountered in practical experiments. Conversely, the often encountered situation **B** implies that collisions of a gas at the wall temperature T_r (hot gas) occurs with a target (ice) that is at the low temperature T_{ice} , in which case P_{H_2O} and $[H_2O]$ are given by two temperatures, T_r and T_{ice} . The measured partial pressure of H_2O , $P_{H_2O}^{meas}$, and the measured concentration of H_2O , $[H_2O]^{meas}$, may be calculated by postulating that the equilibrium conditions given in Equations 2.7 and 2.8 hold thus implying no net growth or loss of the quantity of the condensed phase at T_{ice} .

$$J_{ev} = \gamma \frac{\bar{c}}{4} [H_2O] = \gamma \frac{\bar{c}}{4} [H_2O]^{meas} \quad (2.7)$$

$$J_{ev} = \gamma \frac{\bar{c}}{4} \frac{P_{H_2O}^{eq}}{\mathcal{R}T_{ice}} = \gamma \frac{\bar{c}}{4} \frac{P_{H_2O}^{meas}}{\mathcal{R}T_r} \quad (2.8)$$

This means that the constraint of no net change of the condensed phase controls the measured values of P_{H_2O} and $[H_2O]$ according to Equations 2.9 and 2.10 corresponding to a pseudo-equilibrium measured under realistic experimental conditions corresponding to a steady state.

$$[H_2O]^{meas} = [H_2O] \sqrt{\frac{T_{ice}}{T_r}} \quad (2.9)$$

$$P_{H_2O}^{meas} = P_{H_2O}^{eq} \sqrt{\frac{T_r}{T_{ice}}} \quad (2.10)$$

Equations 2.9 and 2.10 show that both T_{ice} and T_r control the measured experimental quantities $P_{H_2O}^{meas}$ and $[H_2O]^{meas}$ with the consequence that $[H_2O]^{meas} < [H_2O]^{eq}$ and $P_{H_2O}^{meas} > P_{H_2O}^{eq}$.

Following these considerations, the measured pressures and concentration in the reactor have been corrected all along this work, whenever it was necessary.

2.5 Mass spectrometry: calibrations and measurements

In the present work mass spectrometry (MS) is used as a residual gas partial pressure or concentration monitor. Under stirred flow (GV closed, LV open) and dynamic (GV open) conditions, corresponding to the transition and molecular flow regime, respectively, the total pressure in the lower chamber enables the operation of the residual gas quadrupole mass spectrometer (Balzers Prisma QMS200). Indeed, even for an ice film at 240 K which is the highest ice temperature used in this work therefore corresponding to the highest evaporation flux of H_2O molecules from ice, the pressure in the lower chamber of the reactor never reaches values larger than $2.0 \cdot 10^{-5}$ Torr thanks to the sufficiently high rate of pumping of the turbomolecular pump (Varian Turbo 300-VHT, $250 \text{ l s}^{-1} \text{ N}_2$). The Prisma MS is particularly designed for partial pressure analysis below $7.5 \cdot 10^{-5}$ Torr (manufacturer data) and more generally the quadrupole mass spectrometers are recognized for having a good linear response in term of the ion current versus partial pressure below $4.0 \cdot 10^{-5}$ Torr and a relative sensitivity that is linear within 30% below this pressure [8, 9]. In the linear range corresponding to the experiments we have performed we have calibrated the MS signal (PC software converted ion current) versus partial pressure or concentration for each gas of interest. Moreover, the knowledge of the partial pressure of the used doping gases, HCl, HBr and HNO_3 , under stirred flow conditions allows us to determine the rate in molecules per second and the absolute dose in number of molecules of doping gas deposited on the ice surface as will be described below.

The first step implies the calibration of the MS signal of H_2O at $m/z=18$ which enables a 1:1 correspondence between MS intensities I_{18} in the lower chamber and the partial pressure $P_{\text{H}_2\text{O}}$ or concentration $[\text{H}_2\text{O}]$ of H_2O in the upper chamber.

Under stirred flow conditions (GV closed, LV open) the calibration of I_{18} is based on establishing the ratio between the MS signal and the partial pressure of H_2O in the upper chamber that is measured using the Baratron pressure gauge (Figure 2.4, item 11). When H_2O is injected into the reactor through the dosing tube at a flow rate $F_r(\text{H}_2\text{O})$ the following equalities hold:

$$F_r(\text{H}_2\text{O}) = \frac{P_{\text{H}_2\text{O}} \times V_r}{\mathcal{R} \times T_r} \times k_{\text{esc}}(\text{H}_2\text{O}) \quad (2.11)$$

$$= [\text{H}_2\text{O}] \times V_r \times k_{\text{esc}}(\text{H}_2\text{O}) \quad (2.12)$$

$$= \text{Conv} \times V_r \times k_{\text{esc}}(\text{H}_2\text{O}) \times P_{\text{H}_2\text{O}} \quad (2.13)$$

$$= C_{18}^{\text{s-flow}} \times I_{18} \quad (2.14)$$

where $F_r(\text{H}_2\text{O})$ is the flow rate of H_2O through the calibrated leak (LV) in molec s^{-1} , Conv is the conversion factor between the partial pressure and the concentration of H_2O into the chamber in $\text{molec Torr}^{-1} \text{ cm}^{-3}$, $P_{\text{H}_2\text{O}}$ the pressure of H_2O in Torr, V_r the volume of the reactor in cm^3 and $k_{\text{esc}}(\text{H}_2\text{O})$ the rate of effusion of H_2O through the calibrated leak (LV) in s^{-1} that is measured as described in Section 2.1. I_{18} corresponds to the intensity of the MS signal for $m/z=18$ in A and $C_{18}^{\text{s-flow}}$ is the calibration factor for $m/z=18$ under stirred flow conditions in $\text{molec s}^{-1} \text{ A}^{-1}$. Equations 2.11, 2.12 and 2.13 are derived from the ideal gas law. By combining Equations 2.13 and 2.14 and measuring both $P_{\text{H}_2\text{O}}$ and I_{18} we may evaluate $C_{18}^{\text{s-flow}}$ following Equation 2.15:

$$C_{18}^{\text{s-flow}} = \text{Conv} \times V_r \times k_{\text{esc}}(\text{H}_2\text{O}) \times \frac{P_{\text{H}_2\text{O}}}{I_{18}} \quad (2.15)$$

Under dynamic conditions (GV open) C_{18}^{dyn} is evaluated using the decrease of the pressure of H_2O in the Teflon coated calibrated volume (CV(H_2O), volume V_c), $P_{\text{H}_2\text{O}}$, used as a reservoir for the H_2O flow into the reactor when the microvalve described in Section 2.1 is opened. The correspondence between the measured $\Delta P_{\text{H}_2\text{O}}/\Delta t$ in CV(H_2O) and the MS signal at $m/z=18$ yields C_{18}^{dyn} , the calibration factor for $m/z=18$ under dynamic conditions following in Equation 2.16 by analogy with Equation 2.15:

$$C_{18}^{\text{dyn}} = \text{Conv} \times V_c \times \frac{\Delta P_{\text{H}_2\text{O}}}{\Delta t} \times \frac{1}{I_{18}} \quad (2.16)$$

The calibration factors for $m/z=18$, $m/z=36$, $m/z=82$ and $m/z=30$, namely $C_{18}^{\text{cs-flow}}$, $C_{36}^{\text{cs-flow}}$, $C_{82}^{\text{cs-flow}}$, $C_{30}^{\text{cs-flow}}$, C_{18}^{dyn} , C_{36}^{dyn} , C_{82}^{dyn} and C_{30}^{dyn} , are all determined using the same method. The numerical values are listed as well as the smallest measurable signals and the rate constants for effusions in Tables and "Supplementary Information" at the beginning of each of the following chapters.

The second step in the evaluation of the absolute amount of the doping gas, HX, deposited on the ice substrate consists in taking the difference of I_{HX} , the MS signal monitored for HX, under stirred flow conditions, with and without an ice film on the cold substrate. This difference in MS signals may be converted into an absolute number of HX molecules that have been deposited onto the ice film located on the effective cold surface of the cryostat compared to the few HX molecules sticking to the NaCl or Si window at 320 K.

The glass tubing used for the directed or backfilling injection of HX was aimed at the center of the window and connected to the ON/OFF valve (VOO), which itself is located upstream of a micrometer dosing valve MV (Swagelok double pattern low pressure metering valve with vernier handle of type SS-SS2-D-TVVH, valve noted V_1 and V_2). Figure 2.5, page 25, presents a schematic illustration of the injection line where VOO separates the Teflon coated calibrated volume used as a reservoir for HX from MV. For a given pressure of HX of approximately 1 to 2 Torr in the calibrated volume we have systematically established the correspondence between the aperture of MV (V_1 and V_2) and I_{HX} . We subsequently have compared I_{HX} when the support for ice growth is at ambient temperature (no ice) and in the presence of an ice film at the same experimental settings of pressure and aperture of V_1 and V_2 of MV. Using the appropriate calibration factor, the time integration of the difference between both I_{HX} signals enables the measurement of the loss of gas phase HX owing to the deposition of HX on the ice substrate thanks to the certainty that there is no cold spot in the chamber other than the window used for deposition.

Figure 2.13 illustrates a specific case of a HCl deposition on a 1.2 μm thick ice substrate at $T_{\text{ice}}=192$ K with apertures of the double metering valve MV set to $V_1=V_2=25$ graduations

and with $P_{\text{HCl}}^0 = 1018$ mTorr in the Teflon coated calibrated volume CV(HX) under stirred flow conditions. Previously, the film was deposited by condensation of water vapor under static conditions at 190 K at a rate of $1 \cdot 10^{17}$ molec $\text{cm}^{-2} \text{s}^{-1}$. Subsequently, the temperature of the film was set to the desired value, 192 K in this example.

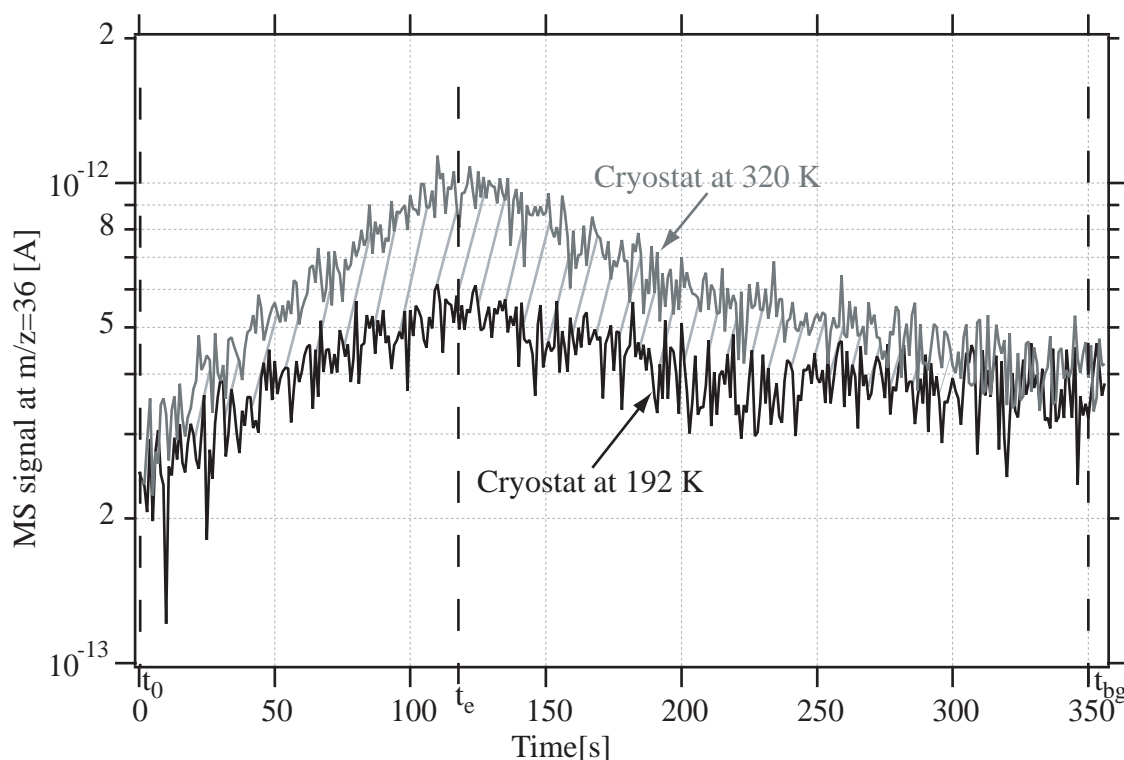


Figure 2.13: Typical MS signals for $m/z=36$ during directed HCl flow onto the cold support: reference experiment with support at 320 K (grey trace) and HCl dosing on an ice film (black trace) deposited on the cold window at 193 K. During deposition on ice (black trace), at $t=t_e$, the ON/OFF valve VOO is closed to halt HCl admission into the reactor.

At t_0 in Figure 2.13, VOO is opened allowing the effusion of HCl from the reservoir CV(HX) across MV and the tubing into the reactor. The grey trace I_{36} corresponds to the case where the support is at 320 K (no ice) which is used as a reference for the deposition of HCl on top of the ice film. The black trace I_{36} corresponds to the identical case as above for a deposition between $t_0=0$ s and $t_{bg}=350$ s which corresponds to the end of the dosing period. At t_e VOO

is closed. The effective deposition occurs between t_0 and t_{bg} .

The hatched area represents the absolute loss of gas phase HCl in the presence of the ice film compared to the reference experiment with no ice. As the window is the unique cold target in the reactor this loss therefore corresponds to the number of HCl molecules deposited on the ice film. Thus, the difference between both I_{36} signals at $t < 350$ s obtains the rate, R_{HCl} , of adsorption of HCl molecules on the ice film and the integration in time of this difference between $t=0$ and 350 s (t_{bg}) gives the absolute number of HCl molecules, N_{HCl}^{dep} , present on the ice substrate. For the case of Figure 2.13, $(2.6 \pm 0.2) \cdot 10^{14}$ molecules of HCl have been deposited during 350 s at an average rate of $8.0 \cdot 10^{11}$ molec s^{-1} . These data are evaluated using the PC based software Igor supplied by Wavemetrics, Inc.

Uncertainties on the measurements will be given in the Table summarizing all the experimental data or in the text in the first section at the beginning of each chapter.

2.6 HeNe interferometry

The measurement of the thin film thickness using optical interferometric methods is a well known technique in the field of optical sciences that has sometimes been used in the study of pure and contaminated ice films [10, 11, 12, 13]. Figure 2.14 presents a schematic drawing of the different paths followed by a Laser beam (HeNe, $\lambda=632.8$ nm) when it reflects both on the surface of the film of interest, ice in the present case, and on the surface of the substrate used for deposition.

Interference phenomena result from the surperposition of two waves originating from the same source having a phase difference due to the different optical paths. A maximum of intensity is observed each time the difference between the optical paths is a multiple of the wavelength such as $\lambda=632.8$ nm used in the present work. Figure 2.14 conveys that a brilliant fringe corresponding to a maximum of intensity occurs each time the condition outlined in Equation 2.17 is satisfied:

$$OPD = [IJK] - [IL] = n_{ice}(IJK) - n_{vacuum}(IL) = \mathcal{P} \times \lambda \quad (2.17)$$

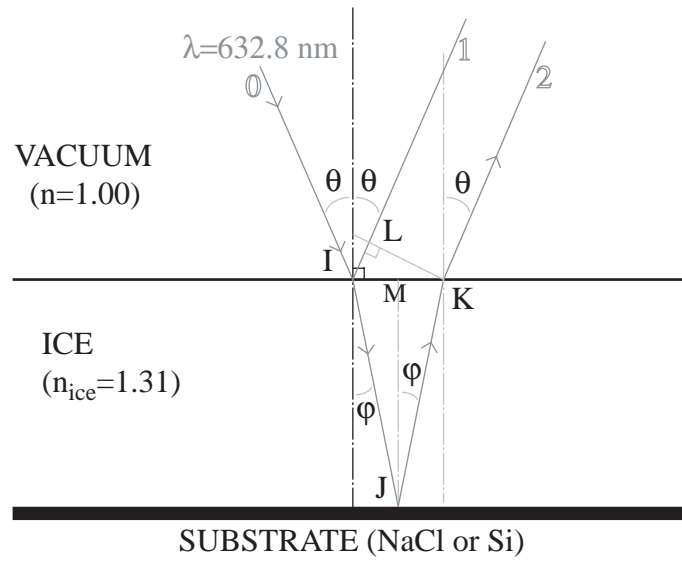


Figure 2.14: Schematic drawing of the optical paths of a laser beam when at reflection off an ice film deposited on a NaCl or Si window

where OPD is the optical path difference, [IJK] and [IL] are the paths of beams 2 and 1, respectively, (IJK) and (IL) their respective lengths and n_{ice} and $n_{\text{vacuum}}=1.00$ the refractive indices of the ice film and vacuum, respectively. $\lambda=632.8$ nm is the HeNe laser wavelength and \mathcal{P} an integer.

The final expression relating the thickness of ice, $\text{Th}_{\mathcal{P}}$, to the fringe count \mathcal{P} is given by Equation 2.18:

$$\text{Th}_{\mathcal{P}} = \mathcal{P} \times \frac{\lambda}{2} \sqrt{\frac{1}{n_{\text{ice}}^2 - \sin^2\theta}} \quad (2.18)$$

Therefore, N_i adjacent interference fringes correspond to a total difference of thickness d_i given by

$$d_i = N_i \times \frac{\lambda}{2} \sqrt{\frac{1}{n_{\text{ice}}^2 - \sin^2\theta}} \quad (2.19)$$

With $n_{\text{ice}}=1.31$ being independent of T_{ice} in the range 180-220 K [12] and $\theta=12^\circ$, one obtains

$d_i=246 \times N_i$ which indicates a difference d_i in ice thickness of 246 nm between the homologous points of two adjacent interference fringes. This leads to the total number of water molecules deposited on the substrate of $N_{\text{H}_2\text{O}}=6.0 \cdot 10^{17} \times N_i$ with the density of ice assumed to be constant and equal to 0.93 g cm^{-3} [1, 12, 14, 15, 16, 17] in the range 180 to 220 K. The mass balance was checked as often as possible between the number of H_2O molecules deposited on the cryostat window measured using interferometric method and the number of H_2O molecules measured during evaporation of the ice film under stirred flow conditions using mass spectrometry at $m/z=18$. It was always satisfied within less than 15% insuring the validity of the chosen density for ice. Interferometry therefore enables the monitoring of the change with time of the thickness of the ice films grown onto the cryostat window that subsequently enables the calibration of the FTIR spectrum of pure H_2O film for given wavelengths.

2.7 FTIR calibrations

FTIR spectroscopy in transmission is a good means to obtain information about the presence of a chemical species in or on a given substrate. The setup we present here allows the spectral investigation in transmission of any deposit on the Si window mounted on the cryostat thanks to a BIORAD FTS-575C Fourier transform spectrometer equipped with a cryogenic HgCdTe detector.

During a preliminary study many experiments on pure ice films have been performed at 100 K the lowest temperatures that the cryostat could reach, that is without temperature control. Ice films were grown at a low rate at approximately $3.0 \cdot 10^{15} \text{ molec cm}^{-2} \text{ s}^{-1}$. They were monitored using HeNe interferometry as described in Section 2.6 and FTIR spectroscopy in transmission. During the growth of an ice film we observed the correspondence between the absorbance in transmission in the mid-infrared region (FTIR) of the ice deposit and the number of interferometric fringes. Using Equation 2.18 and the data of Berland et al. [12] concerning the refractive indices of pure ice films as a function of temperature we have been able to calculate the

change of thickness d_i with time of the growing ice films by correlating them with the absorbance obtained by the FTIR measurement at wavelengths characteristic of pure ice. The thickness d_i was calculated for HeNe interferometric signals corresponding to a maximum or minimum of the intensity on the HeNe detector. Figures 2.15 and 2.16 present results on the dependence of the absorbance at 3250 cm^{-1} corresponding to the OH-stretch of water ice with the ice thickness d_i and a FTIR spectrum representative of ice films deposited at 100 K or so, respectively.

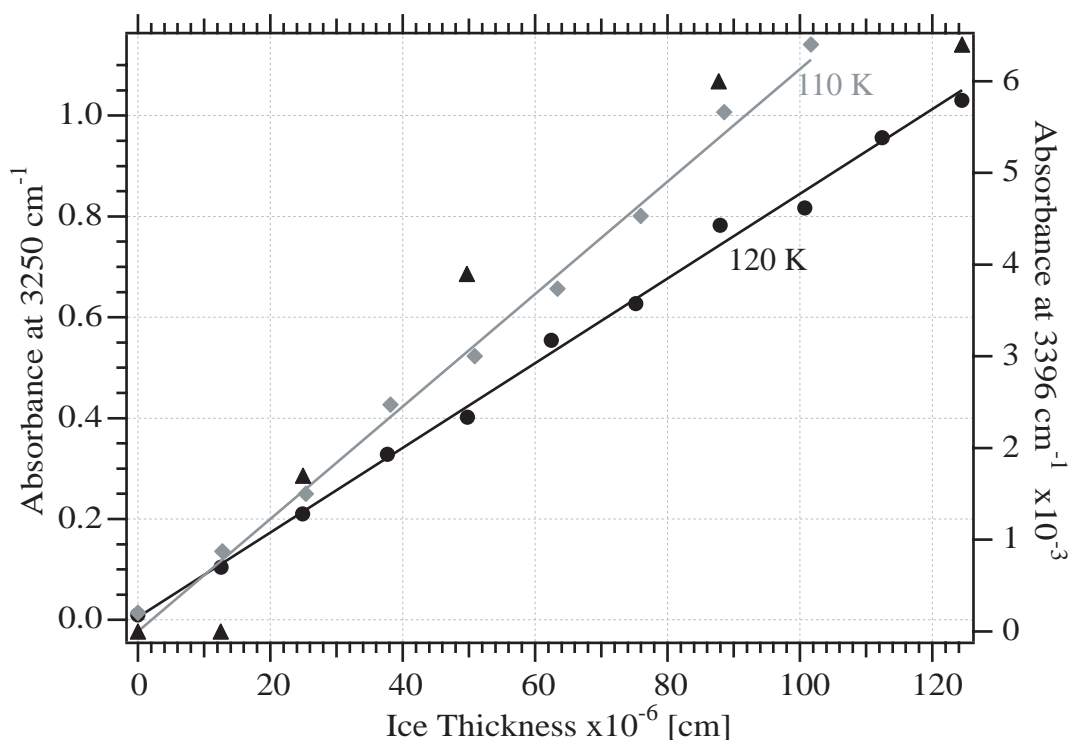


Figure 2.15: Dependence of optical density at two wavelengths on the ice thickness for two ice films grown at 120 K (black points) and 110 K (gray). The left ordinate gives the absorbance at 3250 cm^{-1} (\bullet and \diamond) corresponding to the maximum absorbance in the H_2O OH-stretch region. The right ordinate gives the absorbance corresponding to the dangling bond (\blacktriangle) typical of low density ice [18] at 3396 cm^{-1} at 120 K in the present experiments.

In agreement with the law of Beer-Lambert the optical density (OD) at 3250 cm^{-1} displayed in Figure 2.15 is a linear function of the thickness which also implies a linear dependence of OD with the total number of H_2O molecules. This infrared region corresponding to the OH-stretch

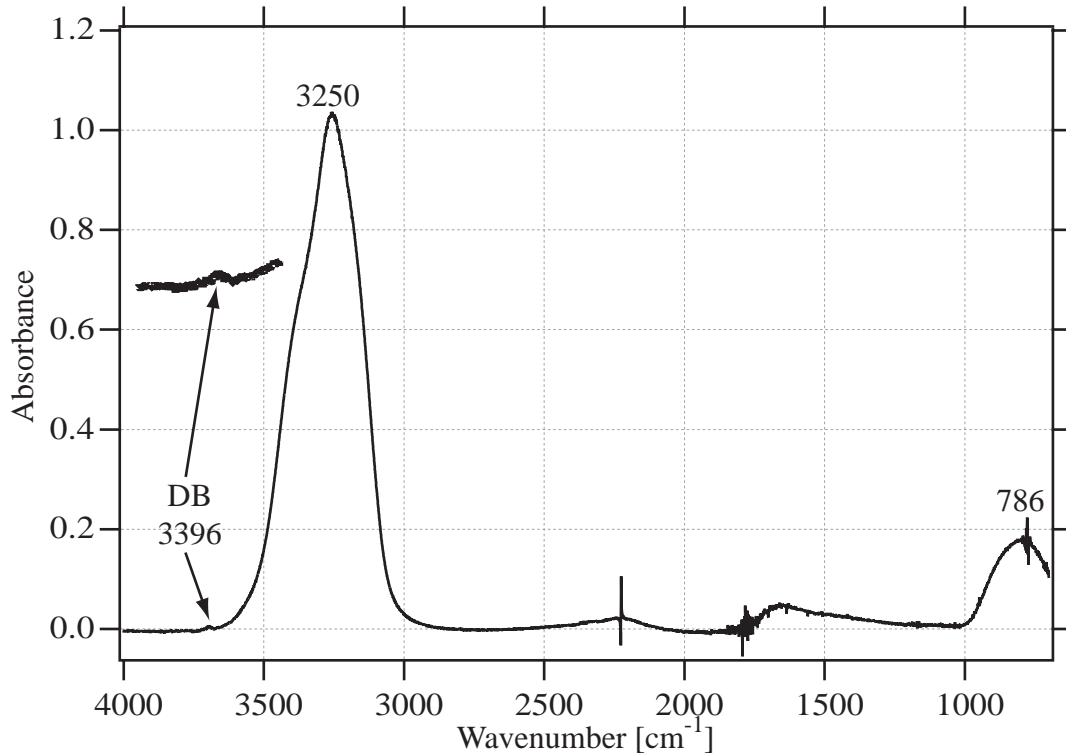


Figure 2.16: Typical FTIR spectrum observed for an ice film deposited at 100 - 120 K and at a growth rate of approximately $3.0 \cdot 10^{15}$ molec $\text{cm}^{-2} \text{s}^{-1}$. It displays the presence of an amorphous ice film [2].

of H_2O molecules in ice only depends on the number of molecules present in the ice film. All the black data in Figure 2.15 correspond to an ice film grown at 120 K and at the previously cited rate of deposition of $3.0 \cdot 10^{15}$ molec $\text{cm}^{-2} \text{s}^{-1}$. The gray data points correspond to a film grown at 110 K under the same conditions. Figure 2.16 corresponds to the FTIR spectrum measured during the growth of the film deposited at 120 K. It presents the characteristics of amorphous water ice [2] which was expected for an ice film deposited at such a low rate [19, 20, 21]. The observation at 3396 cm^{-1} due to the presence of free dangling OH bonds [21, 22] was also expected for such low a rate of growth of the ice film [18, 19] and is correlated with a decrease in density of ice [12] due to a higher porosity even if not visible using HeNe interferometry. One may note that the dangling bond is not truly dependent on the total number of H_2O molecules

because it is a surface species whose concentration does not scale with the volume or thickness.

Using the linear regression of the data in Figure 2.15 for both ice films (black and gray lines) we have evaluated the infrared absorption cross-section, σ_{3250} for ice in transmission at 3250 cm^{-1} . The law of Beer-Lambert provides the following relations for absorption in transmission:

$$\text{OD} = \log\left(\frac{I_0}{I}\right) = \epsilon cd \quad (2.20)$$

$$\ln\left(\frac{I_0}{I}\right) = \sigma nd \quad (2.21)$$

$$\sigma = \frac{2303\epsilon}{\mathcal{N}_A} \quad (2.22)$$

with OD the optical density in standard units at a chosen wavelength, I_0 and I the initial and final intensity at the given wavelength, respectively, ϵ the molar decadic extinction coefficient in $\text{l mol}^{-1} \text{ cm}^{-1}$, c the concentration in mol l^{-1} , d the thickness of the absorber in cm , σ the absorption cross-section in $\text{cm}^2 \text{ molec}^{-1}$ and n the concentration in molec cm^{-3} .

For the ice film deposited at 120 K (black points), the corresponding linear regression on the data (black line) obtains a slope corresponding to $\epsilon c = 8394 \text{ cm}^{-1}$. Berland et al. [12] report an average density of 0.83 g cm^{-3} for such an ice film. Therefore, the average concentration of H_2O in the film is $c = 4.78 \cdot 10^{-2} \text{ mol cm}^{-3}$. It follows from Equation 2.22 that the differential absorption cross-section at 3250 cm^{-1} is:

$$\sigma_{3250} = 6.7 \cdot 10^{-19} \text{ cm}^2 \text{ molec}^{-1} \text{ at } 120 \text{ K}$$

For the ice film deposited at 110 K, $\epsilon c = 11154 \text{ cm}^{-1}$. Berland et al. report a density of 0.84 g cm^{-3} , and the differential absorption cross-section at 3250 cm^{-1} is:

$$\sigma_{3250} = 9.1 \cdot 10^{-19} \text{ cm}^2 \text{ molec}^{-1} \text{ at } 110 \text{ K}$$

We attribute the discrepancy between the last two values to the uncertainty in the densities when average values given by Berland et al. are used. As their data depend on the H₂O partial pressure used for deposition of the ice film and as the change with pressure is more pronounced in the case of ice at 110 K ($6.2 \cdot 10^{-1} \text{ g cm}^{-3} \cdot 10^{-5} \text{ Torr}$ versus $5.5 \cdot 10^{-2} \text{ g cm}^{-3} \cdot 10^{-5} \text{ Torr}$ at 120 K, in the worst case), we propose that the most trustworthy result is the one corresponding to the ice film at 120 K.

For the experiments performed during this work we have chosen to grow the ice films systematically at 190 K at a rate of deposition in the range $5.0 \cdot 10^{16}$ to $1.0 \cdot 10^{17} \text{ molec cm}^{-2} \text{ s}^{-1}$. Under those conditions it is expected that the ice structure corresponds to the thermodynamically stable polycrystalline I_h ice [1, 21]. Figure 2.17 presents a typical FTIR spectrum in transmission of an ice film grown under those conditions.

The spectrum of pure ice that we are presenting reveals effectively the presence of polycrystalline I_h ice in the OH-stretch region as discussed above. It shows an absorption peak at 3236 cm^{-1} with shoulders at 3150 and 3350 cm^{-1} [2, 23, 24, 25] which was expected from previous work for ice films deposited at temperatures higher than 180 K [1]. As in the preliminary study we have calculated the cross-section for absorption at 3236 cm^{-1} using $\rho_{\text{ice}} = 0.93 \text{ g cm}^{-3}$ reported by Berland et al. [12] from the linear dependence of the OD of the OH-stretch vibration with the thickness of the ice film:

$$\sigma_{3236} = 7.9 \cdot 10^{-19} \text{ cm}^2 \text{ molec}^{-1} \text{ at } 190 \text{ K}$$

This value is in good agreement with results reported by Tolbert and Middlebrook [24].

It leads to the following correspondence between thickness of the ice film and optical density that will often be used in this work:

$$\boxed{\text{OD} = 1.08 \iff \text{Thickness} = 10000 \text{ \AA}} \quad (2.23)$$

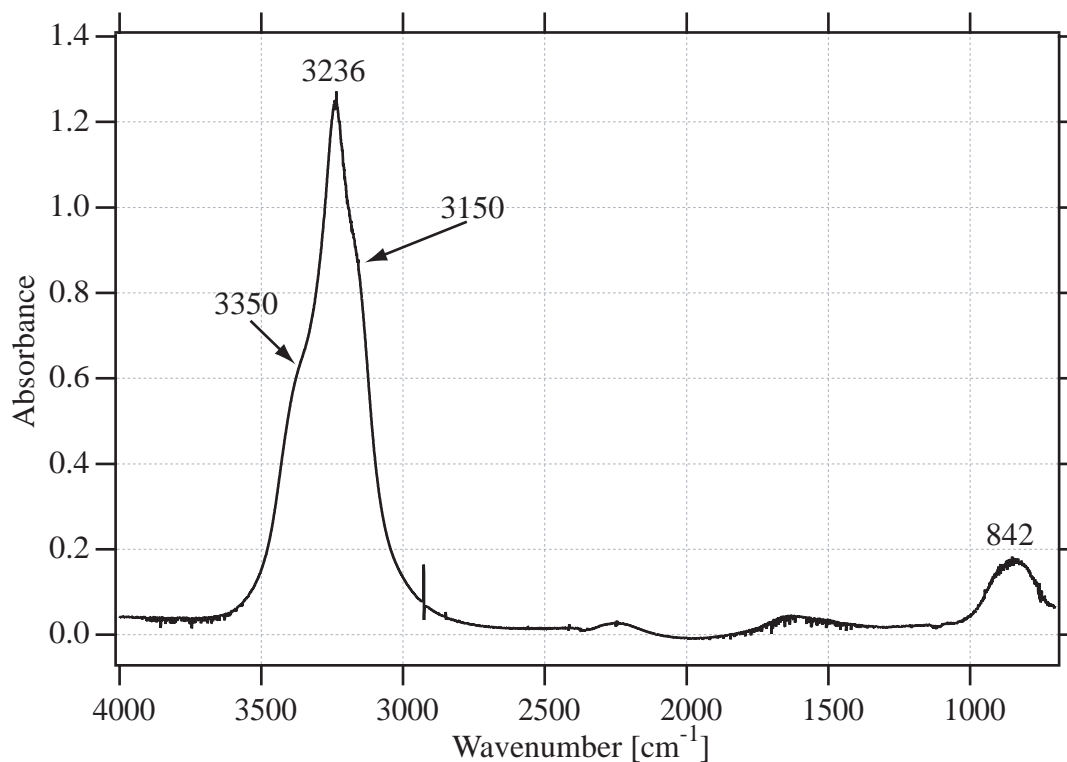


Figure 2.17: Typical FTIR spectrum observed for ice films deposited at 190 K and at a growth rate of approximately $1.0 \cdot 10^{17}$ molec $\text{cm}^{-2} \text{s}^{-1}$. It shows the presence of a polycrystalline I_h ice film [2].

2.8 Aspects of data acquisition

2.8.1 Homemade inexpensive but efficient thermocouple noise-reducer/amplifier

As was previously pointed out in Section 2.1 the temperature is monitored at several locations in the experimental apparatus: the cold window, the reactor wall, the calibrated leak, the different PTFE elements,...

These temperatures are recorded using type T thermocouples (copper-constantan) whose junction were produced in our laboratory. The wires used to make these thermocouples are very thin (diameter smaller than 0.25 mm) and, due to the very small current circulating in them, they are highly sensitive to electromagnetic noise prevailing in the laboratory. When such

thermocouples without filters are used it leads to noise levels in temperature acquisition of peak-to-peak variations sometimes corresponding to 5 to 10 K. Although it is possible to average the recorded data in order to get a good approximation of the real temperature it does not allow a visual control of the temperature trend during an experiment. In order to get rid of this problem we have developed a cheap noise-reducer/amplifier, NRA, whose electronic diagram is given in Figure 2.18.

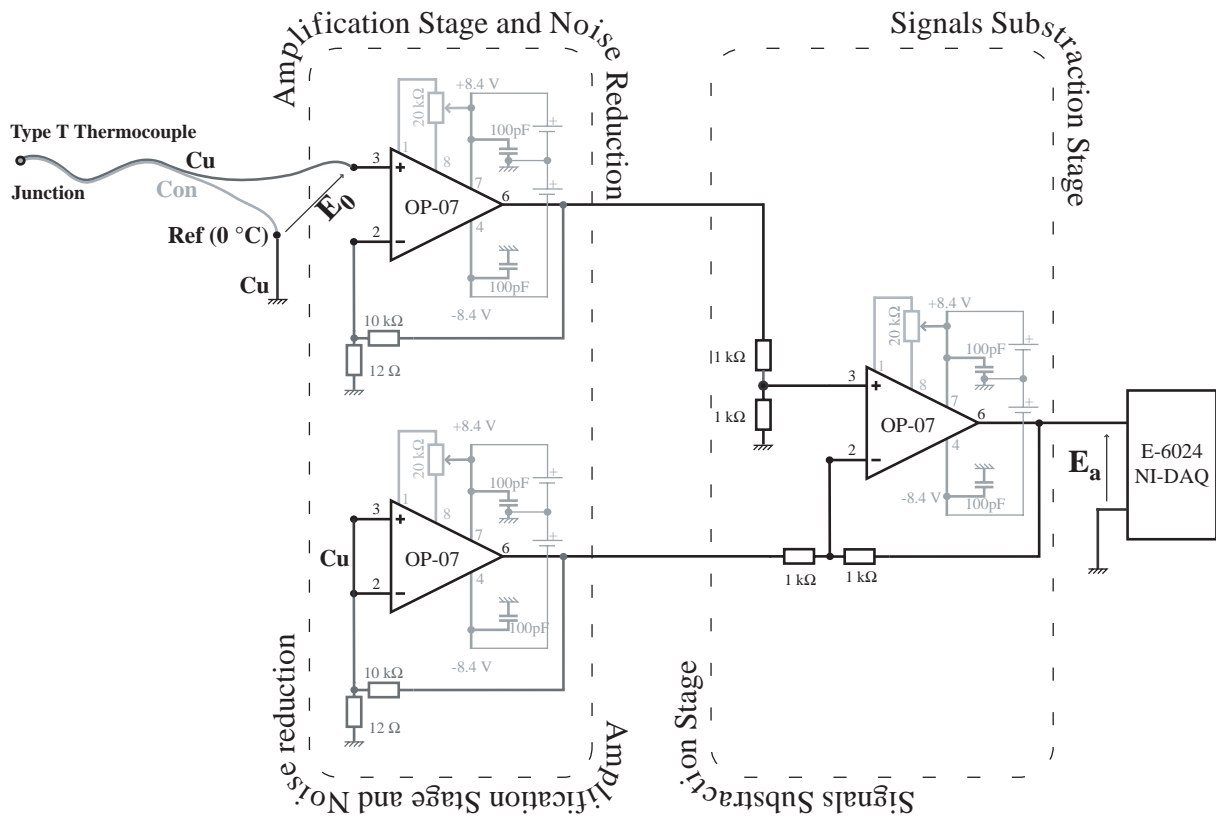


Figure 2.18: Inexpensive, homemade thermocouple noise-reducer and amplifier.

The type T thermocouples are all mounted using junction compensation and are connected to the entry of NRA. As the OP-07 op-amps are relatively slow amplifiers they play a role of smoothing the noisy signals of the thermocouples. The amplification stage has a factor of 834. Suppression of the offsets are available in different parts of NRA. The different op-amps

are battery-powered which also allows a significant reduction of the noise. It finally decreases to levels smaller than 0.1 K measured peak-to-peak. Thanks to the different offset controls the precision and accuracy of the temperature measurement is also increased. Globally, the temperature is measured with a precision of ± 0.5 K and at an accuracy on the order of 1 K. For ice the accuracy of the temperature of the film has periodically been checked against the vapor pressure of H_2O over pure ice [26] using the amplified thermocouple voltage and the Baratron output for comparison. The temperature of the ice film was assumed to be the same as the one of the Si window which is measured.

2.8.2 Data acquisition

All the data acquisition, including the voltage of the thermocouples, are computer based and were enabled by using a data acquisition board supplied by National Instruments of the type DAQ 6024E. The acquisition card is controlled by the graphical programming language Labview, also supplied by NI which manages almost all the experimental equipment. Data are acquired at a rate of approximately 1 Hz. However, in order to prevent problems of synchronisation during the writing of the data (ASCII) on the hard disc, the computer internal clock is systematically acquired at the same time as all other data are. Furthermore, all the existing analog inputs are configured as differential inputs in order to reduce once more the electromagnetically induced noise.

2.9 Appendix: cryostat Mark II dimensions

This section presents the simple one-dimensional thermal transfer model that has helped us in choosing the optimum dimensions of the elements for the finger of the cryostat Mark II.

Figure 2.19 is identical to Figure 2.12 in outline but in addition presents the different heat transfer parameters used in the simple model. Schematically, each part of the axially symmetric cooling finger consists of a cylindrical rod of radius r and of cross-sectional area $A_c = \pi r^2$. The

the thermal flow by conduction [W] in the medium stainless steel, q_x , follows the balance in Equation 2.24 under steady-state conditions:

$$q_x = q_{x+dx} + dq_{\text{conv}} \quad (2.24)$$

with dq_{conv} being the exchange by convection between the element **2** and air. Indeed, air is the only fluid surrounding the rod that allows thermal exchange by convection. Fourier's law for conduction gives results in the following equation:

$$q_x = -k_{\text{ss}} A_c \frac{dT}{dx} \quad (2.25)$$

with T being the temperature at x and A_c a previously defined constant. k_{ss} is the thermal conductivity in $\text{W m}^{-1} \text{K}^{-1}$ of stainless steel.

In the same way,

$$q_{x+dx} = -k_{\text{ss}} A_c \frac{dT}{dx} - k_{\text{ss}} \frac{d}{dx} \left(A_c \frac{dT}{dx} \right) dx \quad (2.26)$$

The heat transfer by convection is

$$dq_{\text{conv}} = h_{\text{ss/air}} dA_l (T - T_a) \quad (2.27)$$

with $h_{\text{ss/air}}$ the average convection heat transfer coefficient in $\text{W m}^{-2} \text{K}^{-1}$, T_a the temperature of air and dA_l the differential surface element between x and $x+dx$.

In the general case the following equation holds:

$$\frac{d^2 T}{dx^2} + \left(\frac{1}{A_c} \frac{dA_c}{dx} \right) \frac{dT}{dx} - \left(\frac{1}{A_c} \frac{h_{\text{ss/air}}}{k_{\text{ss}}} \frac{dA_l}{dx} \right) (T - T_a) = 0 \quad (2.28)$$

Because in the present case A_c is a constant and $\frac{dA_l}{dx} = 2\pi r$ it follows that

$$\frac{d^2T}{dx^2} - \left(\frac{2\pi r h_{ss/air}}{k_{ss} A_c} \right) (T - T_a) = 0 \quad (2.29)$$

If we consider only the stainless steel element **2** without copper element **3** brazed to it the exchange at the end of the element should be driven by convection alone. Under steady-state conditions the temperature T in the stainless steel at x is given by Equation 2.30 after solution of the differential equation as tabulated in [27]:

$$T = T_a + (T_{N_2L} - T_a) \left(\frac{\cosh(m(L-x)) + \frac{h_{ss/air}}{mk_{ss}} \sinh(m(L-x))}{\cosh(mL) + \frac{h_{ss/air}}{mk_{ss}} \sinh(mL)} \right) \quad (2.30)$$

with

$$m^2 = \frac{2\pi r h_{ss/air}}{k_{ss} A_c}$$

and L the total length of the stainless steel cylinder.

This relation gives a value for the temperature at x that is a good approximation even when the copper element **3** is brazed at the end of the stainless steel element **2**. Indeed, in reference [27] we find that k_{Cu} comprised between 480 and 401 $W m^{-1} K^{-1}$ in the range 100-300 K whereas $h_{ss/air} = h_{ss/Cu} = 10 W m^{-2} K^{-1}$ without convection forcing and k_{ss} between 10 and 15 $W m^{-1} K^{-1}$ in the range 100-300 K. This difference is illustrated in Figure 2.19 by the scaled size of the white arrows. Finally, the lower the temperature of the copper finger the better the approximation is as the difference between T_{Cu} and T_{ss} decreases. The main advantage of the stainless steel low thermal conductivity compared to the copper is that it acts as a barrier between the copper part and the liquid nitrogen and will add some inertia to the cooling device which also leads to stability. We have been able to experimentally check that the presence of copper brazed to the stainless steel element just changes the rate of decrease of the temperature but not the lowest temperature that can be reached. Using this simple one-dimensional model we have found that the best compromise between the mechanical properties that must include a reliable brazing weld between the copper and stainless steel elements and the desired thermal

properties was attained for a stainless steel element **2** of 15 mm radius and 20 mm length. The length of the copper element **3** was chosen at 150 mm. Using these parameters and the heating cartridges (Watlow-EB, 8×40 mm, 230 V, 200 W), that are inserted into an aluminium block surrounding the cylindrical Cu element extending into the air, and used for counterheating the system, affords a temperature control between 100 and 250 K with a precision on the order of 0.1 K.

Bibliography

- [1] M. Kumai, *Journal of Glaciology*, 1968, **7**, 95–108.
- [2] M. S. Bergren, D. Schuh, M. G. Sceats, and S. A. Rice, *Journal of Chemical Physics*, 1978, **69**(8), 3477–3482.
- [3] D. E. McCarthy, *Applied Optics*, 1963, **2**(6), 591–595.
- [4] R. C. Weast, *CRC Handbook of Chemistry and Physics*, CRC Press, Boca Raton, FL, 1st student ed., 1988.
- [5] O. Andersson, J. P. Johari, and H. Suga, *Journal of Chemical Physics*, 2004, **120**(20), 9612–9617.
- [6] D. S. Dillard and K. D. Timmerhaus In ed. C. Ho and R. Taylor, *Thermal conductivity - Proceedings of the eighth conference*. Plenum Press, New York, 1969.
- [7] J. M. Lafferty, *Foundations of vacuum science and technology*, Wiley, New York, 1998.
- [8] L. Lieszkovszky, A. R. Filippelli, and C. R. Tilford, *Journal of Vacuum Science and Technology a-Vacuum Surfaces and Films*, 1990, **8**(5), 3838–3854.
- [9] J. A. Basford, M. D. Boeckmann, R. E. Ellefson, A. R. Filippelli, D. H. Holkeboer, L. Lieszkovszky, and C. M. Stupak, *Journal of Vacuum Science and Technology A-Vacuum Surfaces and Films*, 1993, **11**(3), A22–A40.
- [10] D. R. Haynes, N. J. Tro, and S. M. George, *Journal of Physical Chemistry*, 1992, **96**(21), 8502–8509.
- [11] B. S. Berland, D. R. Haynes, K. L. Foster, M. A. Tolbert, S. M. George, and O. B. Toon, *Journal of Physical Chemistry*, 1994, **98**(16), 4358–4364.
- [12] B. S. Berland, D. E. Brown, M. A. Tolbert, and S. M. George, *Geophysical Research Letters*, 1995, **22**(24), 3493–3496.
- [13] M. S. Warshawsky, M. A. Zondlo, and M. A. Tolbert, *Geophysical Research Letters*, 1999, **26**(7), 823–826.
- [14] S. Laplaca and B. Post, *Acta Crystallographica*, 1960, **13**(6), 503–505.
- [15] D. S. Eisenberg and W. Kauzmann, *The structure and properties of water*, Oxford University Press, New York, 1969.
- [16] P. V. Hobbs, *Ice physics*, Clarendon Press, Oxford, 1974.
- [17] A. H. Narten, *Journal of Chemical Physics*, 1976, **64**(3), 1106–1121.
- [18] L. Schriver-Mazzuoli, A. Schriver, and A. Hallou, *Journal of Molecular Structure*, 2000, **554**, 289–300.

-
- [19] V. Buch and J. P. Devlin, *Journal of Chemical Physics*, 1991, **94**(5), 4091–4092.
- [20] S. Mitlin and K. T. Leung, *Surface Science*, 2002, **505**(1-3), L227–L236.
- [21] S. Mitlin and K. T. Leung, *Journal of Physical Chemistry B*, 2002, **106**(24), 6234–6247.
- [22] B. Rowland and J. P. Devlin, *Journal of Chemical Physics*, 1991, **94**(1), 812–813.
- [23] J. E. Bertie and E. Whalley, *Journal Chemical Physics*, 1964, **40**, 1637–1645.
- [24] M. A. Tolbert and A. M. Middlebrook, *Journal of Geophysical Research-Atmospheres*, 1990, **95**(D13), 22423–22431.
- [25] O. B. Toon, M. A. Tolbert, B. G. Koehler, A. M. Middlebrook, and J. Jordan, *Journal of Geophysical Research*, 1994, **99**(12), 25631–25654.
- [26] J. Marti and K. Mauersberger, *Geophysical Research Letters*, 1993, **20**(5), 363–366.
- [27] F. P. Incropera and D. P. DeWitt, *Fundamentals of heat and mass transfer*, J. Wiley,, New York, 4th ed., 1996.

Chapter 3

Kinetics of water condensation and evaporation from ice substrates in the presence of HCl and HBr.

This chapter presents the initial results on the kinetics of evaporation and condensation of H₂O onto ice we have obtained using the multiple diagnostics approach afforded by the experimental setup presented in Chapter 2. These results have been the subject of a publication in 2003 in the *Journal of Atmospheric Chemistry and Physics* under the title *Kinetics of water condensation and evaporation from ice substrates in the presence of HCl and HBr: implications for the lifetime of atmospheric ice particles* whose bibliographic reference may be found at the end of this chapter [1].

In summary, using the multidagnostic approach the rate R_{ev} [molec cm⁻³ s⁻¹] or flux J_{ev} [molec cm⁻² s⁻¹] of evaporation of H₂O and its corresponding rate constant for condensation, k_{cond} [s⁻¹], on a 1 μm thick ice film have been studied in the temperature range 190 to 240 K as well as in the presence of small, albeit metered, amounts of HCl and HBr that left the vapor pressure of H₂O over ice unchanged. The resulting Arrhenius expressions for pure ice are:

$$J_{\text{ev}}=1.6 \cdot 10^{28 \pm 1} \cdot \exp\left(\frac{-10.3 \pm 1.2}{\mathcal{R}} \times \frac{1000}{T}\right) \text{ molec cm}^{-2} \text{ s}^{-1},$$

$$k_{\text{cond}}=1.7 \cdot 10^{-2 \pm 1} \cdot \exp\left(\frac{+1.6 \pm 1.5}{\mathcal{R}} \times \frac{1000}{T}\right) \text{ s}^{-1},$$

in the presence of an average HCl mole fraction in the range $3.2 \cdot 10^{-5}$ to $6.4 \cdot 10^{-3}$:

$$J_{\text{ev}}=6.4 \cdot 10^{26 \pm 1} \cdot \exp\left(\frac{-9.7 \pm 1.2}{\mathcal{R}} \times \frac{1000}{T}\right) \text{ molec cm}^{-2} \text{ s}^{-1},$$

$$k_{\text{cond}}=2.8 \cdot 10^{-2 \pm 1} \cdot \exp\left(\frac{+1.5 \pm 1.6}{\mathcal{R}} \times \frac{1000}{T}\right) \text{ s}^{-1},$$

and an average HBr mole fraction smaller than $6.4 \cdot 10^{-3}$:

$$J_{\text{ev}}=7.4 \cdot 10^{25 \pm 1} \cdot \exp\left(\frac{-9.1 \pm 1.2}{\mathcal{R}} \times \frac{1000}{T}\right) \text{ molec cm}^{-2} \text{ s}^{-1},$$

$$k_{\text{cond}}=7.1 \cdot 10^{-5 \pm 1} \cdot \exp\left(\frac{+2.6 \pm 1.5}{\mathcal{R}} \times \frac{1000}{T}\right) \text{ s}^{-1}$$

where $\mathcal{R}=1.987 \text{ cal mol}^{-1} \text{ K}^{-1}$. The small negative activation energy for H_2O condensation on ice points to a precursor mechanism [2]. The corresponding enthalpies of sublimation are $\Delta H_{\text{subl}}^0=E_{\text{ev}}-E_{\text{cond}}=11.9 \pm 2.7 \text{ kcal mol}^{-1}$, $\Delta H_{\text{subl}}^0=11.2 \pm 2.8 \text{ kcal mol}^{-1}$, and $\Delta H_{\text{subl}}^0=11.7 \pm 2.8 \text{ kcal mol}^{-1}$ whose values are identical within experimental uncertainty to the accepted literature value of $12.2 \text{ kcal mol}^{-1}$ [3, 4]. Interferometric data at 632.8 nm and FTIR absorption spectra in transmission support the kinetic results. The data are consistent with a significant lifetime enhancement for HCl- and HBr-contaminated ice particles by a factor of 3-6 and 10-20, respectively, for submonolayer to monolayer coverages of HX once the fraction of the ice not contaminated by HX has evaporated.

3.1 Supplementary information on the experimental apparatus

During this part of the work the experimental setup has undergone several changes as described in Chapter 2. A valid set of experimental parameters most often used is summarized in Table 3.1.

Configuration number one and two corresponds to cryostat Mark I and II, respectively (see Chapter 2). One may notice the change of the effective volume V_r due to the change of the

Experiment configuration	Reactor Temperature [K] T_r	Reactor Volume [cm ³] V_r	Collision frequency on ice [s ⁻¹]		Rate constant of effusion for calibrated leak [s ⁻¹]	
			$\omega_{\text{H}_2\text{O}}$	ω_{HCl}	$k_{\text{esc}}(\text{H}_2\text{O})$	$k_{\text{esc}}(\text{HCl})$
1	300	1750	6.52	4.62	0.20	0.13
2	330	2450	4.89	3.46	0.055	0.043
	Calculated area of escape orifice [mm ²] A_{esc}	HeNe angle [degree] θ	Thickness equivalent to one HeNe fringe [nm]	Thickness in [nm] for FTIR OD=1.08	MS Calibration factor [molec s ⁻¹ A ⁻¹] $C_{18}^{\text{s-flow}}$ $C_{36}^{\text{s-flow}}$	
1	2.4	12	246	1000	$5.80 \cdot 10^{24}$	$6.31 \cdot 10^{24}$
2	0.8	12	246	1000	$5.70 \cdot 10^{23}$	$6.25 \cdot 10^{23}$

Table 3.1: Data on two different experimental hardware configurations and results of the calibrations. The sample surface area is $A_{\text{Si}}=0.78 \text{ cm}^2$.

cryogenic support. The different rates of effusion for the calibrated leak correspond to different outlet tubings. In the case of configuration number one it consisted of a 10 mm inner diameter Teflon tubing, whereas in number two the outflow is passed across a stainless steel tube of 6 mm inner diameter. The MS calibration factors change within a factor of approximately 10 after the exchange of the mass spectrometer filament from Tungsten to Iridium. The decrease of the calibration factor corresponds to an increased sensitivity in going from W to Ir.

Figure 3.1 presents the typical successive steps in the calibration of the experimental setup for HCl in the case of configuration number two. **Panel 1** displays the decrease of the total pressure (grey trace) in the upper chamber initially filled with HCl when the system is set from static to stirred flow conditions. At $t=0 \text{ s}$ the leak valve (LV) is opened allowing the effusion of HCl from the upper chamber through the calibrated leak. The black trace corresponds to the first order exponential fit to the grey trace displaying the raw data. The fit is performed using the computer based software IGOR (v3.00 to v5.00) from Wavemetrics, Inc., which offers built-in fitting functions. The result of the fit to the grey trace in this case is $k_{\text{esc}}(\text{HCl})=0.043 \pm 0.002 \text{ s}^{-1}$, a value that is reported in Table 3.1. **Panel 2** in Figure 3.1 shows the calibration of the first order rate constants of effusion, k_{esc} , for the calibrated leak (CV) in the case of configuration number two.

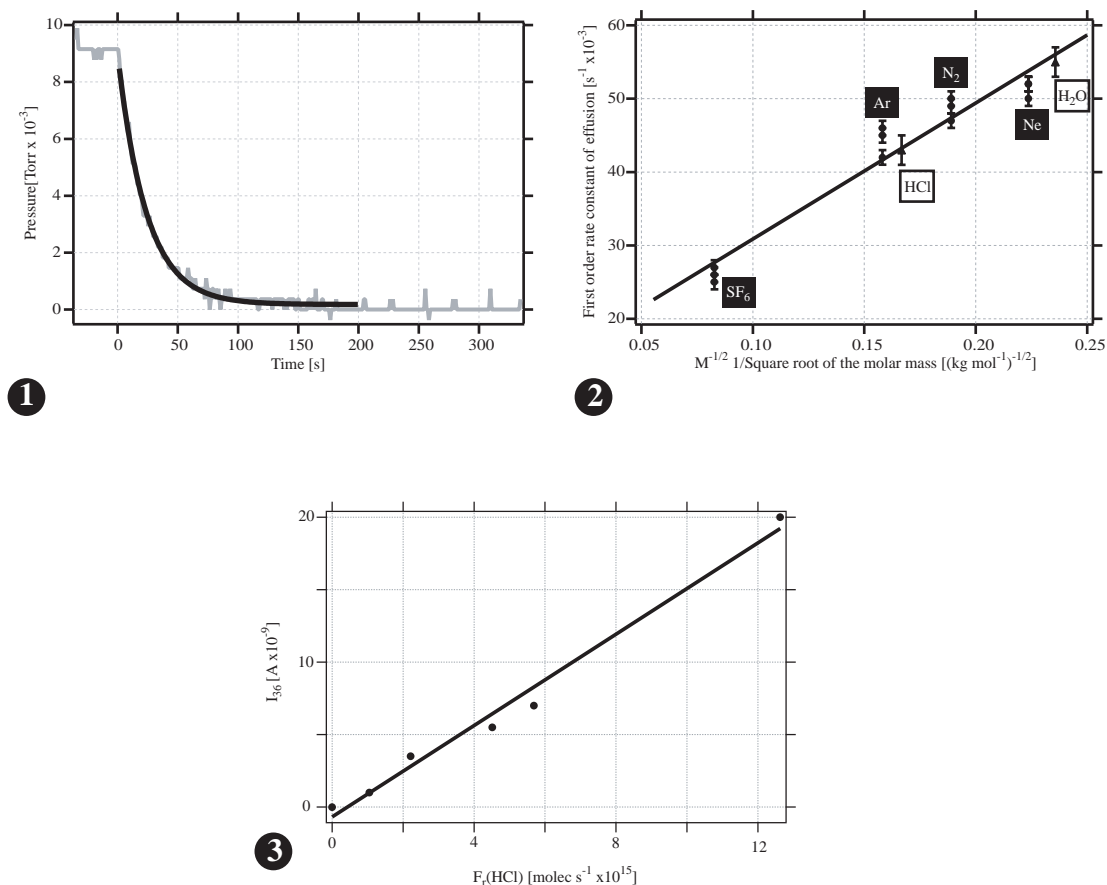


Figure 3.1: Typical calibrations for HCl in the case of configuration 2 of Table 3.1. **Panel 1:** raw HCl pressure decrease (grey) in the upper chamber monitored using the Baratron gauge when the system is set from static ($t < 0$) to stirred flow conditions ($t > 0$). At $t = 0$ s the leak valve (LV) is opened. The black trace corresponds to the first order exponential fit to the grey (data) trace leading to $k_{\text{esc}}(\text{HCl})$. **Panel 2:** calibration of the first order rate constant for effusion through the calibrated leak k_{esc} using Ne, Ar, N_2 and SF_6 (\bullet). The symbol \blacktriangle gives the experimental values of $k_{\text{esc}}(\text{H}_2\text{O})$ and $k_{\text{esc}}(\text{HCl})$ evaluated using the method illustrated in Panel 1. **Panel 3:** calibration of the MS signal at $m/z=36$ versus the flow rate of HCl, $F_r(\text{HCl})$, through the calibrated leak (CL), using the method described in Section 2.5, page 40.

Gases used for calibrations are SF_6 , Ne, Ar and N_2 which are known not to stick on stainless steel. The linear dependence of k_{esc} with $\sqrt{\frac{1}{M}}$, where M is the molar mass in kg mol^{-1} , has been discussed in Section 2.1, and is quite well represented in this case for the previously cited inert gases (\bullet symbol) as well as for HCl and H_2O (\blacktriangle symbol). The values for HCl and H_2O

that are presented using the filled triangle (\blacktriangle) symbol are evaluated using the method described in Panel 1. **Panel 3** presents the calibration of the MS signal at $m/z=36$ monitored in the detection chamber under stirred flow conditions of the reactor versus the flow rate of HCl, $F_r(\text{HCl})$, through the calibrated leak (CL) using the method described in Section 2.5. In the present case we obtain a calibration factor $C_{36}^{\text{s-flow}}=6.25 \cdot 10^{23} \text{ molec s}^{-1} \text{ A}^{-1}$ for $m/z=36$ under stirred flow conditions.

The MS calibrations allow the measurement of the absolute rate of deposition of HCl and HBr onto ice, R_{HCl} and R_{HBr} , respectively. Subsequently, the absolute number of molecules of HCl and HBr dispensed onto the ice film are available following the method described in Section 2.5, page 40.

As a reminder, the measurement of the number of HCl or HBr molecules dispensed on the deposited ice film follows a two-pronged strategy which consists of (1) establishing the absolute flow rate of HX, $F_r(\text{HX})$, admitted into the cryostat chamber under stirred flow conditions using MS signals at $m/z=36$ and $m/z=82$, for HCl and HBr, respectively, and (2) integrating the amount of HCl lost by adsorption from the gas phase to the ice film, by monitoring the gas phase using the residual gas MS. Step (1) involves monitoring of the MS signal at $m/z=36$ for HCl and $m/z=82$ for HBr, with the gate valve (GV) closed and the calibrated leak (CL) open thus enabling on-line gas phase monitoring under stirred flow condition. Previously, the MS signal intensities for HCl, I_{36} , or HBr, I_{82} , had been calibrated thus leading to a 1:1 relationship between the MS signals and the HCl concentration in the chamber by analogy with Equations 2.12 and 2.14. Using the known values of k_{esc} for HCl, $k_{\text{esc}}(\text{HCl})$, the measurement of the partial pressure of the trace gas using the Baratron gauge in the cryostat chamber or the corresponding MS signal, I_{36} , of HCl leads to the absolute flow rate in molec s^{-1} according to the following equations:

$$F_r(\text{HCl}) = \frac{P_{\text{HCl}} \times V_r}{\mathcal{R} \times T_r} \times k_{\text{esc}}(\text{HCl}) \quad (3.1)$$

$$= [\text{HCl}] \times V_r \times k_{\text{esc}}(\text{HCl}) \quad (3.2)$$

$$= \text{Conv} \times V_r \times k_{\text{esc}}(\text{HCl}) \times P_{\text{HCl}} \quad (3.3)$$

$$= C_{36}^{\text{s-flow}} \times I_{36} \quad (3.4)$$

by analogy with what was presented in Section 2.5 for the case of H_2O , Conv is the conversion factor between the partial pressure of HCl, P_{HCl} , and HCl concentration, $[\text{HCl}]$, in molec Torr $^{-1}$ cm $^{-3}$ ($3.2 \cdot 10^{16}$ and $2.9 \cdot 10^{16}$ for configurations number one and two, respectively, displayed in Table 3.1), P_{HCl} is the pressure of HCl in Torr, V_r the volume of the reactor and $k_{\text{esc}}(\text{HCl})$ the rate constant of effusion of HCl through the calibrated leak in s $^{-1}$ (see Table 3.1 for detailed information). The same technique has been used for all gases throughout this work. Moreover, the inlet made out of glass tubing and used for trace gas injection into the upper chamber is equipped with a micrometer dosing valve (Swagelok double pattern low-pressure metering valve with Vernier handle of type SS-SS2-D-TVVH) and is located between the calibrated volume used as a reservoir for HX and the inlet dosing tube. We have calibrated this valve by establishing the correspondence between the size of its aperture and the resulting MS signal, thus leading to an absolute calibration of the flow rate of HX molecules injected versus the aperture size of the micrometer dosing valve. Step (2) consists of integrating the absolute flow of HCl that was condensed onto the ice film in order to determine the HCl dose. As the window of the cryostat exposed to the gas is known to be the only part that is at low temperature (see Section 2.1) during the experiment, the difference of the integrals of the MS signal of HX with the optical substrate at ambient temperature (no ice) and in the presence of an ice film, enables the evaluation of the absolute number of molecules deposited onto the ice whereas the difference between the two MS signals obtains the rate of deposition after suitable calibration of the MS signal in terms of flow rate $F_r(\text{HCl})$ as described in Section 2.5.

In practice a dosing experiment takes place according to two different protocols depending on whether the temperature of the ice substrate is (a) $T \leq 190$ K or (b) $T > 190$ K. Under (a) the dosing experiment is performed under stirred flow conditions because the rate of H_2O evaporation is slow enough which limits its loss from the ice film during the doping process. At first, the MS signal of HCl, I_{36} , is recorded after turning on the HCl at constant flow rate for a given amount of time with the Si window at ambient temperature. Subsequently, the same sequence is repeated with the Si window at low temperature in the presence of an ice film. Figure 3.2 displays a typical experiment performed in order to obtain an absolute calibration of the HCl dose under these conditions. The dose corresponds to the hatched area pertaining to the difference of the integrals of the MS signals. When the dosing experiment is performed under high temperature conditions (b) the first step is identical and serves to establish the total number of HCl molecules dispensed on the Si window at ambient temperature. This experiment is now repeated with the Si window at $T > 190$ K and the gate valve is closed, affording now static conditions, in order to prevent significant H_2O evaporation from the ice film at $T > 190$ K. Although we are "blind" during the deposition of HCl onto the ice film owing to the static nature of the dosing the experiments discussed above reveal an exceedingly small HCl partial pressure in the chamber during the dosing so that we are confident about the HCl dosing, even though we are unable to follow the HCl signal during the dosing process. In practice more than 98 % of the dispensed HCl molecules are adsorbed onto ice, over the examined temperature range, probably owing to the directed injection of HX onto the ice surface. This result is also consistent with mass balance experiments discussed in more detail below.

Indeed, if we use the maximum value of the MS signal corresponding to ambient temperature at $t=7352$ s in Figure 3.2 we find that it approximately corresponds to a flow rate of HCl of $F_r = 6.25 \cdot 10^{23} \times 1.5 \cdot 10^{-11} = 9.4 \cdot 10^{12}$ molec s^{-1} under stirred flow conditions. By combining Equations 3.3 and 3.4 the residual partial pressure of HCl in the upper chamber in that case is

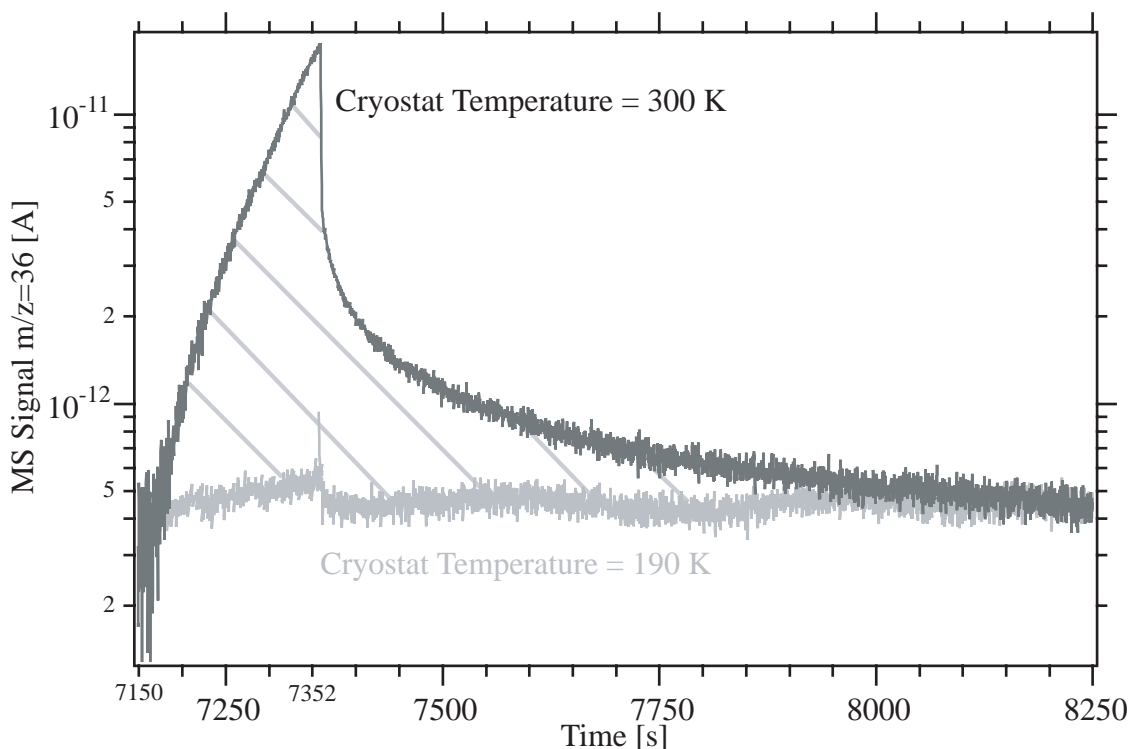


Figure 3.2: Raw MS signal for HCl at $m/z=36$. The black and grey traces correspond to the signal with the cryostat at 300 K and 190 K in the presence of ice, respectively. At $t=7150$ s, the HCl dosing valve is opened to the same extent in both cases, and is closed at $t=7352$ s. In this example the total amount of HCl molecules disappearing from the gas phase is $(8.0 \pm 0.5) \cdot 10^{14}$ molecules and corresponds to the hatched area. These results have been obtained during the transition between configurations number 1 and 2 and correspond mainly to configuration number 2 but with the calibrated leak of configuration number 1.

given as follows:

$$P_{\text{HCl}} = \frac{C_{36}^{\text{S-flow}} \times I_{36}}{\text{Conv} \times V_r \times k_{\text{esc}}(\text{HCl})} = \frac{9.4 \cdot 10^{12}}{2.9 \cdot 10^{16} \times 2450 \times 0.2} = 6.6 \cdot 10^{-7} \text{Torr}$$

Let us consider that in the presence of ice under static conditions a tenth of the above pressure value shall represent an upper limit to the backfilling pressure after initial deposition by directed injection. This assumption is reasonable considering that in Figure 3.2 the MS signal decreases by a factor larger than 30 in the presence of an ice film. At equilibrium or static conditions

the number of molecules disappearing from the gas phase and being adsorbed onto the ice film per second is given by the impingement rate of HCl onto ice, namely $\gamma_{\text{HCl/ice}} \cdot \omega_{\text{HCl}} \cdot [\text{HCl}] \cdot V_r$ or $\gamma_{\text{HCl/ice}} \cdot \omega_{\text{HCl}} \times 2.9 \cdot 10^{16} \times P_{\text{HCl}} \cdot V_r$. Fluckiger et al. [5] provide a value of $\gamma_{\text{HCl/ice}}=0.3$ for the uptake coefficient of HCl onto ice at 190 K. Using this value approximately $4.8 \cdot 10^{12}$ molec s^{-1} disappear from the gas phase and thus condense onto the ice film at the pressure cited above. Moreover, if we consider that the system is set to stirred flow conditions as soon as the deposition of HCl ends the backfilling pressure after the initial HCl deposition is still far smaller than the one we have taken as an upper limit, namely $6.6 \cdot 10^{-8}$ Torr. This implies that the background has almost no impact on the number of deposited molecules on the ice film. Table 3.2 displays the mass balance for six selected dosing experiments in support of the dosing procedure, namely that between HCl dispensed to the ice substrate (column 4 of Table 3.2) and the HCl recovered after complete H_2O and HCl evaporation (column 5 of Table 3.2) once the sample support has reached ambient temperature. The excellent mass balance validates the chosen dosing procedure, in particular it refutes the possibility that the chamber walls act as a significant reservoir for HCl under the present experimental conditions.

Experiment Number	Temperature (K)	HCl/Ice Structure	Number of HCl molecules deposited on ice (according to Figure 3.2)	Number of HCl molecules desorbing from ice during evaporation of the ice film (based on MS signals)
1	180	HCl·6H ₂ O	$8.7 \cdot 10^{14}$	$8.4 \cdot 10^{14}$
2	180	Amorphous	$2.1 \cdot 10^{15}$	$2.0 \cdot 10^{15}$
3	180	Amorphous	$4.3 \cdot 10^{16}$	$3.6 \cdot 10^{16}$
4	190	HCl·6H ₂ O	$1.1 \cdot 10^{15}$	$1.1 \cdot 10^{15}$
5	190	HCl·6H ₂ O	$1.0 \cdot 10^{15}$	$9.8 \cdot 10^{14}$
6	190	Amorphous	$2.0 \cdot 10^{15}$	$1.7 \cdot 10^{15}$

Table 3.2: HCl mass balance for 6 typical experiments.

The smallest measurable MS signal level at $m/z=36$ within an acceptable S/N ratio of 2 in

our apparatus is on the order of $3 \cdot 10^{-13}$ A with a rise time of nearly 10 s. This leads to an estimate of $2.0 \cdot 10^{12}$ molec corresponding to $3 \cdot 10^{-3}$ of a formal monolayer using a calibration factor for the MS signal of $6.25 \cdot 10^{23}$ molec $s^{-1} A^{-1}$ for the smallest measurable amount of HCl deposited on the optical substrate. The lowest achievable deposition rate was $2.0 \cdot 10^{11}$ molec s^{-1} and the lowest detectable partial pressure of HCl monitored by residual gas MS was of the order of $6.0 \cdot 10^{-8}$ Torr. We have estimated that owing to the very small gas phase density of HCl in the presence of an ice film of typically $8.0 \cdot 10^{-8}$ Torr the adsorption of gas phase HCl would take a time exceeding the typical duration of the present experiments. We have therefore ignored the deposition rate of HCl onto the ice sample under HCl background conditions afforded by the maximum pumping speed of the vacuum chamber.

An alternate method of dosing HX onto the ice has been performed by the deposition of the trace gas under static conditions by backfilling the reactor volume with a measured amount of trace gas in addition to the method presented above which corresponds to the directed deposition of pure HCl onto ice across dosing tubes according to Figure 2.8, page 29. No significant differences in the kinetic results have been observed when comparing the backfilling with the directed deposition technique.

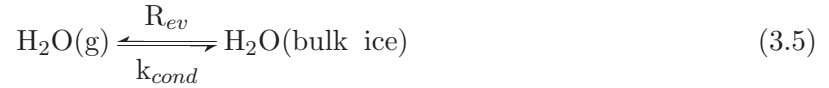
For HBr the present experimental setup does not allow quantitative dosing experiments because the PTFE insulation apparently irreversibly adsorbs small quantities of HBr. However, the used deposition settings for HBr were identical to the ones used for HCl allowing the estimation of upper limits for the concentration of HBr.

3.2 Experimental Results

3.2.1 Gas phase study of the kinetics of condensation and evaporation of H₂O from pure and HX-doped ice

Both the rate of evaporation R_{ev} in molec $s^{-1} cm^{-3}$ and the uptake coefficient γ of H₂O vapor uptake on ice have been measured between 200 and 240 K for pure ice and in the presence of

known amounts of HCl or amounts of HBr corresponding to upper limiting values according to the net reaction:



with $\gamma = k_{\text{cond}}/\omega$, where k_{cond} is the condensation rate coefficient in s^{-1} and ω is the collision frequency of H_2O with the ice film in s^{-1} (see Table 3.1). In this work the kinetic data will always refer to the system $\text{H}_2\text{O}/\text{Ice}$, with pure or doped ice, unless mentioned otherwise. Both the rate of evaporation R_{ev} and the rate of condensation $R_{\text{cond}} = k_{\text{cond}}[\text{H}_2\text{O}]$ are expressed in units of $\text{molec s}^{-1} \text{cm}^{-3}$ and address the gain and loss, respectively, of H_2O vapor with respect to the gas phase. Both processes may also be expressed in terms of fluxes of gas phase molecules to and from the substrate surface of area A_{Si} . The rate R_{ev} and flux J_{ev} of evaporation are connected through the relationship

$$J_{\text{ev}} = \frac{R_{\text{ev}}}{\frac{A_{\text{Si}}}{V_{\text{r}}}} \quad (3.6)$$

where $(A_{\text{Si}}/V_{\text{r}})$ is the surface-to-volume ratio of the used experimental arrangement (see Table 3.1). Both rates and fluxes express the same physicochemical process, the rate being normalized per unit vessel volume, the flux for unit substrate surface.

The separation of the rates of evaporation and condensation was enabled by using a method which consisted of the consecutive use of the reactor in the static (GV and LV closed) and the stirred flow (GV closed, LV open) mode. By measuring P_{eq} , the equilibrium H_2O vapor pressure in the reactor (upper chamber) under static condition, and P_{ss} , its corresponding steady state partial pressure under stirred flow condition, R_{ev} and k_{cond} were calculated using the following equations:

$$P_{\text{eq}} = \frac{R_{\text{ev}}}{k_{\text{cond}}} \times RT \quad P_{\text{ss}} = \frac{P_{\text{eq}}}{\frac{k_{\text{esc}}}{k_{\text{cond}}} + 1} \quad (3.7)$$

derived from Equilibrium 3.5 and thus from the following equilibrium (static) and steady-state (stirred flow) balances:

$$R_{ev} = k_{cond}[H_2O]_{eq} \quad \text{Equilibrium} \quad (3.8)$$

$$R_{ev} = k_{cond}[H_2O]_{ss} + k_{esc}[H_2O]_{ss} \quad \text{Steady - state} \quad (3.9)$$

In all experiments presented in this work ice was always deposited at 190 K at a rate of $1.0 \cdot 10^{17}$ molec s^{-1} and heated to the desired temperature after deposition. Both P_{eq} and P_{ss} have been corrected for the fact that the colliding gas, namely water vapor, was at ambient or slightly higher temperature as it is controlled by the temperature of the chamber walls, whereas the target consisting of the ice film deposited on the optical support was at low temperature. Under those conditions both the pressures, P_{eq} and P_{ss} as well as $[H_2O]$ are related to the measured values by both the temperature of the cold target and the chamber walls at ambient temperature. The correction procedure has been explained in more detail in Section 2.4.

The protocol for the deposition of ice leading to samples of typically $1 \mu m$ thickness was kept the same throughout the present study. The deposition temperature of 190 K was deliberately chosen so as to lead to the formation of thermodynamically stable polycrystalline ice of hexagonal I_h crystal structure thus minimizing the occurrence of mixtures with cubic and amorphous phases that are metastable at 190 K. A mixture of ice phases may lead to a H-bonding environment that is different compared to the thermodynamically stable pure ice phase I_h crystal structure as has been shown by Schaff and Roberts [6] using FTIR reflection-absorption spectroscopy. In addition, we may exclude the presence of a significant degree of porosity in the present ice films as shown by Keyser et al. [7]. We have therefore chosen an ice deposition protocol that should always lead to a homogeneous film of thermodynamically stable I_h crystal structure irrespective of the temperature of the film used for further investigations.

A known quantity (number of molecules) of HX, N_{HX} , was subsequently deposited on the

pure ice film, and both the equilibrium vapor pressure P_{eq} of H_2O as well as its steady state value P_{ss} were measured using the absolute pressure gauge or the MS signal at $m/z=18$ for P_{ss} . This allowed the determination of R_{ev} and γ of H_2O in the presence of HX in comparison with pure ice. The number of HCl molecules adsorbed on the ice was in the range $1.0 \cdot 10^{13}$ - $1.0 \cdot 10^{15}$ molec corresponding approximately to 0.01 to 1 formal monolayer with an upper limit of the HCl deposition rate of $1.0 \cdot 10^{14}$ molec s^{-1} . For HBr the number of molecules adsorbed and the deposition rate are similar to HCl as only limiting values can be given (see above). During the measurement of P_{eq} of H_2O no HX desorption has been observed while H_2O was evaporating from the ice, and a change in $m/z=36$ and $m/z=82$ for HCl and HBr, respectively, was only observable during the evaporation of the last few tens of nm film thickness as observed by simultaneous monitoring of the change in thickness of the ice deposit and the gas phase composition using HeNe interferometry and MS, respectively.

One must keep in mind that steady state conditions for H_2O , P_{ss} , in the case of doped ice were attained once a significant fraction of the ice sample evaporated in contrast to pure ice where steady state conditions are attained instantaneously. The remaining thickness corresponded to the last few hundred nanometers of ice between points **C** and **D** of the HeNe interferogram displayed in Figure 3.3 corresponding to 25-50 % of the quarter of the thickness of the original ice film (25-50 % of the last HeNe fringe). Thus the mean HCl mole fraction in the remaining ice film, χ_{HCl} , was in the range $3.2 \cdot 10^{-5}$ to $6.4 \cdot 10^{-5}$ for a dose of $1.0 \cdot 10^{13}$ adsorbed HCl molecules, and between $3.2 \cdot 10^{-3}$ and $6.4 \cdot 10^{-3}$ for a dose of $1.0 \cdot 10^{15}$ adsorbed HCl. The latter case corresponds to the situation between points **C** and **D** of the displayed HeNe interferogram in Figure 3.3 and suggests that one adsorbed HCl molecule may exert a significant kinetic effect on roughly 500 H_2O molecules on average.

The kinetic results are shown in Figures 3.4 and 3.5 which display J_{ev} , the evaporative flux and γ , the uptake coefficient. It is important to point out that in the presence of a dose of adsorbed HX in the range given above, the measured equilibrium vapor pressure P_{eq} of $\text{H}_2\text{O}(\text{g})$ is that over pure ice and therefore independent of the doses of HX over the range explored.

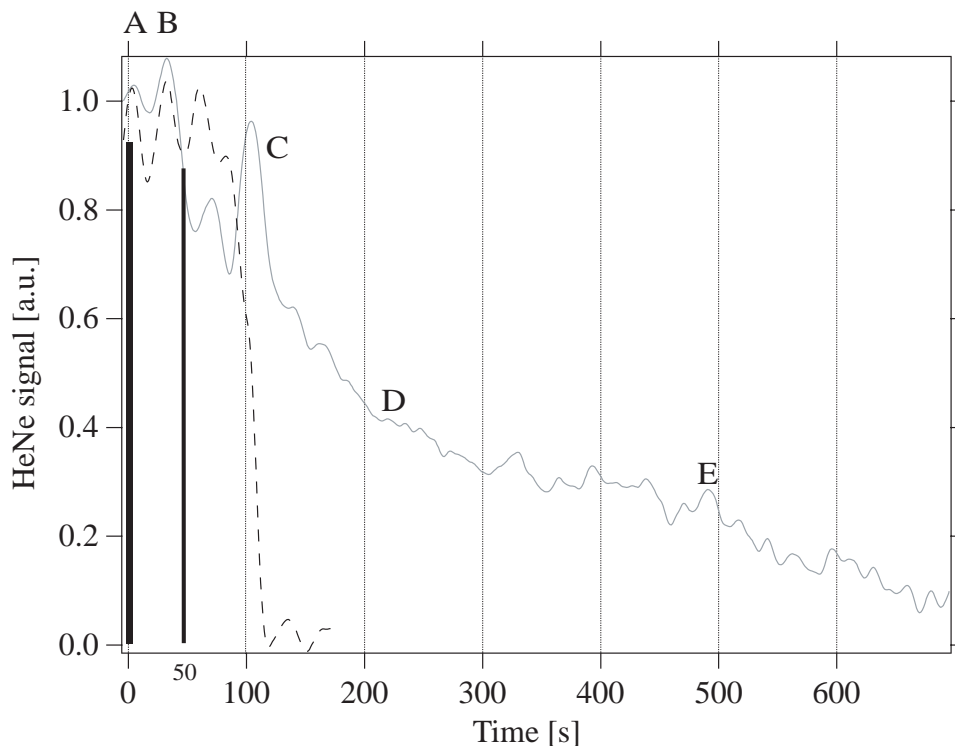


Figure 3.3: Interferometric signal of evaporating: (a) pure ice (black dashed), (b) HCl-doped ice film of $1.0 \cdot 10^{15}$ deposited HCl at 190 K (gray). At $t=0$, the static system (GV and LV closed) is set to stirred flow (GV closed, LV open) condition by opening the leak valve (LV) (first black vertical line). The second vertical line corresponds to the first noticeable difference between interferograms.

Figure 3.4 shows the decrease of J_{ev} in the presence of HCl relative to that of pure ice by a factor of 3 to 6 at doses smaller than $1.0 \cdot 10^{15}$ molec cm^{-2} corresponding to a maximum of one formal monolayer of HCl. The uptake coefficient γ displayed in Figure 3.5 undergoes the same change as J_{ev} owing to the constraint that the measured $P_{\text{H}_2\text{O}}^{\text{eq}}$ is that of pure ice. This decrease in J_{ev} and γ depends upon the number of HCl molecules deposited on the surface of the ice, but stays roughly constant for amounts larger than $1.0 \cdot 10^{14}$ molecules of HCl adsorbed on ice as displayed in Figure 3.6. It shows the HCl dose dependence of J_{ev} together with a discontinuity around $6 \cdot 10^{13}$ of deposited HCl molecules which corresponds to a mole fraction for HCl in ice between $1.9 \cdot 10^{-4}$ and $3.8 \cdot 10^{-4}$. It seems that for doses of deposited HCl up to $1 \cdot 10^{14}$, J_{ev}

stabilizes around $5 \cdot 10^{16}$ molec $\text{cm}^{-2} \text{s}^{-1}$ which is the value displayed in Figure 3.4 at 210 K. Same trends are observable for HBr doping in Figure 3.7 both for J_{ev} and γ but the dependence is scaled with relative dose of HBr as the absolute number of HBr molecules dispensed on ice is not available. However, for larger doses of HCl both J_{ev} and γ continue to decrease. Figures 3.4 and 3.5 display all values obtained in this work including the ones at very large HCl doses (∇ symbol in Figures 3.4 and 3.5).

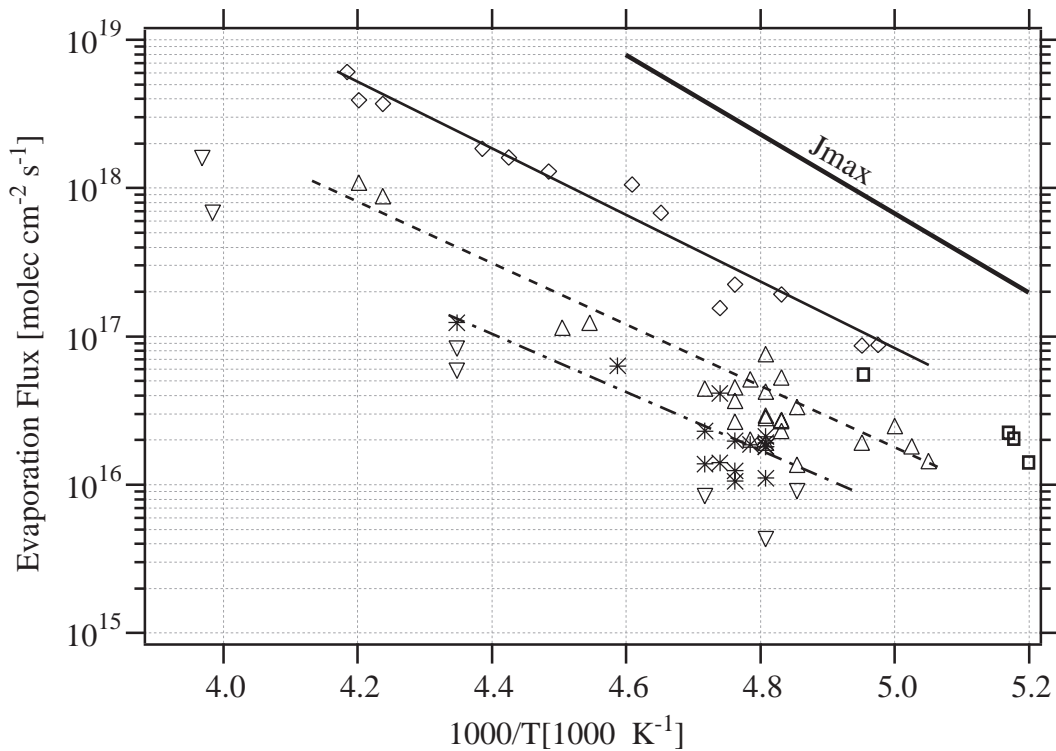


Figure 3.4: Arrhenius plot of the evaporative flux of H_2O (J_{ev}) from pure and HX doped ice films (\square : condensed ice, Chaix et al. [8, 9]; \diamond : condensed ice, this work; \triangle : HCl-doped ice, this work; $*$: HBr-doped ice, this work). The typical uncertainty of individual points are within the size of the symbols. ∇ : value observed for a very large dose of HCl leading to the formation of a liquid HCl/ H_2O mixture on the ice surface. J_{max} corresponds to the theoretical maximum value for the evaporative flux of a pure ice film ($\gamma=1$).

The energy of activation for the flux of evaporation, J_{ev} , and the rate constant for condensation, k_{cond} of H_2O from pure ice are calculated to be

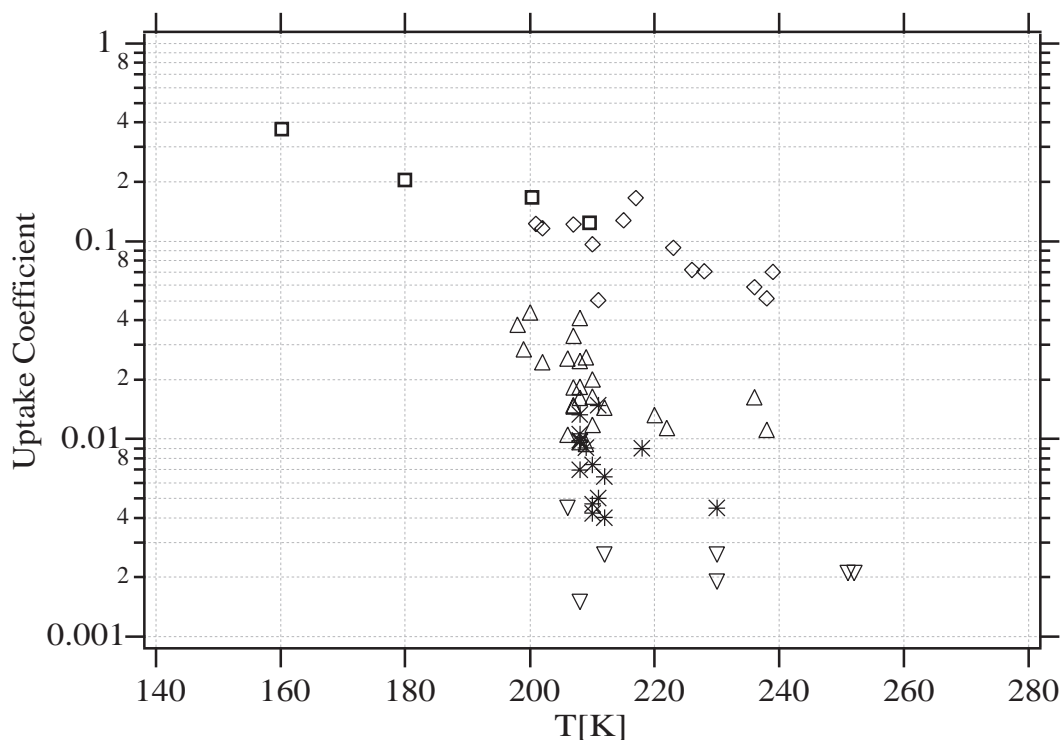


Figure 3.5: Temperature dependence of the uptake coefficient γ of H_2O from pure and HX-doped ice films. \square : condensed ice, Chaix et al. [8, 9]; \diamond : condensed ice, this work; \triangle : HCl-doped ice, this work; $*$: HBr-doped ice, this work. ∇ : value observed for a very large dose of HCl leading to the formation of a liquid HCl/ H_2O mixture on the ice surface.

$$E_{\text{ev}} = 10.3 \pm 1.2 \text{ kcal mol}^{-1} \quad (3.10)$$

and

$$E_{\text{cond}} = -1.6 \pm 1.5 \text{ kcal mol}^{-1} \quad (3.11)$$

respectively, leading to the Arrhenius expressions

$$J_{\text{ev}} = 1.6 \cdot 10^{28 \pm 1} \exp\left(\frac{-10.3 \pm 1.2}{\mathcal{R}} \times \frac{1000}{T}\right) [\text{molec cm}^{-2} \text{ s}^{-1}] \quad (3.12)$$

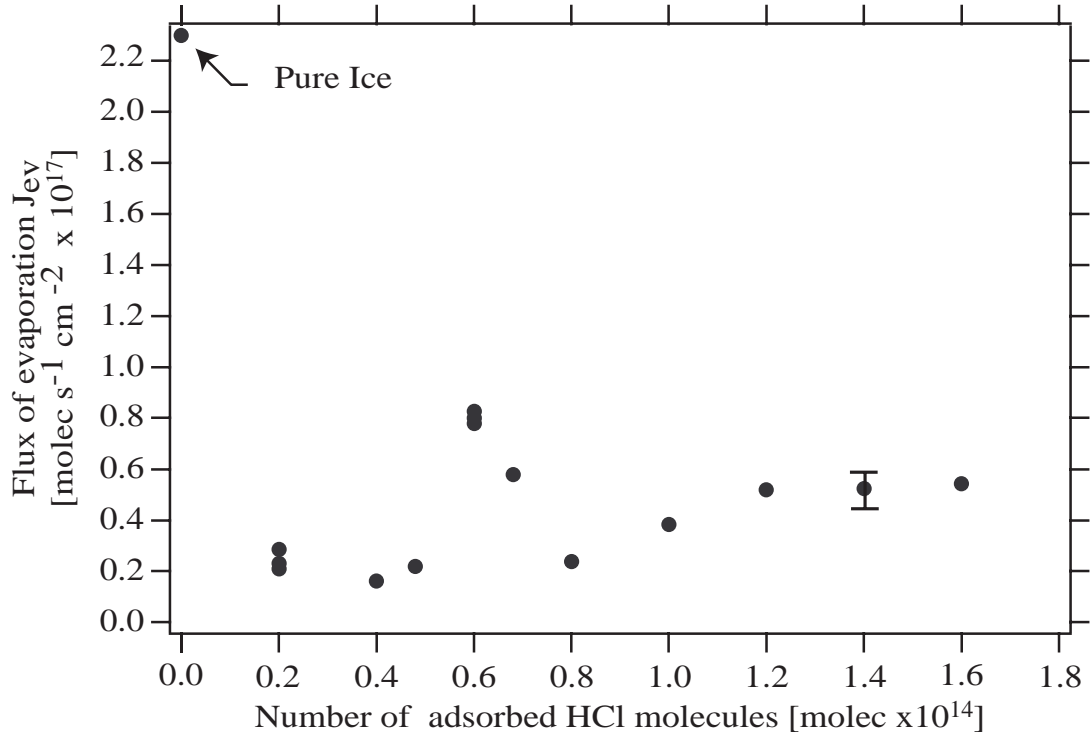


Figure 3.6: Dependence of J_{ev} on the number of HCl molecules adsorbed on 0.78 cm^2 of ice substrate at 210 K. The stable level appearing for a dose higher than $1 \cdot 10^{14}$ molec was chosen for the data displayed in Figure 3.4. The remaining ice film thickness is between 200 and 70 nm.

and

$$\boxed{k_{\text{cond}} = (1.7 \cdot 10^{-2 \pm 1}) \cdot \exp\left(\frac{+1.6 \pm 1.5}{\mathcal{R}} \times \frac{1000}{T}\right) [\text{s}^{-1}]}$$
 (3.13)

for the range 200 to 240 K, with $\mathcal{R} = 1.987 \text{ cal mol}^{-1} \text{ K}^{-1}$.

For HCl doped-ice the values are

$$\boxed{E_{\text{ev}} = 9.7 \pm 1.2 \text{ kcal mol}^{-1}}$$
 (3.14)

and

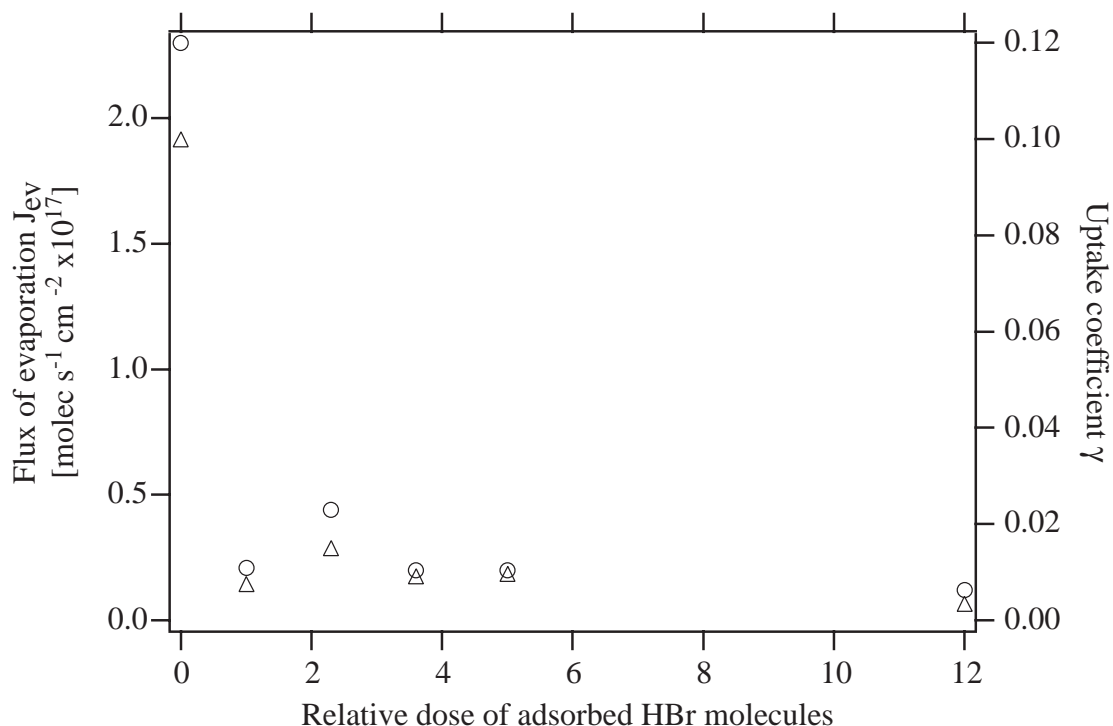


Figure 3.7: Dependence of J_{ev} (\circ) and γ (\triangle) on the number of HBr molecules adsorbed on the ice surface at 210 K. The stable level for a dose higher than 3.6 was used in Figure 3.4. A dose of 1 corresponds to a maximum of $5 \cdot 10^{13}$ adsorbed molecules. The remaining ice film thickness is between 200 and 70 nm.

$$E_{\text{cond}} = -1.5 \pm 1.6 \text{ kcal mol}^{-1} \quad (3.15)$$

leading to

$$J_{ev} = 6.4 \cdot 10^{26 \pm 1} \cdot \exp\left(\frac{-9.7 \pm 1.2}{\mathcal{R}} \times \frac{1000}{T}\right) [\text{molec cm}^{-2} \text{ s}^{-1}] \quad (3.16)$$

and

$$k_{\text{cond}} = (2.8 \cdot 10^{-2 \pm 1}) \cdot \exp\left(\frac{+1.5 \pm 1.6}{\mathcal{R}} \times \frac{1000}{T}\right) [\text{s}^{-1}] \quad (3.17)$$

in the range 200 to 240 K, with $\mathcal{R} = 1.987 \text{ cal mol}^{-1} \text{ K}^{-1}$.

In the presence of HBr, the decrease of J_{ev} is more important than for HCl and J_{ev} is almost 20 times smaller than on pure ice for similar, albeit estimated doses of HBr. This led to an activation energy for H_2O evaporation and condensation from HBr-doped ice of

$$\boxed{E_{\text{ev}} = 9.1 \pm 1.2 \text{ kcal mol}^{-1}} \quad (3.18)$$

and

$$\boxed{E_{\text{cond}} = -2.6 \pm 1.6 \text{ kcal mol}^{-1}} \quad (3.19)$$

, respectively, leading to

$$\boxed{J_{\text{ev}} = 7.4 \cdot 10^{25 \pm 1} \cdot \exp\left(\frac{-9.1 \pm 1.2}{\mathcal{R}} \times \frac{1000}{\text{T}}\right) [\text{molec cm}^{-2} \text{ s}^{-1}]} \quad (3.20)$$

and

$$\boxed{k_{\text{cond}} = (7.1 \cdot 10^{-5 \pm 1}) \cdot \exp\left(\frac{+2.6 \pm 1.5}{\mathcal{R}} \times \frac{1000}{\text{T}}\right) [\text{s}^{-1}]} \quad (3.21)$$

in the range 200 to 240 K, with $\mathcal{R}=1.987 \text{ cal mol}^{-1} \text{ K}^{-1}$.

Following these results, the decrease of the pre-exponential factor in J_{ev} is responsible for the most part for the change of the rate of evaporation of H_2O .

3.2.2 HeNe monitoring of the change of thickness of the ice film

Observations of the condensed phase in the absence and the presence of HCl have also been performed using HeNe interferometry at 632.8 nm simultaneously with MS and FTIR measurements. Figure 3.3 shows the decrease of the thickness of a 1 μm thick film of pure and HCl-doped ice at 190 K with time. First, the ice film is grown under static conditions at 190 K at a rate of $1.0 \cdot 10^{17} \text{ molec s}^{-1}$, and is subsequently doped with $1.0 \cdot 10^{15}$ molecules of HCl or HBr. The decrease in the net rate of H_2O evaporation, which corresponds to the balance

between H_2O molecules evaporating and H_2O molecules condensing onto the ice substrate, of the $1\mu\text{m}$ thick ice film in the presence of $1.0\cdot 10^{15}$ deposited HCl molecules corresponding to less than 2 monolayers amounts to a factor of 5 to 6 compared to pure ice once steady state is achieved between points **C** and **D** and maintained to point **E**. This is also the time period during which P_{ss} (Equations 3.7, page 71) has been measured. The portion of the interferogram between $t=100$ and 300 s in Figure 3.3 containing points **C** and **D** describes quite well a sinusoidal change of the photodiode signal which in turn corresponds to a linear change of thickness with time according to Equation 2.19, page 45. This result is in good agreement with the decrease of R_{ev} observed in the presence of HCl discussed above, albeit not directly comparable. The present observation of the condensed phase under stirred flow conditions implies a **net** change, that is the difference between evaporation and condensation rates whereas the gas phase measurement results in the separation of elementary rates R_{ev} and $k_{\text{cond}}[\text{H}_2\text{O}]_{\text{ss}}$. The net change observed interferometrically is somewhat less than the change given by R_{ev} alone within a factor of two as condensation of H_2O onto the remaining ice film counteracts the decrease of the thickness owing to R_{ev} .

One may note that the spacing between the interferometric fringes is gradually becoming larger which corresponds to a decrease of the net rate of evaporation starting at approximately $t=50$ s as shown in Figure 3.3, point **B**, where $1.5\cdot 10^{18}$ molecules of H_2O still remain in the ice film compared to $2.5\cdot 10^{18}$ at the beginning of the evaporation. Therefore, 60 % of the original ice film thickness is still present at **B**. As no desorption of HX from the film was observed using MS, we therefore claim that the amount of HX adsorbed on the ice film is responsible for this change of J_{ev} as discussed above. At first only the H_2O molecules that are not influenced by the presence of HX are evaporating at the characteristic rate of pure ice which corresponds to the portion of the interferogram of Figure 3.3 between points **A** and **B**. The presence of adsorbed HCl molecules therefore does not hinder H_2O molecules from the deeper hence pure portion of the ice film to evaporate as if it were a pure ice sample. Between points **B** and **E** of the interferogram the decrease of the rate of evaporation of H_2O is due to the effect of HX on the

water molecules making up the remainder of the ice substrate. The presence of HX is being felt more strongly with time by the remaining H₂O molecules as the mole fraction of HX in ice becomes more important owing to the fact that only H₂O but no HCl (or HBr) is desorbing. This results in an upper limit average value of $\chi_{\text{HCl}}=1.2\cdot 10^{-2}$ at point **E** in Figure 3.3. From point **E** of the interferogram to the end of the evaporation of the film we have observed HCl in the gas phase using MS detection which indicates that HCl evaporates from the ice film together with H₂O.

Table 3.3 displays some typical observations of the temporal evolution of the HeNe interferogram for different doping conditions of the ice film under stirred flow conditions.

Case (a),(b) and (c) refer to experimental configuration number one, whereas cases (a') and (b') differ from the former by the change of the calibrated leak (configuration number two). The comparison between (a) and (b), on the one hand, and (a') and (b') on the other hand illustrates the conclusions cited above concerning the change in the net rate of H₂O evaporation from ice in the presence of HCl. In the cases (b), (c) and (b') corresponding to HCl doping the evaporation rate for 50 to 75 % of the film thickness is that of pure ice and therefore not affected by the presence of $1.0\cdot 10^{15}$ HCl molecules. Cases (c) and (b') make for an interesting comparison. The stable hydrate HCl·6H₂O (case (b')), whose formation will be discussed in Section 3.2.3, significantly slows down the net rate of evaporation, say by a factor of less than 20 corresponding to 600 vs. 35 s per fringe. This latter time is the time needed to evaporate pure ice film of 246 nm thickness corresponding to one interference fringe of the HeNe interferogram. In contrast, the crystalline hydrate (case (b')) makes its presence felt over the last fringe at the used HCl dose whereas the presence of the amorphous hydrate (case (c)) affects 50 % of the sample thickness as it is apparently distributed in a more diffuse manner across the ice sample. In contrast, its presence affects the H₂O evaporation rate to a lesser extent corresponding to a decrease of a factor between 2 and 3. We would like to stress, however, that the resolution of the HeNe interferogram is too crude to allow quantitative conclusions in the present case. We just underline the qualitatively similar conclusions between the interferometric and the quantitative

Ice Substrate Temperature [K]	Ice Thickness at end of deposition [nm]	Dose of HCl molecules	Rate of deposition [molec s ⁻¹]	Time for complete film evaporation [s]	Trapped H ₂ O molecules	FTIR Spectral characterization at fringe 4
(a) 180	1000	Pure Ice	Null	217		
(b) 180	1000	1 · 10 ¹⁵	1 · 10 ¹³	320		
(c) 190	1000	1 · 10 ¹⁵	6 · 10 ¹²	450		
(a') 190	1000	Pure Ice	Null	125		
(b') 190	1000	1 · 10 ¹⁵	1 · 10 ¹³	708		
Last 4 periods between fringes [s]						
	1	2	3	4		
(a)	67	60	50	40	Null	Pure Ice
(b)	74	69	58	116	1.2 · 10 ¹⁸	HCl·6H ₂ O
(c)	73	75	120	160	1.8 · 10 ¹⁸	Amorphous HCl·H ₂ O
(a')	30	30	30	35	Null	Pure Ice
(b')	35	35	38	600	1.2 · 10 ¹⁸	HCl·6H ₂ O

Table 3.3: Experimental observations of the HeNe interferogram during the evaporation of a 1 μm thick pure ice film, as well as doped with HCl, under stirred flow conditions and for different doping conditions. Cases (a), (b), (c) correspond to experimental configuration number 1 (Table 3.1), cases (a') and (b') to configuration number 2 (Table 3.1).

kinetic results obtained from gas phase observations discussed above. For HBr doping, the decrease in the net rate of evaporation as observed from the corresponding interferogram is on the order of 30 to 40 for HBr levels similar to HCl which is within a factor of two of the results on R_{ev} discussed above (Figure 3.4). One needs to be reminded, however, that in contrast to the measurement of R_{ev} presented above the observation of the change in ice film thickness addresses the net rate of evaporation and is therefore smaller than R_{ev} at a given partial pressure of H_2O .

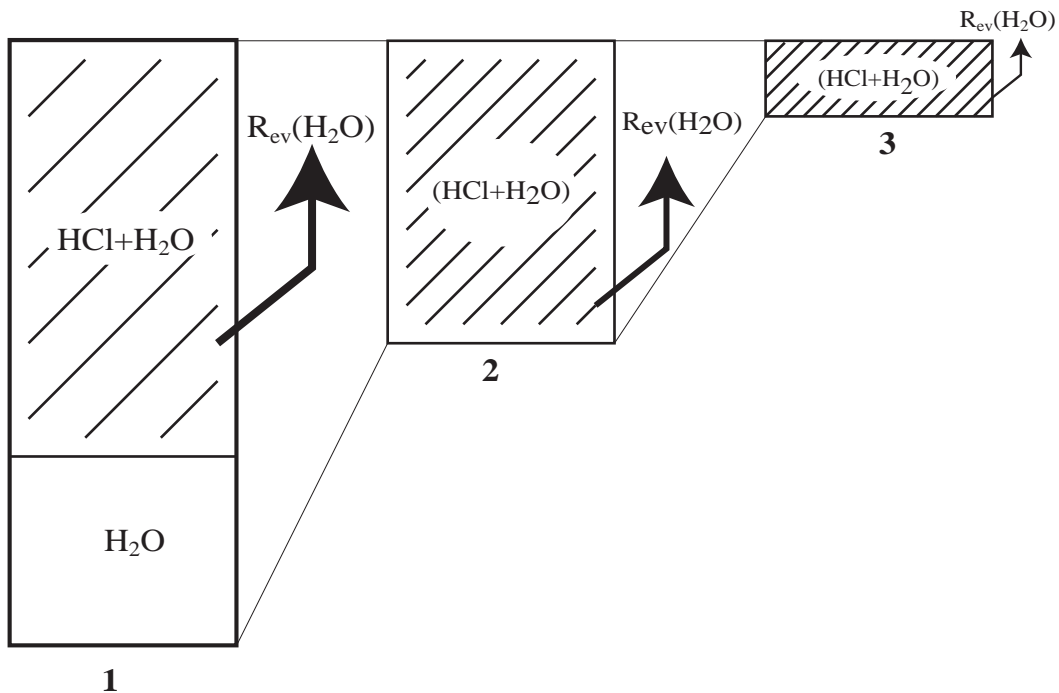


Figure 3.8: Cartoon of the fate of a HCl-doped ice film upon evaporation of H_2O (see text for explanation). Hatched areas represents the mixture of $\text{HCl}/\text{H}_2\text{O}$.

Figure 3.8 presents a cartoon describing these processes where **1** corresponds to the composition of the substrate within the time period between **A** and **B** of the interferogram, **2** to the period between **B** and **C** and **3** to the period between **C** and **E**. However, it does not differentiate between cases (c) and (b), (b)' displayed in Table 3.3, namely between the amorphous $\text{HCl}/\text{H}_2\text{O}$ mixture and the crystalline hexahydrate, respectively. The spatial extent of these two different phases containing HCl are summarily earmarked by the shading in Table 3.3. Interestingly, the

spatial extent of the amorphous phase is larger by roughly a factor of two compared to the crystalline HCl hexahydrate, the latter of which seems to be a more compact layer compared to the former. Nevertheless, the evaporation of pure underlying H₂O seems to go on unabatedly at the evaporation rate characteristic of pure ice regardless of the nature of the "capping" phases. This result is in stark contrast to the conclusions presented by Biermann et al. [10] in the case of HNO₃ and highlights the effect that small doses of HCl in the range of one to two formal monolayers may have on the kinetics of condensation and evaporation of H₂O. However, this contaminated layer of ice does not seem to constitute a barrier for the evaporation of the underlying pure ice.

3.2.3 FTIR spectroscopic study in transmission of the condensed phase

In addition to the kinetics considerations the FTIR absorption spectroscopic study in transmission we have performed has led to four sets of results that have been obtained at 190 K on a 1 μm thick ice film and which are summarized in Table 3.4.

All the FTIR scans presented in this work have been recorded on a cryogenic mercury cadmium telluride (HgCdTe) detector using a resolution of 1 cm^{-1} and correspond to averaging of 4 consecutive scans.

First, the spectrum of pure ice in Figure 3.9 reveals the presence of polycrystalline I_h ice in the OH-stretch region as discussed previously in Section 2.7. The spectrum shows an absorption peak at 3236 cm^{-1} with shoulders at 3150 and 3350 cm^{-1} [11] which is expected from previous work on films deposited at temperatures higher than 180 K [12]. For a dose of less than $1 \cdot 10^{13}$ molecules of HCl deposited at a rate of less than $1 \cdot 10^{13}$ molec s^{-1} (Table 3.4, case (a)), no change in optical density was observed across the entire IR absorption spectrum from 700 to 4000 cm^{-1} which remained that of pure I_h ice. However, the presence of HCl on ice was ascertained by the decrease of J_{ev} of H₂O as described above. For a dose of HCl of more than $1 \cdot 10^{14}$ molecules that is evaluated from the integral under the measured MS signal of HCl as displayed in Figure 3.2 and a deposition rate of more than $1 \cdot 10^{14}$ molec s^{-1} (Table 3.4, case (d)) the formation of an

Dose (<i>molecule</i>)	(a) Low $< 10^{13}$	(b) $5 \cdot 10^{13}$ to 10^{15}	(c) $5 \cdot 10^{13}$ to 10^{15}	(d) $> 10^{14}$
Flow rate (<i>molec s⁻¹</i>)	Low $< 10^{13}$	10^{13} to $5 \cdot 10^{13}$	Low $< 10^{13}$	Large $> 10^{14}$
Spectral observation	No absorption attributable to HCl	3230 cm^{-1} Split+ shift Sharp 1644 and 1618 cm^{-1}	3350 cm^{-1} broadening 1100 and 1700 cm^{-1} absorption	3350 cm^{-1} broadening 1100 and 1700 cm^{-1} absorption
Identification	FTIR absorption spectrum is that of pure ice	Crystalline HCl hexahydrate (Fig. 3.9)	Amorphous HCl/H ₂ O mixture (Fig. 3.10)	Amorphous HCl/H ₂ O mixture (Fig. 3.10)

Table 3.4: FTIR spectral observations of a $1 \mu\text{m}$ thick ice film doped with HCl using different dosing protocols at 190 K.

amorphous HCl/H₂O mixture was observed whose absorption spectrum is in agreement with results found in the literature [13].

The obtained spectra for amorphous HCl/H₂O mixtures are displayed in Figure 3.10 and are in good agreement with the literature [14]. They are characterized by the appearance of new peaks between 1100 and 1200 as well as at 1700 cm^{-1} and by the broadening of the sharp OH-stretch band leading to a broad absorption around 3350 cm^{-1} . Ritzhaupt et al. [14] have identified a stretching vibration of H₃O⁺ at 1079 cm^{-1} whereas H₂O bending and H₃O⁺ bond deformation modes contribute to the absorption at 1696 cm^{-1} in their FTIR absorption spectra. Koch et al. [15] attribute a 1250 cm^{-1} band to the H₃O⁺ stretching mode and a 1780 cm^{-1} vibration to the H₂O and H₃O⁺ deformation mode. We therefore follow these assignments

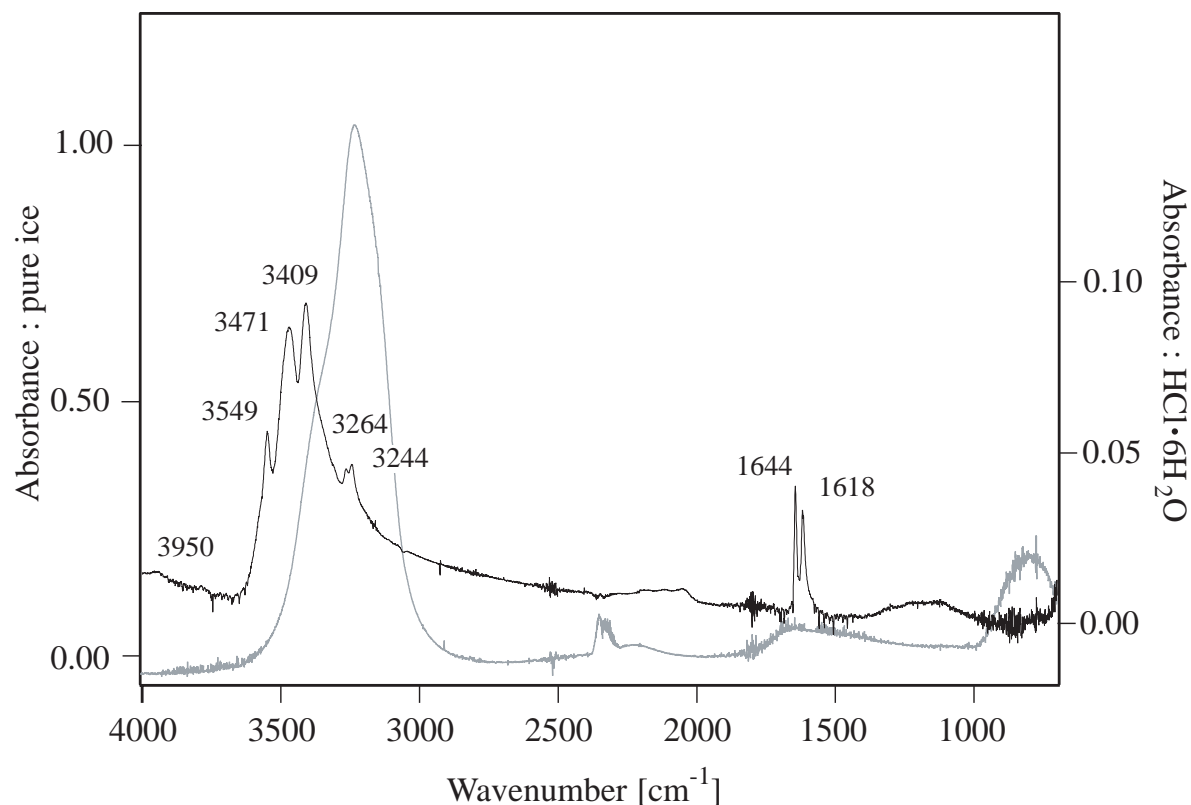


Figure 3.9: FTIR absorption spectrum of pure (grey, left scale) and HCl-doped ice (black, right scale). Both traces are rescaled for legibility. The ice film is doped with $1.0 \cdot 10^{15}$ molecules of HCl at a flow rate of $1.0 \cdot 10^{13}$ molec s⁻¹.

in this work and identify the broad absorption band centered at approximately 1100 cm^{-1} in Figures 3.9 and 3.10 with the presence of H_3O^+ . The sharp absorptions at 1618 and 1644 cm^{-1} in the case of the HCl hexahydrate (Figure 3.9) as well as the broader peaks centered at 1640 and 1720 cm^{-1} in the case of the amorphous HCl/ H_2O mixture (Figure 3.10), whose IR bands are broadened throughout the IR absorption spectrum in line with the amorphous nature of the absorber, point to the activity of the bending and deformation modes in H_2O and H_3O^+ , respectively. Although no proof in itself, we claim that the significant intensity of these absorptions points towards the existence of ionic HCl hydrates of the form $\text{H}_3\text{O}^+\text{Cl}^-$ being present on ice in the temperature range investigated as no hint of molecularly adsorbed HCl

could be found in the region of the H-Cl stretching vibration in the covered temperature range.

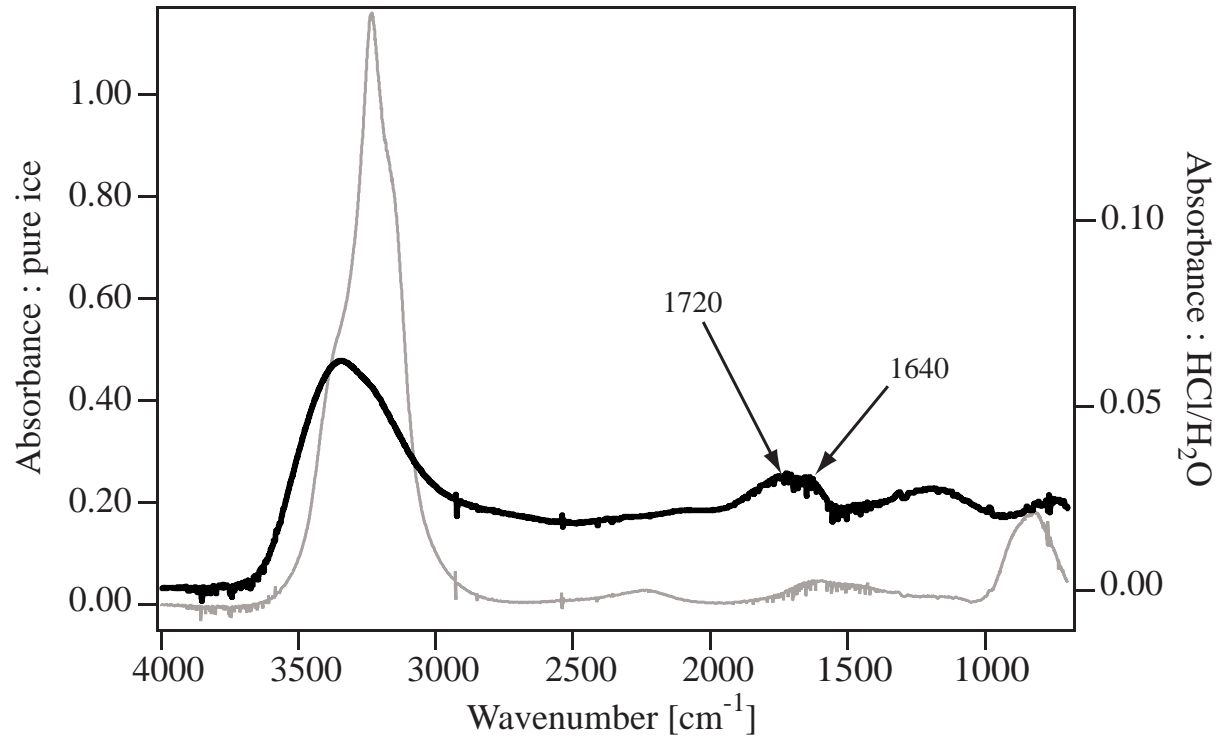


Figure 3.10: FTIR absorption spectrum of pure (grey, left scale) and HCl-doped ice (black, right scale). Both traces are rescaled for legibility. The ice film is doped with $1 \cdot 10^{15}$ molecules of HCl at a flow rate higher than $1 \cdot 10^{14}$ molec s^{-1} .

The most interesting result of these deposition experiments is the ability to control the growth of the crystalline HCl hexahydrate $HCl \cdot 6H_2O$ at 190 K presented as case (b) compared to case (c) displayed in Table 3.4. Figure 3.9 presents a FTIR absorption spectrum corresponding to case (b), where the ice film was doped with $1.0 \cdot 10^{15}$ HCl molecules at a flow rate of $1.0 \cdot 10^{13}$ molec s^{-1} . The presence of crystalline $HCl \cdot 6H_2O$ is characterized by the shift and split of the 3236 cm^{-1} peak representative of the pure ice OH-stretch, and by the appearance of sharp peaks at 1644 cm^{-1} and 1618 cm^{-1} discussed above [14]. The spectrum of Figure 3.9 corresponds to the deposition conditions of case (b) displayed in Table 3.4 and reveals the formation of a crystalline ionic hydrate of HCl with ice in agreement with the literature [15, 16] and with

theoretical studies [17, 18, 19]. We point out that this spectrum has been measured at a time in the film evaporation history that corresponds to the end of the time interval given by points **B** and **D** of the interferogram displayed in Figure 3.3 where all or almost all of the free water molecules constituting the underlying pure ice film have evaporated. This explains the importance of the FTIR absorptions attributed to the presence of the hydrates compared to the pure ice OH-stretch around 3236 cm^{-1} as nearly all other H_2O molecules not involved in crystalline hydrate formation have evaporated leaving behind the "bare essentials" of the stable crystalline hydrate. The fact that the (almost) unperturbed ice OH-stretch splits at 3244 and 3264 cm^{-1} (compared to 3236 cm^{-1} in pure ice) is still observable at this stage of the evaporation suggests the presence of weakly-bound water molecules not totally involved in the formation of the hydrates, although both their rate of evaporation and condensation are influenced by the presence of HCl as indicated by their slight shift and split in the IR absorption spectrum.

The results are consistent with the fact that HCl hydrates have a H_2O vapor pressure that is lower than that of pure ice although it has not been measured in this work. It is also important to notice that the IR absorption peaks corresponding to the presence of HCl hydrates were also observable down to a dose of $5.0 \cdot 10^{13}$ molecules of HCl towards the end of an evaporation experiment. This HCl dose corresponds to approximately 10 % of a formal monolayer of HCl on ice. At the beginning of the evaporation experiment the crystalline hydrate structure was not apparent perhaps because of the abundance of "pure" ice whose absorption spectrum is centered at 3236 cm^{-1} (Figure 3.9). After most of the ice film evaporated at the rate characteristic of pure ice the remaining sample was monitored using the disappearance of the spectral fingerprints of the hydrates as given in Figure 3.9. At this time the average mole fraction of HCl in ice was between $1.6 \cdot 10^{-4}$ and $3.2 \cdot 10^{-4}$ as indicated by the volume of remaining ice monitored by the interferogram for the time period between **C** and **D** of Figure 3.3. We are unable at this point to determine the defining moments of the crystallization of the HCl hexahydrate. If the HCl/ H_2O mixture crystallized already at the end of the doping process the sensitivity of the FTIR absorption spectrometer in transmission may not have been sufficient to monitor the characteristic

features of the crystalline HCl hexahydrate at 3549, 3471 and 3409 cm^{-1} . On the other hand, crystallization as probed by the appearance of the sharp hydrate structure in the OH-stretching region may have occurred when most of the pure ice had evaporated and the HCl concurrently concentrated at the interface thus enabling crystallization. This process would resemble closely the crystallization of nitric acid hydrates ($\text{NAT} = 3\text{H}_2\text{O}\cdot\text{HNO}_3$, $\text{NAD} = 2\text{H}_2\text{O}\cdot\text{HNO}_3$) under laboratory conditions as observed by Zondlo and coworkers [20]. As a supplement to this spectroscopic study data on the evaluation of the infrared absorption cross-section of $\text{HCl}\cdot 6\text{H}_2\text{O}$ structure at characteristic wavenumbers are presented below in Appendix 3.4.

A surprising case is **c** in Table 3.4 which indicates the absence of crystalline $\text{HCl}\cdot 6\text{H}_2\text{O}$ and reveals that the formation of the crystalline hexahydrate depends on the rate of HCl deposition rather than on the HCl dose. For very low deposition rates of less than $1\cdot 10^{13}$ molec s^{-1} one concludes that the diffusion of HCl in ice is presumably faster than crystallization preventing the formation of the HCl hexahydrate. At the other extreme of a large deposition rate (case (d) in Table 3.4) formation of an amorphous HCl/ H_2O mixture is preferred over formation of crystalline hexahydrate. Whatever the reason, it seems that at 190 K both the crystalline and amorphous HCl hydrates may be observed depending on the rate of deposition of HCl on ice. This case is of importance because the change in the net rate of evaporation as well as the duration of this change seems to depend on the presence or absence of crystalline hydrates as displayed in Table 3.3, cases (c) and (b'). The data suggest that the presence of the hexahydrate significantly slows down the evaporation of H_2O during a relatively short period of time corresponding to an evaporation time of 600 s between the last two fringes. In contrast, the presence of an amorphous mixture affects the evaporation rate to a lesser extent albeit for a longer period of time. In conclusion, the formation of these crystalline hydrates observed by FTIR absorption spectroscopy has a large impact on the rate of H_2O evaporation for a sample comprising the last 100 to 200 nanometers of ice whereas in the case of the formation of an amorphous HCl/ H_2O this impact is less which may be an indication of the importance of diffusion of HCl in the formation of the crystalline hydrates. In this case the extent of the HCl diffusion into

the remaining pure ice film is longer compared to the case where the HCl hexahydrate is formed. Table 3.3 qualitatively shows the difference of the impact of the presence of HCl·6H₂O (case (b')) versus amorphous HCl/H₂O mixture (case (c)) as far as the temporal spacings between the interference fringes that are related to the net evaporation rate of H₂O are concerned. It also shows the difference in spatial extent (volume) of the HCl/H₂O layer discussed above.

For ice films doped with HBr, we have not been able to observe any spectral changes in the pure ice spectrum except for a broadening of the absorption due to the OH-stretch region and a shift of the 1641 cm⁻¹ peak as displayed in Figure 3.11. This peak at 1641 cm⁻¹ is assigned to the bending mode of H₂O which is shifted to 1745 cm⁻¹ upon HBr adsorption shift which is attributed to the conversion to H₃O⁺ bending mode [21]. This observation suggests complete ionization of HBr and is in agreement with the literature [21, 22]. However, similar to the case of HCl, where no spectral change was observed (case (a), Table 3.4) the presence of HBr was ascertained by the measurement of the decrease of J_{ev} of H₂O, as presented in Figure 3.4.

3.3 Discussion and atmospheric implications

This experiment has enabled the separation of the rate or flux of evaporation R_{ev} or J_{ev} and the rate constant for condensation k_{cond} of H₂O from pure and doped water ice under the same experimental conditions. The separate rates and especially their temperature dependence have shed light on a complex adsorption/desorption mechanism as evidenced by the negative temperature dependence of k_{cond} as has been pointed out by Fluckiger et al. [2]. The resulting value for the enthalpy of sublimation of H₂O from pure water ice deduced from Arrhenius expressions given on page 76 in Equations 3.10 and 3.11 is $\Delta H_{\text{subl}}^0 = E_{\text{ev}} - E_{\text{cond}} = 11.9 \pm 2.7 \text{ kcal mol}^{-1}$ which is in good agreement with values found in the literature [23, 24, 25]. In contrast to most other results found in the literature, we assert that H₂O condensation on ice has a small negative activation energy in the range studied (190-240 K). The study of R_{ev} alone is therefore a necessary, but not sufficient condition to assess ΔH_{subl} or the binding energy of H₂O on ice at

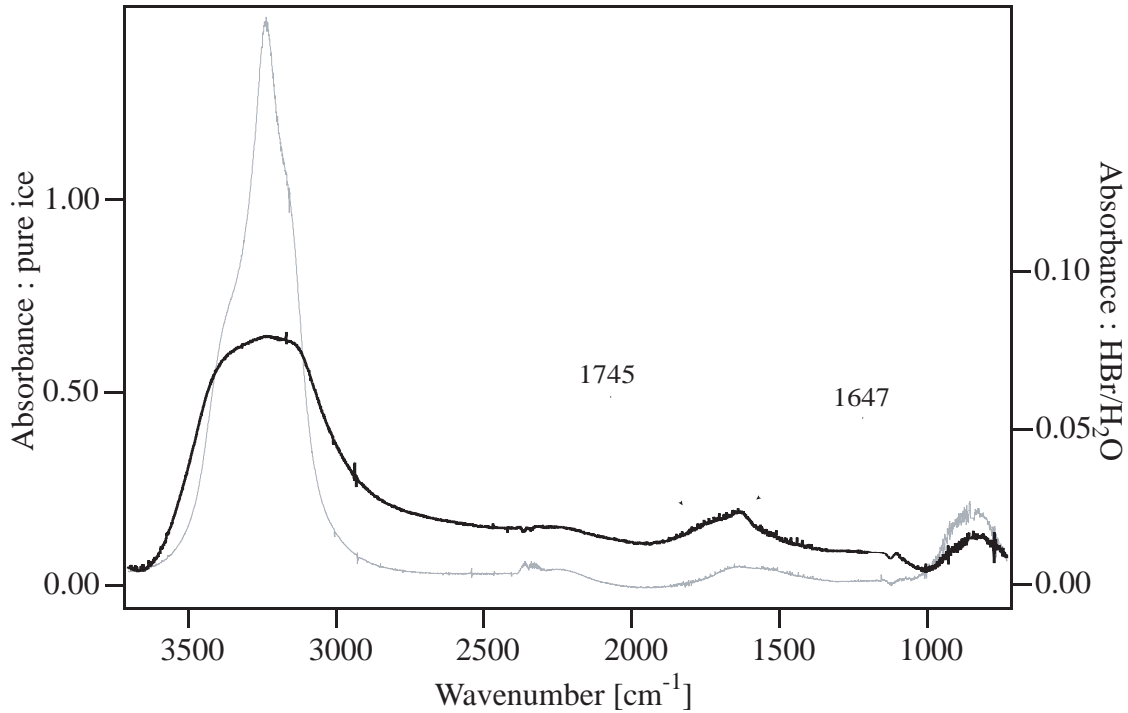


Figure 3.11: FTIR absorption spectrum of pure (grey, left scale) and HBr-doped ice (black, right scale). Both traces are rescaled for legibility. The ice film is doped with an estimated amount of HBr.

temperatures in excess of 190 K, as has been repeatedly done in the past [23]. For HCl-doped ice $\Delta H_{\text{subl}}^0 = 11.2 \pm 2.8 \text{ kcal mol}^{-1}$ and for HBr-doped ice $\Delta H_{\text{subl}}^0 = 11.7 \pm 2.8 \text{ kcal mol}^{-1}$, the latter of which is in good agreement with Hudson et al. [22]. ΔH_{subl}^0 is independent of the presence of HX in the given concentration range and equal to ΔH_{subl}^0 (pure ice) within experimental uncertainty in agreement with the H_2O vapor pressure being that of ice even for the HX-doped ice samples in the given concentration range. However, a small counterintuitive decrease of E_{ev} may be noted in the sequence pure ice>HCl/ice>HBr/ice which is offset by a preexponential factor whose trend counteracts that of E_{ev} . The constant value of ΔH_{subl}^0 is consistent with the fact that the vapor pressure of H_2O is independent of the amount of adsorbed HX in the range of $1 \cdot 10^{13}$ to $1 \cdot 10^{15}$ molecules deposited on a 0.78 cm^2 ice film. These conditions lead to low concentrations of [HX] in our experiments with an upper limit for $\chi_{\text{HCl}} = 1.2 \cdot 10^{-2}$ estimated for

an ice sample a few tens of nanometers thick corresponding to point **E** of the interferogram and displayed in Figure 3.3. Finally, we conclude that the doped ice films presented in this study exhibit a H_2O vapor pressure that is the one of pure ice owing to the fact that both the rate of evaporation and condensation are lowered in the same extent in the presence of HX.

The unexpected stability of the vapor pressure of H_2O above the ice film in the presence of HCl follows the observation made in previous experiments concerning the increase of the lifetime of ice particles due to a NAT-coating [10] in which no change of the H_2O vapor pressure was observed. However, Biermann et al. report the observation of the net rate of evaporation of pure ice and NAT/ice films and conclude that both rates are identical within experimental error which differs from our conclusions on R_{ev} and k_{cond} on pure, HCl- and HBr-doped ice as well as on NAT samples discussed below. Their work also leads to H_2O mass accommodation coefficients that are in the range 0.025 to 0.050 which is at least an order of magnitude smaller than recent measurements on ice, including this and other works [2, 8, 9]. Most likely transport limitations of H_2O owing to the used high total pressure corresponding to a mbar or so may have led to these results at variance with all other experiments to date.

In our work, the decrease of the pre-exponential factor of the rate of evaporation of water from ice by 2 and 3 orders of magnitude for HCl and HBr, respectively, is consistent with previous results found in the literature [22] and represents the most significant effect of HX on the H_2O evaporation from ice and thus on the lifetime of atmospheric ice particles. The observation of the negative temperature dependence of k_{cond} implies the presence of a surface-bound precursor for adsorption, hence a complex adsorption/desorption mechanism as has been discussed previously by Chaix et al. [8, 9] and Fluckiger et al. [2]. The decrease of both R_{ev} and k_{cond} in the presence of HX therefore may imply a modification of the ice surface at atmospherically relevant conditions. Indeed, cases (b) and (c) of Table 3.4 lead to an average mole fraction of HCl in a 1 μm thick ice film of $\chi_{\text{HCl}}=2$ to $4 \cdot 10^{-5}$ for an adsorbed dose of $5 \cdot 10^{13}$ to $1 \cdot 10^{14}$ HCl molecules. These concentrations represent lower limits and may be higher by at most a factor of four if one allows for the evaporation of 50 and 75 % of the pure ice in the sample that is not affected by

the presence of HCl as displayed in Table 3.3 for the amorphous and crystalline HCl hydrate, respectively.

In most cases the modification of the ice is observable by FTIR spectroscopy as displayed in Figures 3.9 and 3.10 and clearly shows the importance of the deposition conditions, especially under atmospheric conditions, as shown by the results displayed in Table 3.4. We have evaluated the required HCl partial pressure in order to obtain the same rate of HCl adsorption on ice, R_{HCl} , by backfilling as those that lead to the observation of the crystalline HCl·6H₂O in Table 3.4, namely $1 \cdot 10^{13}$ and $5 \cdot 10^{13}$ molec s⁻¹. Using the same reasoning as the one proposed on page 69 the expression for the calculation of R_{HCl} is given by Equations 3.22 and 3.23:

$$R_{\text{HCl}} = \gamma_{\text{HCl/ice}} \cdot \omega_{\text{HCl}} \cdot [\text{HCl}] \cdot V_r \quad (3.22)$$

or

$$R_{\text{HCl}} = \gamma_{\text{HCl/ice}} \cdot \omega_{\text{HCl}} \times 2.9 \cdot 10^{16} \times P_{\text{HCl}} \cdot V_r \quad (3.23)$$

Using the uptake coefficients for HCl on ice at 180 and 190 K from Fluckiger et al. [5] where $\gamma_{\text{HCl/ice}}=0.38$ and 0.30, respectively, has been measured, the required range of HCl partial pressure to obtain crystalline HCl·6H₂O ranges between $1.1 \cdot 10^{-7}$ and $6.4 \cdot 10^{-7}$ Torr in this temperature range. We have reported this result in Figure 3.12 which illustrates the phase diagram of the HCl/H₂O system constructed by Molina and coworkers [26]. The white hashed area represents the HCl pressures effectively used in our experiments which are in good agreement with the stability range for crystalline HCl·6H₂O.

According to these results we agree with Koehler et al. [27] when they conclude that nucleation may not be facile in the stratosphere. Nevertheless, we have been able to observe HCl·6H₂O crystallisation by HCl vapor phase deposition, indeed under laboratory conditions, but in disagreement with the temperature constraints of 148-181 K noted by Vuillard [28] for crystallisation or the necessary temperature increase of a supercooled phase described by Abbatt

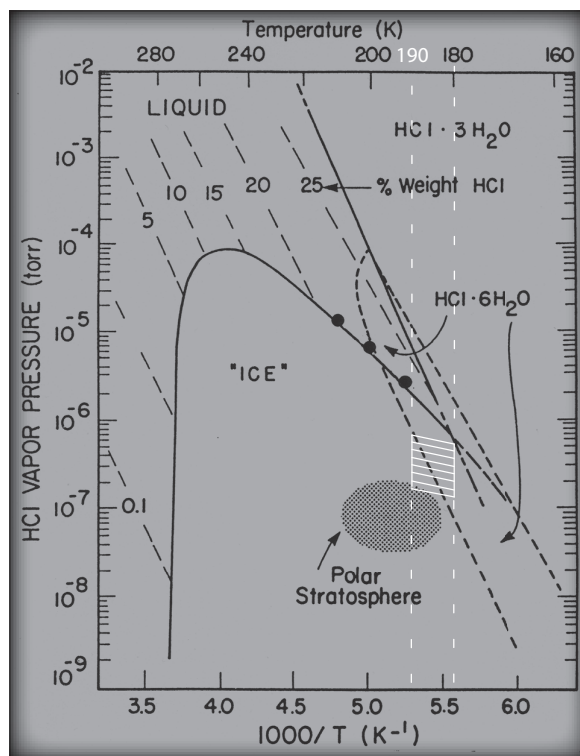


Figure 3.12: Phase diagram of the HCl/H₂O system constructed by Molina and coworkers [26]. The white hashed area represents the pressure range used in our experiments and evaluated from our data for the formation of HCl·6H₂O. The 3 points on the ice-liquid coexistence curve in the range 190-210 K are from the work of Fluckiger et al [5].

et al. [29]. Type II polar stratospheric (ice) clouds have been found on occasion in stratospheric air much warmer than the ice frost point T_{ice} [30]. A particularly pertinent observation has been made by Deshler et al [30] from a balloon-borne sounding of arctic stratospheric air when large ice particles with radii in the range 1-5 μm have been observed surviving for hours at temperatures several degrees (3-10) above T_{ice} . These observations and others by Goodman et al. [31] have led to the hypothesis that a NAT coating around the ice particle prevented rapid evaporation of ice that would occur on the time scale of a few minutes in the absence of NAT coating. In light of the present results it may be asked whether the existence of a crystalline NAT coating may be required for the decrease of the evaporation rate of H₂O or if simply the presence of adsorbed HNO₃, perhaps as amorphous HNO₃/H₂O mixture as described by Zondlo

et al. [20] may already be a sufficient requirement. A more precise answer to this question will be given in Chapter 5. This hypothesis begs the question as to the mole fraction or absolute concentration of HNO_3 required to lead to an effective decrease of the net evaporation rate which will be presented in Chapter 5.

The results displayed in Figure 3.4 that are expressed in the Arrhenius expressions given on page 76 for the net rate of H_2O evaporation from pure ice and ice contaminated by adsorbed HX amount to a decrease of R_{ev} and k_{cond} by a factor of 5 to 6 and 15 for HCl and HBr adsorption in the indicated concentration and temperature range, respectively. These results have been obtained under conditions of molecular or stirred flow in the interest of separating the individual rates of Equilibrium 3.5 and correspond to a relative humidity rh of a fraction of a percent. However, owing to the fact that the measured equilibrium vapor pressure of H_2O does not change upon adsorption of HX the relative decrease in R_{ev} and k_{cond} is independent of relative humidity rh because the net rate of evaporation $\Delta R_{\text{N}} = k_{\text{cond}}[\text{H}_2\text{O}] \times (\text{rh} - 1)$ is a linear function of rh and affects the net rate of evaporation of pure ice and ice contaminated with HX to the same extent. Therefore, the ratio r of the net rate of H_2O evaporation from pure ice compared to HX doped ice given in Equation 3.24 and the relative decrease f of the net rate of H_2O evaporation upon doping of ice with HX displayed in Equation 3.25 are independent of the relative humidity rh.

$$r = \frac{k_{\text{cond}}^{\text{HX}}}{k_{\text{cond}}} = \frac{R_{\text{ev}}^{\text{HX}}}{R_{\text{ev}}} \quad (3.24)$$

$$f = \frac{k_{\text{cond}}^{\text{HX}} - k_{\text{cond}}}{k_{\text{cond}}} = \frac{R_{\text{ev}}^{\text{HX}} - R_{\text{ev}}}{R_{\text{ev}}} \quad (3.25)$$

where the symbols with the superscript HX correspond to the kinetic constants pertaining to HX doped ice samples.

The significant effect of HX deposition on R_{ev} from ice may also be seen in HeNe interferograms shown in Figure 3.3 and summarized in Table 3.3, and has been observed in two other

studies of the condensed phase, one for HBr [22], the other for HCl [32]. Our values for HBr are consistent with those in the literature [22] and in fact lead to a surprising increase of the lifetime for an ice particle. For HCl, Krieger et al. [32] report a decrease of the net rate of evaporation of H₂O from ice of only 30 %, whereas we observe a decrease of a factor of 2 to 15 depending on the structure and the concentration ratio of the HCl/ice surface according to Table 3.3. The increase of the lifetime of a 1 μ m thick ice film in the presence of HX may be extrapolated to the case of Cirrus clouds. As Cirrus cloud particles are large they may be approximated by bulk substrates so that the results obtained in this study may be transferable to the case of PSC's type II. We therefore claim that HX-doped ice particles should have an increased lifetime in the presence of HX depending on the amount of HCl adsorbed. They should thus be more available for heterogeneous reactions and so be more effective in ozone depletion processes as discussed in Solomon et al. [33]. The importance of the decrease of the net rate of evaporation of atmospheric ice particles will depend on the dose of adsorbed HX which in turn depends on the length of exposure to air masses containing HX. The HCl concentration amounts to approximately 10 % of that for HNO₃ as a lower limit based on the inorganic halogen budget compared to an absolute HNO₃ concentration of roughly 10 ppb. The atmospheric HBr concentration is significantly smaller, probably on the order of up to a few ppt. The present work clearly shows that already a monolayer or two of adsorbed HCl may significantly slow down the H₂O evaporation rate of ice over a large volume corresponding to a layer thickness of 250 nm or more. It suggests that stoichiometric formation of crystalline hydrates such as NAT or NAM requiring large amounts of HNO₃ may not be necessary in the case of HX molecules adsorbed on ice. For HBr the smaller atmospheric abundance may be partially offset by the larger effect on the H₂O evaporation rate as far as lifetimes of HBr-contaminated ice particles are concerned.

3.4 Appendix: Infrared absorption cross-sections at characteristic wavelengths for crystalline hexahydrate $\text{HCl}\cdot 6\text{H}_2\text{O}$

This appendix presents the infrared absorption cross-sections for the crystalline $\text{HCl}\cdot 6\text{H}_2\text{O}$ hexahydrate that have been obtained during experiments some of which are summarized in Table 3.4. To our knowledge such data have never been presented in the literature. Figure 3.13 presents the dependence of the absorbance at selected wavelengths that are characteristic of the HCl hexahydrate structure, namely $\tilde{\nu}=1618, 1644, 3244, 3264, 3409, 3471, 3549 \text{ cm}^{-1}$ which have previously been listed in Section 3.2.3. These results are summarized in Table 3.5.

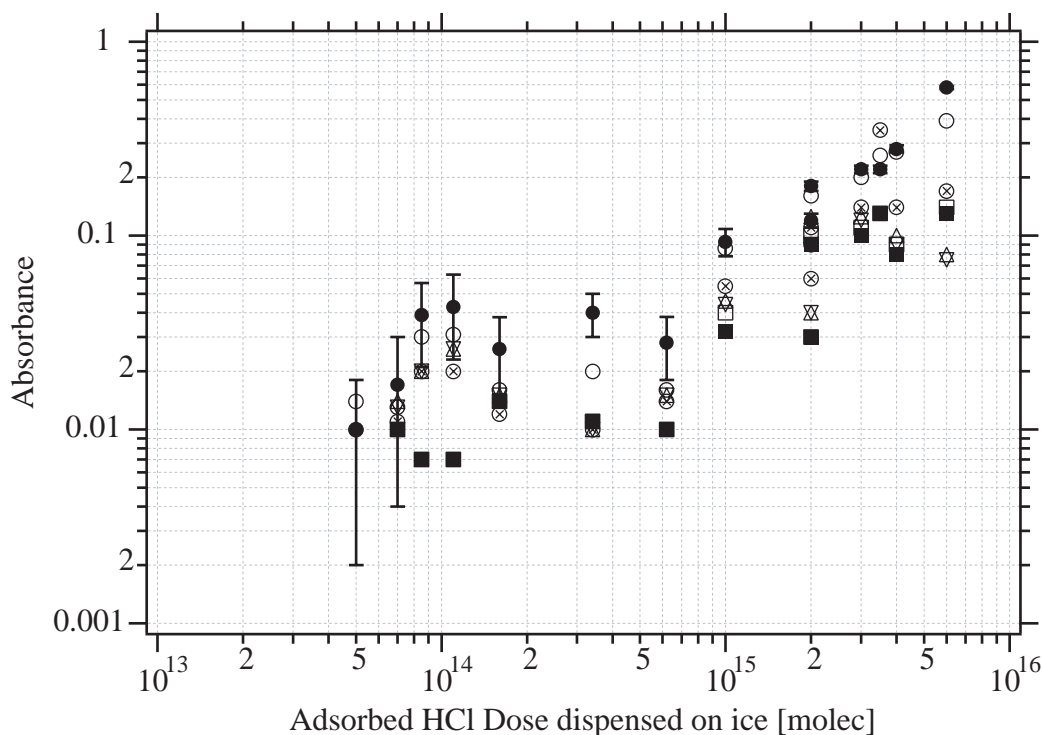


Figure 3.13: Infrared absorbance in transmission at different wavelengths of interest for the characterization of the crystalline $\text{HCl}\cdot 6\text{H}_2\text{O}$ hexahydrate. ■: absorbance at $\tilde{\nu}=1618 \text{ cm}^{-1}$, □: $\tilde{\nu}=1644 \text{ cm}^{-1}$, △: $\tilde{\nu}=3244 \text{ cm}^{-1}$, ▽: $\tilde{\nu}=3264 \text{ cm}^{-1}$, ●: $\tilde{\nu}=3409 \text{ cm}^{-1}$, ○: $\tilde{\nu}=3471 \text{ cm}^{-1}$ and ⊗: $\tilde{\nu}=3549 \text{ cm}^{-1}$. Error bars correspond to the uncertainties of experimental measurements.

We have focused on two wavelengths corresponding to the shift and split of the OH-stretch

Number of adsorbed HCl [molec]	ABSORBANCE						
	Wavenumber $\tilde{\nu}$ [cm^{-1}]						
	3549	3471	3409	3264	3244	1644	1618
$3.0 \cdot 10^{15}$	0.140	0.200	0.220	0.120	0.125	0.110	0.100
$2.0 \cdot 10^{15}$	0.110	0.160	0.180	0.090	0.125	0.100	0.090
$1.0 \cdot 10^{15}$	0.055	0.086	0.093	0.044	0.046	0.040	0.032
$3.5 \cdot 10^{15}$	0.350	0.260	0.220	-	-	0.130	0.130
$6.0 \cdot 10^{15}$	0.170	0.390	0.580	0.075	0.080	0.140	0.130
$4.0 \cdot 10^{15}$	0.140	0.270	0.280	0.090	0.100	0.090	0.080
$2.0 \cdot 10^{14}$	0.060	0.090	0.120	0.040	0.040	0.030	0.030
$1.1 \cdot 10^{13}$	0.020	0.031	0.043	0.026	0.026	0.007	0.007
$8.5 \cdot 10^{13}$	0.020	0.030	0.039	0.020	0.020	0.007	0.007
$5.0 \cdot 10^{13}$	0.010	0.014	0.010	-	-	-	-
$3.4 \cdot 10^{14}$	0.010	0.020	0.040	0.010	0.010	0.011	0.011
$1.6 \cdot 10^{14}$	0.012	0.016	0.026	0.015	0.015	0.014	0.014
$6.2 \cdot 10^{14}$	0.014	0.016	0.028	0.015	0.015	0.010	0.010
$7.0 \cdot 10^{13}$	0.011	0.013	0.017	0.013	0.014	0.010	0.010

Table 3.5: Infrared absorbance in transmission at different wavelengths of interest for the characterization of the crystalline HCl·6H₂O hexahydrate. These results are presented in Figure 3.13.

vibration characteristic of pure ice films and to the observation of the presence of H₃O⁺, 3409 and 1618 cm⁻¹, respectively. The absorbance has been measured nearly at the end of the evaporation of the ice film in the vicinity of point **D** in Figure 3.3. At this point no "free" H₂O molecules are observable when monitored by the peak vibration of the OH-stretch of pure ice at 3236 cm⁻¹. The broadening followed by the disappearance of the librational mode of pure ice at 842 cm⁻¹ confirms the likely absence of free water molecules as the presence of this librational mode is known to be correlated with disorder [34]. It is expected to decrease when the intermolecular coupling increases [35] which should be the case in the presence of the crystalline HCl·6H₂O structure. Based on the fact that pure ice or "free" H₂O molecules show an absorption band at 842 cm⁻¹ we have scaled the pure ice spectrum a sample of which is displayed in Figure 3.9 in the range 700 - 4000 cm⁻¹ with the intensity at 842 cm⁻¹ assuming that it was representative of pure ice following reference [36] in analogy to the system HNO₃/ice. Subsequently, we have subtracted the scaled pure ice spectrum from the doped one, at that

point in the film evaporation history corresponding to the time interval between points **B** and **C** in Figure 3.3. Because no HCl desorption is observed during this period using MS at $m/z=36$ the difference between the two spectra should have resulted in the same absorbance at the previously given wavelengths of interest as the one measured at the end of the evaporation of pure ice. This method was not really satisfactory as the resulting differences were connected to a large uncertainty. We have therefore decided to report only the values measured directly at the end of the "free" H₂O molecule evaporation. The increasing error associated with each point is due to the difficulty of measuring very small FTIR signals when the dose decreases in Figure 3.13. The linear dependence of the absorbance on the number of HCl molecules adsorbed is expected following Beer-Lambert's law (see Section 2.7). We make the assumption that all HCl molecules are involved in HCl hexahydrate units which may be questionable. The black and grey lines in Figure 3.14 represent the linear fits of the data at 3409 and 1618 cm⁻¹, respectively. Figure 3.14 presents the linear dependence of the absorbance at $\tilde{\nu}=3409$ and 1618 cm⁻¹ on the number of deposited HCl molecules using linear scale for the sake of clarity.

Using these linear regressions and the Equations 2.20, 2.21 and 2.22 (page 49) that are recalled below,

$$\begin{aligned} \text{OD} &= \log\left(\frac{I_0}{I}\right) = \epsilon cd \\ \ln\left(\frac{I_0}{I}\right) &= \sigma nd \\ \sigma &= \frac{2303\epsilon}{\mathcal{N}_A} \end{aligned}$$

as well as the present experimental data, the differential cross-sections for crystalline HCl·6H₂O at 1618 and 3409 cm⁻¹, namely $\sigma_{1618}^{\text{hexa}}$ and $\sigma_{3409}^{\text{hexa}}$, are

$$\boxed{\sigma_{1618}^{\text{hexa}} = (5 \pm 1) \cdot 10^{-17} \text{ cm}^2} \quad (3.26)$$

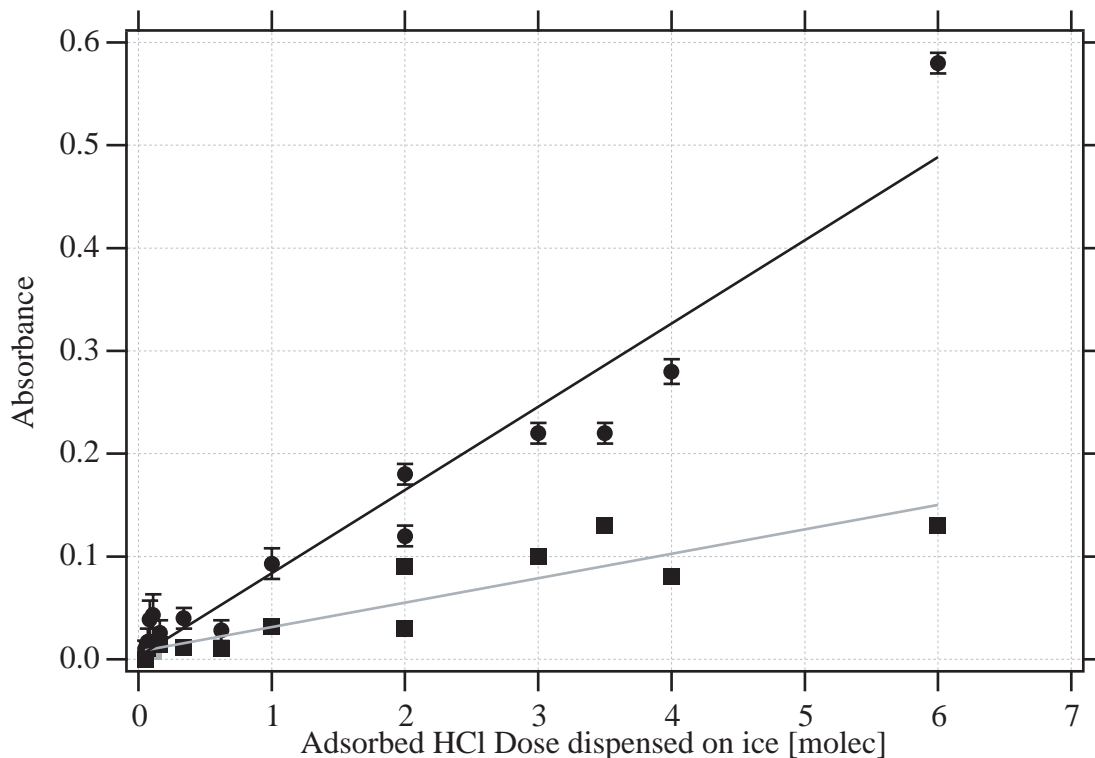


Figure 3.14: Infrared absorbance in transmission at two wavelengths of interest for the characterization of the crystalline $\text{HCl}\cdot 6\text{H}_2\text{O}$ hexahydrate. ■: absorbance at $\tilde{\nu}=1618 \text{ cm}^{-1}$, ●: $\tilde{\nu}=3409 \text{ cm}^{-1}$. The black and grey traces correspond to the linear fits of the data at $\tilde{\nu}=3409 \text{ cm}^{-1}$ and $\tilde{\nu}=1618 \text{ cm}^{-1}$, respectively. Error bars correspond to the uncertainties of experimental measurements.

and

$$\sigma_{3409}^{\text{hexa}} = (1.5 \pm 0.3) \cdot 10^{-16} \text{ cm}^2 \quad (3.27)$$

These values are very large compared to $\sigma_{3236} = 7.9 \cdot 10^{-19} \text{ cm}^2 \text{ molec}^{-1}$, obtained for pure ice OH-stretch vibration, but to date are the only ones that are available such that for the moment no meaningful comparison may be undertaken.

The only quantitative result available for a comparison was found in the work of Koehler et al. [27]. Their data exhibit an absorbance of 0.27 for $\text{HCl}\cdot 6\text{H}_2\text{O}$ in the region $1618\text{-}1644 \text{ cm}^{-1}$

when roughly $3 \cdot 10^{17}$ molecules of HCl are deposited on a 5 cm diameter ice film. Their results lead to a value of the molar decadic extinction coefficient $\epsilon_{1618-1644} = 1.1 \cdot 10^{17} \text{ l mol}^{-1} \text{ cm}^{-1}$ using Equations 2.20, 2.21 and 2.22 recalled above. In comparison, our data result in $\epsilon_{1618} = 1.3 \cdot 10^{17} \text{ l mol}^{-1} \text{ cm}^{-1}$ which is in good agreement with their results. However, some information is lacking in their work so as to question a critical comparison with our data in a meaningful way.

Bibliography

- [1] C. Delval, B. Fluckiger, and M. J. Rossi, *Atmospheric Chemistry and Physics*, 2003, **3**, 1131–1145.
- [2] B. Fluckiger and M. J. Rossi, *Journal of Physical Chemistry A*, 2003, **107**(20), 4103–4115.
- [3] D. S. Eisenberg and W. Kauzmann, *The structure and properties of water*, Oxford University Press, New York,, 1969.
- [4] J. Marti and K. Mauersberger, *Geophysical Research Letters*, 1993, **20**(5), 363–366.
- [5] B. Fluckiger, A. Thielmann, L. Gutzwiller, and M. J. Rossi, *Berichte Der Bunsen-Gesellschaft-Physical Chemistry Chemical Physics*, 1998, **102**(7), 915–928.
- [6] J. E. Schaff and J. T. Roberts, *Journal of Physical Chemistry*, 1996, **100**(33), 14151–14160.
- [7] L. F. Keyser and M. T. Leu, *Journal of Colloid and Interface Science*, 1993, **155**(1), 137–145.
- [8] L. Chaix, H. van den Bergh, and M. J. Rossi, *Journal of Physical Chemistry A*, 1998, **102**(50), 10300–10309.
- [9] L. Chaix, H. van den Bergh, and M. J. Rossi, *Journal of Physical Chemistry A*, 1999, **103**(15), 2906–2906.
- [10] U. M. Biermann, J. N. Crowley, T. Huthwelker, G. K. Moortgat, P. J. Crutzen, and T. Peter, *Geophysical Research Letters*, 1998, **25**(21), 3939–3942.
- [11] M. S. Bergren, D. Schuh, M. G. Sceats, and S. A. Rice, *Journal of Chemical Physics*, 1978, **69**(8), 3477–3482.
- [12] M. Kumai, *Journal of Glaciology*, 1968, **7**, 95–108.
- [13] F. Dominé and I. Xueref, *Analytical Chemistry*, 2001, **73**(17), 4348–4353.
- [14] G. Ritzhaupt and J. P. Devlin, *Journal of Physical Chemistry*, 1991, **95**(1), 90–95.
- [15] T. G. Koch, S. F. Banham, J. R. Sodeau, A. B. Horn, M. R. S. McCoustra, and M. A. Chesters, *Journal of Geophysical Research-Atmospheres*, 1997, **102**(D1), 1513–1522.
- [16] N. Uras-Aytemiz, C. Joyce, and J. P. Devlin, *Journal of Physical Chemistry A*, 2001, **105**(46), 10497–10500.
- [17] G. J. Kroes and D. C. Clary, *Geophysical Research Letters*, 1992, **19**(13), 1355–1358.
- [18] B. J. Gertner and J. T. Hynes, *Science*, 1996, **271**(5255), 1563–1566.
- [19] M. Svanberg, J. B. C. Pettersson, and K. Bolton, *Journal of Physical Chemistry A*, 2000, **104**(24), 5787–5798.

-
- [20] M. A. Zondlo, P. K. Hudson, A. J. Prenni, and M. A. Tolbert, *Annual Review of Physical Chemistry*, 2000, **51**, 473–499.
- [21] S. B. Barone, M. A. Zondlo, and M. A. Tolbert, *Journal of Physical Chemistry A*, 1999, **103**(48), 9717–9730.
- [22] P. K. Hudson, K. L. Foster, M. A. Tolbert, S. M. George, S. R. Carlo, and V. H. Grassian, *Journal of Physical Chemistry A*, 2001, **105**(4), 694–702.
- [23] D. R. Haynes, N. J. Tro, and S. M. George, *Journal of Physical Chemistry*, 1992, **96**(21), 8502–8509.
- [24] H. J. Fraser, M. P. Collings, M. R. S. McCoustra, and D. A. Williams, *Monthly Notices of the Royal Astronomical Society*, 2001, **327**(4), 1165–1172.
- [25] B. G. Koehler, *International Journal of Chemical Kinetics*, 2001, **33**(5), 295–309.
- [26] T.-L. Shen, P. J. Wooldridge, and M. J. Molina, van Nostrand Reinhold, 1995.
- [27] B. G. Koehler, L. S. McNeill, A. M. Middlebrook, and M. A. Tolbert, *Journal of Geophysical Research-Atmospheres*, 1993, **98**(D6), 10563–10571.
- [28] G. Vuillard, *Comptes Rendus Hebdomadaires Des Seances De L Academie Des Sciences*, 1955, **241**(19), 1308–1311.
- [29] J. P. D. Abbatt, K. D. Beyer, A. F. Fucaloro, J. R. McMahon, P. J. Wooldridge, R. Zhang, and M. J. Molina, *Journal of Geophysical Research-Atmospheres*, 1992, **97**(D14), 15819–15826.
- [30] T. Deshler, T. Peter, R. Muller, and P. Crutzen, *Geophysical Research Letters*, 1994, **21**(13), 1327–1330.
- [31] J. Goodman, S. Verma, R. F. Pueschel, P. Hamill, G. V. Ferry, and D. Webster, *Geophysical Research Letters*, 1997, **24**(5), 615–618.
- [32] U. K. Krieger, T. Huthwelker, C. Daniel, U. Weers, T. Peter, and W. A. Lanford, *Science*, 2002, **295**(5557), 1048–1050.
- [33] S. Solomon, S. Borrmann, R. R. Garcia, R. Portmann, L. Thomason, L. R. Poole, D. Winker, and M. P. McCormick, *Journal of Geophysical Research-Atmospheres*, 1997, **102**(D17), 21411–21429.
- [34] L. Schriver-Mazzuoli, A. Schriver, and A. Hallou, *Journal of Molecular Structure*, 2000, **554**, 289–300.
- [35] M. W. Severson, J. P. Devlin, and V. Buch, *Journal of Chemical Physics*, 2003, **119**(8), 4449–4457.
- [36] M. A. Tolbert and A. M. Middlebrook, *Journal of Geophysical Research-Atmospheres*, 1990, **95**(D13), 22423–22431.

Chapter 4

The kinetics of condensation and evaporation of H₂O from pure ice in the range 173 to 223 K: a quartz crystal microbalance study.

Both the previous cryostats, namely Mark I and Mark II presented in Section 2.2, have yielded interesting results concerning the kinetics of evaporation and condensation of H₂O onto pure and doped ice as well as spectral characterization of species forming on or within the doped ice film that have been identified thanks to FTIR spectroscopy in transmission. Nevertheless, both of these equipments have intrinsic limitations due to some of the methods of measurement used. For example, in the case of the evaluation of the thickness of the ice film using HeNe interferometry the refractive index of ice, n_{ice} , is considered constant even after doping it with trace gases. On the other hand it is clear from Figure 3.3 (page 74) that the contrast, C_{HeNe} , defined as the ratio between the minimum and the maximum level of the HeNe signal of the fringes generated in HeNe interferometry, varies substantially during the evaporation of the

doped ice film (grey trace). This variation is known to be linked to a change of refractive index as the contrast itself in such an interferometric configuration depends on the three refractive indices of the media involved in this work [1], namely vacuum, the ice film and the silicon substrate (see Figure 2.14, page 45). Foster et al. [2] have used this change in contrast C_{HeNe} to measure the index of refraction of a HCl·3H₂O (trihydrate) structure. They have found a value of $n_{\text{HCl}\cdot 3\text{H}_2\text{O}}=1.44$ at 632.8 nm and 140 K which is significantly different from $n_{\text{ice}}=1.31$ we use as a constant. Unfortunately, to our knowledge, no data are available in the literature concerning the crystalline hexahydrate structure. We could have evaluated the change in index of refraction due to the presence of HCl·6H₂O using the Lorenz-Lorentz equation [1] as Foster et al. [2] did in their work or as it is found in other papers [3], but this method implies that the investigated medium, doped-ice in the present case, is homogeneous which may perhaps not be the case in our work. Finally, this change of index introduces an error on the estimation of the remaining thickness (Equation 2.19, page 45) that is probably less than 15 % regarding the results obtained for HCl·3H₂O by Foster et al. As we do not know exactly how the refractive index varies with adsorbed trace gas quantities HeNe interferometry is probably not the best measurement method to determine the true remaining ice thickness and consequently the average mole fraction, χ_{HCl} , for HCl doping of ice, for example. In addition, it was an obstacle we had to surmount in order to determine to which extent the average mole fraction of the doping gas on or in an ice film may be responsible for the decrease of J_{ev} of doped compared to pure ice. The answer to this question perhaps explains the scatter of the data for doped ice in Figures 3.4 and 3.5 as the true average mole fraction is not well known for the data presented in these cases.

Consequently, we have decided to design and construct a new apparatus in order to enhance the existing experimental setup. The kinetics of H₂O evaporation and condensation on ice condensed from the vapor phase at 190 K have been studied in the range 173-223 K using the new apparatus based on a suitably calibrated quartz crystal microbalance, or piezoelectric mass sensor, that was put inside the vacuum chamber. It could be used either as a molecular or a stirred flow reactor, depending on the chosen pumping speed.

This chapter presents the features of the reactor that is equipped with the Mark II cryostat as well as experiments dealing with the kinetics of pure ice films that enable the validation of the reactor.

The Arrhenius representation of the zero order evaporative flux J_{ev} (molec $\text{cm}^{-2} \text{s}^{-1}$) of H_2O from pure ice displays a discontinuity at 193 ± 2 K that could be observed owing to the degree of precision of the present measurements.

For $223 > T > 193$ K,

$$J_{\text{ev}} = (1.6 \pm 0.7) \cdot 10^{28} \times \exp\left(\frac{-10.2 \pm 0.5}{\mathcal{R}} \times \frac{1000}{T}\right) \text{ molec cm}^{-2} \text{ s}^{-1}$$

and for $173 < T < 193$ K,

$$J_{\text{ev}} = (2.2 \pm 0.9) \cdot 10^{30} \times \exp\left(\frac{-12.0 \pm 0.5}{\mathcal{R}} \times \frac{1000}{T}\right) \text{ molec cm}^{-2} \text{ s}^{-1}$$

where $\mathcal{R} = 1.987 \text{ cal mol}^{-1} \text{ K}^{-1}$. The corresponding measured rate constant k_{cond} for H_2O condensation on ice satisfies the measured vapor pressure $P_{\text{H}_2\text{O}}^{\text{eq}}$ together with J_{ev} thereby affording thermochemical closure of the kinetics which results in the heat of sublimation $\Delta H_{\text{subl}}^0 = 11.7 \pm 0.6$ and $12.3 \pm 0.5 \text{ kcal mol}^{-1}$ from the above high and low T-range, respectively. J_{ev} is significantly lower than the maximum theoretically allowed value throughout the T-range in agreement with an uptake coefficient for H_2O on ice that is significantly smaller than unity. In addition, the negative temperature dependence of k_{cond} or γ reveals once more a precursor-mediated adsorption/desorption process for the $\text{H}_2\text{O}/\text{ice}$ system. The increased evaporative lifetime of pure ice may be important under atmospheric conditions. These results have been the subject of a publication in 2004 in *Physical Chemistry Chemical Physics* whose bibliographic reference may be found at the end of this chapter [4].

4.1 Experimental section

4.1.1 Apparatus

The results presented here have been obtained thanks to the further development of the existing multiple diagnostics experiment that was described in detail in Chapter 2 and is equipped with the cryostat Mark II as described in Section 2.2.

The new feature of the experiment is the addition of a temperature controlled quartz crystal microbalance (QCM) in the reactor chamber, the piezoelectric crystal being used as a monitor of growth or loss of a solid condensed phase thus allowing the realtime observation of the mass changes of adsorbed H₂O that is deposited as a thin ice film on the quartz crystal microbalance (QCM).

The experimental apparatus (Figure 4.1) consisting of the existing stainless steel chamber underwent a volume change with the new volume now being $V_r=2400\text{ cm}^3$. The temperature of the reactor is continuously maintained at $T_r=320\text{ K}$ during all experiments. The calibrated leak on the bypass line, item 4 including the leak valve LV displayed in Figure 4.1, has been replaced and allows now the effusion of residual gas from the upper (UC) into the lower (LC) chamber at a rate constant of effusion for H₂O given by $k_{\text{esc}}(\text{H}_2\text{O})=0.064\text{ s}^{-1}$. New specific data on the hardware configuration and the calibration factors are summarized in Table 4.1.

The present experiment has been performed in the three configurations described in Section 2.3 which will briefly be recalled hereafter:

- *Static* operation: GV and LV closed. This leads to equilibrium conditions within the chamber.
- *Stirred flow* operation at a low rate of pumping: GV closed and LV open. This leads to a typical (stirred flow) residence time of 15 s for H₂O.
- *Dynamic* operation at a high rate of pumping: GV open. This corresponds to molecular flow conditions whose estimated gas phase residence time for H₂O is 1 ms.

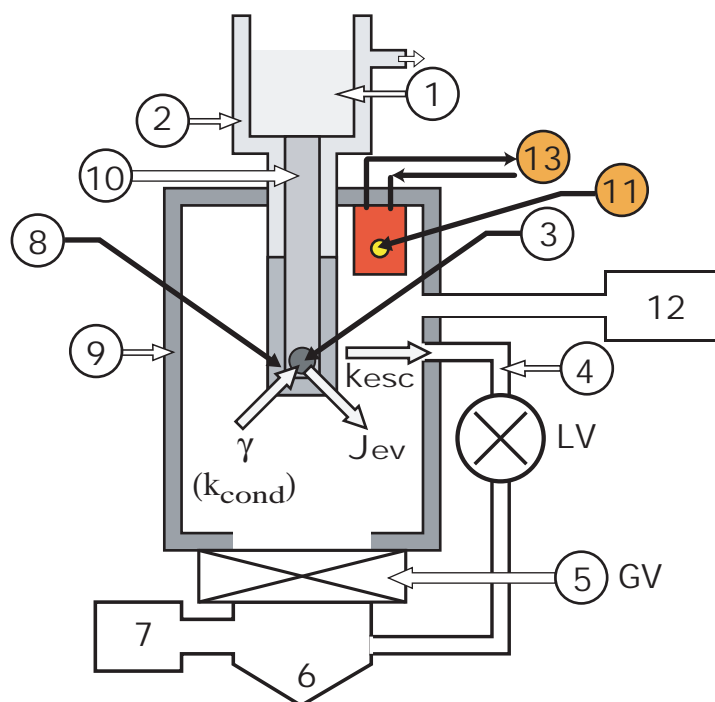


Figure 4.1: Schematic drawing of the experimental apparatus: **1** Liquid nitrogen reservoir, **2** Evacuated Dewar vessel, **3** Silicon window of 0.78 cm^2 area used as a substrate for H_2O deposition, **4** Calibrated leak equipped with valve LV allowing *Static* (valve and **5** closed) and *Stirred flow or Low pumping rate* (valve open and **5** closed) experiments, **5** 6" diameter gate valve GV allowing *Dynamic or High pumping rate* experiments when opened, **6** Flange for Turbo Pump, **7** Quadrupole Mass spectrometer, **8** PTFE thermal insulation isolating the whole cryostat but the Si window, **9** Reactor chamber, **10** Solid copper finger with cartridge heaters for control of the temperature of the Si Substrate, **11** Quartz crystal microbalance (QCM) with Delrin insulation preventing significant molecular exchange between the gas phase and the QCM device but the 0.50 cm^2 piezoelectric crystal itself, **12** Absolute pressure gauge (Baratron, MKS 220-AHS). Several type T thermocouples (not shown here) are located throughout the vacuum side of the cryostat in order to measure the temperature in different areas (Si window, PTFE Insulation, Reactor and Calibrated Leak walls, etc). In addition, two 2" diameter NaCl windows allow the FTIR monitoring of the condensed phase, and two inlet tubes allow the injection of H_2O as well as the trace gas into the reactor. The hollow arrows (γ , J_{ev} and k_{esc}) describe the important kinetic processes taking place, such as adsorption, desorption and effusion of H_2O vapor. **13** Independent temperature controlled cooling of QCM (see Appendix 4.5).

In addition to the measurement techniques discussed above a quartz crystal microbalance (QCM), that is a piezoelectric mass sensor (item **11** in Figure 4.1) has been installed on the top

Table 4.1: Hardware parameters of both cryogenic sample supports for the kinetic study of pure ice.

	Si Optical Window	QCM
Reactor temperature T_r [K]	320	320
Reactor volume V_r [K]	2400	2400
Ice sample surface [cm ²]	0.78	0.50
Collision frequency with ice sample ω_{H_2O} [s ⁻¹]	4.98	3.19
Effusion rate constant of calibrated leak k_{esc} [s ⁻¹]	0.064	0.064
Calculated escape orifice A_{esc} [mm ²]	1.0	1.0
Conversion factor (1/RT) Conv [molec cm ⁻³ Torr ⁻¹]	$3.0 \cdot 10^{16}$	$3.0 \cdot 10^{16}$
M/S calibration factor at $m/z=18$ [molec s ⁻¹ A ⁻¹]	$2.4 \cdot 10^{24}$	$2.4 \cdot 10^{24}$
	Thickness for FTIR O.D. = 1.08 [Å]	QCM calibration factor C_f [a.u.]
	10000	Temperature [K] C_f
		170 9.0
		180 8.0
		190 7.8
		193 6.0
		205 2.0
		208 1.9

flange of the upper chamber. The temperature of the crystal is regulated by a controller that will be described later on having a precision of 0.1 K. The mass measurement of a deposited thin film based on the resonant frequency of a piezoelectric crystal used as a support for deposition has been pioneered in the 60's by Sauerbrey [5]. The basic governing relationship is given in Equation 4.1

$$\Delta f = \frac{-\Delta m_d f^2}{\rho_q V_q} \quad (4.1)$$

in terms of the empirical relation between the change in mass, Δm_d , the shift of frequency, Δf , of an AT-cut SiO_2 crystal oscillating at the resonance frequency f , ρ_q the density of quartz (approximately 2650 kg m^{-3}) and V_q the propagation of sound in quartz (3340 m s^{-1}).

Recent devices have taken advantage of the advances in electronics by gaining in accuracy using more sophisticated approaches such as the Z-Match technique described by Lu [6]. However, this implies the knowledge of a new parameter, the acoustic impedance ratio, Z , based on the densities and the shear moduli of the deposit and the crystal, respectively. It is this method that is used in our commercial device in conjunction with the quartz crystal sensor (Inficon 750-211-G1 compact head with a 6 MHz crystal) that is controlled by an Inficon IC/5 thin film deposition controller whose thickness resolution is 0.00577 \AA set for a material with a density of 1 and a Z -ratio of 1, according to the specifications of the manufacturer.

We would like to point out that for ice neither the shear modulus nor the Z -ratio are commonly known due to the unknown structure of the ice deposit depending on the rate and the temperature of deposition [7, 8] as well as the nature of the substrate used for ice deposition [9]. QCM has been used in ice research before [10], however, only scant information about the mechanical properties of vapor deposited ice is known from the literature [11, 12].

In order to get rid of the constraint imposed by the absolute knowledge of the impedance ratio for ice, Z_{ice} , we have chosen to calibrate the raw signal, given as an equivalent thickness in \AA , and displayed on the IC/5 monitor by using the optical cryostat Mark II that had been

calibrated previously (see Section 2.7). The principle of this cross calibration is presented below. To obtain an absolute number of water molecules of the ice film deposited on the piezoelectric crystal of effective surface $A_{\text{QCM}}=0.5 \text{ cm}^2$, we have thermally insulated the whole QCM crystal holder (Figure 4.2, left) but the crystal itself using a tightly fitted assembly of Delrin * elements (Figure 4.2, right). The reason for the use of the Delrin insulation is identical to the one presented in Section 2.2 concerning the PTFE sleeve surrounding the copper finger of the cryostat. The design criteria were to adjust the elements as closely as possible without providing in fact mechanical contact to the QCM sensing element (quartz crystal), thereby avoiding a perturbation to the inherent resonance condition. Delrin as inert insulation material has replaced PTFE in view of future experiments involving HBr. Uptake experiments performed in our laboratory in a Knudsen low pressure flow reactor whose principle is described in reference [13] have shown that the uptake of hydrogen bromide on Delrin is negligible compared to the case of HBr interacting with PTFE which absorbed HBr without reaching saturation. Moreover, according to our mechanical technician, Flavio Comino, who has always given good advice in the course of the development of each part of the present equipment, Delrin is easier to machine than PTFE and which consequently permits more precise manufacturing of the parts constituting the insulating assembly. Finally, this leaves 0.5 cm^2 of temperature-controlled surface area, A_{QCM} , for ice deposition onto the single crystal quartz element. This surface is therefore the only cold part of the QCM exposed to the gas phase.

This assertion has been validated using the set of measurements described in Section 2.1. Briefly, we first measured the absolute H₂O flow rate using a Teflon PFA-coated calibrated volume as a reservoir for the injection of a known number of H₂O molecules into the reactor by measuring the H₂O partial pressure decrease with time $\frac{dP_{\text{H}_2\text{O}}}{dt}$. At the low temperatures of the Si-window essentially all injected molecules were deposited on the QCM. Subsequently, the H₂O mass balance is verified during evaporation of the ice film by measuring the time integrated calibrated MS signal at $m/z=18$ in order to determine the number of H₂O molecules

*Delrin® acetal resin (DuPont)

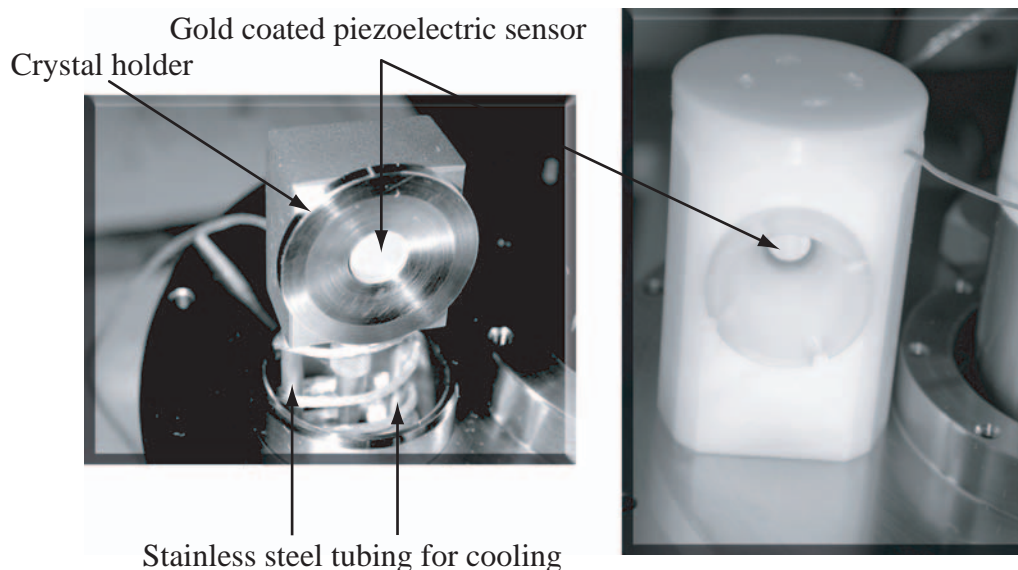


Figure 4.2: Quartz crystal microbalance (QCM) support housed in its tightly fitted Delrin insulation preventing H_2O deposition on the QCM except on the 0.5 cm^2 piezoelectric element.

evaporating from the QCM crystal. Usually, the mass balance agrees to within less than 15 %. In addition, the temperature of the Delrin insulation is permanently recorded at a position close to the QCM crystal. The temperature of the Delrin never reaches values lower than 250 K. This measurement in itself implies the absence of a cold spot as this region should be the coldest part of the Delrin assembly by design.

A complete description of the cooling device allowing the precise control of the temperature of the QCM will be given in Appendix 4.5 at the end of this chapter.

4.1.2 Quartz Crystal Microbalance Calibration

In order to avoid uncertainties in Z depending on the deposition protocol used to grow the ice films, we have cross-calibrated the ice film deposited on the Si-window (optical support) by monitoring the FTIR transmission with the one on the QCM sensor after quantitative mass transfer from the Si-window to the QCM sensor. This calibration relies on the mass transfer of a known quantity of H_2O between both measurement supports, namely optical and QCM

element. It allows a quantitative comparison of the loss of H₂O molecules on one support with the gain on the other.

In all calibration experiments the ice films were first grown under static conditions on the optical cryostat at 190 K by the deposition of bidistilled water vapor at a typical rate between $5 \cdot 10^{16}$ and $1 \cdot 10^{17}$ molec cm⁻² s⁻¹ using the inlet configuration shown as a reminder in Figure 4.3. As expected for ice films deposited at such rates and temperatures higher than 180 K [7], the thin film FTIR spectrum in transmission revealed the presence of thermodynamically stable hexagonal polycrystalline ice I_h [14]. The application of this protocol for deposition ensured the reliable and reproducible formation of a thermodynamically stable I_h crystal structure of ice deposited from the vapor phase.

After the initial deposition of the ice film the temperature of the Si window T_{Si} was set to the one desired for the study of the mass transfer between the supports. Several experiments have been performed in the range 170-208 K in order to quantitatively characterize the sensitivity of the QCM.

Subsequently, the temperature of the QCM, T_{QCM}, was decreased down to T_{Si} and beyond. T_{QCM} is measured using a type T thermocouple that is fixed in the crystal holder, as close as possible to the piezoelectric sensor, using a very small screw for the fixation of the thermocouple. Figure 4.4 shows a complete sequence of a transfer at 180 K. When T_{QCM}=T_{Si} at t=9.25·10³ s in Figure 4.4, we observe the onset of the mass transfer from the cryostat Si-window to the quartz crystal of the QCM. After a short time delay (t_a in Figure 4.4) owing to a likely small differential between the temperature of the thermocouple and the QCM quartz sensor the change in the QCM signal at point **B** is clearly visible. At point **C** the mass transfer is completed. Subsequently, T_{QCM} is increased to allow the transfer of H₂O molecules back to the Si window of the optical cryostat. The QCM signal shows a rapid evaporation rate until all H₂O molecules are desorbed at **D** (Figure 4.4).

The short time delay mentioned above may be attributed to a small differential between the recorded temperature of the QCM crystal holder and either the temperature of the piezoelectric

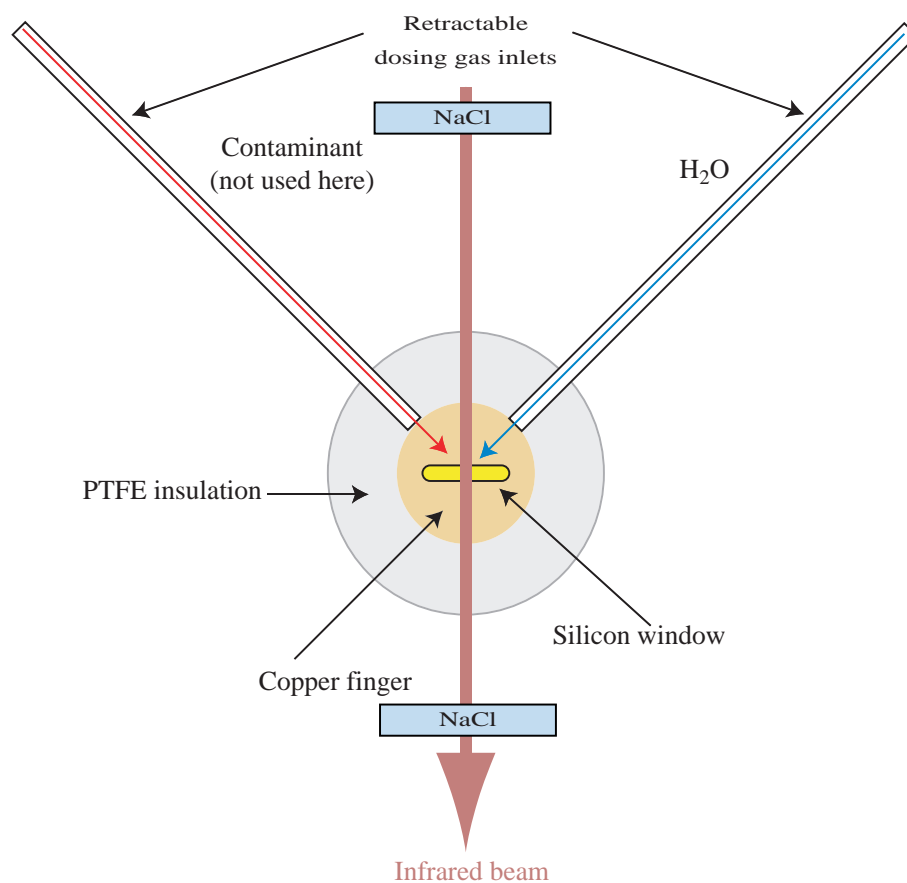


Figure 4.3: Horizontal cut (view from the top) through dosing tubes and IR beam transmitted across the Si window attached to the cryostat. The PTFE-insulated cryostat is perpendicular to the reference (paper) plane. Both the dosing inlets are retractable allowing either direct injection of the gas onto the cryostat or deposition on the QCM by backfilling of the chamber.

quartz crystal, due to the thermal exchange between the gold coating of the crystal and the stainless steel crystal holder, or with the ice film, the latter of which, naturally, cannot be directly measured. This time lag (t_a in Figure 4.4) has been measured by evaluating the time response of the QCM signal to different temperature ramps when there is no deposit on the sensor. For example, when the temperature is decreased from 240 to 180 K the QCM offset tends to increase. When the temperature is suddenly increased there is a temperature differential or a short delay corresponding to the time period for equalization of the temperature differential

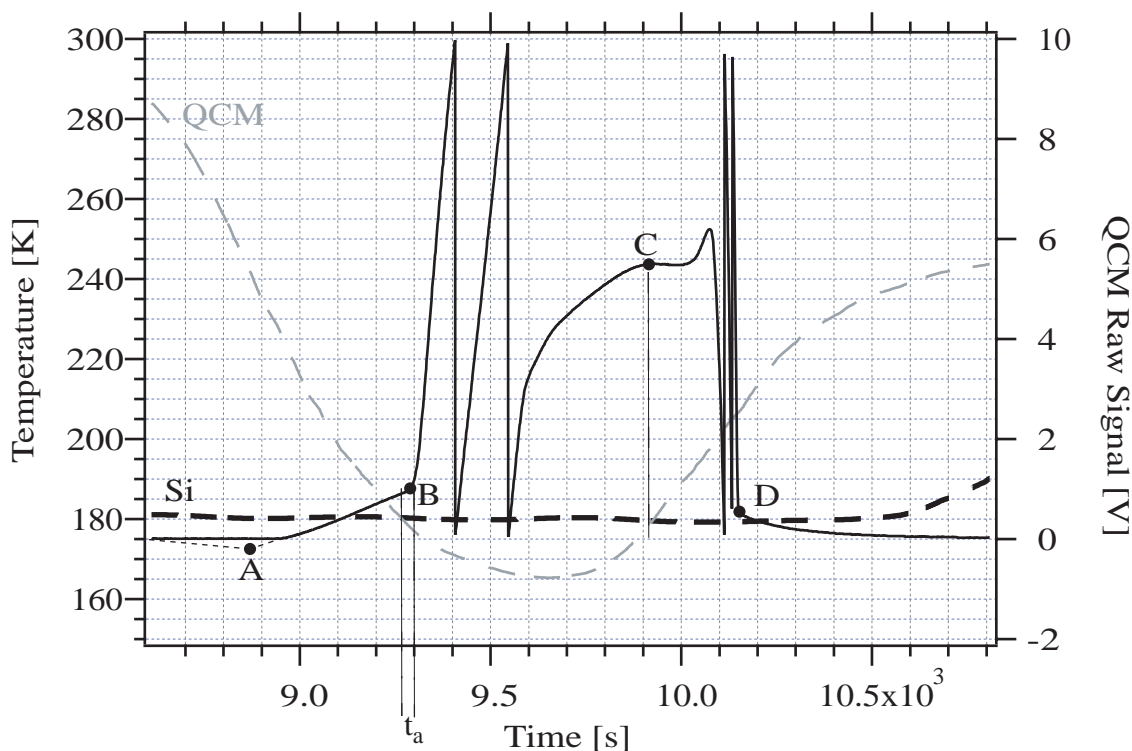


Figure 4.4: Complete recording of an exchange sequence (mass transfer) between the optical cryostat and the QCM. The solid line corresponds to the time dependent QCM initial signal, namely S_{QCM} ; the thin dashed line with point **A** shows the negative offset of the QCM signal due to the change of temperature. The bold and gray dashed line show the temperature of the Si window T_{Si} and the piezoelectric element T_{QCM} , respectively. Points **B**, **C** and **D** are explained in the text.

between the QCM holder and the crystal. When the temperature changes at a rate larger than 6 to 8 K min⁻¹, there was a 30 to 50 s time lag for reaching identical temperatures. For a change of up to 4 K min⁻¹ the lag was always smaller than 20 s. Under typical experimental conditions, say at a rate smaller than 2.5 K min⁻¹, the delay is shorter than 10 s which may be considered negligible in the current set of experiments. These observations are carried over to the lag between the temperature of the holder and the ice film proper. By observing the change of slope of the evaporation flux of H₂O from ice due to a change of temperature of the QCM crystal holder when it successively increases and decreases under the typical conditions of the

experiments we essentially found time lags up to 20 s at most.

Figure 4.5 displays the peak optical density in FTIR spectra of the ice film on the Si window before (A_b) and after (A_e) a complete round trip of the H_2O molecules from the Si window to the QCM followed by the transfer back to the Si window. Apart from a small difference in optical density discussed below this experiment indicates quantitative transfer of the H_2O molecules from the Si-window to the QCM sensing element. We conclude that the apparent loss of molecules after a complete roundtrip measured by the difference in optical density A_b-A_e corresponds to 12 % in the worst case and is most probably due to the passivation of the stainless steel walls of the reactor. The initial deposition of the ice film is performed using the directed injection of the H_2O molecules on the Si surface as displayed in Figure 4.3 rather than by back-filling the whole reactor volume. In this way the chamber walls did not have a chance to become passivated during ice film deposition. We have checked using mass spectrometric measurements that for the experiments described below this H_2O reservoir given by H_2O molecules adsorbed on the internal surface of the reactor leads to a residual pressure of $1.5 \cdot 10^{-6}$ Torr at most after desorption. It has therefore no impact on the kinetics of condensation and evaporation of water from ice in the temperature range of this study.

The hypothesis of the passivation of the reactor wall is confirmed by the fact that after the first complete roundtrip an additional transfer sequence of H_2O from the Si- to the QCM support leads to a final FTIR spectrum whose optical density is identical to A_e , its starting point. Nevertheless, a change in the scattering properties of the thin film such as its roughness, may also lead to a change in optical density that may be observed in Figure 4.5 at $\tilde{\nu}$ higher than 3600 cm^{-1} . This dilemma can not be solved at this point of the study.

One must pay attention to the offset in the QCM raw signal taken between points **A** and **B** of Figure 4.4. This is an expected frequency shift due to the temperature change of the crystal and must be taken into account for the calculation of the mass of H_2O present on the QCM during temperature dependent experiments. Point **A** and the associated dashed line have been extrapolated because negative values of the QCM signal S_{QCM} are set to zero by the QCM

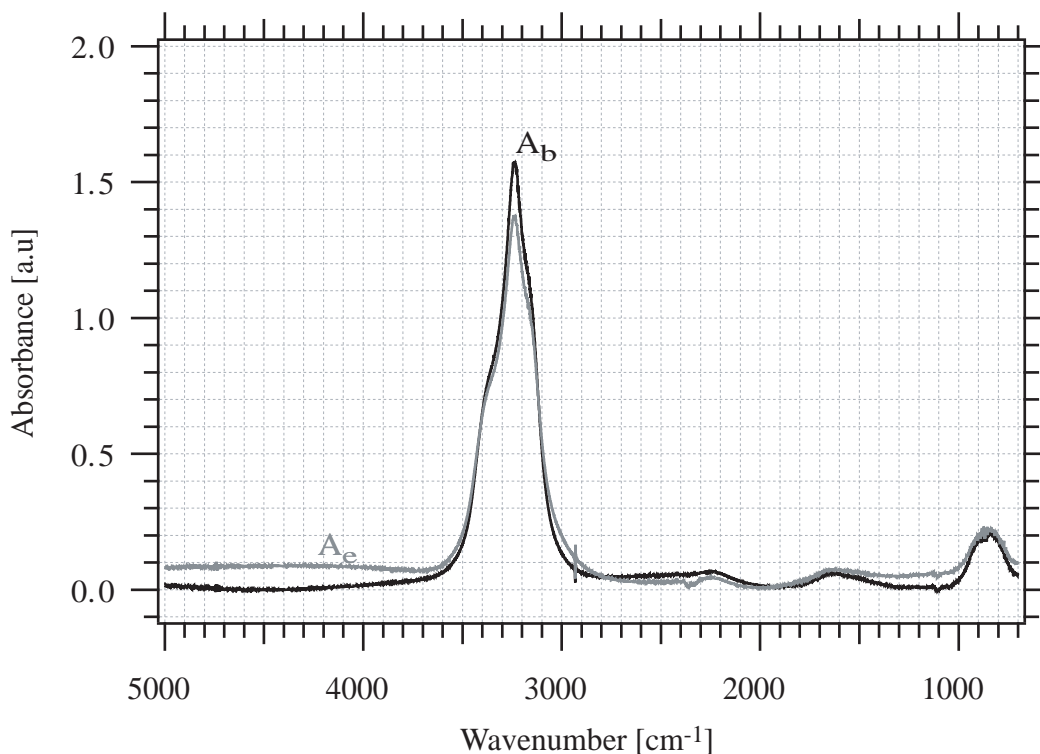


Figure 4.5: FTIR spectra in transmission of the ice film on the Si window at the beginning and the end of the sequence recorded in Figure 4.4 corresponding to points **B** and **D** and optical densities A_b and A_e , respectively.

control unit although they are displayed as negative values on the controller screen. Generally, this offset has a value between 1.00 and 1.20 V depending on the temperature of the QCM in the range 170-208 K. In Figure 4.4 it corresponds to 1.15 V. For experiments at a given low sample temperature the value of the QCM signal at point **B** must be considered as the zero thickness value given the complex dependence of the frequency shift with temperature. Owing to the low background H₂O pressure smaller than $5 \cdot 10^{-5}$ Torr no deposition of H₂O vapor on the QCM crystal is expected during the cooling period from $t=8.6 \cdot 10^3$ to $9.3 \cdot 10^3$ s corresponding to the change from 285 to 180 K.

In the particular case presented in Figures 4.4 and 4.5 we calculate using the data given in Table 4.1 that the FTIR spectrum of H₂O ice resulting in $A_e=1.38$ logarithmic units corresponds

to $3.05 \cdot 10^{18}$ molecules of H_2O . On the other hand, the QCM raw signal S_{QCM} indicates that at the end of the condensation of H_2O on the piezoelectric crystal at point **C** the thickness evaluated by the IC/5 controller corresponds to 25.5 Volts with a density and a Z-ratio set to unity. We deduce a detected mass equivalent to $3.80 \cdot 10^{17}$ molecules of H_2O on the QCM for $S_{\text{QCM}}=25.5$ V and a density of 0.93 for the ice film [15] using a factory-set nominal correspondence of $S_{\text{QCM}}=10$ V for a 1000 Å thick ice film. We define the calibration factor of the QCM, C_f , at the given temperature of 180 K at point **B** by the ratio of the real versus the displayed (factory-set, $Z=1$, $\rho=1$ g cm^{-3}) mass or thickness, thus

$$C_f(180\text{K}) = \frac{3.05 \cdot 10^{18}}{3.80 \cdot 10^{17}} = 8.0$$

implying that the real mass or thickness of an ice film deposited at 180 K from the vapor phase at a rate of $5 \cdot 10^{16}$ molec $\text{cm}^{-2} \text{s}^{-1}$ is 8.0 times the displayed one. This rate of deposition is checked in hindsight in Figure 4.4 during the deposition process on the QCM (between **B** and **C**). The rate of deposition of H_2O on the QCM is calculated as the temporal change of S_{QCM} and corresponds to the slope of the QCM raw signal represented in Figure 4.4 which, after the application of the calibration factor, falls in the desired range $5 \cdot 10^{16} - 1 \cdot 10^{17}$ molec $\text{cm}^{-2} \text{s}^{-1}$.

A series of C_f values for different temperatures used for ice deposition in the range 170-208 K is given in Table 4.1. The temperature of deposition of the ice film is the only parameter determining C_f under the typical conditions for H_2O deposition in this work. Throughout this study it has been chosen as 190 K corresponding to $C_f(190 \text{ K})=7.8 \pm 0.8$. Based on the stated resolution of 0.00577 Å for the IC/5 equipped with a 6 MHz crystal and on the present calibration factor (see Table 4.1) we may estimate an accuracy of the number of H_2O molecules present as ice on the QCM to better than $1.4 \cdot 10^{13}$ molec cm^{-2} which roughly corresponds to 1.5 % of a formal monolayer of ice.

4.1.3 The residual gas mass spectrometer

Under stirred flow conditions (6" GV closed, LV open) the MS still can be used to measure the steady state partial pressure (or concentration) of each residual gas, such as H₂O vapor, present in the upper chamber of the reactor thanks to the effusion of the gas across the calibrated leak. We evaluate the flow rate $F_r(\text{H}_2\text{O})$ using Relations 2.11, 2.12, 2.13 and 2.14 (see page 41) that follow hereafter:

$$\begin{aligned}
 F_r(\text{H}_2\text{O}) &= \frac{P_{\text{H}_2\text{O}} \times V_r}{\mathcal{R} \times T_r} \times k_{\text{esc}}(\text{H}_2\text{O}) \\
 &= [\text{H}_2\text{O}] \times V_r \times k_{\text{esc}}(\text{H}_2\text{O}) \\
 &= \text{Conv} \times V_r \times k_{\text{esc}}(\text{H}_2\text{O}) \times P_{\text{H}_2\text{O}} \quad (\text{Equation 2.13, page 41}) \\
 &= C_{18}^{\text{s-flow}} \times I_{18}
 \end{aligned}$$

where $\text{Conv} = \frac{1}{\mathcal{R}T}$ is the conversion factor describing the relationship between the partial pressure $P_{\text{H}_2\text{O}}$ of H₂O and the H₂O concentration $[\text{H}_2\text{O}]$ in molec cm⁻³ Torr⁻¹. The value of Conv is 3.0·10¹⁶ molec cm⁻³ Torr⁻¹ for a reactor temperature $T_r=320$ K. $V_r=2400$ cm³ is the volume of the reactor, and $k_{\text{esc}}=k_{\text{esc}}(\text{H}_2\text{O})$ is the first order rate constant of effusion of H₂O through the calibrated leak that has a value of $k_{\text{esc}}=0.064$ s⁻¹ displayed in Table 4.1.

The smallest measurable MS signal level at $m/z=18$ at a signal-to-noise ratio $S/N=2:1$ is of the order of $1.0 \cdot 10^{-12}$ A. Using the MS calibration factor for $m/z=18$ of $2.4 \cdot 10^{24}$ molec s⁻¹ A⁻¹ this detection limit leads to the smallest measurable flow rate of effusion of H₂O vapor of $2.4 \cdot 10^{12}$ molec s⁻¹ and a pressure of H₂O of $5.2 \cdot 10^{-7}$ Torr which is smaller than the vapor pressure of H₂O given in the literature [16] for the temperature range 170 to 220 K. It corresponds to $5.5 \cdot 10^{-6}$ to $2.0 \cdot 10^{-2}$ Torr, respectively.

4.1.4 Check of the ice sample temperature

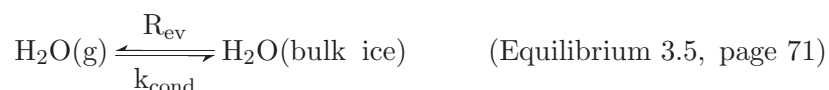
Above 170 K the temperature of the ice film measured by a type T thermocouple is periodically checked against the vapor pressure of H₂O over ice [16], $P_{\text{H}_2\text{O}}^{\text{eq}}$, using the MKS Baratron absolute pressure gauge (220-AHS) under static conditions for temperatures higher than 190 K. Another check of $P_{\text{H}_2\text{O}}^{\text{eq}}$ is based on the residual gas MS signal under stirred flow conditions using Equation 2.13 to relate the measured effusion rate to the pressure $P_{\text{H}_2\text{O}}^{\text{ss}}$ in the stirred flow reactor. The relation $P_{\text{H}_2\text{O}}^{\text{eq}} = P_{\text{H}_2\text{O}}^{\text{ss}} \times \left(\frac{k_{\text{esc}}}{k_{\text{cond}}} + 1 \right)$ is used to obtain the equilibrium vapor pressure $P_{\text{H}_2\text{O}}^{\text{eq}}$ from $P_{\text{H}_2\text{O}}^{\text{ss}}$ when the temperature is lower than 190 K. By applying the necessary corrections presented in Section 2.4 we obtain results in agreement with those of Marti and Mauersberger [16] at an accuracy better than 1 K.

4.2 Experiments and Results

In all further experiments the ice films are grown at standard conditions at a rate of $1 \cdot 10^{17}$ molec cm⁻² s⁻¹ and a temperature of 190 K in order to satisfy the constraints discussed in Section 4.1.2 and to enable the use of the established QCM calibration factor $C_f=7.8$.

4.2.1 Kinetics of evaporation and condensation based on the measurement of water vapor in the gas phase

As a first approach the evaporation flux J_{ev} [molec cm⁻² s⁻¹] of H₂O from ice and the corresponding rate of condensation k_{cond} , from Equilibrium 3.5 recalled below, have been evaluated at approximately 200 K in a few experiments based on the technique described in the previous chapter in Section 3.2 (page 71). It uses the QCM as a temperature controlled support for the ice films deposition from the vapor phase.



Described in full detail in Section 3.2 this method is based on two gas phase measurements:

on the one hand the partial pressure P_{ss} of H₂O under stirred flow conditions, and on the other hand the equilibrium pressure P_{eq} in the reactor under static conditions given by Equilibrium 3.5 recalled above.

By analogy with Equation 3.7, but using this time the QCM sensor as a substrate for ice deposition, J_{ev} and k_{cond} are evaluated using the following equations:

$$P_{eq} = \frac{J_{ev} A_{QCM}}{k_{cond} V_r} \times RT \quad P_{ss} = \frac{P_{eq}}{\frac{k_{esc}}{k_{cond}} + 1} \quad (4.2)$$

and using the relationship obtained from Equation 3.6, page 71:

$$J_{ev} = R_{ev} \times \frac{V_r}{A_{QCM}} \quad (4.3)$$

where R_{ev} is the rate of evaporation of H₂O vapor from the QCM in molec cm⁻³ s⁻¹ and A_{QCM} is the effective surface area of the QCM crystal exposed to the gas phase (see Table 4.1).

The values of J_{ev} resulting from this set of experiments are presented in Figure 4.6 using the symbol \oplus , and the resulting uptake coefficients γ for water over ice are displayed in Figure 4.7 using symbol \oplus .

In addition, results for k_{cond} or γ , where $\gamma = \frac{k_{cond}}{\omega}$ is the uptake coefficient of H₂O onto ice and ω the collision frequency of H₂O molecules with the ice sample (see Table 4.1) are given in Figure 4.7 (\square). The measurement of the rate constant k_{cond} is based on the approach of P_{ss} to P_{eq} when the system is set from stirred flow (GV closed, LV open in Figure 4.1) to static conditions (GV and LV closed). This method is explained in more detail in Section 4.2.2.

One must take note that as these three sets of results are based on the measurement of P_{ss} and P_{eq} the correction described in Section 2.4 has been applied. As a reminder, this correction is based on the fact that the temperature of the stainless steel vessel, T_r , and the low temperature of the QCM, T_{QCM} , are both controlling the calculated true equilibrium pressure P_{eq} based on the measured pressure P_{meas} . If the temperature of the reactor walls were the same as T_{QCM} no such correction would be necessary. The following relation may be given for

molecular and stirred flow conditions which shows that $P_{\text{meas}} > P_{\text{eq}}$ for $T_r > T_{\text{QCM}}$:

$$P_{\text{meas}} = P_{\text{eq}} \times \left(\frac{T_r}{T_{\text{QCM}}} \right)^{1/2} \quad (4.4)$$

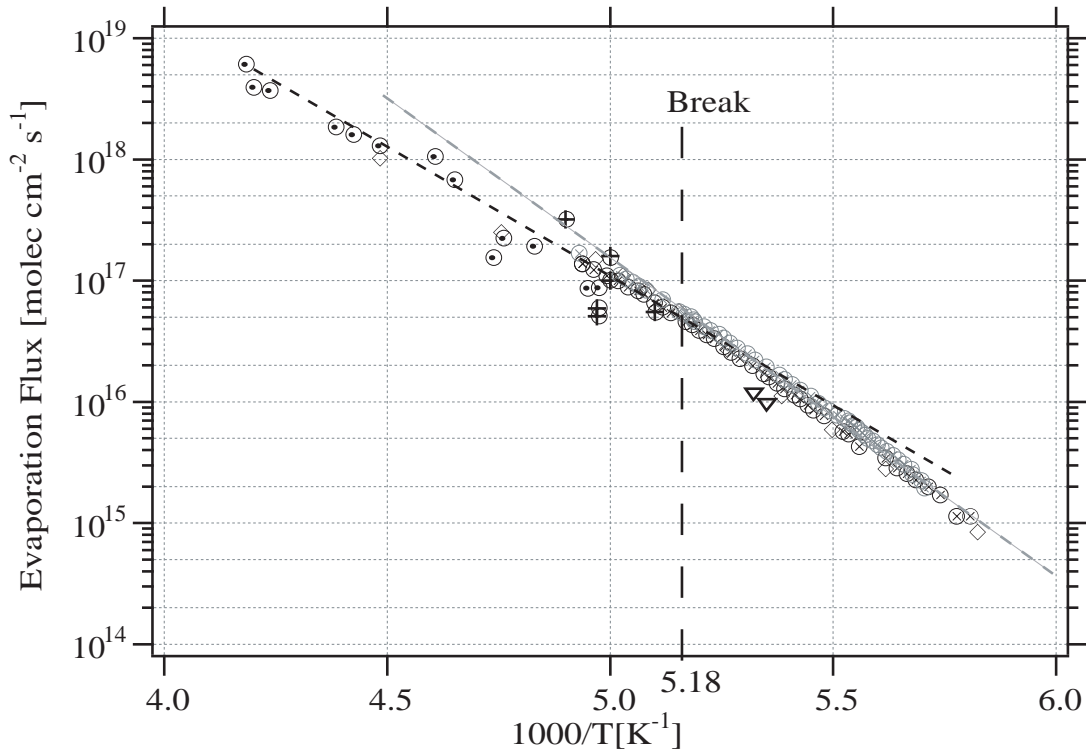


Figure 4.6: Synopsis of experimental results on the evaporative flux J_{ev} [$\text{molec cm}^{-2} \text{s}^{-1}$] of H_2O from pure ice using either the cryostat or the QCM as substrate for deposition. (\odot): cryostat experiments from Delval et al. [17] presented in Section 3.2, (\oplus): QCM experiments based on gas phase monitoring, presented in this section, (\otimes) (black and grey) and (\diamond): QCM experiments based on the condensed phase investigation of J_{ev} , presented in Section 4.2.3. Point **B** indicates the temperature ($193 \pm 2 \text{ K}$) which corresponds to the change of slope of the Arrhenius representation of J_{ev} . (∇): QCM experiments based on the condensed phase investigation for ice condensed at 208 K and conducted at temperature, presented in Section 4.2.3.

The QCM results that are based on using the piezoelectric crystal as an ice film support and measuring the partial pressure P_{ss} of H_2O are in good agreement with the previously published data [17] reported in Section 3.2. The degree of scatter of the data is similar to the one for the J_{ev} values previously measured; as expected, the data are well distributed on each side of

the dashed line given by the Arrhenius expression that is based on the data set of the optical cryostat experiment and is referred to as Equation 3.12 on page 76 of Section 3.2. For further reference, this Arrhenius expression is recalled below in the following equation:

$$J_{\text{ev}} = 1.6 \cdot 10^{28 \pm 1} \times \exp\left(\frac{-10.3 \pm 1.2}{\mathcal{R}} \times \frac{1000}{T}\right) \text{ molec cm}^{-2} \text{ s}^{-1} \quad 200 < T < 240 \text{ K} \quad (4.5)$$

with $\mathcal{R} = 1.987 \text{ cal mol}^{-1} \text{ K}^{-1}$.

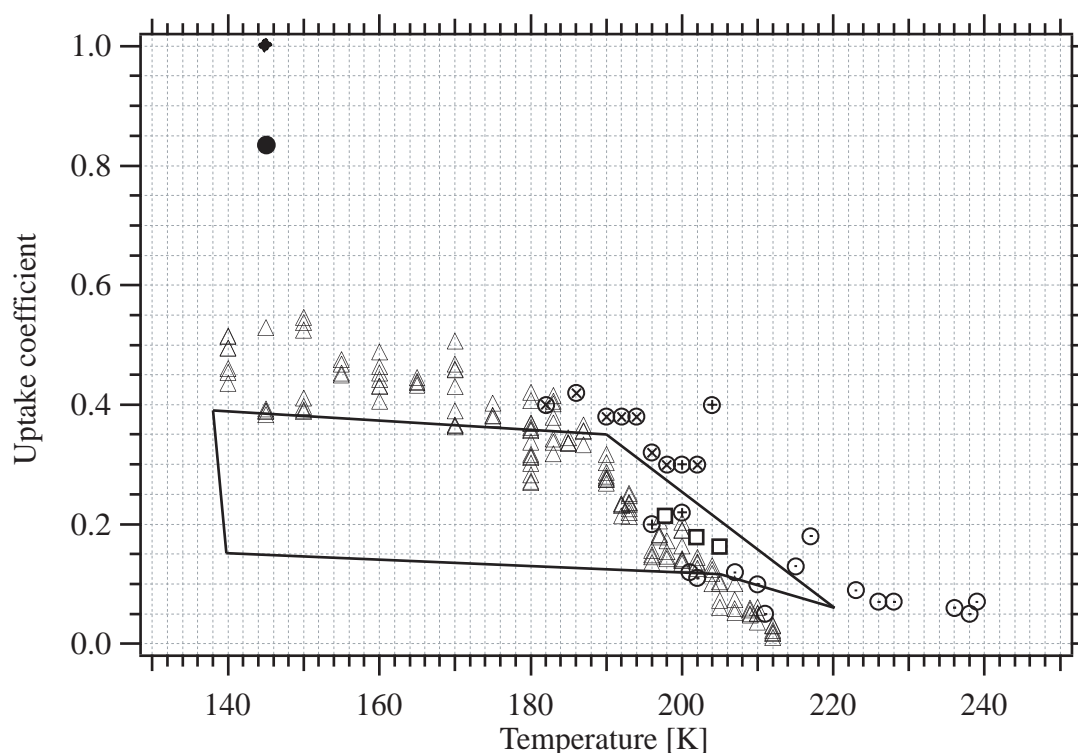


Figure 4.7: Synopsis of results on the uptake coefficient from pure ice as a function of temperature. (\odot): cryostat experiment results from Delval et al. [17] presented in Section 3.2, (\otimes): QCM experiments based on the condensed phase investigation of k_{cond} , presented in Section 4.2.3, (\oplus): QCM experiments based on MS detection of the partial pressure of H₂O, this section, (\square): QCM experiments based on the approach to equilibrium of the water vapor pressure in the reactor, presented in Section 4.2.2, (Δ): realtime kinetic experiments using a pulsed valve in a Knudsen flow reactor [18], (\blacklozenge): Brown et al. [19], (\bullet): results from Koros et al. The area outlined represents results from Chaix et al. involving different types of ice [20, 21].

Concerning γ both methods based exclusively on the gas phase measurement lead to similar

scatter compared to J_{ev} . Data reported in Figure 4.7 using \oplus and \square symbols present the same degree of scatter as the ones published previously thus showing good agreement among the absolute values. The main conclusion from this set of experiments is that γ is significantly smaller than unity around 200 K.

4.2.2 Kinetics of condensation of H_2O on pure ice: approach to pressure equilibrium

In addition to the gas phase monitoring techniques presented in Section 4.2.1 and in Chapter 3 in relation to the measurement of γ or k_{cond} , we propose a third method based on the approach of P_{ss} to P_{eq} for water vapor when the experiment is switched from *stirred flow* to *static* conditions.

The relevant kinetic processes in the $\text{H}_2\text{O}/\text{Ice}$ interaction are schematically represented in Figure 4.1 in terms of the kinetic constants k_{esc} , k_{cond} and J_{ev} .

When the system is at *stirred flow* conditions with GV closed and LV open, $[\text{H}_2\text{O}]_{\text{ss}}$ follows the steady-state Equation 3.9 given on page 72 and recalled as follows:

$$R_{\text{ev}} = [\text{H}_2\text{O}]_{\text{ss}} \times (k_{\text{cond}} + k_{\text{esc}}) \quad (4.6)$$

Equation 4.7 explicitly displays $[\text{H}_2\text{O}]_{\text{ss}}$:

$$[\text{H}_2\text{O}]_{\text{ss}} = \frac{R_{\text{ev}}}{(k_{\text{cond}} + k_{\text{esc}})} \quad (4.7)$$

When the system is at equilibrium under *static* conditions P_{eq} is ruled by Equation 4.8:

$$R_{\text{ev}} = [\text{H}_2\text{O}]_{\text{eq}} \times k_{\text{cond}} \quad (4.8)$$

resulting in Equation 4.9:

$$[\text{H}_2\text{O}]_{\text{eq}} = \frac{R_{\text{ev}}}{k_{\text{cond}}} \quad (4.9)$$

When the system under *stirred flow* is set to *static* conditions at t=0, the evolution of [H₂O]_{ss} to [H₂O]_{eq} follows Equation 4.10:

$$\frac{d[\text{H}_2\text{O}](t)}{dt} = R_{\text{ev}} - k_{\text{cond}} \times [\text{H}_2\text{O}](t) \quad (4.10)$$

which is a linear differential equation with the following solution:

$$[\text{H}_2\text{O}](t) = \frac{R_{\text{ev}}}{k_{\text{cond}}} + C_0 \times e^{-k_{\text{cond}} \times t} = [\text{H}_2\text{O}]_{\text{eq}} + C_0 \times e^{-k_{\text{cond}} \times t} \quad (4.11)$$

with the integration constant C₀.

The use of the boundary condition: [H₂O](t=0)=[H₂O]_{ss}, leads to the solution presented in Equations 4.12 or 4.13:

$$[\text{H}_2\text{O}](t) = [\text{H}_2\text{O}]_{\text{eq}} \times (1 - e^{-k_{\text{cond}} \times t}) + [\text{H}_2\text{O}]_{\text{ss}} \times e^{-k_{\text{cond}} \times t} \quad (4.12)$$

$$P_{\text{H}_2\text{O}}(t) = P_{\text{eq}} \times (1 - e^{-k_{\text{cond}} \times t}) + P_{\text{ss}} \times e^{-k_{\text{cond}} \times t} \quad (4.13)$$

where P_{H₂O}(t)=P_{ss} at t=0.

As an example Figure 4.8 shows a fit based on Equation 4.13 for the approach of P_{ss} to equilibrium P_{eq} when the system is set from *stirred flow* to *static* conditions in the presence of an ice film at T_{ice}=201 K. The fit was made using the PC based software Igor vs 5.0 from Wavemetric, Inc. It results in γ=0.17, which is reported in Figure 4.7(□).

As already discussed in Section 4.2.1 the gas phase investigation of the rate of condensation, k_{cond} or of the uptake coefficient, γ, using the quartz crystal microbalance as a substrate for ice film growth, is in good agreement with previously presented data displayed in Figure 4.7.

Finally, the next section will deal with the new technique based on the condensed phase investigation of the kinetics of condensation and evaporation of H₂O in the presence of an ice film.

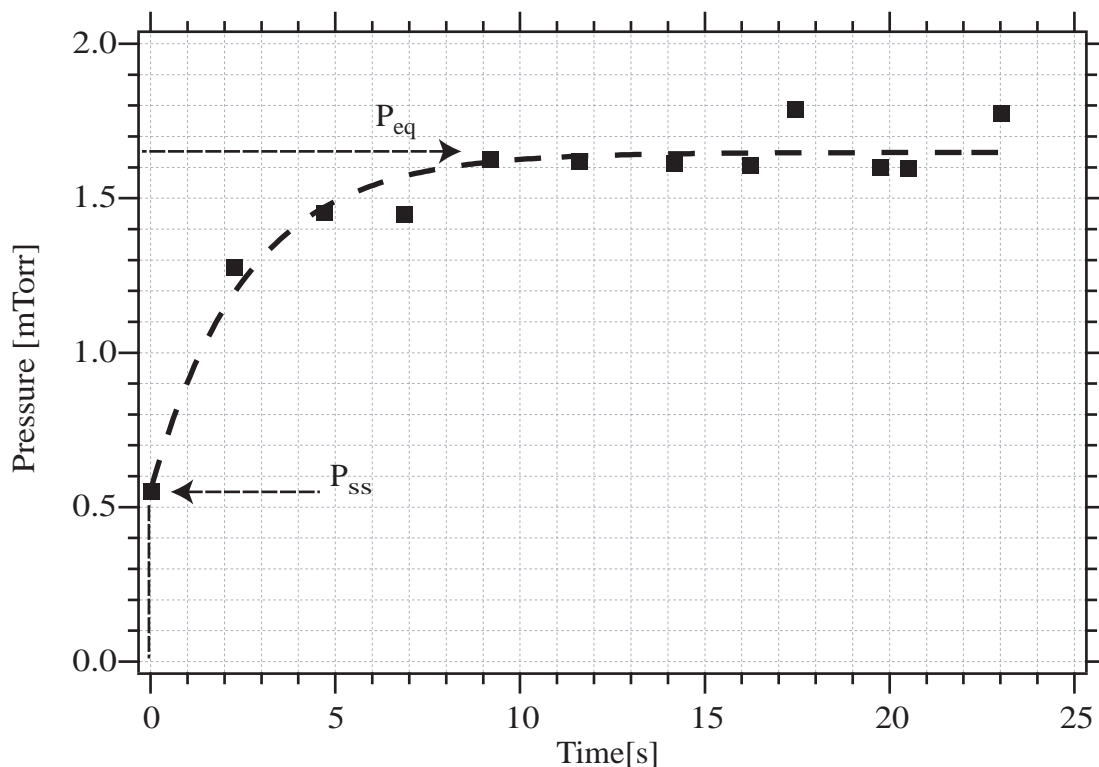


Figure 4.8: Pressure reading (■) using the Baratron pressure gauge and fit (dashed line) of the approach to equilibrium of the partial pressure of H_2O in the reactor when the system is set from *stirred flow* to *static* conditions in the presence of ice at 201 K and $t=0$. The fit is based on Equation 4.13 with variable k_{cond} and known values for P_{eq} and P_{ss} . The result obtains $k_{\text{cond}}=0.55 \text{ s}^{-1}$ or $\gamma=0.17$ at 201 K, which is reported in Figure 4.7.

4.2.3 Use of the QCM to measure the kinetics of evaporation and condensation of water over ice

We have introduced a new method for the measurement of J_{ev} and k_{cond} or γ of H_2O over ice by taking advantage of the condensed phase measurement capability of the QCM.

After the deposition of H_2O molecules on the piezoelectric crystal following the above mentioned experimental protocol by backfilling the reactor with H_2O vapor at 190 K under static conditions the QCM is set to the desired temperature for the study. Subsequently, the reactor is switched from static to dynamic (GV open, see Figure 4.1), that is molecular flow conditions

described in Section 2.3. Under this particular condition the realtime measurement of the mass change of H₂O on the QCM directly leads to the measurement of the evaporation flux J_{ev} of H₂O from ice using the calibration factor C_f established before and presented in Table 4.1. The high pumping rate does not allow the condensation of water onto the QCMB sensor owing to the low partial pressure P_{ss} of H₂O vapor under dynamic flow conditions.

If we use $R_{\text{QCM}}^{\text{Dyn}}$ as the initial rate of change of thickness of the ice film in \AA s^{-1} given by the derivative of the time dependent IC/5 raw output signal $S_{\text{QCM}}^{\text{Dyn}}$ in Volts under dynamic conditions we may evaluate J_{ev} in $\text{molec cm}^{-2} \text{s}^{-1}$ using the following relation:

$$J_{\text{ev}} = C_f \times 3.11 \cdot 10^{14} \times \frac{dS_{\text{QCM}}^{\text{Dyn}}}{dt} \times 100 = C_f \times 3.11 \cdot 10^{14} \times R_{\text{QCM}}^{\text{Dyn}} \quad (4.14)$$

where $3.11 \cdot 10^{14}$ in $[\text{molec cm}^{-2} \text{\AA}^{-1}]$ corresponds to the number of water molecules in a 1 cm^2 by 1\AA thick slab of ice of density 0.93 [15] and the factor of 100 to the conversion of the initial voltage of 10 V given by the output of the QCM corresponding to a 1000\AA thick ice film.

The most important advantage of this method is that it is totally independent of the gas phase and is only based on the condensed phase realtime measurement with a precision of better than $1.4 \cdot 10^{13} \text{ molec cm}^{-2} \text{s}^{-1}$ as explained in Section 4.1.2.

Figure 4.9 shows a typical realtime acquisition of the raw output signal of the IC/5 controller in Volts (black trace) and the temperature of the QCM or the ice film (gray trace). The film was grown at 190 K at approximately $1 \cdot 10^{17} \text{ molec cm}^{-2} \text{s}^{-1}$ and the temperature was subsequently lowered to 173 K. At $t=t_0$ the reactor is switched from *static* to *dynamic* condition by opening the gate valve whereupon the ice film started to evaporate at a rate R_{ev} [$\text{molec cm}^{-3} \text{s}^{-1}$] or flux J_{ev} [$\text{molec cm}^{-2} \text{s}^{-1}$] that is controlled only by the temperature of the ice film.

Indeed, in the case of the *dynamic* experimental condition the condensation rate of H₂O on the QCM is negligible due to the exceedingly low partial pressure of H₂O as pointed out above. Therefore, the net rate of evaporation $V_r \times \tilde{R}$ recorded by the IC/5, that is the difference between H₂O molecules evaporating and condensing in analogy with the remark made on page 80, is

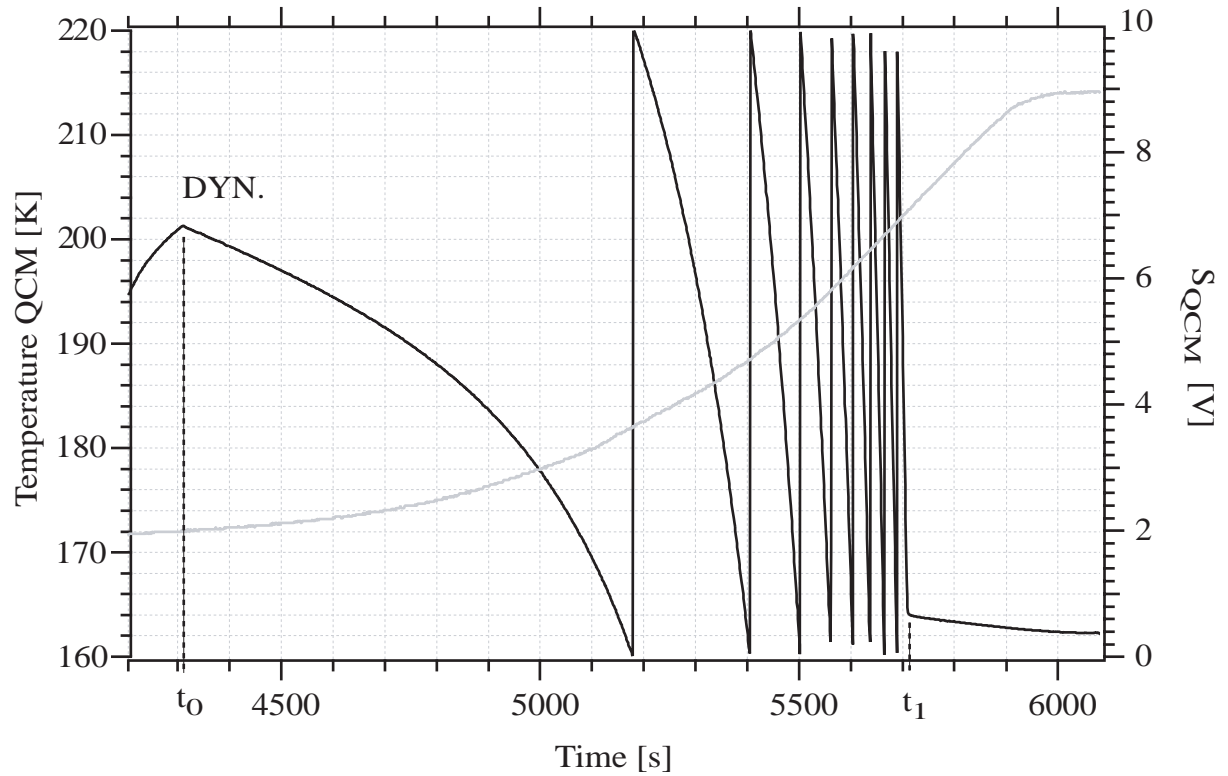


Figure 4.9: Realtime change of the raw QCM signal $S_{\text{QCM}}^{\text{DYN}}$ recorded at the output of the IC/5 controller (black) and temperature of the QCM (gray) under *dynamic* condition. At $t=t_0$ the system is set to *dynamic* (GV open), that is molecular flow, condition.

given in Equation 4.15:

$$V_r \times \tilde{R} = A_{\text{QCM}} \times \tilde{J}_{\text{ev}} = A_{\text{QCM}} \times J_{\text{ev}} - V_r \times [\text{H}_2\text{O}]_{\text{ss}} \times k_{\text{cond}} \quad (4.15)$$

and equals the absolute rate of evaporation $A_{\text{QCM}} \times J_{\text{ev}}$ of H_2O from the QCM because of the vanishing condensation term. Therefore, we find $J_{\text{ev}} = \tilde{J}_{\text{ev}}$ for the molecular flow regime.

Subsequently, the temperature of the ice film, T_{ice} , is increased and the QCM signal continuously recorded in order to be able to evaluate J_{ev} versus temperature. This is done by calculating $R_{\text{QCM}}^{\text{DYN}}$ which corresponds to the derivative of the signal $S_{\text{QCM}}^{\text{DYN}}$ presented in Figure 4.9 when the temperature is slowly increased. Subsequently J_{ev} is evaluated by inserting $R_{\text{QCM}}^{\text{DYN}}$ into Equa-

tion 4.14. The temperature-dependent values of J_{ev} lead to a value of the activation energy of evaporation of H₂O using the Arrhenius representation of J_{ev} versus $\frac{1000}{T}$ as described below.

The measurement of k_{cond} or γ of H₂O over ice is different because it has to be performed in the stirred flow regime where P_{ss} is significant in order to make the condensation reaction competitive with the rate of evaporation. It therefore requires the knowledge of the partial pressure P_{ss} or concentration of water vapor $[H_2O]_{ss}$ in the reactor in order to determine k_{cond} . The correction described in Section 2.4 must therefore be applied to P_{ss} . Indeed, in order to measure k_{cond} the system is set from dynamic to stirred flow conditions at the desired temperature. In this case the values of both R_{QCM}^{Dyn} and R_{QCM}^{S-Flow} , which is equal to the rate of change of the QCM signal under stirred flow conditions by analogy, are necessary in order to calculate k_{cond} or γ as $[H_2O]_{ss}$ in the reactor chamber under stirred flow condition is given by the steady-state Equation 4.6 given above.

For the sake of clarity, k_{cond} is calculated using the relation 4.16 derived in Appendix 4.4:

$$k_{cond} = \frac{C_f \times 3.11 \cdot 10^{14} \times A_{QCM}}{V_r \times [H_2O]_{ss}} \left[R_{QCM}^{Dyn} - R_{QCM}^{S-Flow} \right] \quad (4.16)$$

Two sets of experiments dealing with the measurement of J_{ev} are reported in Figure 4.6 represented by gray and black \otimes symbols. They correspond to ice films deposited at 190 K under static conditions using the directed injection device displayed in Figure 4.3. The film temperature is lowered to nearly 173 K before opening the 6" gate valve (GV) that sets the reactor to dynamic conditions. Subsequently, the temperature of the substrate is increased until complete evaporation of the ice film is achieved. One of the sets of raw data (gray \otimes symbol) is the one shown in Figure 4.9. The necessary corrections due to the change of temperature of the QCM crystal, namely the subtraction of the linear offset discussed in Section 4.1.2, have been applied to the raw data as well as the calibration factor of $C_f=7.8$ valid for the deposition of an ice film at 190 K.

Evidence of the increased precision of the measurements is clearly visible in Figure 4.6. We

note that both sets of data are in good agreement with those previously published for $T > 190$ K [17] and presented in Chapter 3 in the range where both sets overlap. In the temperature range of 193-223 K the evaluation of the Arrhenius expression of J_{ev} versus $\frac{1000}{T}$ based on the two sets of data is the following:

$$J_{\text{ev}} = (1.6 \pm 0.7) \cdot 10^{28} \times \exp\left(\frac{-10.2 \pm 0.5}{R} \times \frac{1000}{T}\right) \text{ molec cm}^{-2} \text{ s}^{-1} \quad 193 < T < 223 \text{ K} \quad (4.17)$$

which is in very good agreement with Expression 4.5 concerning both the preexponential factor and the activation energy for evaporation of $E_{\text{ev}} = 10.2 \pm 0.5$ kcal mol⁻¹ of water from ice.

At 193 ± 2 K a break is observed in the Arrhenius representation of J_{ev} . Such an observation has already been made by Chaix et al. [20, 21], but the temperature corresponding to the break was not defined as precisely as in this work. Schmitt [22] observes a continuous sintering process upon annealing of crushed single crystal ice to temperatures from 77 K up to 238 K, whereby the BET surface is greatly reduced. Such sintering processes upon annealing may well be responsible for a change in physico-chemical behavior of H₂O adsorption as observed in the present work.

Annealing experiments of ice films performed over the range 187 to 208 K dispelled the influence of structural changes of the ice film on the T-dependence of J_{ev} displayed in Figure 4.6. An ice film deposited at 208 K was cooled to 187 K, the starting point of an evaporation experiment to determine J_{ev} under dynamic conditions (symbol ∇ in Figure 4.6). The resulting absolute value of J_{ev} of the annealed film is less than a factor of two lower than J_{ev} of the original film deposited at 190 K (black and grey \otimes symbols in Figure 4.6) which is indistinguishable within random experimental error. For this series of experiments the appropriate calibration factor C_f of 1.9 (see Table 4.1) was used which is significantly different from the standard value of $C_f = 7.8$ valid for ice deposited at 190 K. In addition, J_{ev} of the annealed thin ice film increases with temperature. We take these two facts to mean that the standard deposition conditions of the pure ice film at 190 K leads to the formation of thermodynamically stable rather than

metastable ice films. However, in agreement with Schmitt [22], Murray and Plane [23] observed a decrease of the ratio (BET Surface Area/Geometric Surface Area) of thin vapour-deposited ice films with temperature thereby leading to a loss of between a factor of 2.5 and 3.0 in going from 190 to 208 K. We believe that the observed decrease of J_{ev} by less than a factor of two discussed above is not consistent with a T-dependent structural relaxation of the present ice film. Moreover, this discrepancy is expected to increase with temperature as the surface roughness should diminish with temperature. In agreement with the results of the present work both Davy and Branton [24] as well as Davy and Somorjai [25] concluded that a decrease in surface roughness, and thus in surface area, of ice crystals at $T > 188$ K was insufficient to explain the change of J_{ev} with temperature. Both groups [24, 25] reach the conclusion that J_{ev} does not scale 1:1 with the internal surface of rough ice surfaces in agreement with the present work as well as with others [26]. In summary, the T-dependence of both evaporation and annealing should be most revealing as they should counteract each other. This means that the activation energy of J_{ev} should be independent of the annealing history in case that the sample is thermodynamically stable. This has been checked in the present work for a few samples.

For temperatures below 193 K, $E_{ev} = 12.0 \pm 0.5$ kcal mol⁻¹ was obtained according to the following Arrhenius expression:

$$J_{ev} = (2.2 \pm 0.9) \cdot 10^{30} \times \exp\left(\frac{-12.0 \pm 0.5}{R} \times \frac{1000}{T}\right) \text{ molec cm}^{-2} \text{ s}^{-1} \quad 173 < T < 193 \text{ K} \quad (4.18)$$

which is significantly different from Expression 4.17.

One may notice that the change in the uncertainties of the preexponential factor of J_{ev} is now significantly lower than the order of magnitude uncertainty displayed in Expression 4.5. This fact, in addition to the good agreement between the gas phase probing in combination with the optical cryostat and results obtained from the measurement of the temporal change of the mass of the deposited ice film using the QCM, makes us confident that this device is adapted to the

study of the ice evaporation kinetics under atmospherically relevant conditions.

Figure 4.10 shows typical experimental data during the evaporation of a 1.4 μm thick ice film at 193 K after deposition at 190 K. Prior to $t=3150$ s the ice film thickness is constant because the system is under static conditions. As the system is set from static to dynamic conditions at $t=3150$ s the film maintained at the constant temperature of 193 K (± 1 K) evaporates at a constant rate of $3.6 \cdot 10^{16}$ molec cm^{-2} s^{-1} until $t=3260$ s. During this period the ratio $r_{j-m} = \frac{I_{\text{MS}}}{J_{\text{ev}}}$ between the measured MS signal at $m/z=18$ and J_{ev} is constant and equal to $(9 \pm 1) \cdot 10^{-27}$ A molec $^{-1}$ cm^2 s. As the thickness of the remaining film reaches the low value of 80 nm at $t=3260$ s, we observe the sudden appearance of a discrepancy between J_{ev} and the MS signal at $m/z=18$ that is proportional to $[\text{H}_2\text{O}]_{\text{ss}}$. This disagreement is revealed by the precipitous decrease of r_{j-m} showing that the measured MS signal is significantly higher than the one expected based on J_{ev} given by the QCM. In Figure 4.10, the symbol (\oplus) indicates the MS signal at $m/z=18$ calculated from J_{ev} using a constant value of r_{j-m} established for a thick ice film. The black vertical arrows illustrate the increasing discrepancy between the calculated and the measured MS signal at $m/z=18$. It is therefore clear that the rate of evaporation based on the time derivative of the QCM signal decreases too rapidly compared to the MS signal for ice film thicknesses smaller than 80 nm.

This kind of experiment has been repeated at different temperatures in the range 170-210 K and the same phenomenon was always observed for an ice film thickness lower than 80 ± 10 nm. We postulate a change in the mechanical properties of the ice film as it is thinning out owing perhaps to structural changes. This apparently leads to a change in the calibration factor which we have not studied in this work. An observation that makes us confident of this conclusion is the decrease of the MS signal that occurred at $t=3260$ s in Figure 4.10 which is evidence for a change in J_{ev} of H_2O from ice. We will explain this phenomenon in Section 4.6 by considering the state of the surface of the gold coating of the QCM sensing element. Whatever the reasons for the decreased rate of the QCM signal decline for small values of the ice film thickness, we consider that the realtime data acquired from the QCM measurements are trustworthy in the

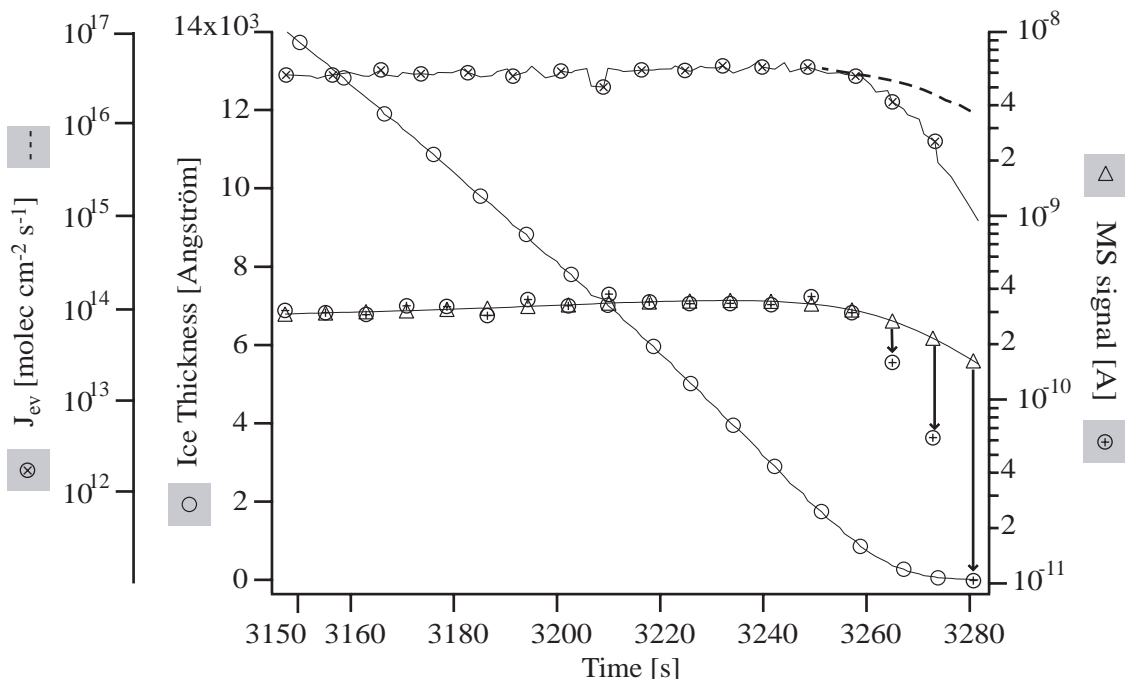


Figure 4.10: Temporal change of several experimental observables of importance during the evaporation of a 1.4 μm thick ice film deposited at 190 K and evaporated at 193 K. (\circ): absolute thickness of the ice film in \AA after calibration, (\otimes): absolute flux of evaporation J_{ev} of H₂O from the ice film based on the QCM signal, (Δ): measured MS signal at $m/z=18$, (\oplus): MS signal at $m/z=18$ calculated from J_{ev} , (dashed line): J_{ev} evaluated from measured MS at $m/z=18$. For the purpose of clarity the labels of the ordinate axes have been marked with the corresponding symbols describing the data and only a few data points at 1 Hz acquisition are reported. The lines are just guides to the eye.

range of a few microns down to 80 nm because of the close agreement between QCM- and MS-based data.

Table 4.2 summarizes some obtained experimental results on J_{ev} and k_{cond} and indicates d_{D} , the thickness below which a decrease in J_{ev} towards the end of ice film evaporation is observed using the QCM. For ice films doped with HCl, HBr and HNO₃, d_{D} corresponds to the ice thickness which is affected by the deposited trace gas as far as the departure of J_{ev} from that of pure ice is concerned.

When the thickness is larger than d_{D} in the case of doped ice films, we have observed that

$T_{\text{ice}}^{\text{evap}}$ [K]	$T_{\text{ice}}^{\text{dep}}$ [K]	d_D [Å]	J_{ev} [molec cm ⁻² s ⁻¹]	R_{ev} [molec cm ⁻³ s ⁻¹]	k_{cond} [s ⁻¹]	Type of experiment
190	180	830	$3.6 \cdot 10^{16}$	$7.6 \cdot 10^{12}$	1.15	Pure Ice
186			$1.3 \cdot 10^{16}$	$2.7 \cdot 10^{12}$	1.27	
198			$1.1 \cdot 10^{17}$	$3.3 \cdot 10^{13}$	0.84	
194			$5.3 \cdot 10^{16}$	$1.1 \cdot 10^{13}$	1.13	
202			$1.9 \cdot 10^{17}$	$4.1 \cdot 10^{13}$	0.77	
196	193	805	$8.7 \cdot 10^{16}$	$1.8 \cdot 10^{13}$	0.98	Pure Ice
192			$4.6 \cdot 10^{16}$	$9.8 \cdot 10^{12}$	1.13	
203	193	760	$2.0 \cdot 10^{17}$	$5.6 \cdot 10^{13}$	0.66	Pure Ice
211	190	730	$8.1 \cdot 10^{17}$	$1.7 \cdot 10^{14}$		
223	193		$1.0 \cdot 10^{18}$	$2.1 \cdot 10^{14}$	0.35	Pure Ice
205	190		$1.9 \cdot 10^{17}$	$3.9 \cdot 10^{13}$		Pure Ice
198	190	3290	$9.7 \cdot 10^{16}$	$2.0 \cdot 10^{13}$		HCl/Ice
197	190		$8.3 \cdot 10^{16}$	$1.7 \cdot 10^{13}$	1.00	HCl/Ice
197			$8.2 \cdot 10^{16}$	$1.7 \cdot 10^{13}$	1.00	
197			$7.0 \cdot 10^{16}$	$1.4 \cdot 10^{13}$	1.00	
188			$1.9 \cdot 10^{16}$	$3.9 \cdot 10^{12}$	1.35	
191			$3.5 \cdot 10^{16}$	$7.3 \cdot 10^{12}$	1.09	
186	190	2521	$1.3 \cdot 10^{16}$	$2.7 \cdot 10^{12}$		HCl/Ice
190	190		$1.9 \cdot 10^{16}$	$3.9 \cdot 10^{12}$		
194	190		$2.8 \cdot 10^{16}$	$5.8 \cdot 10^{12}$		
193	190	4421	$3.4 \cdot 10^{16}$	$7.1 \cdot 10^{12}$		HCl/Ice
193	190	4978	$1.2 \cdot 10^{17}$	$2.5 \cdot 10^{13}$		HCl/Ice
193	190		$5.7 \cdot 10^{16}$	$1.2 \cdot 10^{13}$		
195	190	3956	$4.3 \cdot 10^{16}$	$8.9 \cdot 10^{12}$		HCl/Ice
186	190	2106	$1.0 \cdot 10^{16}$	$2.0 \cdot 10^{12}$		HCl/Ice
204	190	3892	$2.0 \cdot 10^{17}$	$4.1 \cdot 10^{13}$		HCl/Ice
211	190	5091	$2.5 \cdot 10^{17}$	$5.2 \cdot 10^{13}$		HCl/Ice
181	190	3008	$4.8 \cdot 10^{15}$	$1.0 \cdot 10^{12}$		HBr/Ice

Table 4.2: Representative results for J_{ev} and k_{cond} for H₂O vapor in the presence of ice in the range 181-223 K. $T_{\text{ice}}^{\text{evap}}$ and $T_{\text{ice}}^{\text{dep}}$ correspond to the temperatures of deposition and evaporation of the ice films, respectively. d_D corresponds to the film thickness below which J_{ev} decreases compared to pure ice whose initial films thickness is approximately 1 μm .

$T_{\text{ice}}^{\text{evap}}$ [K]	$T_{\text{ice}}^{\text{dep}}$ [K]	d_D [Å]	J_{ev} [molec cm ⁻² s ⁻¹]	R_{ev} [molec cm ⁻³ s ⁻¹]	k_{cond} [s ⁻¹]	Type of experiment
192	190	853	$3.5 \cdot 10^{16}$	$7.3 \cdot 10^{12}$		Pure Ice
193			$4.0 \cdot 10^{16}$	$8.3 \cdot 10^{12}$		
195			$4.6 \cdot 10^{16}$	$9.5 \cdot 10^{12}$		
190	190	2049	$3.1 \cdot 10^{16}$	$6.4 \cdot 10^{12}$		HNO ₃ /Ice
189			$2.8 \cdot 10^{16}$	$5.8 \cdot 10^{12}$		
189			$2.0 \cdot 10^{16}$	$4.2 \cdot 10^{12}$		
192	190	4775	$1.8 \cdot 10^{16}$	$3.8 \cdot 10^{12}$		HNO ₃ /Ice
191			$1.7 \cdot 10^{16}$	$3.5 \cdot 10^{12}$		
191	190	970	$3.0 \cdot 10^{16}$	$6.2 \cdot 10^{12}$		HNO ₃ /Ice
190			$2.2 \cdot 10^{16}$	$4.6 \cdot 10^{12}$		
192	190	2162	$3.7 \cdot 10^{16}$	$7.7 \cdot 10^{12}$		HNO ₃ /Ice
193			$4.5 \cdot 10^{16}$	$9.4 \cdot 10^{12}$		
194	190	5123	$3.4 \cdot 10^{16}$	$7.1 \cdot 10^{12}$		HNO ₃ /Ice
193	190	1245	$2.3 \cdot 10^{16}$	$4.8 \cdot 10^{12}$		HNO ₃ /Ice
194			$3.1 \cdot 10^{16}$	$6.4 \cdot 10^{12}$		
193			$2.2 \cdot 10^{16}$	$4.6 \cdot 10^{12}$		
202	190	950	$1.1 \cdot 10^{17}$	$2.3 \cdot 10^{12}$		Pure Ice
207			$1.8 \cdot 10^{17}$	$3.8 \cdot 10^{12}$		
193	190	1854	$4.1 \cdot 10^{16}$	$8.7 \cdot 10^{12}$		HNO ₃ /Ice
195			$4.7 \cdot 10^{16}$	$1.0 \cdot 10^{13}$		
196			$5.3 \cdot 10^{16}$	$1.1 \cdot 10^{13}$		

Table 4.2: *Continued...*

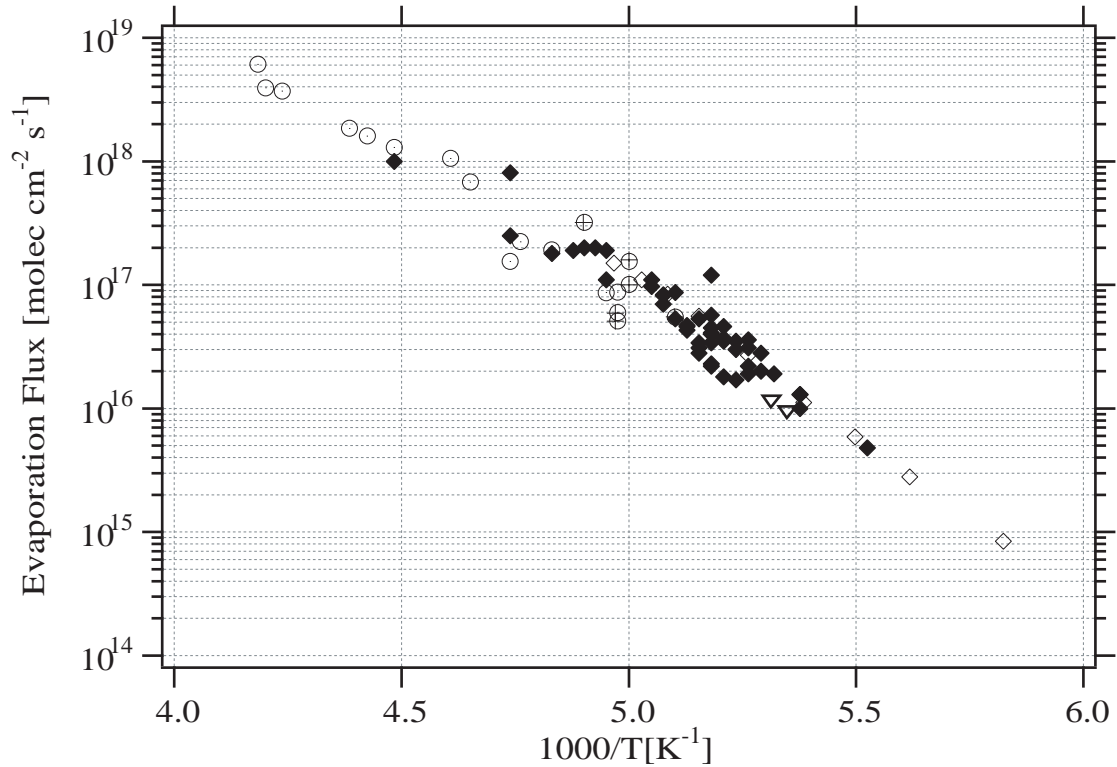


Figure 4.11: Experimental results on the evaporative flux J_{ev} ($\text{molec cm}^{-2} \text{s}^{-1}$) of H_2O from ice using either the cryostat or the QCM as substrate for deposition. (\odot): cryostat experiment results presented in Chapter 3. (\oplus): QCM experiments based on gas phase monitoring, presented in Section 4.2.1. (\diamond) and (\blacklozenge): QCM experiments based on the condensed phase investigation (results for pure and doped ice condensed at 190 K presented in Table 4.2), this section. (∇): QCM experiments based on the condensed phase investigation for ice condensed at 208 K, this section.

J_{ev} remains that of pure water ice, a fundamental point that will be developed in the following Chapters 5 and 6. The results on J_{ev} and k_{cond} are not all reported systematically in Figures 4.6 and 4.7 for the sake of clarity of presentation. Figure 4.11 presents selected data of Table 4.2 together with others to afford a synopsis of the results obtained using the QCM each for a separate ice sample. In particular, it shows that J_{ev} of the annealed sample is well within the scatter of the ice samples deposited under standard conditions as discussed above.

Experiments dedicated to the evaluation of k_{cond} for ice deposited under the typical conditions described before have been performed between 180 and 202 K. k_{cond} was calculated using

Equation 4.16 for different temperatures which leads to the γ values reported in Figure 4.7 (\otimes). The results are in good agreement with those available from gas phase experiments. Even if the evaluation of k_{cond} requires the measurement of $[\text{H}_2\text{O}]_{\text{ss}}$ in the reactor, it seems that the results based on QCM experiments present a lower degree of scatter than for the case of the pure gas phase investigation.

4.3 Discussion

Subsequent to many sets of experiments allowing the calibration and the validation of the new technique presented above, we have performed several types of experiments leading to the successful separation of the kinetic processes of condensation γ and evaporation J_{ev} of H₂O molecules from thermodynamically stable condensed I_h ice films in the range 173-223 K. Our results based on QCM experiments lead to thermochemical closure because the experimental values of J_{ev} and γ that have been determined independently of each other lead to the equilibrium vapor pressure of H₂O, P_{eq} , over the studied temperature range within experimental uncertainty.

The evaluation of P_{eq} or $[\text{H}_2\text{O}]_{\text{eq}}$ from the results presented here and based on Equilibrium 3.5 leads to the following governing equation

$$R_{\text{ev}} - k_{\text{cond}} \times [\text{H}_2\text{O}]_{\text{eq}} = 0 \quad (4.19)$$

which obtains values that are in good agreement with those from Marti and Mauersberger, 1993 [16]. The deviation between their values for P_{eq} and the ones determined from our experimental results is always smaller than 20 % in the range 182-202 K.

Figures 4.7 and 4.12 present the values for γ and J_{ev} resulting from our experiments and are displayed together with those available in the literature [18, 27, 28, 29, 30].

Regarding the temperature dependence of J_{ev} displayed in Figure 4.12 we notice that the data resulting from the QCM work based on the direct investigation of the condensed phase blend in nicely with our results for pure ice evaporation obtained from the monitoring of the gas phase

discussed in Chapter 3 as well as with data obtained from pulsed injection into a Knudsen flow reactor [18]. The combination of these three data sets using different experimental techniques allows us to obtain values of J_{ev} over the extended range 140-240 K with a particularly precise evaluation in the range 173-223 K investigated using the QCM and discussed in this section.

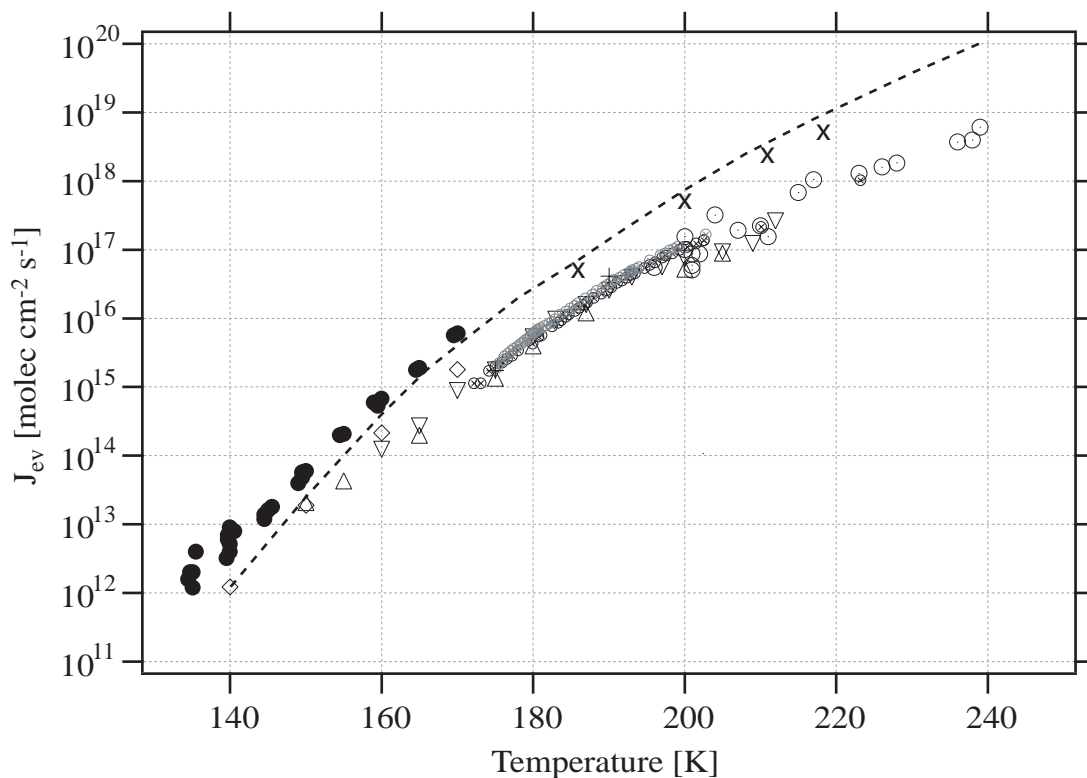


Figure 4.12: Synopsis of results on the flux of evaporation J_{ev} [$\text{molec cm}^{-2} \text{s}^{-1}$] from pure ice as a function of temperature (K). (\odot): cryostat experiment results from Delval et al., 2003 [17] presented in Chapter 3 of this work, (\otimes) (black and grey): QCM experiments based on the condensed phase monitoring of J_{ev} , this chapter, (dashed curve): theoretical maximum value of J_{ev} calculated from the vapor pressure of water above ice [16] and $\gamma=1$; results for bulk (Δ) and condensed (∇) ice from pulsed valve experiments in a Knudsen flow reactor [18] (Pratte and Rossi), (\diamond): Fraser et al. [27], (+): Smith et al. [28], (\bullet): Sack and Baragiola [29], (X): Davy and Somorjai [25].

Thanks to the increased precision afforded by the QCM measurements in the range 173-223 K we have been able to observe a change of slope in the Arrhenius representation of J_{ev} , visible in Figure 4.6, which leads to a change in the energy of activation for evaporation of H_2O and

thus to two different kinetic regimes. This has already been pointed in Chaix et al. [20, 21] using a different technique.

The two regimes are characterized by the following Arrhenius expressions:

$$223 > T > 193 \text{ K, } J_{\text{ev}} = (1.6 \pm 0.7) \cdot 10^{28} \times \exp\left(\frac{-10.2 \pm 0.5}{R} \times \frac{1000}{T}\right) \text{ molec cm}^{-2} \text{ s}^{-1}$$

and

$$173 < T < 193 \text{ K, } J_{\text{ev}} = (2.2 \pm 0.9) \cdot 10^{30} \times \exp\left(\frac{-12.0 \pm 0.5}{R} \times \frac{1000}{T}\right) \text{ molec cm}^{-2} \text{ s}^{-1}$$

with R in cal mol⁻¹ K⁻¹.

Thus the energy of activation for evaporation has two distinct values depending on the range of temperature, namely

$$E_{\text{ev}} = +10.2 \pm 0.5 \text{ kcal mol}^{-1} \text{ for } 223 > T > 193 \text{ K}$$

and

$$E_{\text{ev}} = +12.0 \pm 0.5 \text{ kcal mol}^{-1} \text{ for } 173 \text{ K} < T < 193 \text{ K}.$$

The value from this work for the low temperature regime is in good agreement with 11.5 kcal mol⁻¹ published by Fraser and coworkers [27]. In contrast to their conclusion, we claim that the evaluation of E_{ev} is in general not sufficient to determine the enthalpy of sublimation of H₂O corresponding to the binding energy of H₂O on ice depending on the range of temperature concerned because the assumption of zero activation energy for the reverse process of condensation may not always be valid. An example of this case is the situation for T > 193 K.

The experimental results from this work obtain a negative activation energy of condensation E_{cond} for H₂O on ice of -1.5 ± 0.5 kcal mol⁻¹ for T > 193 K in agreement with results presented in Chapter 3. It corresponds to a complex process with at least one precursor for condensation [31, 32]. Such a mechanism had already been proposed by George et al. [32] before their results using optical interference measurements led them to set γ equal to unity [19], which is reported in Figure 4.7. E_{cond} is -0.3 ± 0.1 kcal mol⁻¹ for T < 193 K indicating a change in the reaction

mechanism for condensation of H₂O. These results follow from data reported in Figure 4.13 which presents an Arrhenius plot of k_{cond} and lead to the conclusion that both rate processes must always be separately measured except in cases where one of the rates has a confirmed zero activation energy. The Arrhenius expressions of k_{cond} for $T > 193$ K and $T < 193$ K are:

$$182 < T < 193 \text{ K, } k_{\text{cond}} = (56 \pm 1) \cdot 10^{-2} \times \exp\left(\frac{0.3 \pm 0.1}{R} \times \frac{1000}{T}\right) \text{ s}^{-1}$$

and

$$223 > T > 193 \text{ K, } k_{\text{cond}} = (2 \pm 1) \cdot 10^{-2} \times \exp\left(\frac{1.5 \pm 0.5}{R} \times \frac{1000}{T}\right) \text{ s}^{-1}$$

For $T < 193$ K it is important to notice that the value of E_{cond} remains unchanged whether or not the data of [18] are considered. The measured values for k_{cond} together with J_{ev} afford thermochemical closure of the kinetics resulting in the following heats of sublimation for H₂O ΔH_{subl}^0 for $T < 193$ K and $T > 193$ K:

$$182 < T < 193 \text{ K, } \Delta H_{\text{subl}}^0 = 12.3 \pm 0.5 \text{ kcal mol}^{-1}$$

and

$$223 > T > 193 \text{ K, } \Delta H_{\text{subl}}^0 = 11.7 \pm 0.6 \text{ kcal mol}^{-1}$$

Both values are in good agreement with previously published values [17, 33, 34]. Across the temperature range of our experiments we note that J_{ev} is always lower than the theoretical maximum of J_{ev} , represented by the dashed line in Figure 4.12 which has been obtained by using P_{eq} of Marti and Mauersberger [16] with γ set to unity. The discrepancy between the maximum theoretically allowed and experimental values of J_{ev} increases with temperature indicating the continuous decrease of γ . For temperatures below 170 K the theoretical maximum of J_{ev} has been extrapolated to lower temperatures by using P_{eq} beyond the range of validity stated by Marti and Mauersberger [16]. This leads to maximum values of J_{ev} that are lower than J_{ev} published by Sack and Baragiola [29]. However, the lack of explanation in their paper concerning the evaluation of the absolute evaporation flux of H₂O using a QCM does not allow us to evaluate

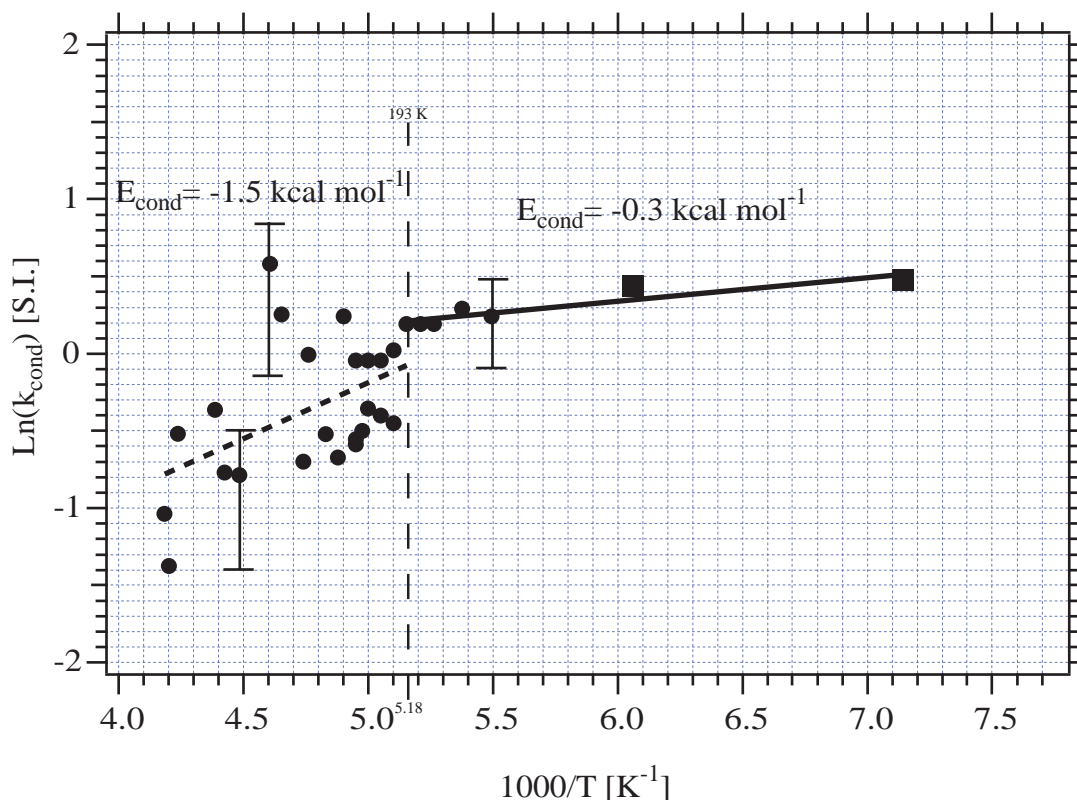


Figure 4.13: Arrhenius representation of k_{cond} showing a change of slope, and thus a change in the energy of activation for condensation of H₂O on ice at T=193 K. (●): QCM and cryostat experiments confounded together. (■): realtime kinetic experiments in a Knudsen flow reactor using pulsed valve admission of H₂O [18] with an experimental uncertainty comparable to the size of the symbol.

their work in a meaningful way. In contrast, in this work we propose a well defined calibration protocol with several validation sequences allowing the absolute measurement of J_{ev} using the QCM as presented above.

The data for J_{ev} of Fraser et al. [27] and of Smith et al. [28] are comparable to ours, albeit slightly larger than the present data of J_{ev} of H₂O from crystalline ice. The results for J_{ev} of Davy and Somorjai [25], however, are almost a factor of ten larger compared to ours at the high temperature end of T=220 K for reasons unknown to us. However, they were the first to apply a precursor model to the H₂O/Ice condensation/evaporation kinetics and thereby provided

leadership to others [31, 32].

The change of slope in the Arrhenius expression of J_{ev} mentioned above is experimentally confirmed by the results on the independently determined γ presented in Figure 4.7 or k_{cond} in Figure 4.13. For temperatures between 182 and 193 K the activation energy of k_{cond} is $E_{cond} = -0.3 \pm 0.1$ kcal mol⁻¹ which is preserved if we add the results of Pratte and Rossi [18] down to $T = 140$ K despite widely differing uncertainty limits as displayed in Figure 4.13. In addition, we note from the present study that k_{cond} decreases between 193 and 202 K. The agreement between the experimental results of Pratte and Rossi and the ones presented here that are based on very different techniques, makes us confident that γ is indeed far from unity over the whole temperature range of 140-240 K in contrast to the assumption that $\gamma = 1.0$ that is sometimes used [19]. Moreover, the combined results indicate a complex, that is non-elementary reaction mechanism for the H₂O/ Ice interaction as exemplified by the negative temperature dependence of γ in the studied range 182-202 K [31].

There is a whole literature treating the crystal growth of various morphological forms of ice from a macroscopic point of view [35, 36]. However, it is difficult to compare the results from a typical growth study to the fundamental chemical kinetics such as pursued in this work. For instance, the empirical condensation coefficient used by Libbrecht [35] is a function of the degree of supersaturation and may not be directly linked to the one resulting from the separation of the condensation from the evaporation rate processes that is independent of $[H_2O]$ or P_{eq} . However, an interesting emerging concept that should be explored further is the proposed crystallographic face-dependent attachment kinetics [36]. In contrast, the present work addresses the kinetics of H₂O interaction involving a properly averaged distribution of crystallographic faces.

The most important result from the present work concerning γ is that it is always smaller than 1 over the whole range of 140-240 K. This is important in the case of atmospheric sciences as far as the evaporative lifetime of ice particles is concerned. Indeed, it implies that J_{ev} is lower than the theoretical maximum. At temperatures in excess of 200 K the evaporative lifetime of pure ice is longer by at least a factor of six, independent of relative humidity, compared to

the theoretical maximum as it may be seen in Figure 4.12. This will have ramifications as to the dynamics of the global cloud cover and its repercussions on the cloud radiative forcing that controls global climate.

4.4 Appendix : Kinetics of condensation of H₂O on pure ice from QCM measurements

This appendix explains how k_{cond} or γ which corresponds to $\frac{k_{\text{cond}}}{\omega}$ may be evaluated from QCM signals S_{QCM} .

The relevant kinetic processes in the H₂O/ ice interaction are schematically represented in Figure 4.1.

Considering the evaporation flux J_{ev} of H₂O from ice we have seen in Section 4.2.3 that J_{ev} directly follows from the QCM signal obtained under molecular flow conditions following Expression 4.14:

$$J_{\text{ev}} = C_f \times 3.11 \cdot 10^{14} \times \frac{dS_{\text{QCM}}^{\text{Dyn}}}{dt} \times 100 = C_f \times 3.11 \cdot 10^{14} \times R_{\text{QCM}}^{\text{Dyn}} \quad (\text{Equation 4.14, page 128})$$

where $S_{\text{QCM}}^{\text{Dyn}}$ is the initial QCM signal in Volts under *dynamic* conditions.

Under stirred flow conditions the H₂O partial pressure in the reactor chamber follows the steady state equation given in Equation 4.6:

$$R_{\text{ev}} - [\text{H}_2\text{O}]_{\text{ss}} \times (k_{\text{cond}} + k_{\text{esc}}) = 0 \quad (\text{Equation 4.6, page 125})$$

As indicated in Expression 4.15, on page 129, the net rate of evaporation $A_{\text{QCM}} \times \tilde{J}_{\text{ev}} = V_r \times \tilde{R}_{\text{ev}}$ is given by:

$$A_{\text{QCM}} \times \tilde{J}_{\text{ev}} = A_{\text{QCM}} \times J_{\text{ev}} - V_r \times [\text{H}_2\text{O}]_{\text{ss}} \times k_{\text{cond}} \quad (\text{Equation 4.15, page 129})$$

and is also proportional to the temporal derivative of the resulting signal of the QCM, $S_{\text{QCM}}^{\text{S-Flow}}$.

Therefore, under stirred flow conditions, we have the following equality:

$$C_f \times 3.11 \cdot 10^{14} \times R_{\text{QCM}}^{\text{S-Flow}} \times A_{\text{QCM}} = A_{\text{QCM}} \times J_{\text{ev}} - V_r \times [\text{H}_2\text{O}]_{\text{ss}} \times k_{\text{cond}} \quad (4.20)$$

The left part of Equation 4.20 represents the measured net rate of evaporation of H_2O by monitoring the condensed phase. Using Expression 4.14 for J_{ev} one obtains

$$C_f \times 3.11 \cdot 10^{14} \times R_{\text{QCM}}^{\text{S-Flow}} \times A_{\text{QCM}} = A_{\text{QCM}} \times C_f \times 3.11 \cdot 10^{14} \times R_{\text{QCM}}^{\text{Dyn}} - V_r \times [\text{H}_2\text{O}]_{\text{ss}} \times k_{\text{cond}}$$

where $R_{\text{QCM}}^{\text{S-Flow}}$ is the initial rate of change of the thickness of the ice film deposited on the QCM in \AA s^{-1} under stirred flow conditions that is proportional to the (first) time derivative of the QCM raw signal $S_{\text{QCM}}^{\text{S-Flow}}$. Collection of terms yields the final Expression 4.16 for k_{cond} :

$$k_{\text{cond}} = \frac{C_f \times 3.11 \cdot 10^{14} \times A_{\text{QCM}}}{V_r \times [\text{H}_2\text{O}]_{\text{ss}}} \left[R_{\text{QCM}}^{\text{Dyn}} - R_{\text{QCM}}^{\text{S-Flow}} \right]$$

which is Equation 4.16 given on page 130.

4.5 Appendix : QCM temperature control device

The temperature of the quartz crystal microbalance sensor is controlled in the range 100-250 K using a homemade regulation device. Figures 4.14 and 4.15 present images and a schematic drawing of the whole temperature control device. First, initially dried air at 4 % rh under a pressure of 4 bars is injected into a closed stainless steel tank containing liquid nitrogen. All the walls of the tank, comprising the top cover, are pumped to a primary vacuum at a pressure of approximately $1 \cdot 10^{-3}$ Torr in order to prevent thermal exchange between the liquid nitrogen and the ambient air through the stainless steel walls. The dry air is injected into the liquid nitrogen (LN_2 in Figure 4.15) generating an overpressure in the zone labelled N_2 in Figure 4.15.

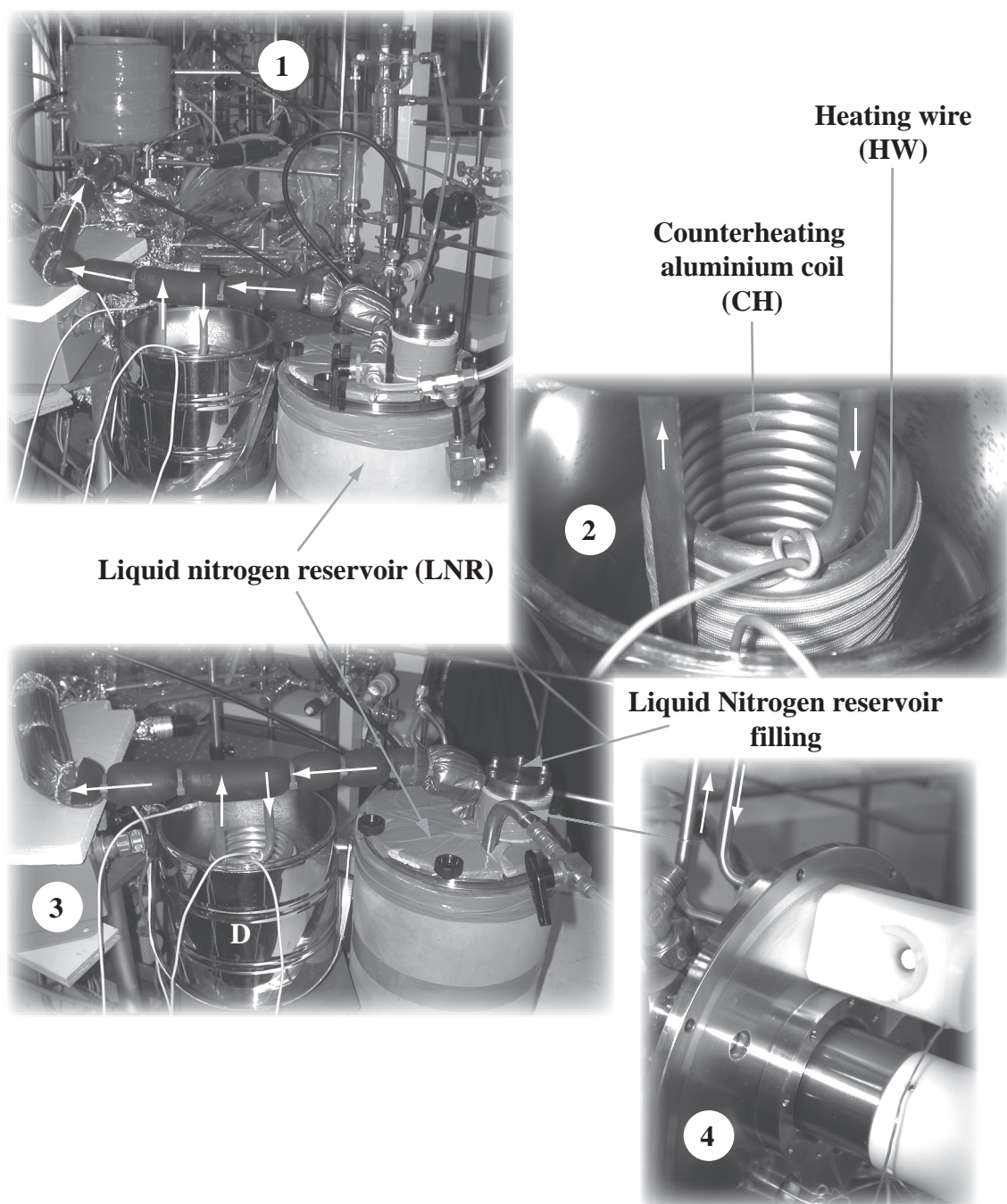


Figure 4.14: **1:** global view of the cooling device. **2:** detail of the counterheating part consisting of an aluminium coil (CH) and a heating wire (HW). The whole part is insulated from ambient air in a closed Dewar vessel marked **D** in panel **3**. **4:** detail of the flange supporting the QCM. The two visible 6 mm stainless steel tubes used as inlet and outlet for thermally controlled gaseous nitrogen are welded onto two 1/8" stainless steel tubes that are connected to the QCM support that contains the crystal holder. In all the panels the white arrows indicate the air or nitrogen flow.

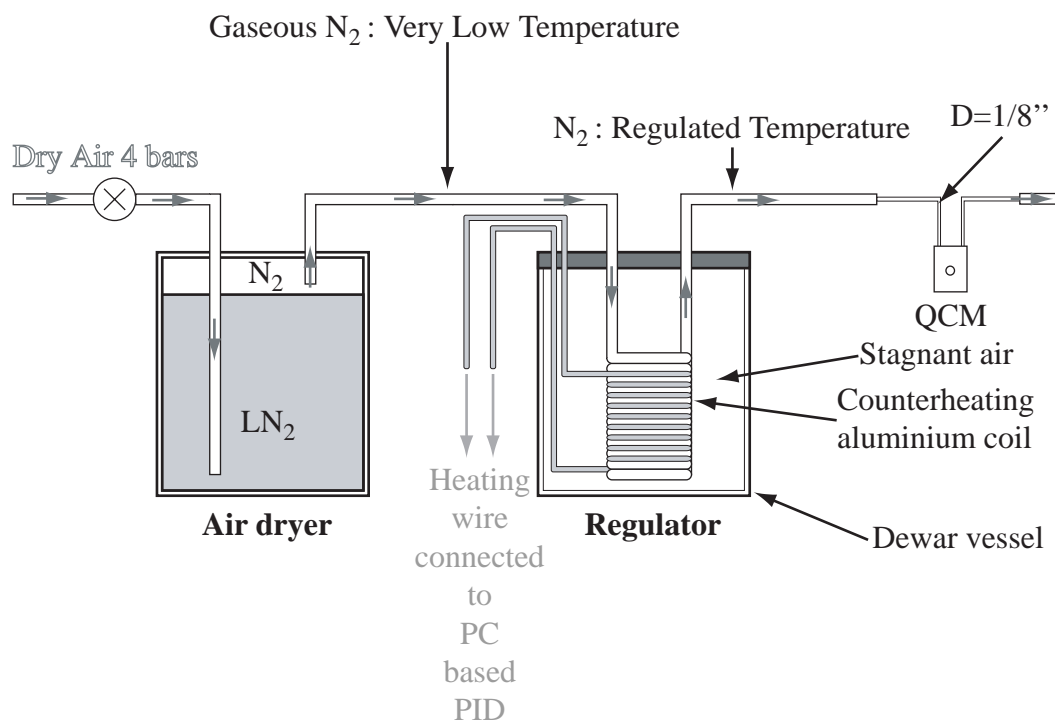


Figure 4.15: Schematic drawing of the temperature controlling device. The grey arrows indicate the direction of the dry air and the subsequent cold gaseous nitrogen. LN_2 indicates liquid nitrogen and N_2 cold gaseous nitrogen. After temperature regulation the nitrogen passes the 1/8" diameter tubes of the QCM. The heating wire is controlled using a PC based PID afforded by the Software Labview 7.0 of National Instruments, Inc.

The gas above the liquid phase of nitrogen mainly consists of gaseous nitrogen N_2 and oxygen as water vapor will condense and remain in the liquid N_2 . Indeed, we have chosen to develop this homemade regulation device in order to prevent water from condensing in the very sharp 1/8" diameter tube chosen by the QCM manufacturer (Inficon, Inc.) for the control of the QCM temperature. As the QCM support containing the crystal holder was not really designed for temperatures as low as 190 K the condensation of water in the cooling tubes occurs quite quickly even when initially dried air is used. The overpressure within the air dryer in Figure 4.15 sustains a very cold N_2 flow which is water free and that originates from the cryogenic "air dryer" through the regulation device itself and across the QCM cooling tubes. The counterheating

part of the device consists of an aluminium coil which is insulated from the ambient air in a closed Dewar vessel displayed in Figure 4.15. Here, the cold gaseous nitrogen is heated in order to reach the desired temperature owing to a heating wire that surrounds the coil in a mechanically close contact. The heating wire dissipative energy is controlled using a PC based PID controller library that is available for the software Labview 7.0 from National Instruments, Inc. In order to increase the stability the temperature the PID controls the percentage of a 10 s time period during which the heating wire is submitted to the constant voltage of 100 V. This also prevents the occurrence of a significant current peak that causes electromagnetic noise that strongly perturbs the apparatus. It is clear that owing to the thermal exchange between the cold Nitrogen and the ambient air across the pipes separating the regulation unit and the QCM tubes the nitrogen must be regulated at a lower temperature than the desired one. In order to get rid of this constraint the feedback temperature used to control the time aperture of the PID controller is measured at the piezoelectric crystal holder and used after amplification of the type T thermocouple voltage. Owing to the properties of the amplifier/noise reducer described in Section 2.8.1 the temperature of the sensor may be controlled in the range 100-250 K with a precision of 0.1 K.

4.6 Appendix : Surface roughness of the gold coating of the QCM sensing element and its probable impact on J_{ev} for pure ice films

This section tries to give a first answer to the question posed when considering Figure 4.10: why does J_{ev} of H₂O decrease when the remaining ice film reaches a mass equivalent to a 80 ± 7 nm thick homogeneous ice film?

First, we attributed this decrease of J_{ev} that we observed by monitoring the QCM signal to a change in the morphological properties of the remaining ice film due to its changing thickness to low values [12].

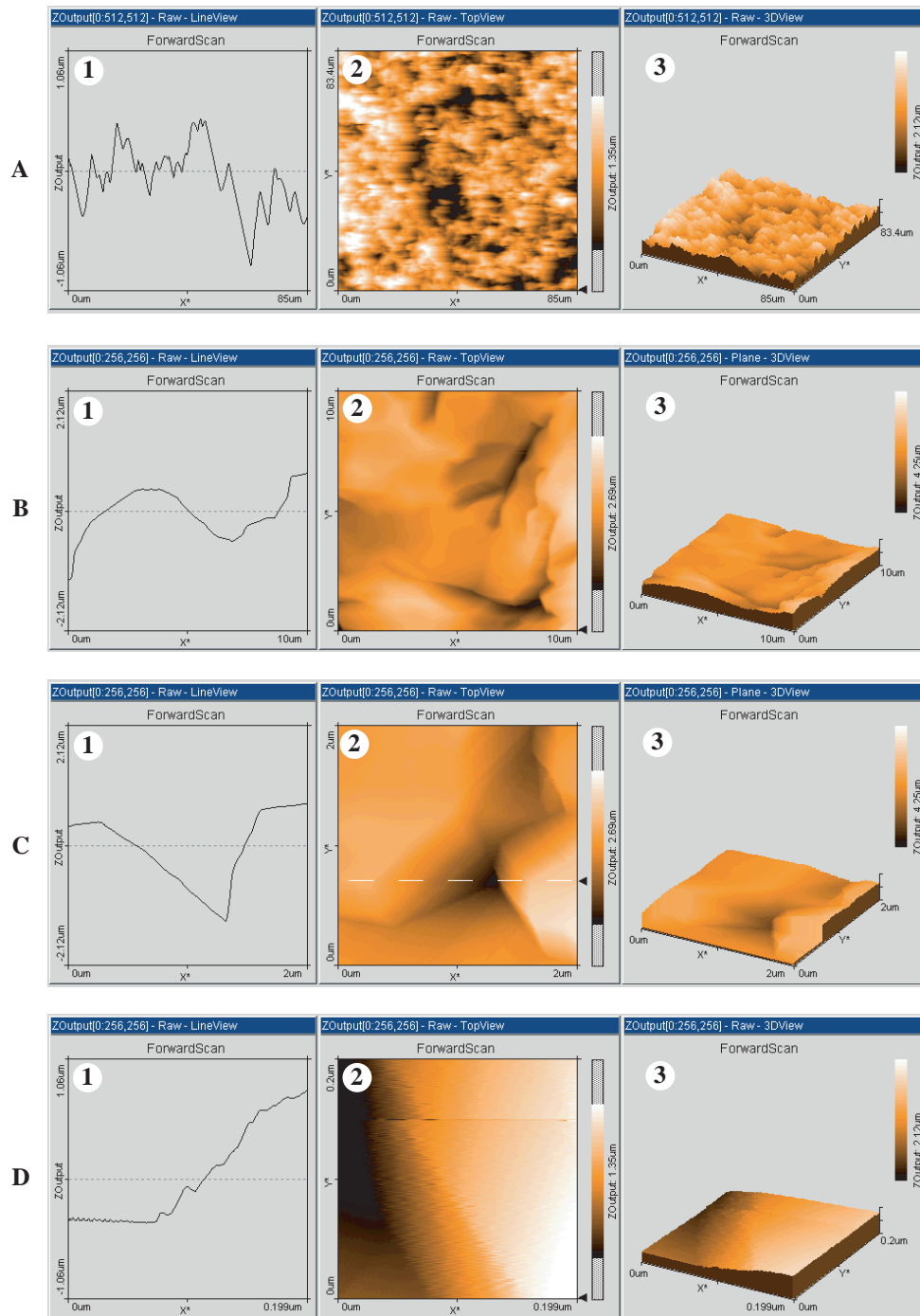


Figure 4.16: Investigation of the morphology of the gold coating of the piezoelectric crystal using Atomic Force Microscopy. All measurements are performed using the contact mode of the AFM at different spatial resolution. **Set A**: resolution of $85 \times 85 \mu\text{m}$, **Set B**: $10 \times 10 \mu\text{m}$, **Set C**: $2 \times 2 \mu\text{m}$, **Set D**: $0.2 \times 0.2 \mu\text{m}$. Panels **A1** to **D1** represent the cross-section of the respective scanned area at the position indicated by the small black arrow in Panels labelled **2**. Panels labelled **2** and **3** present the top view and the 3D view of each scanned areas, respectively.

This may have resulted in a change of the calibration factor, C_f , of the quartz crystal microbalance sensor for pure ice. However, the fact that the MS signal at $m/z=18$ also decreases to a different extent at the same time has led us to conclude that the morphological properties of the ice film may not be held solely responsible for the change of the true rate of evaporation as measured using mass spectrometry at $m/z=18$. Subsequently, we have decided to investigate the morphological properties of the gold coating of the piezoelectric quartz sensor of the QCM inspired by the fact that often the morphology of the substrate is recognized to have an influence on the structure of adsorbed ice [9]. We are not so much interested in the structure of the ice film but rather on the surface roughness of the gold coating of the quartz crystal that may be responsible for the change of J_{ev} .

We have performed experiments using an Atomic Force Microscope (AFM) in order to obtain information on the morphology of the gold coating. Figure 4.16 presents an overview of different measurements of the geometric surface properties for four resolutions of the AFM ranging from 200×200 nm to 85×85 μ m.

The cross-sections in Panels **A1** to **D1** correspond to a horizontal scan along the line that is indicated by a small cursor arrow in Panels **A2** to **D2**. They all seem to indicate the existence of deep pits of depths larger than 1μ m and of approximately 500 nm width that are statistically well distributed among all scanned samples as displayed in Panel **A2**. Figure 4.17 presents a 3D view corresponding to **set C** of Figure 4.16, namely the sampling of a $2 \times 2 \mu$ m area of the gold coating of the quartz sensing element. The sharp hole indicated by the black area in Panel **C2** of Figure 4.16 is clearly visible as the black region in Figure 4.17.

Using the data given by the AFM acquisition software, which consist of a 256×256 to 512×512 point matrix, we have calculated the change of the total volume represented by these pits when the height, H , from the bottom of the holes, Z_0 , is increased from 0 to 1μ m in increments of 50 nm. The results for data **set A**, **B** and **C** are presented in Figure 4.18 by symbols \blacksquare , \blacktriangle and \blacklozenge , respectively. The data are presented in terms of an equivalent volume V_v on a 0.5 cm^2 surface area as a function of the height H defined above. Most of the time H corresponds to the

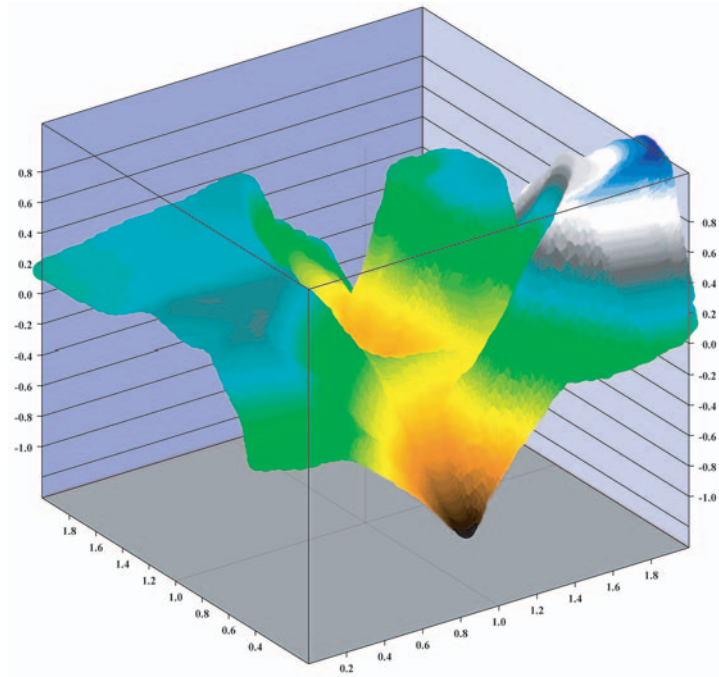


Figure 4.17: 3D view corresponding to set **C** of Figure 4.16. Distances are given in μm . A pit deeper than $1 \mu\text{m}$ is indicated by the black area.

height above the geometrically flat quartz crystal as for instance defined in Panel **D**. Panel **D1** is interpreted in the sense that the flat bottomed area in Panel **D1** corresponds to the atomically smooth SiO_2 surface at the bottom of a pit.

First, the change of the pit volume, V_v , with increasing height, H , above the bottom, Z_0 , of each pit was calculated for the scanned sample surface area. We then assumed a statistical distribution of these pits throughout the whole surface area of the gold coating extending over 0.5 cm^2 which led to the surface weighted volume V_v . A volume of $4 \cdot 10^{-6} \text{ cm}^3$ corresponds to the measured thickness of 80 nm of a homogeneous ice film spread out over the 0.5 cm^2 surface area of the QCM sensor and is plotted as the dashed horizontal line in Figure 4.18. At this thickness of 80 nm J_{ev} starts to decrease as observed both by MS and QCM measurements. As the change of the pit volume V_v with H obtains well correlated results for the three considered resolutions as displayed in Figure 4.18 we may estimate that in our simple model the pits of

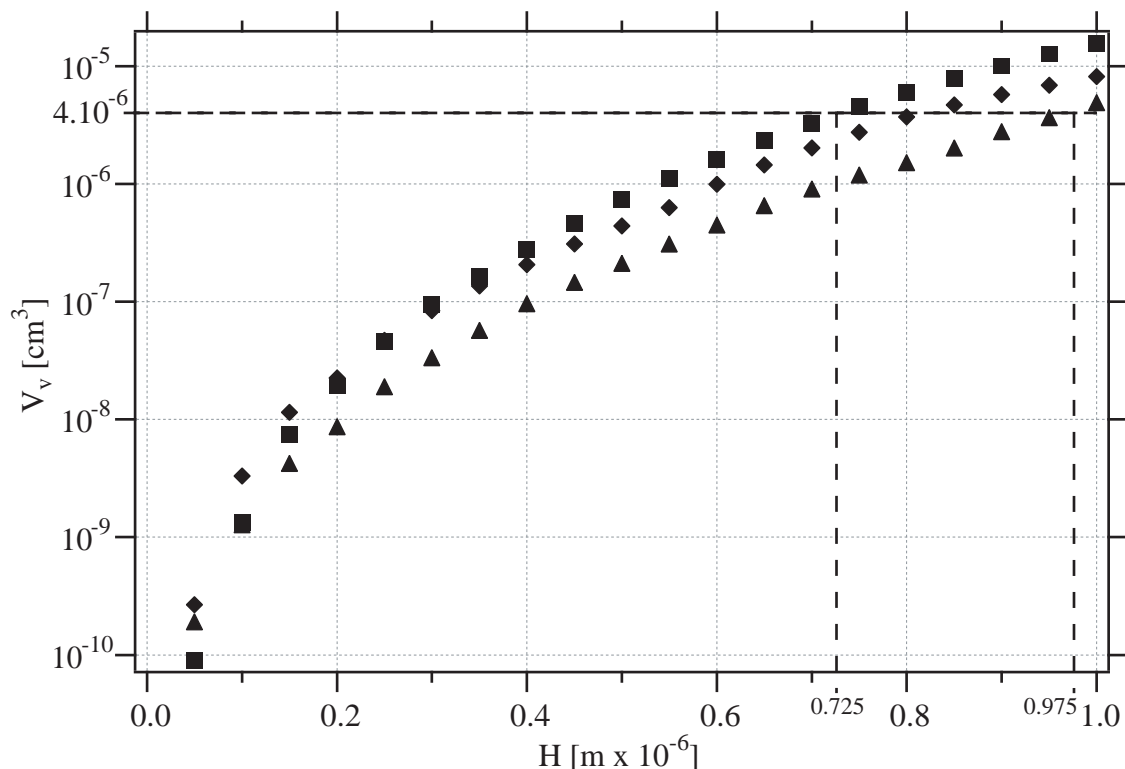


Figure 4.18: Change of the equivalent pit volume V_v over a 0.5 cm^2 surface area in terms of the calculated total volume of the pits as a function of height H for each scanned surface area of data set **A**, **B** and **C**. The results for data set **A**, **B** and **C** are represented by symbols \blacksquare , \blacktriangle and \blacklozenge , respectively. The calculated value of $4 \cdot 10^{-6} \text{ cm}^3$ indicated by the horizontal dashed line corresponds to the volume represented by a homogeneous coating of 80 nm of ice spread out over 0.5 cm^2 of the quartz substrate. It corresponds to the equivalent volume of pits that are between 0.725 to $0.975 \text{ }\mu\text{m}$ deep.

depth in the range between 0.725 and $0.975 \text{ }\mu\text{m}$ each result in an effective volume of $4 \cdot 10^{-6} \text{ cm}^3$. As a corollary the morphology of the Au-coating of the quartz sensing element is such that the existing pits are roughly ten times as deep as the thickness of the homogeneous ice films of 80 nm under the constraint of equal volume.

Figure 4.19 presents a cross-section of the sample area presented in Panel **C2** of Figure 4.16. This scan corresponds to a line from the upper-left to the lower-right diagonal of the image presented as Panel **C2**. We chose this representation because it presents a very deep pit which

is representative of all the pits that may be observed on the gold surface supported by the quartz crystal.

Inspired by the well documented capillarity phenomenon [37, 38] we have tried to determine how the presence of these pits may affect the evaporative flux J_{ev} of H_2O from ice occupying the pits on the gold coating.

In Figure 4.19 we consider the pit defined by points A, Z_0 and A'. The white dashed line labelled (N) bisects the angle $\widehat{AZ_0A'}$. Points C and D are chosen in a way that $\widehat{A'C}(N)$ and $\widehat{AD}(N)$ correspond to 30° . It is well known that molecules that are desorbing from a surface present a desorption flux that obeys the cosine law, $\cos(\theta)$ [37, 39, 40] under equilibrium conditions. Some cases are known where the molecular desorption follows a $\cos^n(\theta)$ law, $n > 1$ [39, 41]. By choosing the cosine law and the given 30° angles from (N) we determine the position of C and D for which statistically only 85 % of the desorbing molecules reach the exit that is virtually represented by the segment [AA'] without colliding with the walls of the pit represented by (AZ₀A'). It follows that all H_2O molecules filling the pit volume up to level given by D have a residence time inside the pit that may not be negligible due to the cold gold surface. This may be a possible reason for the decrease of J_{ev} of H_2O observed using the MS at $m/z=18$. If we compare the height defined by the bottom of the pits, Z_0 and D, for which 15 % the molecules have a slower desorption rate, namely $Z_D=0.9 \mu\text{m}$ with the calculated value of H for V_v corresponding to 80 nm thick homogeneous ice film presented in Figure 4.18 (0.725 to 0.975 μm) we find that they agree quite well, namely 900 nm versus 725 to 975 nm.

Even if this consideration only consists of a rough approximation we claim that the high surface roughness of the gold coating of the QCM is most probably responsible for the decrease of J_{ev} of H_2O observed from the gas phase using MS at $m/z=18$. From the condensed phase point of view it is probable that the calibration factor C_f may also change due to the fact that the ice film is no longer continuous when the bottom of the pits are filled with H_2O towards the end of ice evaporation. This may surely change the mechanical properties of the remaining ice film in that it becomes discontinuous.

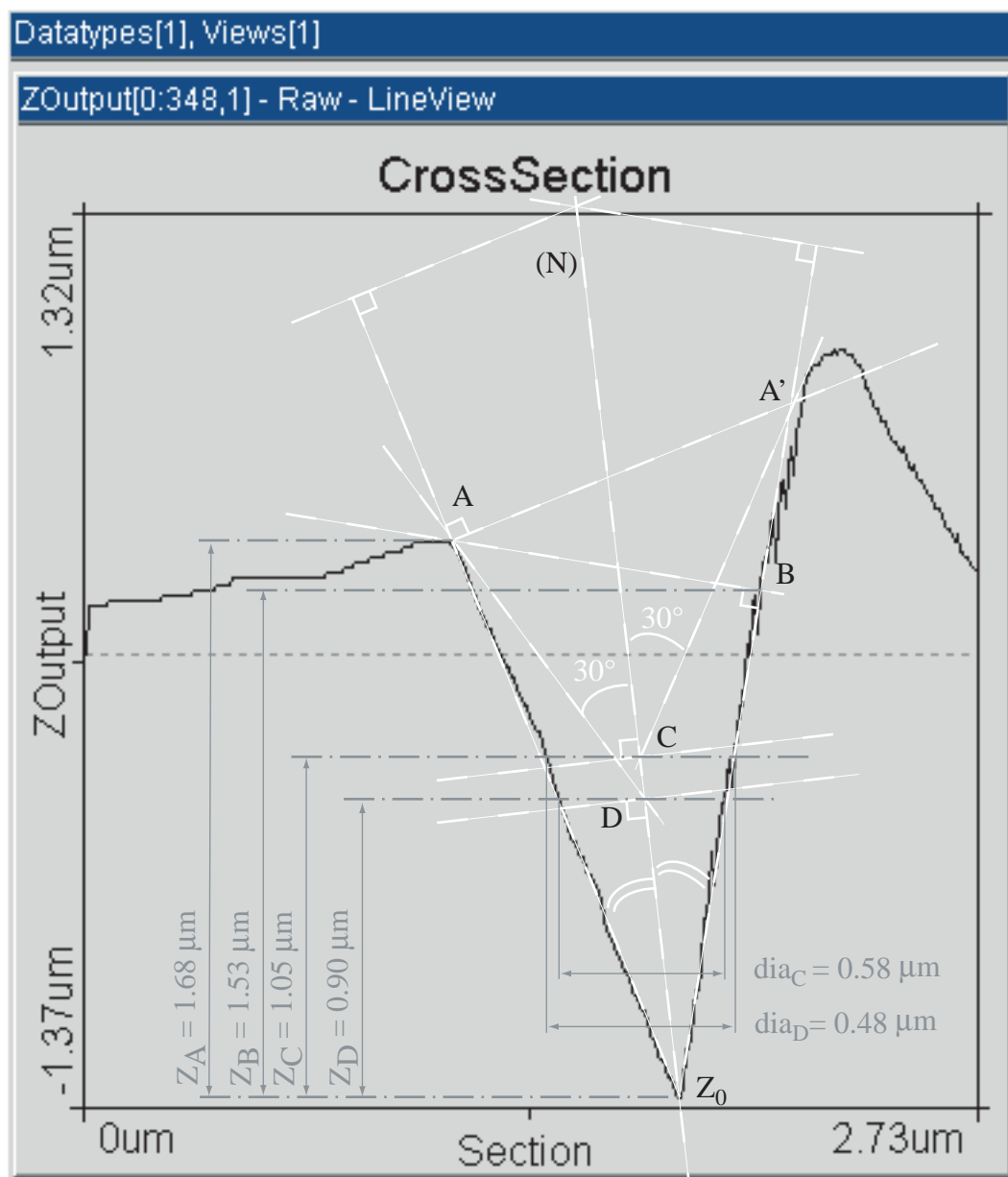


Figure 4.19: Cross-section of the scanned sample area presented in Panel C2 of Figure 4.16. The significance of the white and grey lines is explained in the text.

Bibliography

- [1] M. Born and E. Wolf, *Principles of optics : electromagnetic theory of propagation, interference and diffraction of light*, Cambridge University Press, Cambridge ; New York, 7th (expanded) ed., 1999.
- [2] K. L. Foster, M. A. Tolbert, and S. M. George, *Journal of Physical Chemistry A*, 1997, **101**(27), 4979–4986.
- [3] N. G. Tsierkezos and I. E. Molinou, *Journal of Chemical and Engineering Data*, 1998, **43**(6), 989–993.
- [4] C. Delval and M. J. Rossi, *Physical Chemistry Chemical Physics*, 2004, **6**, 4665–4676.
- [5] G. Sauerbrey, *Zeitschrift Fur Physik*, 1959, **155**(2), 206–222.
- [6] C. S. Lu and O. Lewis, *Journal of Applied Physics*, 1972, **43**(11), 4385–4390.
- [7] M. Kumai, *Journal of Glaciology*, 1968, **7**, 95–108.
- [8] S. Mitlin and K. T. Leung, *Journal of Physical Chemistry B*, 2002, **106**(24), 6234–6247.
- [9] S. Trakhtenberg, R. Naaman, S. R. Cohen, and I. Benjamin, *Journal of Physical Chemistry B*, 1997, **101**(26), 5172–5176.
- [10] B. L. Mason and J. G. Dash, *Journal of Geophysical Research-Atmospheres*, 2000, **105**(D8), 10185–10192.
- [11] J. Hessinger and R. O. Pohl, *Journal of Non-Crystalline Solids*, 1996, **208**(1-2), 151–161.
- [12] A. A. Elvin, J. J. Connor, and D. H. Choi, *Journal of Engineering Mechanics-Asce*, 1998, **124**(1), 54–60.
- [13] F. Caloz, F. F. Fenter, K. D. Tabor, and M. J. Rossi, *Review of Scientific Instruments*, 1997, **68**(8), 3172–3179.
- [14] M. S. Bergren, D. Schuh, M. G. Sceats, and S. A. Rice, *Journal of Chemical Physics*, 1978, **69**(8), 3477–3482.
- [15] B. S. Berland, D. E. Brown, M. A. Tolbert, and S. M. George, *Geophysical Research Letters*, 1995, **22**(24), 3493–3496.
- [16] J. Marti and K. Mauersberger, *Geophysical Research Letters*, 1993, **20**(5), 363–366.
- [17] C. Delval, B. Fluckiger, and M. J. Rossi, *Atmospheric Chemistry and Physics*, 2003, **3**, 1131–1145.
- [18] P. Pratte and M. J. Rossi, *Submitted*, (2004).

- [19] D. E. Brown, S. M. George, C. Huang, E. K. L. Wong, K. B. Rider, R. S. Smith, and B. D. Kay, *Journal of Physical Chemistry*, 1996, **100**(12), 4988–4995.
- [20] L. Chaix, H. van den Bergh, and M. J. Rossi, *Journal of Physical Chemistry A*, 1998, **102**(50), 10300–10309.
- [21] L. Chaix, H. van den Bergh, and M. J. Rossi, *Journal of Physical Chemistry A*, 1999, **103**(15), 2906–2906.
- [22] B. Schmitt *La surface de la glace : structure, dynamique et interactions : implications astrophysiques. (Thèse numéro 493)* PhD thesis, Laboratoire de Glaciologie et Géophysique de l'Environnement, Université de Grenoble, 1986.
- [23] B. J. Murray and J. M. C. Plane, *Physical Chemistry Chemical Physics*, 2003, **5**(19), 4129–4138.
- [24] J. G. Davy and D. Branton, *Science*, 1970, **168**(3936), 1216–1218.
- [25] J. G. Davy and G. A. Somorjai, *Journal of Chemical Physics*, 1971, **55**(8), 3624–3636.
- [26] M. T. Leu, L. F. Keyser, and R. S. Timonen, *Journal of Physical Chemistry B*, 1997, **101**(32), 6259–6262.
- [27] H. J. Fraser, M. P. Collings, M. R. S. McCoustra, and D. A. Williams, *Monthly Notices of the Royal Astronomical Society*, 2001, **327**(4), 1165–1172.
- [28] J. A. Smith, F. E. Livingston, and S. M. George, *Journal of Physical Chemistry B*, 2003, **107**(16), 3871–3877.
- [29] N. J. Sack and R. A. Baragiola, *Physical Review B*, 1993, **48**(14), 9973–9978.
- [30] R. M. Koros, J. M. Deckers, R. P. Andres, and M. Boudart, *Chemical Engineering Science*, 1966, **21**(10), 941–950.
- [31] B. Fluckiger and M. J. Rossi, *Journal of Physical Chemistry A*, 2003, **107**(20), 4103–4115.
- [32] D. R. Haynes, N. J. Tro, and S. M. George, *Journal of Physical Chemistry*, 1992, **96**(21), 8502–8509.
- [33] D. S. Eisenberg and W. Kauzmann, *The structure and properties of water*, Oxford University Press, New York,, 1969.
- [34] M. W. Chase, *NIST-JANAF Thermochemical Tables, Fourth Edition, JPCRD, Monograph 9*, 1998.
- [35] K. G. Libbrecht, *Journal of Crystal Growth*, 2003, **247**(3-4), 530–540.
- [36] K. G. Libbrecht, *Journal of Crystal Growth*, 2003, **258**(1-2), 168–175.
- [37] J. M. Lafferty, *Foundations of vacuum science and technology*, Wiley, New York, 1998.

-
- [38] L. H. Cohan, *Journal of the American Chemical Society*, 1938, **60**(2), 433–435.
- [39] G. Comsa and R. David, *Chemical Physics Letters*, 1977, **49**(3), 512–515.
- [40] G. Comsa, *Surface Science*, 1994, **300**(1-3), 77–91.
- [41] W. van Willigen, *Physics Letters A*, 1968, **A 28**(2), 80.

Chapter 5

The influence of monolayer amounts of HNO_3 on the evaporation rates of H_2O over ice in the range 179 to 208 K: a QCM study.

We have performed several sets of experiments with ice films doped with atmospherically relevant pollutants following the previous chapter that dealt with the validation of the experimental setup based on the measurements of H_2O kinetics in the presence of pure ice films using a quartz crystal microbalance. In a first step HNO_3 was chosen due to the constant interest this trace gas garners in the present atmospheric chemistry arena. Field measurements reveal the abundance of HNO_3 in the stratosphere mainly in the form of solid NAT crystals in the case of Polar Stratospheric Clouds [1] as well as the presence of large HNO_3 -containing particles [2] that may be involved in the denitrification of the lower stratosphere. The concept of the potential of a NAT-coating on the surface of ice particles to prolong the lifetime of polar stratospheric ice particles is also a recurrent idea [3] in order to explain the observation of ice particles several degrees above the

stratospheric ice frost point [4]. A NAT-coating is sometimes suspected to decrease the H₂O vapor pressure of the coated particles [4, 5] or to decrease the mass accommodation coefficient of H₂O onto ice [3] resulting in a longer lifetime of the above cited particles. In the case of Cirrus clouds the recent study of Gao et al. [6] based on in situ measurements have led to the conclusion that the observed increased relative humidity in natural and contrail Cirrus clouds may be attributed to the presence of HNO₃ leading to the formation of a new type of HNO₃-containing ice, namely Δ -ice, that has a mass accommodation of H₂O vapor onto Δ -ice that is lower than that of pure ice. Faced with the fact that the presence of nitric acid undoubtedly increases the lifetime of contaminated ice particles we propose in this chapter a detailed study of the effect of HNO₃-doping on the kinetics of condensation and evaporation of H₂O over ice films.

The flux of evaporation J_{ev} in molec cm⁻² s⁻¹ of H₂O from thin ice films containing between 0.5 to 7 monolayers of HNO₃, with one monolayer of HNO₃ consisting of between 5 and 7·10¹⁴ molec cm⁻² [7, 8], has been measured in the range 179 to 208 K under both molecular and stirred flow conditions. The kinetics of evaporation of H₂O was measured using both residual gas mass spectrometry as well as the quartz crystal microbalance as thickness or mass monitor as described in Chapter 4.

FTIR absorption in transmission of the condensate revealed the formation of the metastable crystalline α -NAT, whose composition is HNO₃·3H₂O, and which converted over time to the stable β -NAT at approximately 205 K. The crystallisation process seemed to occur whatever the doping protocol as opposed to the case of the HCl/H₂O system where only well-defined conditions of deposition led to the formation of the crystalline HCl·6H₂O as described in Chapter 3.

Right after the end of the HNO₃ doping process of the 1 μ m thick ice film performed at deposition times in the range of 16 to 80 s and at a rate in the range (6-60)·10¹² molec cm⁻² s⁻¹ the evaporative flux $J_{ev}(\text{H}_2\text{O})$ was always that of pure ice. Subsequently, the evaporation flux of H₂O, $J_{ev}(\text{H}_2\text{O})$, gradually decreased with the evaporation of H₂O from the doped ice film. Concomitantly, the average concentration of HNO₃ increased depending on a complex interplay

between experimental parameters such as temperature and doping conditions to final values of $J_{\text{ev}}(\text{H}_2\text{O})$ that were smaller by factors varying from 2.7 to 65 relative to pure ice.

Depending on the doping conditions and temperature of the ice film the depth (thickness) d_{D} of the ice film that was affected by the presence of HNO_3 varied between 130 to 700 nm compared to the approximately 1000 nm thick original ice film.

The significant decrease of $J_{\text{ev}}(\text{H}_2\text{O})$ with increasing average concentration of HNO_3 leads to an increase of the evaporative lifetime of atmospheric ice particles in the presence of HNO_3 and may help explain the occurrence of persistent and/or large ice particles under certain favorable atmospheric conditions. The results presented in this chapter have been prepared for submission as a publication to the *Journal of Physical Chemistry*.

5.1 Supplementary information on the experimental apparatus

In this section we present results on the evaporation kinetics of H_2O that have been obtained using the reactor equipped with multiple diagnostics whose hardware parameters have been given in detail in Chapter 2 and in Section 4.1 of Chapter 4. The experimental apparatus itself is schematically represented in Figure 4.1, page 109.

The main change in the experimental setup compared to the version presented in the previous chapter is that the reactor is now equipped with two glass dosing tubes (DT) for vapor injection, one for H_2O , $\text{DT}_{\text{H}_2\text{O}}$, the other for HNO_3 , DT_{HNO_3} . The latter may be oriented towards the Si-window of the cryostat (position $\text{DT}_{\text{HNO}_3}^{\text{Si}}$) or the QCM sensor (position $\text{DT}_{\text{HNO}_3}^{\text{QCM}}$) depending on where the ice film to be doped is located, thus allowing the directed deposition of HNO_3 onto the ice film as shown in Figure 5.1 for the case $\text{DT}_{\text{HNO}_3}^{\text{QCM}}$.

Directed injection of HNO_3 towards the ice films is favored in the present study due to the known efficient interaction of HNO_3 with the reactor walls, be they Teflon-coated [9, 10] or made of stainless steel.

As a reminder, the 6" gate valve (Figure 4.1, **GV**) is used to separate the reactor into an

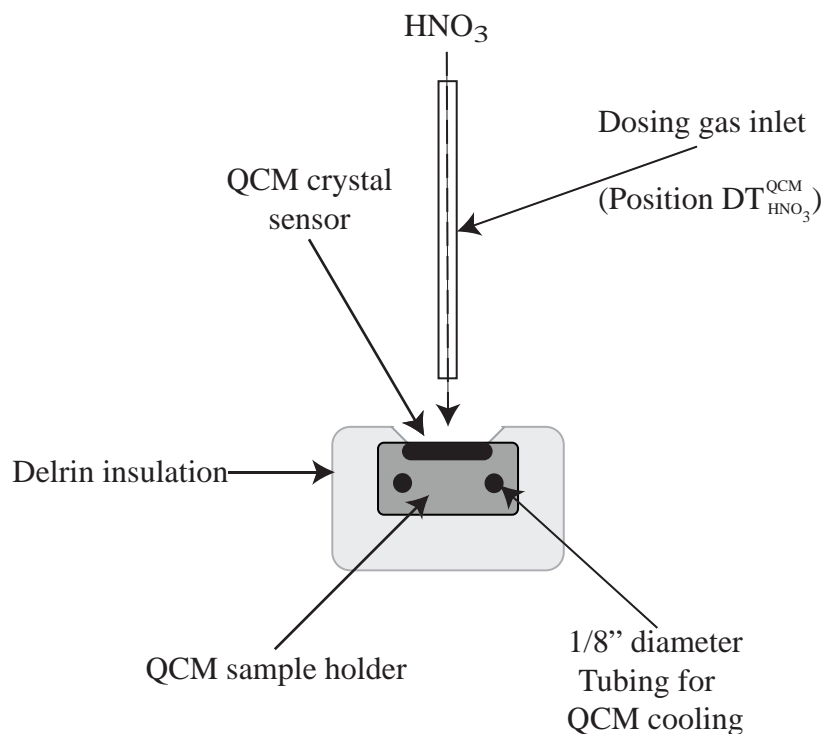


Figure 5.1: Horizontal cut (view from the top) containing the HNO_3 dosing tube (DT). The Delrin-insulated QCM and the piezoelectric crystal sensor are positioned perpendicular to the reference (paper) plane.

upper (UC) and a lower (LC) chamber, the latter of which is pumped by a turbomolecular pump leading to an ultimate pressure of $5 \cdot 10^{-8}$ Torr. This pressure enables the operation of a residual gas mass spectrometer in the lower chamber. The bypass line (Figure 4.1, item 4) allows the flow of residual gas between the chambers through the calibrated leak LV (Figure 4.1). In the present work typical rate constants for effusion for H_2O and HNO_3 are $k_{\text{esc}}(\text{H}_2\text{O})=0.064 \text{ s}^{-1}$, and $k_{\text{esc}}(\text{HNO}_3)=0.042 \text{ s}^{-1}$, respectively.

Characteristic data on the hardware are summarized in Table 5.1.

The following three configurations afforded by the experimental apparatus have been used:

- *Static* operation: GV and LV closed leading to equilibrium conditions within the chamber.

Table 5.1: Hardware parameters of both cryogenic sample supports for the kinetic study of HNO₃-doped ice.

Reactor temperature T_r [K]	Si Optical Window	QCM	
Reactor volume V_r [K]	320		
Conversion factor (1/RT) Conv [molec cm ⁻³ Torr ⁻¹]	2400		
Sample surface area [cm ²]	3.0·10 ¹⁶		
H ₂ O collision frequency with ice sample $\omega_{\text{H}_2\text{O}}$ [s ⁻¹]	0.78	0.50	
H ₂ O effusion rate constant of calibrated leak $k_{\text{esc}}(\text{H}_2\text{O})$ [s ⁻¹]	4.98	3.19	
MS calibration factor for H ₂ O (m/z=18, <i>Stirred Flow</i>) $C_{18}^{\text{s-flow}}$ [molec s ⁻¹ A ⁻¹]	0.064		
MS calibration factor for H ₂ O (m/z=18, <i>Dynamic</i>) C_{18}^{dyn} [molec s ⁻¹ A ⁻¹]	2.4·10 ²⁴		
HNO ₃ collision frequency with ice sample ω_{HNO_3} [s ⁻¹]	1.7·10 ²⁵		
HNO ₃ effusion rate constant of calibrated leak $k_{\text{esc}}(\text{HNO}_3)$ [s ⁻¹]	2.67	1.71	
MS calibration factor for HNO ₃ (m/z=30, <i>Stirred Flow</i>) $C_{30}^{\text{s-flow}}$ [molec s ⁻¹ A ⁻¹]	0.042		
MS calibration factor for HNO ₃ (m/z=30, <i>Dynamic</i>) C_{30}^{dyn} [molec s ⁻¹ A ⁻¹]	6.2·10 ²⁵		
Calculated escape orifice area A_{esc} [mm ²]	2.2·10 ²⁵		
	1.0		
	Thickness for FTIR O.D.= 1.08 [Å] ^a	calibration factor	
	10000	Temperature [K]	Cf [a.u.]
		170	9.0
		180	8.0
		190	7.8
		193	6.0
		205	2.0
		208	1.9

^asee Equation 2.23, page 50

- *Stirred flow* operation (low rate of pumping): GV closed and LV open. These conditions lead to a typical (stirred flow) residence time of 15 s for H₂O and 24 s for HNO₃.
- *Dynamic* operation (high rate of pumping): GV open. This corresponds to molecular flow conditions whose estimated gas phase residence time for H₂O and HNO₃ is 1 and 2 ms, respectively.

The knowledge of the absolute number of molecules of H₂O that are present on the sensor of the QCM are based on the calibrations that are discussed in Chapter 4. One must remember that these calibrations are mandatory due to the fact that the use of a QCM for the measurement of the mass of any deposit requires the accurate knowledge of the shear modulus of the film. For ice only scant information has been published on this subject [11, 12, 13] and due to the significant dependence of the mechanical properties of ice on the film porosity [12] these data cannot be extrapolated to our experimental conditions. As stated in Chapter 4 this has led us to apply a well established protocol for QCM signal calibration in order to obtain the absolute number of water molecules deposited on the sensor. The cross calibration between the Si-window and the QCM uses a H₂O ice film deposited from the gas phase at 190 K at a rate of $5 \cdot 10^{16}$ to $1 \cdot 10^{17}$ molec cm⁻² s⁻¹. This results in a calibration factor for the QCM signal $C_f=7.8$ (see Table 5.1) that leads to a precision of $1.4 \cdot 10^{13}$ molec cm⁻² for the number of H₂O molecules deposited on the QCM sensor element. This roughly corresponds to 1.5 % of a formal monolayer. These calibrations enable the measurement of the mass change or the growth of a deposited ice film of known thickness using a density for the present films of 0.93 g cm^{-3} [14] that are subsequently used as a substrate for HNO₃ deposition.

The absolute amount of HNO₃ adsorbed on the ice film is evaluated following the method originally described in Section 2.5, page 40. First, we have established the absolute flow rate of HNO₃, $F_r(\text{HNO}_3)$, into the chamber under stirred flow conditions (GV closed, LV open) using mass spectrometry (MS) at $m/z=30$. Second, the calibrated MS signal corresponding to the measured HNO₃ loss by adsorption on the ice substrate was integrated in order to determine

the absolute number of deposited HNO_3 molecules. In the following we briefly recall this method described in Section 2.5 but apply it this time to HNO_3 as well as remind the reader of the calibration of the MS signal under dynamic pumping conditions.

The first step relies on the calibration of the MS signal of HNO_3 at $m/z=30$ which enables a 1:1 correspondence between MS intensities I_{30} and the partial pressure or concentration of HNO_3 in the chamber.

Under stirred flow conditions (GV closed, LV open) the calibration of I_{30} is based on establishing the ratio between the MS signal and the partial pressure of HNO_3 in the upper chamber that is measured using the Baratron absolute pressure gauge (Figure 4.1, item 12). When HNO_3 is injected into the reactor through the dosing tube in position $\text{DT}_{\text{HNO}_3}^{\text{QCM}}$ the following equalities hold by analogy to Equations 2.11 to 2.14 (page 41):

$$F_r(\text{HNO}_3) = \frac{P_{\text{HNO}_3} \times V_r}{R \times T_r} \times k_{\text{esc}}(\text{HNO}_3) \quad (5.1)$$

$$= [\text{HNO}_3] \times V_r \times k_{\text{esc}}(\text{HNO}_3) \quad (5.2)$$

$$= \text{Conv} \times V_r \times k_{\text{esc}}(\text{HNO}_3) \times P_{\text{HNO}_3} \quad (5.3)$$

$$= C_{30}^{\text{s-flow}} \times I_{30} \quad (5.4)$$

where Conv is the conversion factor between the partial pressure and the concentration of HNO_3 in the chamber in $\text{molec Torr}^{-1} \text{ cm}^{-3}$ (Table 5.1), P_{HNO_3} the pressure of HNO_3 in Torr, V_r the volume of the reactor in cm^3 and $k_{\text{esc}}(\text{HNO}_3)$ the rate of effusion of HNO_3 through the calibrated leak (LV) in s^{-1} . I_{30} corresponds to the intensity of the MS signal for $m/z=30$ in A and $C_{30}^{\text{s-flow}}$ is the calibration factor for $m/z=30$ under stirred flow conditions in $\text{molec s}^{-1} \text{ A}^{-1}$. By combining Equations 5.3 and 5.4 and measuring both P_{HNO_3} and I_{30} we may evaluate $C_{30}^{\text{s-flow}}$ following Equation 5.5:

$$C_{30}^{\text{s-flow}} = \text{Conv} \times V_r \times k_{\text{esc}}(\text{HNO}_3) \times \frac{P_{\text{HNO}_3}}{I_{30}} \quad (5.5)$$

Under dynamic conditions (GV open) C_{30}^{dyn} is evaluated using the decrease of the pressure of HNO₃ in the Teflon coated calibrated volume (CV, volume V_c), P_{HNO_3} , used as a reservoir for the HNO₃ flow into the reactor when the ON/OFF valve, VOO, displayed in Figure 5.2 is opened. The correspondence between the measured $\Delta P_{\text{HNO}_3}/\Delta t$ and the MS signal at $m/z=30$ yields C_{30}^{dyn} , the calibration factor for $m/z=30$ under dynamic conditions in Equation 5.6 by analogy to Equation 5.5:

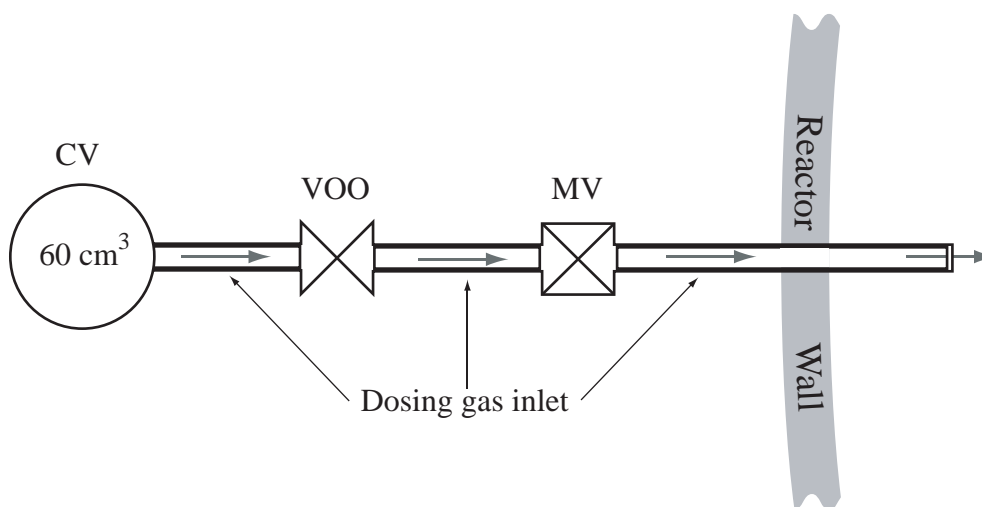


Figure 5.2: Schematic drawing of the gas admission line: VOO allows the effusion of the trace gas (HNO₃) from the 60 cm³ Teflon-coated calibrated volume (CV) through the dosing tube and across the metering valve MV into the reactor.

$$C_{30}^{\text{dyn}} = \text{Conv} \times V_c \times \frac{\Delta P_{\text{HNO}_3}}{\Delta t} \times \frac{1}{I_{30}} \quad (5.6)$$

The calibration factors for $m/z=30$ and $m/z=18$, namely $C_{30}^{\text{s-flow}}$, $C_{18}^{\text{s-flow}}$, C_{30}^{dyn} and C_{18}^{dyn} , are all determined using the same method and are listed in Table 5.1.

The smallest measurable MS signal for HNO₃ at $m/z=30$ at a signal-to-noise ratio $S/N=2:1$ is of the order of $8.0 \cdot 10^{-14}$ A. Using the appropriate calibration factor for $m/z=30$ this limit leads to the smallest measurable flow rate of $4.9 \cdot 10^{12}$ molec s⁻¹ under stirred flow conditions. Under dynamic conditions the detection limit is approximately $1.0 \cdot 10^{-13}$ A leading to the minimum

measurable flow rate of $2.2 \cdot 10^{12}$ molec s^{-1} .

The second step in the evaluation of the absolute amount of HNO_3 deposited on the ice substrate consists in taking the difference of I_{30} under stirred flow conditions, with and without an ice film on the QCM. This difference in MS signals may be converted into an absolute number of HNO_3 molecules that have been deposited onto the ice film located on the QCM quartz sensor compared to the few HNO_3 molecules sticking to the quartz sensor set at 320 K (Table 5.1).

The glass tubing used for the directed injection of HNO_3 was aimed at the center of the QCM sensor and connected to the ON/OFF valve (VOO) described previously (see Section 2.1), which itself is located upstream of the micrometer dosing valve MV (Swagelok double pattern low pressure metering valve with vernier handle of type SS-SS2-D-TVVH, valves noted V_1 and V_2). Figure 5.2 presents a schematic illustration of the injection line where VOO separates the Teflon coated calibrated volume used as a reservoir for HNO_3 from MV. For a given pressure of HNO_3 of approximately 2 Torr in the calibrated volume we have systematically established the correspondence between the aperture of MV and I_{30} . We subsequently have compared I_{30} when the QCM sensor is at ambient temperature (no ice) and in the presence of an ice film at the same experimental settings of pressure and aperture of V_1 and V_2 of MV. Using the appropriate calibration factor, the time integration of the difference between both I_{30} signals enables the measurement of the loss of gas phase HNO_3 owing to the deposition of HNO_3 on the ice substrate thanks to the certainty that once more there is no cold spot in the chamber other than the QCM sensor.

Figure 5.3 illustrates a specific case of a HNO_3 deposition on a $1.2 \mu\text{m}$ thick ice substrate at $T_{\text{ice}}=189$ K with apertures of the double metering valve MV set to $V_1=V_2=15$ units and with $P_{\text{HNO}_3}^0=2034$ mTorr in the Teflon coated calibrated volume CV under stirred flow conditions. Previously, the film was deposited by condensation of water vapor under static conditions at 190 K at a rate of $1 \cdot 10^{17}$ molec $\text{cm}^{-2} \text{s}^{-1}$. Subsequently the temperature of the film was set to the desired value, 189 K in this example.

At $t=t_0=0$ s in Figure 5.3, VOO is opened allowing the effusion of HNO_3 from the reservoir

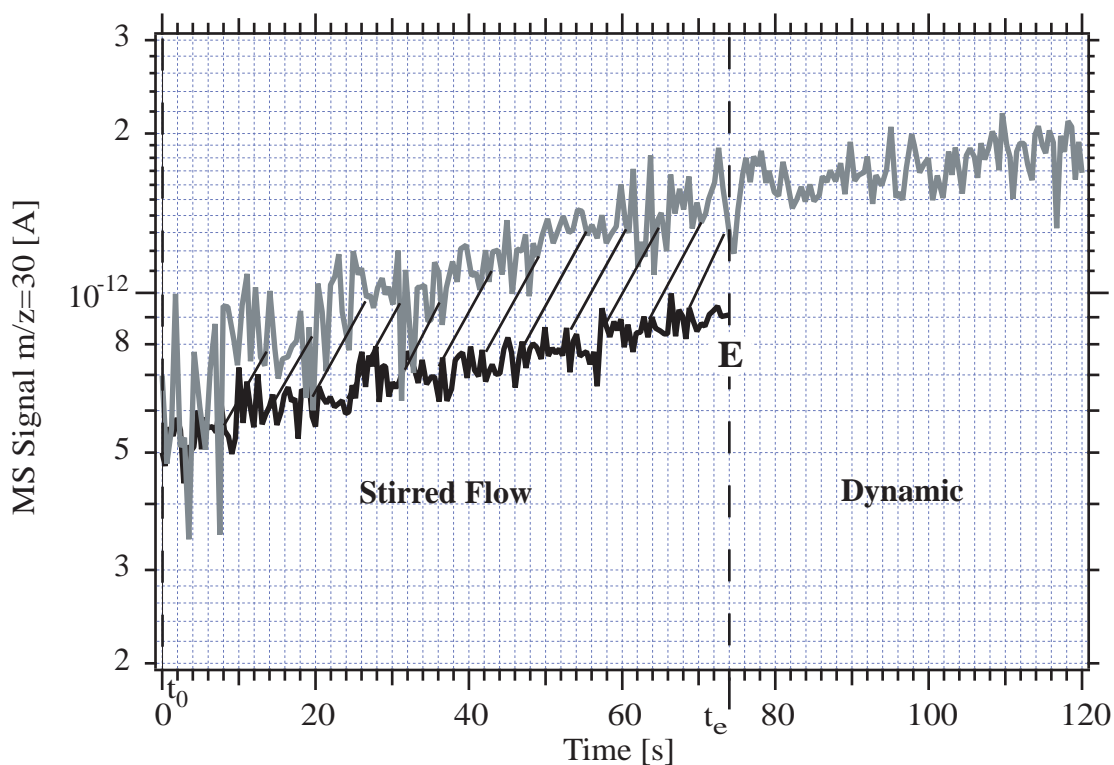


Figure 5.3: Typical MS signals for $m/z=30$ during directed HNO_3 admission onto the quartz sensor of the QCM: reference experiment with QCM at 320 K (grey trace) and HNO_3 dosing at 189 K on an ice film (black trace) deposited on the QCM. After the deposition on ice (black trace), the system is set from stirred flow to dynamic conditions at $t=t_e$ and VOO is closed to halt HNO_3 admission into the reactor.

CV across MV and the tubing into the reactor. The grey trace I_{30} corresponds to the case where the QCM is at 320 K (no ice) which is used as a reference for the deposition of HNO_3 on top of the ice film. The black trace I_{30} corresponds to the identical case as above for deposition between t_0 and $t_e=74$ s which corresponds to the end of the dosing period when the reactor is set to dynamic conditions and VOO is closed. Indeed, we have shown in Section 3.1 that the directed deposition of dopants onto ice under stirred flow conditions leads to a residual pressure of the doping gas that is low enough to prevent a competitive deposition by backfilling of the chamber. This is all the more the case in the present example where the system is set to molecular flow conditions once the end of the chosen deposition time has been reached at t_e .

Depending on the total pressure in the upper chamber the MS was turned off or not just when the system was set from stirred flow to dynamic conditions in order to protect the MS filament from an occasional sudden pressure surge. In the case presented above we have chosen to display only the time period during which HNO_3 direct deposition occurs.

The hatched area represents the absolute loss of gas phase HNO_3 in the presence of the ice film compared to the reference experiment with no ice. As the piezoelectric sensor is the unique cold target in the reactor this loss therefore corresponds to the number of HNO_3 molecules deposited onto ice. Thus, the difference between both I_{30} signals at $t < 74$ s obtains the rate, R_{HNO_3} , of HNO_3 adsorption on the ice film. The time integration of this difference in the $m/z=30$ MS signals between $t=0$ (t_0) and 74 s (t_e) yields the absolute number of HNO_3 molecules, $N_{\text{HNO}_3}^{\text{dep}}$, present on the ice substrate. For the case of Figure 5.3 $(1.7 \pm 0.2) \cdot 10^{15}$ molecules of HNO_3 have been deposited during 74 s at an average rate of $2.2 \cdot 10^{13}$ molec s^{-1} .

Figure 5.4 shows I_{30} during the evaporation of the ice film that was the substrate for HNO_3 condensation in Figure 5.3. The hatched area limited by points A and B corresponds to evaporating HNO_3 molecules, $N_{\text{HNO}_3}^{\text{evap}}$, which in the present case corresponds to $(1.8 \pm 0.2) \cdot 10^{15}$ molecules of HNO_3 . This value is in excellent agreement with the value obtained previously during deposition and corresponds to a satisfied mass balance.

For each of the experiments presented in this work the mass balance was routinely established between HNO_3 deposited on the ice film measured using the above mentioned method and HNO_3 recovered in the process of evaporation of the $\text{H}_2\text{O}/\text{HNO}_3$ ice film. The mass balance varied in all the cases within less than a factor of 2.1 which corresponds to the worst case. Table 5.2 summarizes several experiments performed in this study using different rates of deposition of HNO_3 as well as different doses of HNO_3 .

Different experiments have been performed using the QCM as a means to monitor the sample mass or thickness of a typically 1 μm thick ice film at temperatures between 179 and 208 K in

Table 5.2: Representative experimental results for the kinetics of H₂O evaporation in the presence of HNO₃ for three temperature ranges. Different rates of deposition as well as different doses of HNO₃ are presented. In the third column, the symbols refer to the corresponding figures listed in the second column as well as to the corresponding numbers used in Figures 5.13 to 5.16.

T range [K]	Figure	Symbol & Number	T _{ice} [K]	R _{HNO₃} [molec s ⁻¹]	t _{dep} [s]	N _{HNO₃} ^{dep} ^a [molec]	N _{HNO₃} ^{evap} ^b [molec]	r ₁₈ ^{QCM} [Å cm ² s molec ⁻¹]	dd [Å]	J _{ev} ^b [molec cm ⁻² s ⁻¹]	J _{ev} ^e [molec cm ⁻² s ⁻¹]	r ^{b/e}	
189-195 range 1	Fig. 5.10	Pure Ice	192										
			○ 1	191	7.9·10 ¹²	16	1.5·10 ¹⁴	3.2·10 ¹⁴	9.0·10 ⁻²⁷	853	4.0·10 ¹⁶	-	-
			△ 2	190	2.0·10 ¹³	22	4.7·10 ¹⁴	4.4·10 ¹⁴	2.3·10 ⁻²⁶	1626	3.8·10 ¹⁶	1.7·10 ¹⁵	22.3
			□ 3	193	2.1·10 ¹³	42	9.4·10 ¹⁴	1.4·10 ¹⁵	1.6·10 ⁻²⁶	1270	3.0·10 ¹⁶	9.7·10 ¹⁴	30.9
			▽ 4	191	2.9·10 ¹³	80	2.2·10 ¹⁵	2.2·10 ¹⁵	1.5·10 ⁻²⁶	2826	4.8·10 ¹⁶	1.9·10 ¹⁵	25.3
			⊕ 5	195	3.1·10 ¹²	17	4.0·10 ¹³	2.6·10 ¹³	2.9·10 ⁻²⁶	6970	4.0·10 ¹⁶	7.1·10 ¹⁵	5.6
			⊗	193	-	44	-	2.9·10 ¹⁴	3.0·10 ⁻²⁶	2190	5.0·10 ¹⁶	3.0·10 ¹⁵	16.7
			× 6	189	1.9·10 ¹³	51	9.5·10 ¹⁴	2.2·10 ¹⁵	2.3·10 ⁻²⁶	3058	4.9·10 ¹⁶	2.3·10 ¹⁵	21.3
			7	189	3.1·10 ¹³	75	2.4·10 ¹⁴	-	2.4·10 ¹⁶	3458	2.4·10 ¹⁶	1.9·10 ¹⁵	12.6
			8	189	2.2·10 ¹³	74	1.7·10 ¹⁵	1.8·10 ¹⁵	2.5·10 ⁻²⁶	2426	-	-	-
179-185 range 2	Fig. 5.11	Pure Ice	181	1.8·10 ¹³	32	5.9·10 ¹⁴	3.3·10 ¹⁴	2.9·10 ⁻²⁶	3089	2.2·10 ¹⁶	1.6·10 ¹⁵	13.7	
			△ 11	181	1.8·10 ¹³	32	5.9·10 ¹⁴	3.3·10 ¹⁴	2.9·10 ⁻²⁶	4524	7.0·10 ¹⁵	1.0·10 ¹⁵	7.0
			● 12	180	5.5·10 ¹²	44	2.4·10 ¹⁴	3.3·10 ¹⁴	5.2·10 ⁻²⁶	4786	6.0·10 ¹⁵	9.3·10 ¹⁴	6.4
			○ 13	184	1.7·10 ¹³	32	5.4·10 ¹⁴	5.5·10 ¹⁴	2.8·10 ⁻²⁶	3709	9.0·10 ¹⁵	1.2·10 ¹⁵	7.5
			⊕ 14	180	1.4·10 ¹³	30	4.3·10 ¹⁴	-	2.5·10 ⁻²⁶	3255	4.8·10 ¹⁵	1.8·10 ¹⁵	2.7
			⊗ 15	185	1.9·10 ¹³	64	1.2·10 ¹⁵	1.8·10 ¹⁵	3.2·10 ⁻²⁶	5103	1.2·10 ¹⁶	3.6·10 ¹⁴	33.3
			× 16	181	1.6·10 ¹³	23	3.6·10 ¹⁴	-	3.1·10 ⁻²⁶	4787	4.0·10 ¹⁵	1.1·10 ¹⁵	3.6
			□ 17	179	1.4·10 ¹³	31	4.9·10 ¹⁴	6.0·10 ¹⁴	1.9·10 ⁻²⁶	3568	6.0·10 ¹⁵	4.0·10 ¹⁴	15.0
			◇ 18	185	2.1·10 ¹³	60	1.4·10 ¹⁵	1.9·10 ¹⁵	2.5·10 ⁻²⁶	1984	1.2·10 ¹⁶	3.6·10 ¹⁴	33.3
			⊕ 21	207	3.0·10 ¹³	60	1.8·10 ¹⁵	-	4.0·10 ⁻²⁶	3709	2.2·10 ¹⁷	3.4·10 ¹⁵	64.7
205-208 range 3	Fig. 5.12	Pure Ice	205										
			○ 22	207	5.6·10 ¹²	66	4.1·10 ¹⁴	8.4·10 ¹⁴	2.5·10 ⁻²⁶	864	2.0·10 ¹⁷	-	-
			⊗ 23	208	6.2·10 ¹²	60	3.2·10 ¹⁴	1.7·10 ¹⁴	2.3·10 ⁻²⁶	2000	3.0·10 ¹⁷	5.0·10 ¹⁵	60.0

^aExplained in the text.
^bExplained in the text.

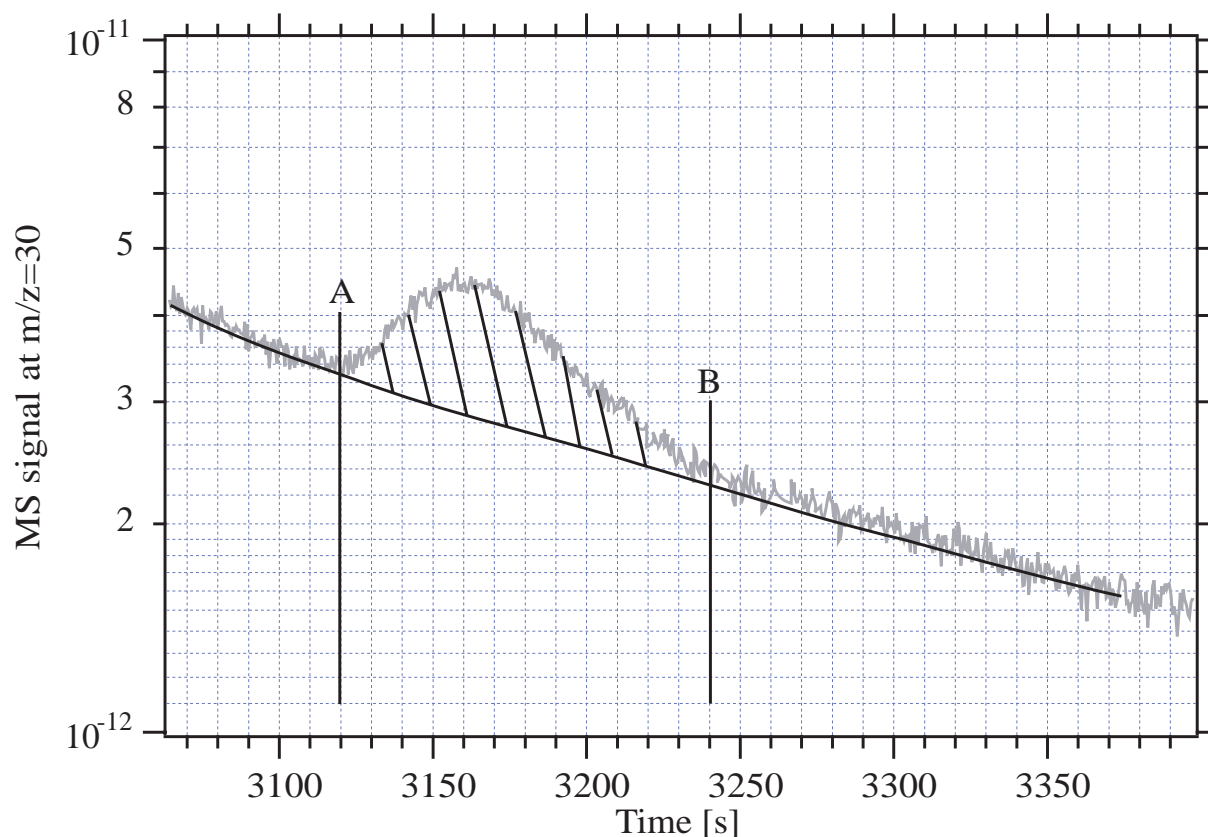


Figure 5.4: Typical MS signal at $m/z=30$ during evaporation of an ice film, here at 189 K. The hatched area limited by point A and B is proportional to the number of HNO_3 molecule evaporating from the ice surface and corresponds to $1.8 \cdot 10^{15}$ molec of HNO_3 .

order to obtain information on the kinetics of evaporation of H_2O in the presence of small albeit known amounts of HNO_3 .

In all of these experiments the ice film was first grown by deposition of bidistilled water vapor under static conditions (GV, LV closed) on the 0.5 cm^2 surface of the QCM sensor at 190 K and a typical rate of $1 \cdot 10^{17} \text{ molec cm}^{-2} \text{ s}^{-1}$. Such ice films consist of thermodynamically stable polycrystalline ice I_h [15, 16, 17] as pointed out previously. Subsequently, the ice film temperature is set to the value of interest for the study. Once the temperature is reached the system is set to stirred flow condition and steady-state H_2O evaporation is achieved in the upper chamber (UC) of the reactor. HNO_3 is then deposited on the ice surface through the directed

gas inlet by setting the micrometer valve MV to the desired flow rate for deposition. As soon as the chosen dose of HNO₃ molecules is dispensed VOO is closed and the system is set to dynamic conditions by opening GV in order to halt HNO₃ dosing (Figure 5.3, point E). Starting from t_e the HNO₃ doped ice sample evaporation history is tracked and recorded using the QCM as well as residual gas mass spectrometry.

Under the molecular flow conditions afforded by the high pumping rate used in this work no condensation of water onto the temperature-controlled piezoelectric sensor is taking place owing to the low partial pressure of H₂O. Thereby, J_{ev} is directly evaluated from the derivative of the time dependence of the thickness or number of H₂O molecules present on the crystal as described in Section 4.2.3 and following Equation 5.7:

$$J_{ev} = C_f \times 3.11 \cdot 10^{14} \times \frac{dS_{QCM}^{dyn}}{dt} \times 100 \quad (5.7)$$

where S_{QCM}^{dyn} is the initial raw output signal given by the IC/5 controller, $C_f=7.8$ the calibration factor of the QCM for an ice film deposited under the conditions of this work and $3.11 \cdot 10^{14}$ in [molec cm⁻² s⁻¹] the number of molecules forming a 1 cm² by 1 Å thick ice film of density 0.93 [14]. The factor of 100 in Equation 5.7 corresponds to the conversion of the initial IC/5 output voltage of 10 V for a thickness of 1000 Å of a material of unity density and Z-ratio which is the acoustic impedance ratio derived from the shear modulus of the deposited thin film [18]. Validation and limits of the quantitative aspects of the QCM technique for pure ice films have been discussed before in Section 4.2.3.

5.2 Experimental Strategy

Figure 5.5 illustrates the typical evaporation history of a 1.2 μm thick ice film grown at 190 K from deposition of bidistilled water vapor at a rate of $1 \cdot 10^{17}$ molec cm⁻² s⁻¹ under static conditions. The temperature of the film is subsequently fixed at 189 K and the system is set to stirred flow (GV closed, LV open). Once steady-state conditions for H₂O in the upper chamber

of the reactor had been attained, HNO_3 was deposited at an average rate of $2.2 \cdot 10^{13}$ molec s^{-1} during 74 s at the end of which the system was set to dynamic conditions and the HNO_3 injection halted. This corresponds to time $t=t_{\text{dyn}}=0$ s in Figure 5.5. It follows that $1.7 \cdot 10^{15}$ molecules of HNO_3 were deposited onto the ice film in this experiment which approximately corresponds to 5 formal monolayers. From the beginning of the evaporation of the ice film to point D at 189 K in Figure 5.5 the evaporative flux J_{ev} is nearly constant and equal to $2.2 \cdot 10^{16}$ molec $\text{cm}^{-2} \text{s}^{-1}$ which indicates that J_{ev} remains that of pure ice in agreement with the results we have published previously for the kinetics of evaporation of pure ice [17, 19, 20] as well as with results from the literature [21].

At point D, J_{ev} measured using the QCM, $J_{\text{ev}}^{\text{QCM}}$, begins to decrease. This apparent change in evaporative flux of H_2O is confirmed by the change of the MS signal at $m/z=18$ which follows the same decreasing trend. However, $J_{\text{ev}}^{\text{QCM}}$ and I_{18} do not change to the same extent so that we suspect a change of C_f to occur due to the presence of HNO_3 . This discrepancy between $J_{\text{ev}}^{\text{QCM}}$ and J_{ev} obtained from the MS signal at $m/z=18$ has been found before [19] and presented in Section 4.2.3, page 127, for pure ice films. In the case of the previous study of pure water ice films we have attributed this sudden discrepancy to a probable structural change for a thickness smaller than 80 nm that may lead to a modification of the mechanical properties of the ice films and thus of C_f once the film is thinning out caused by the probable impact of the roughness of the gold coating of the QCM sensing element (see Section 4.6, page 148). For the present study we take note that the presence of HNO_3 for doses even smaller than one formal monolayer (see Table 5.2) leads to a nonlinear change of C_f which will not be pursued further in this work. It occurs for a thickness smaller than d_D whereas the evaporation kinetics of pure ice films presented in Table 5.2 agree perfectly with results presented in Section 4.2.3.

We have extrapolated the diffusion coefficient for HNO_3 in ice obtained for the range 238-265 K by Thibert and Dominé [22], $D=1.37 \cdot 10^{-2610/T} \text{ cm}^2 \text{ s}^{-1}$, which may be regarded as a lower limit for diffusion, to the present range of temperatures as their work deals with single crystal ice whereas our films are polycrystalline.

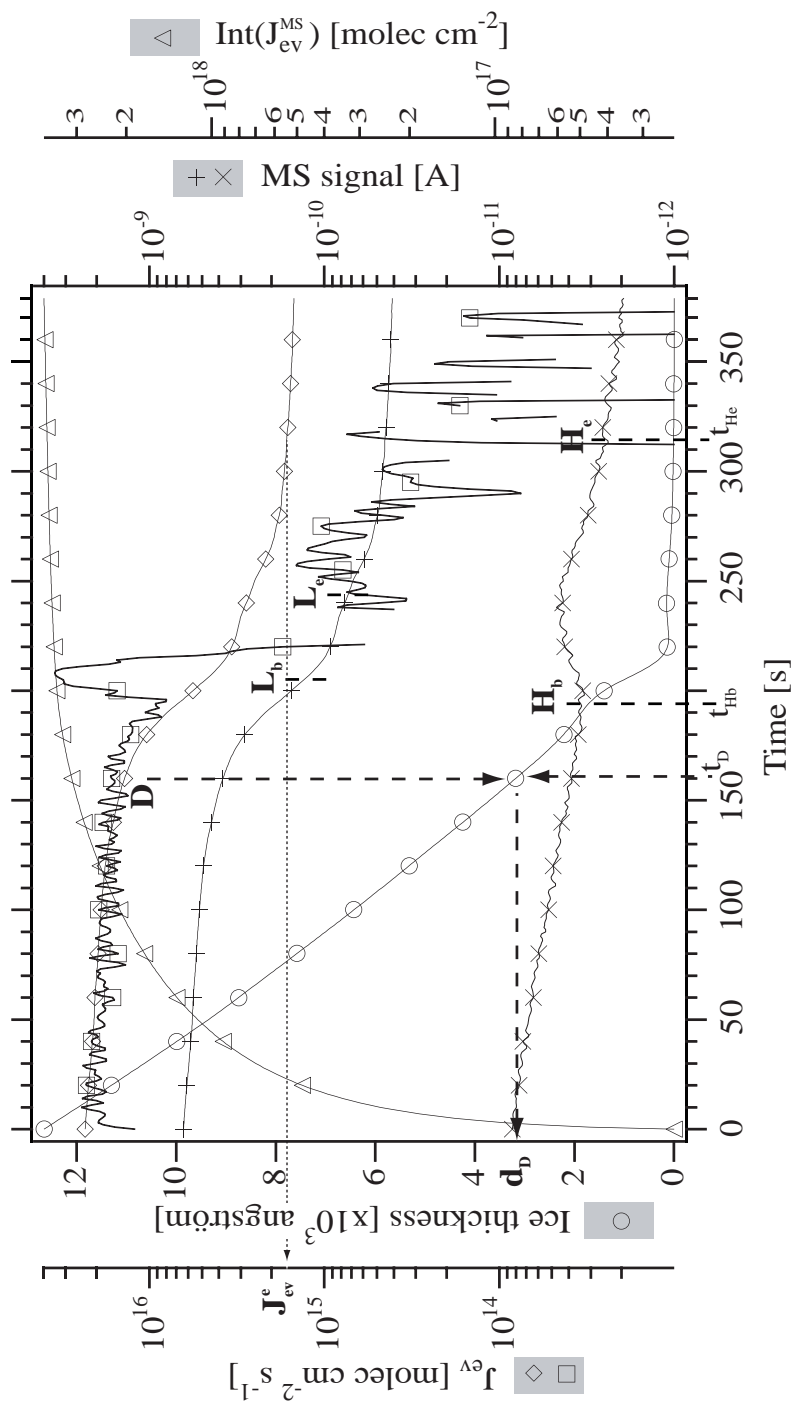


Figure 5.5: Typical experimental protocol of the evaporation at 189 K of a $1.2 \mu\text{m}$ thick ice film doped with approximately 5 monolayers of HNO_3 . This illustration corresponds to the experiment whose HNO_3 deposition and evaporation are described in Figures 5.3 and 5.4, respectively. (o): ice thickness monitored by QCM (\AA), (\square): "apparent" H_2O evaporative flux, $J_{\text{ev}}^{\text{QCM}}$, monitored by QCM ($\text{molec cm}^{-2} \text{ s}^{-1}$), (+): I_{18} MS signal for H_2O (A), (\times): I_{30} MS signal for HNO_3 (A), (\diamond): J_{ev}^{18} evaporative flux calculated from I_{18} ($\text{molec cm}^{-2} \text{ s}^{-1}$), (Δ): $\text{Int}(J_{\text{ev}}^{18})$ time integral of J_{ev}^{18} (molec cm^{-2}). Different points correspond to specific instants during ice evaporation described in the text.

At 189 K, the calculated value of $D=2.1 \cdot 10^{-14} \text{ cm}^2 \text{ s}^{-1}$ results in a HNO_3 diffusion time across 25 % of the ice film thickness larger by at least a factor of 40 than the duration of the evaporation experiment. This essentially excludes the possibility for HNO_3 molecules to reach the surface of the piezoelectric crystal by diffusion. Therefore, the change in C_f must be due to the change of the mechanical properties of ice doped with HNO_3 and probably not due to the presence of HNO_3 on the gold coated sensor surface. Whatever the reason, it was not the aim of this work to elucidate the reasons for the mismatch between $J_{\text{ev}}^{\text{QCM}}$ and J_{ev} evaluated from the gas-phase H_2O concentration monitored at $m/z=18$. We claim that QCM data are trustworthy from $t=t_{\text{dyn}}=0$ to point D in Figure 5.5 such that the QCM signal may be used to obtain the mass or thickness of the pure ice film as well as the volume of ice whose kinetics of H_2O evaporation is subsequently affected by the presence of HNO_3 . This remaining ice thickness is denoted as d_D in Figure 5.5.

From point D on the rate of change of the ice thickness or the evaporative flux of H_2O from ice, J_{ev} , may be evaluated from the MS signal intensity at $m/z=18$ and is called J_{ev}^{18} . For the sake of clarity J_{ev}^{18} is calculated from I_{18} as early as the system is set to dynamic conditions corresponding to the remaining ice thickness given by the QCM denoted with $d_{\text{QCM}}(t_{\text{dyn}})$. First, we have established the correspondence ratio, r_{QCM}^{18} , between the evaporative flux established by the QCM, $J_{\text{ev}}^{\text{QCM}}$, and the analogous flux, J_{ev}^{18} , given by the MS signal at $m/z=18$ at the beginning of the evaporation. As $J_{\text{ev}}^{\text{QCM}}$ pertains to pure ice and C_f is constant during this period we may express r_{QCM}^{18} as follows:

$$r_{\text{QCM}}^{18} = \frac{I_{18}}{J_{\text{ev}}^{\text{QCM}}} \quad (5.8)$$

This definition implies that r_{QCM}^{18} is a constant between t_{dyn} and t_D as both $J_{\text{ev}}^{\text{QCM}}$ and I_{18} track each other and reflect the true evaporative flux of H_2O from pure ice up to point D.

Nevertheless, from t_{dyn} on we have calculated the true evaporative flux J_{ev}^{18} from I_{18} for thicknesses lower than $d_{\text{QCM}}(t_{\text{dyn}})$ using relation 5.9:

$$J_{ev}^{18} = \frac{I_{18}}{r_{QCM}^{18}} \quad (5.9)$$

The resulting signal is represented in Figure 5.5 by symbol (\diamond) and is significantly different from J_{ev}^{QCM} labelled by symbol (\square) for $t > t_D$.

One must take note that as J_{ev}^{QCM} does not correspond to the true evaporation rate for $t > t_D$ the thickness of the film present on the crystal sensor and monitored by the QCM signal is also erroneous. Knowledge of the remaining number of H₂O molecules at any given instant may be obtained from the thickness of the film given by the QCM at the time when the system is set from static to dynamic conditions at $t = t_{dyn} = 0$ or $d_{QCM}(t_{dyn})$, and from the knowledge of J_{ev}^{18} as a function of time as described in the following.

In Figure 5.5 symbol (Δ) represents the integral amount of H₂O molecules per cm² at time t that have desorbed from the ice substrate between t_{dyn} and t . This signal, namely $Int(J_{ev}^{18})$, corresponds to the time integration of J_{ev}^{18} and is calculated as follows:

$$Int(J_{ev}^{18})(t) = \int_{t_{dyn}}^t J_{ev}^{18}(t) dt \quad (5.10)$$

The absolute number of H₂O molecules that are present on the crystal sensor of the QCM, N_{H_2O} , at time t may be calculated using Equation 5.11:

$$\begin{aligned} N_{H_2O}(t) &= N_{H_2O}(t_{dyn}) - Int(J_{ev}^{18})(t) \times A_{QCM} \\ &= d_{QCM}(t_{dyn}) \times 3.11 \cdot 10^{14} \times A_{QCM} - Int(J_{ev}^{18})(t) \times A_{QCM} \end{aligned} \quad (5.11)$$

where $N_{H_2O}(t_{dyn})$ is the number of molecules present on the sensor at $t = t_{dyn}$ when the system is set from static to dynamic flow conditions, $A_{QCM} = 0.5 \text{ cm}^2$ is the effective surface of the QCM sensing element and $d_{QCM}(t_{dyn})$ the thickness given at t_{dyn} by the QCM already multiplied by the calibration factor $C_f = 7.8$.

The calculated absolute number of H_2O molecules present on the QCM during evaporation, $N_{\text{H}_2\text{O}}(t)$, is represented in Figure 5.6 by symbol (\otimes) and the thickness, $d_{\text{QCM}}(t)$, given by the QCM is labelled by (\circ), the different scales notwithstanding. As expected, the signals \otimes and \circ are identical and track each other (apart from their units) from t_{dyn} up to $t_{\text{D}}=160$ s corresponding to point D in Figure 5.5 and thickness d_{D} .

There is no release of HNO_3 before the point noted H_b at t_{Hb} as displayed in Figure 5.5. Indeed, in all the experiments presented in this work HNO_3 always evaporates at the end of ice film sublimation. Such a preferential desorption of H_2O molecules under conditions of H_2O undersaturation and in the presence of HNO_3 is a known phenomenon that has already been reported [23, 24]. As a consequence, the number of HNO_3 molecules present on the ice substrate, $N_{\text{HNO}_3}(t)$ may be considered to be constant up to t_{Hb} , the point of appearance of HNO_3 desorption monitored at $m/z=30$.

We have calculated the average relative concentration of HNO_3 in ice as a function of time, $\chi_{\text{HNO}_3}(t)$ up to t_{Hb} which implies uniform concentration of HNO_3 throughout the remaining ice film. By definition,

$$\chi_{\text{HNO}_3}(t) = \frac{N_{\text{HNO}_3}(t_{\text{dyn}})}{N_{\text{H}_2\text{O}}(t) + N_{\text{HNO}_3}(t_{\text{dyn}})} \quad (5.12)$$

with N_x the total number of molecules of species x to consider.

In the present work N_{HNO_3} is always smaller than $3 \cdot 10^{15}$ molecules for all experiments we have performed. Taking for example a 50 nm thick ice film doped with $3.0 \cdot 10^{15}$ molecules of HNO_3 , we have $500 \times 0.5 \times 3.11 \cdot 10^{14} = 7.8 \cdot 10^{16}$ molecules of H_2O . As the thickness of the ice films dealt with in the present work is always larger than 50 nm we conclude that $N_{\text{HNO}_3}(t_{\text{dyn}})$ is always significantly smaller compared to $N_{\text{H}_2\text{O}}(t)$. Consequently, χ_{HNO_3} was calculated using the simplified Equation 5.13:

$$\begin{aligned} \chi_{\text{HNO}_3}(t) &= \frac{N_{\text{HNO}_3}(t_{\text{dyn}})}{N_{\text{H}_2\text{O}}(t)} \\ &= \frac{N_{\text{HNO}_3}(t_{\text{dyn}})}{d_{\text{QCM}}(t_{\text{dyn}}) \times 3.11 \cdot 10^{14} \times A_{\text{QCM}} - \text{Int}(J_{\text{ev}}^{18})(t) \times A_{\text{QCM}}} \end{aligned} \quad (5.13)$$

The resulting average relative concentration as a function of time, $\chi_{\text{HNO}_3}(t)$ for the experiment presented in Figure 5.5 is displayed in Figure 5.6 using the (∇) symbol. One must note that the calculated $\chi_{\text{HNO}_3}(t)$ is only strictly valid for the range $t_{\text{dyn}}=0$ to $t_{\text{Hb}}=192$ s as is specified in Figure 5.6. Indeed, we have considered N_{HNO_3} as constant for the calculation of the average relative concentration of HNO₃, χ_{HNO_3} , in the evaporating ice film. However, this assumption is strictly valid only from t_{dyn} to $t_{\text{Hb}}=192$ s at point H_b in Figure 5.5 which corresponds to the time where HNO₃ desorption starts to be observable using MS.

The main goal of the present work is to investigate the dependence of the evaporative flux J_{ev} of H₂O on the average relative concentration of HNO₃ in ice, $\chi_{\text{HNO}_3}(t)$. With this goal in view, we have switched the evaporative flux data from the time dependence of J_{ev} to the concentration scale given by χ_{HNO_3} . From now on J_{ev} will always refer to J_{ev}^{18} , the evaporative flux of H₂O from ice evaluated using the MS signal at $m/z=18$, unless otherwise mentioned.

Figure 5.7 displays the results of $J_{\text{ev}}=f(\chi_{\text{HNO}_3})$ for the experiment presented in Figures 5.5 and 5.6. It illustrates the decrease of J_{ev} with increasing χ_{HNO_3} in an ice film condensed at 190 K and subsequently doped with $1.7 \cdot 10^{15}$ molecule of HNO₃ at 189 K under stirred flow conditions at a rate of $2.2 \cdot 10^{13}$ molec s⁻¹ before the system is set to dynamic conditions. For the purpose of clarity the initial value of J_{ev} at the beginning of the evaporation of the ice film at t_{dyn} has been reported on the left axis labelled "b" of Figure 5.7. In addition, the right axis labelled "e" stands for the value of J_{ev} towards the end of the evaporation after the desorption of most of the adsorbed HNO₃, that is at t_{He} corresponding to point H_e in Figure 5.5.

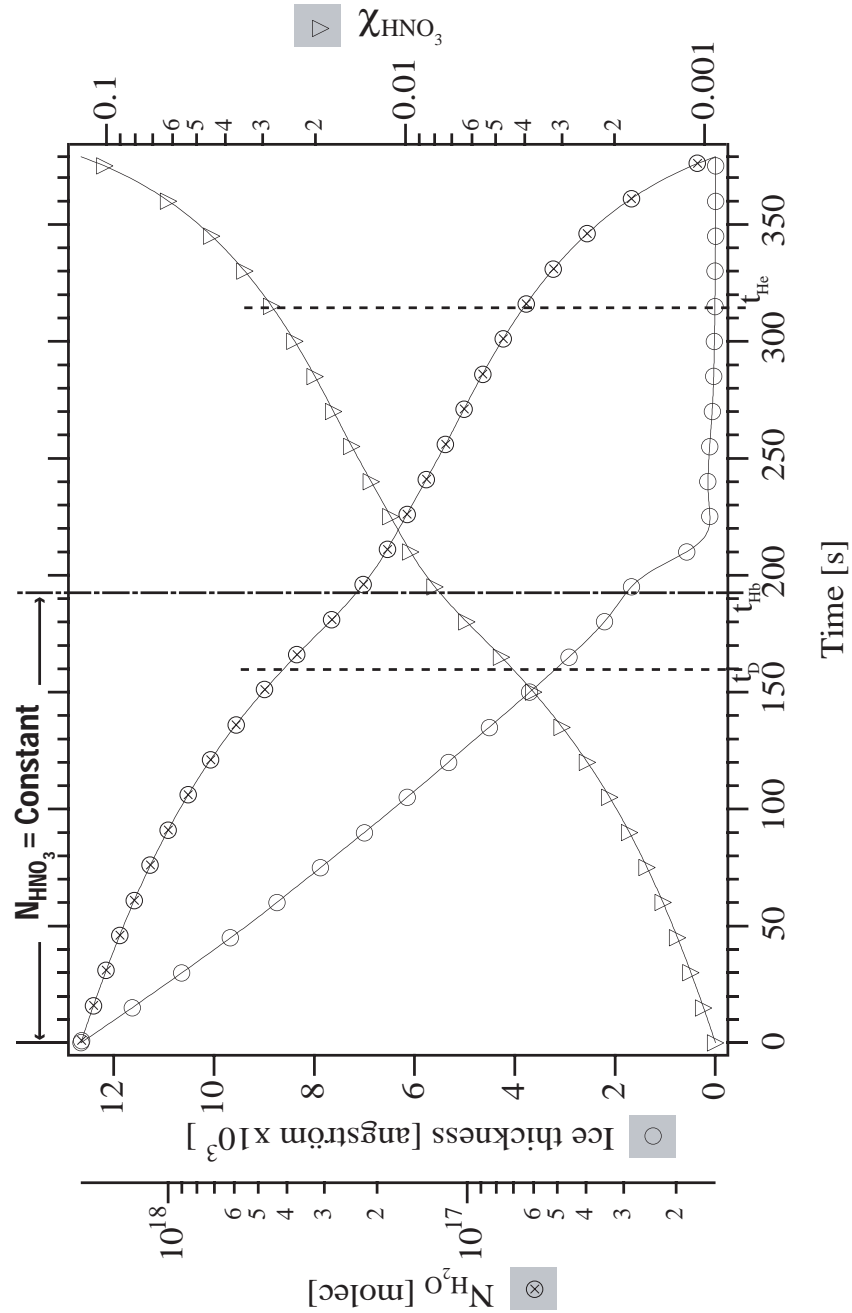


Figure 5.6: Profile of the change of the average relative concentration of HNO₃ at 189 K, χ_{HNO_3} , in the ice film treated in Figure 5.5 during water evaporation. (o): Thickness given by the QCM, $d_{\text{QCM}}(t)$. (\otimes): True number of H₂O molecules on the QCM calculated using Equation 5.11. (∇): Resulting $\chi_{\text{HNO}_3}(t)$ under the assumption of constant N_{HNO_3} (no HNO₃ evaporation observable) and uniform [HNO₃] throughout the whole ice film.

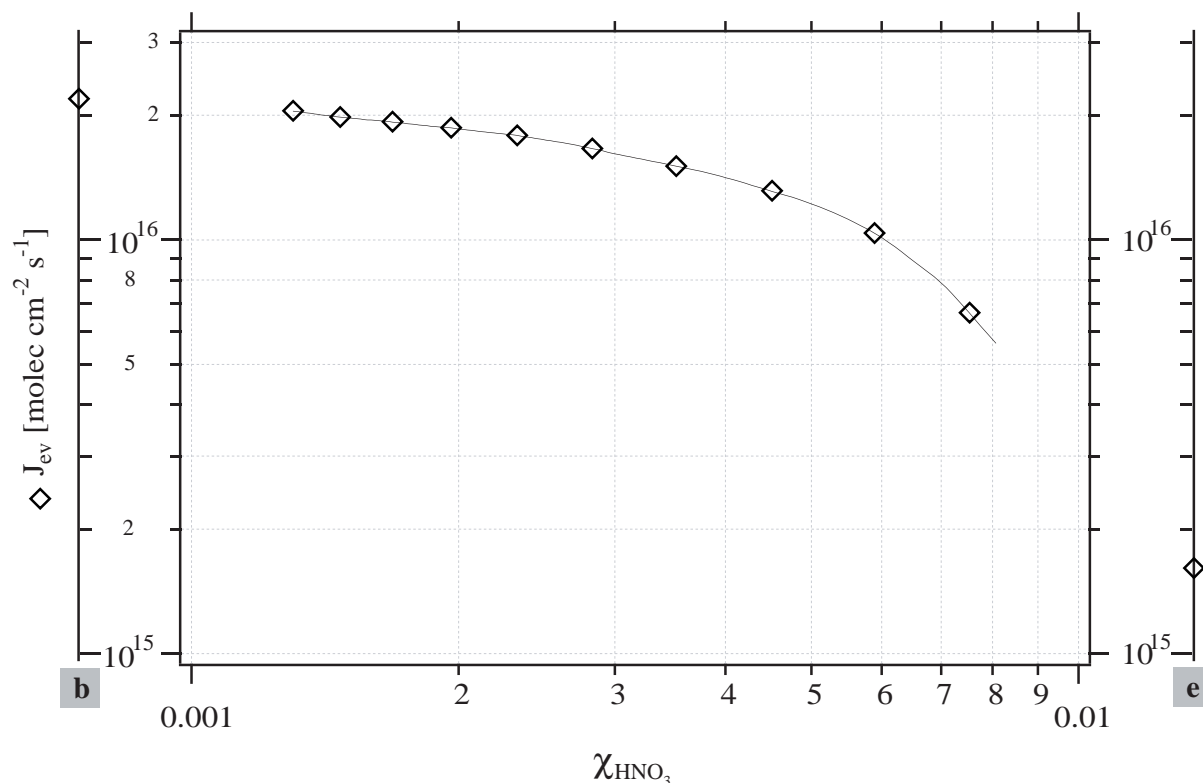


Figure 5.7: Change of the evaporative flux of H_2O , J_{ev} , with the average relative concentration, χ_{HNO_3} , for the case illustrated in Figures 5.5 and Figure 5.6. The significance of the axes with the second label "b" and "e" is explained in the text.

The value of $J_{\text{ev}}^{\text{b}} = 2.2 \cdot 10^{16}$ molec cm⁻² s⁻¹ at the beginning of the evaporation when χ_{HNO_3} is the smallest, that is approximately $8.5 \cdot 10^{-4}$, is in perfect agreement with previously published data for pure ice [19] presented in Chapter 4. It tends to confirm that very small amounts of HNO_3 , corresponding to $\chi_{\text{HNO}_3} \leq 8.5 \cdot 10^{-4}$ in this example, do not affect the kinetics of H_2O evaporation from ice that is characteristic of pure ice [3, 25]. This is true only for the beginning of the evaporation process because the impact of HNO_3 doping on J_{ev} becomes increasingly significant as χ_{HNO_3} increases as displayed in Figure 5.7. According to Figure 5.7 a decrease of a factor of 2 in J_{ev} already occurs for $\chi_{\text{HNO}_3} = 5.6 \cdot 10^{-3}$ which corresponds to a remaining ice film thickness of 193 nm.

During H_2O evaporation from HNO_3 -contaminated ice J_{ev} steadily decreases down to the

value reported on the axis labelled "e". This continuous decrease of J_{ev} with the increase of χ_{HNO_3} has already been reported in Chapter 3 for the cases of HCl and HBr doping. We have chosen to calculate J_{ev}^e , the smallest evaporative flux of H_2O from ice based on I_{18} just before the end of the observable evaporation of HNO_3 at t_{He} corresponding to point H_e in Figure 5.5. Indeed, in most of the experiments reported in the present work J_{ev} varies at a slower rate from t_{Hb} to t_{He} compared to the initial rate as displayed in Figure 5.6 (symbol \otimes). As will be discussed later we attribute this more slowly varying portion of $J_{\text{ev}}(t)$ displayed in Figure 5.6 to the decomposition of NAT. In order to quantitatively express the impact of the presence of HNO_3 on ice we have taken the ratio J_{ev}^b to J_{ev}^e , namely $r^{b/e}$, as follows:

$$r^{b/e} = \frac{J_{\text{ev}}^b}{J_{\text{ev}}^e} \quad (5.14)$$

This ratio brackets J_{ev} between a maximum value, namely that of the evaporation of pure ice, J_{ev}^b , and a minimum value J_{ev}^e that is characteristic of J_{ev} of H_2O at the end of NAT decomposition obtained when the HNO_3 MS signal decreases to the background level after desorption.

For the experiment presented in Figure 5.7 the value of $r^{b/e}$ is 13.7 which illustrates the extent of the decrease of J_{ev} of H_2O due to the presence of HNO_3 on ice for the above cited protocol of HNO_3 deposition.

In addition to the study of the kinetics of evaporation of H_2O from HNO_3 -contaminated ice film we have performed some FTIR spectroscopic investigation of the species that form on ice films when the typical rate and dose for HNO_3 deposition presented in Table 5.2 are applied. The Si window of the cryostat Mark II was then used for ice deposition as was the directed injection of HNO_3 .

The FTIR spectrum presented in Figure 5.8 results from the deposition of a $1.7 \mu\text{m}$ thick ice film on the spectroscopic Si-window at a rate of $1.0 \cdot 10^{17} \text{ molec cm}^{-2} \text{ s}^{-1}$ at 190 K under static conditions.

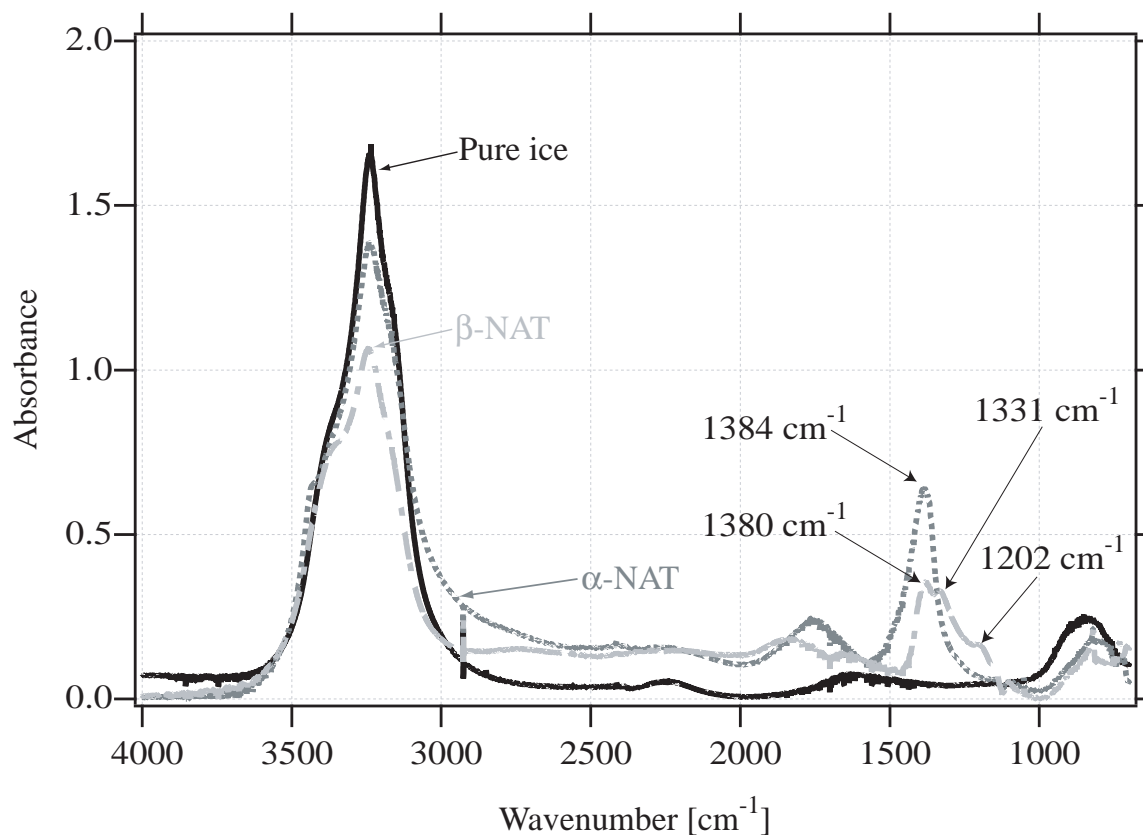


Figure 5.8: Typical transmission FTIR spectra recorded during experiments to evaluate the impact of the deposition of HNO_3 on the vapor pressure of H_2O upon ice. The black spectrum corresponds to pure I_h ice deposited at 190 K before HNO_3 doping. The dark grey trace corresponds to the remaining H_2O and HNO_3 film just before the change in H_2O vapor pressure occurred in the reactor at point **A** in Figure 5.9. It exhibits the sharp 1384 cm^{-1} peak of α -NAT as well as a structure reminiscent of pure ice. All the experiments presented in Table 5.2, performed at a lower rate of deposition and lower dose of HNO_3 , have given similar spectra in experiments on the Si-window. The light grey trace identified as β -NAT appears just after the sudden change in the increasing pressure which begins at point labelled **A** in Figure 5.9.

Subsequently, the system was set to stirred flow conditions and HNO_3 was deposited on top of the ice film by direct injection with the dosing tube in position $\text{DT}_{\text{HNO}_3}^{\text{Si}}$. The rate of deposition of HNO_3 was $7.0 \cdot 10^{14}$ molec s^{-1} to a total adsorbed dose of $4.1 \cdot 10^{17}$ molecules of HNO_3 corresponding to approximately 200 formal monolayers. The system was set to dynamic conditions (GV open) in order to evacuate the excess HNO_3 and H_2O still present in the gas

phase and finally to static conditions. The temperature of the doped ice film was increased at a rate of 4 K min^{-1} in this non-isothermal experiment and the pressure in the reactor under static conditions was monitored using the Baratron pressure gauge (Figure 4.1 item 12, page 109). In Figure 5.8 the black trace represents the FTIR spectrum recorded at the beginning of the experiment without HNO_3 on the ice film under static conditions at 190 K. It corresponds to pure thermodynamically stable I_h ice described in Section 2.7.

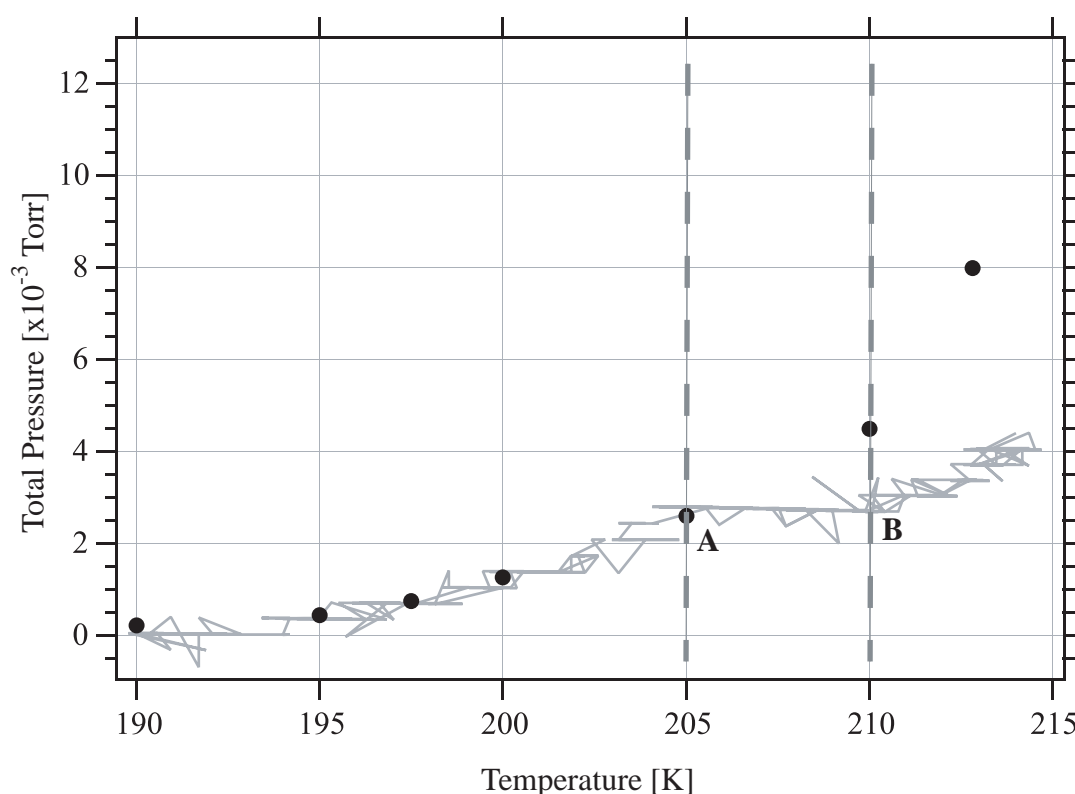


Figure 5.9: Change in $P_{\text{H}_2\text{O}}$ in the presence of ice for the experiment that leads to the FTIR spectra given in Figure 5.8. Experimental conditions and protocol of deposition of $4.1 \cdot 10^{17}$ molecules of HNO_3 are given in the text. The light grey trace corresponding to the measured pressure in the reactor follows the \bullet symbol representing the values for the vapor pressure of H_2O on pure ice of Marti and Mauersberger [26] up to point **A**. The plateau in the pressure observed between points **A** and **B** corresponds to the conversion of α - to β -NAT as shown in Figure 5.8.

The dark grey trace exhibiting a sharp peak at 1384 cm^{-1} typical of metastable α -NAT

corresponds to the last FTIR spectrum recorded for HNO₃-doped ice before departure of P_{H₂O} from the equilibrium vapor pressure P_{H₂O}^{eq} over pure ice occurs. This will be discussed in more detail below.

Indeed, during most of the ice film evaporation with increasing temperature P_{H₂O} corresponds to the equilibrium vapor pressure of H₂O, P_{H₂O}^{eq} despite the large HNO₃ dose applied. In order to illustrate this point Figure 5.9 shows the change of H₂O vapor pressure in the reactor (light grey trace) when the temperature of the ice film is increased. The necessary corrections of the measured pressure caused by the difference in temperature between the ice sample and the reactor wall have been applied following the discussion given in Section 2.4. The black • symbol gives the values for P_{H₂O}^{eq} over ice from Marti and Mauersberger [26]. Up to 205 K and point **A** the total pressure measured in the reactor in the presence of a HNO₃-doped ice film is in excellent agreement with the values of Marti and Mauersberger for pure ice. Beyond T>205 K the total pressure measured using a Baratron pressure gauge was less than P_{H₂O}^{eq} at equilibrium.

5.3 Systematic Results and Discussion

We have focused this work on the influence of the protocol used for the deposition of HNO₃ on an ice film on the resulting kinetics of evaporation of H₂O from ice. Indeed, most of the existing studies dealing with the impact of HNO₃ on ice evaporative rates have been performed in terms of the dependence of the desorption rate of H₂O on the continuous or timed exposure of the ice film to a certain partial pressure of HNO₃ [25], or in terms of the type of nitric acid hydrates or coating [4, 6, 27] without knowledge of the quantities of HNO₃ that were adsorbed on ice as a result of HNO₃ exposure. We are proposing in this work to examine in close detail the dependence of the adsorbed HNO₃ quantities as well as its doping protocol on the changes of the evaporative flux J_{ev} of H₂O during sublimation of a HNO₃/H₂O ice film. In the following we will present and discuss the impact of both the rate of deposition as well as the quantity of HNO₃ adsorbed on the kinetics of H₂O evaporation from a contaminated ice film.

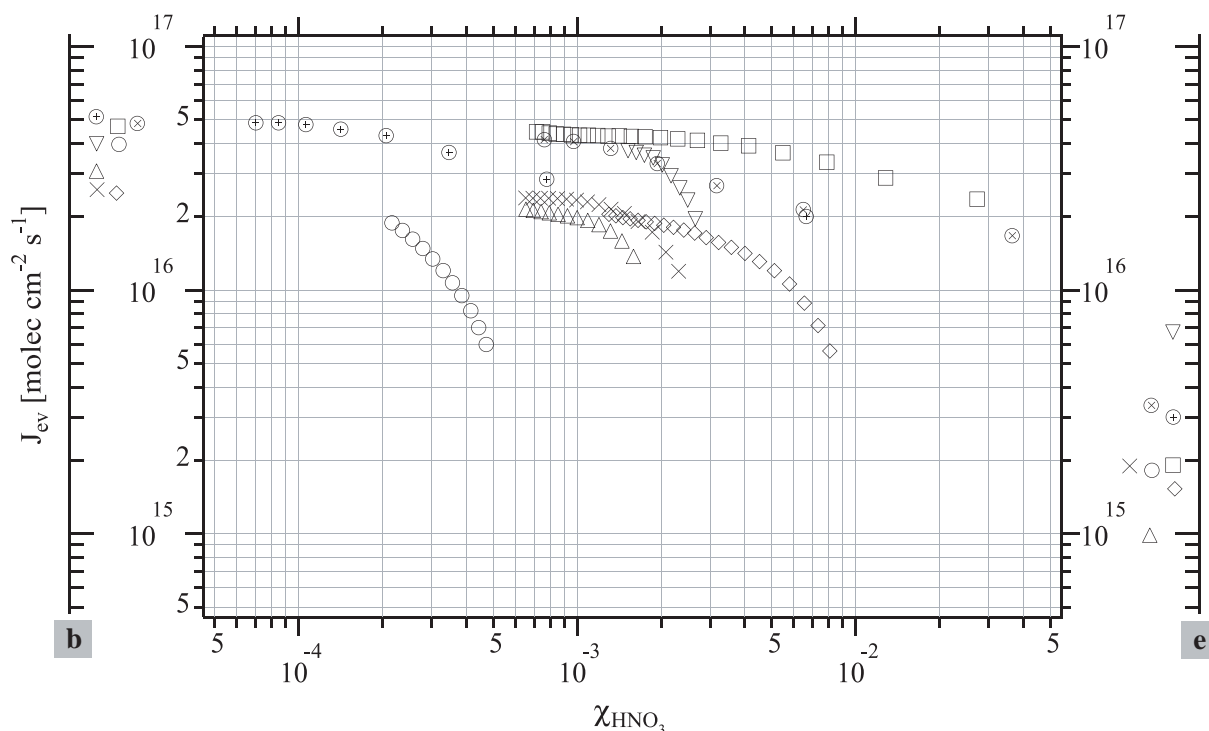


Figure 5.10: Change of evaporative flux, J_{ev} , of H_2O with the average relative concentration, χ_{HNO_3} , for different protocols of HNO_3 deposition on ice in the temperature range $189 < T < 195$ K. Information concerning each experimental set (symbol, rate of deposition and quantity of HNO_3 adsorbed) is listed in Table 5.2. Significance of axes labelled "b" and "e" is given in the text.

Several experiments have been performed to study J_{ev} of H_2O in the temperature range 179-208 K. Selected experimental results are presented in Table 5.2. For the sake of clarity we have arbitrarily broken down the data into three temperature ranges as follows:

- **Range 1:** $189 < T < 195$ K, data displayed in Figure 5.10
- **Range 2:** $179 < T < 185$ K, data displayed in Figure 5.11
- **Range 3:** $205 < T < 208$ K, data displayed in Figure 5.12

For temperature **range 1**, $4.0 \cdot 10^{13}$ to $2.2 \cdot 10^{15}$ molec of HNO_3 were adsorbed on an ice film in the range 189 to 195 K under stirred flow conditions at a rate of HNO_3 deposition

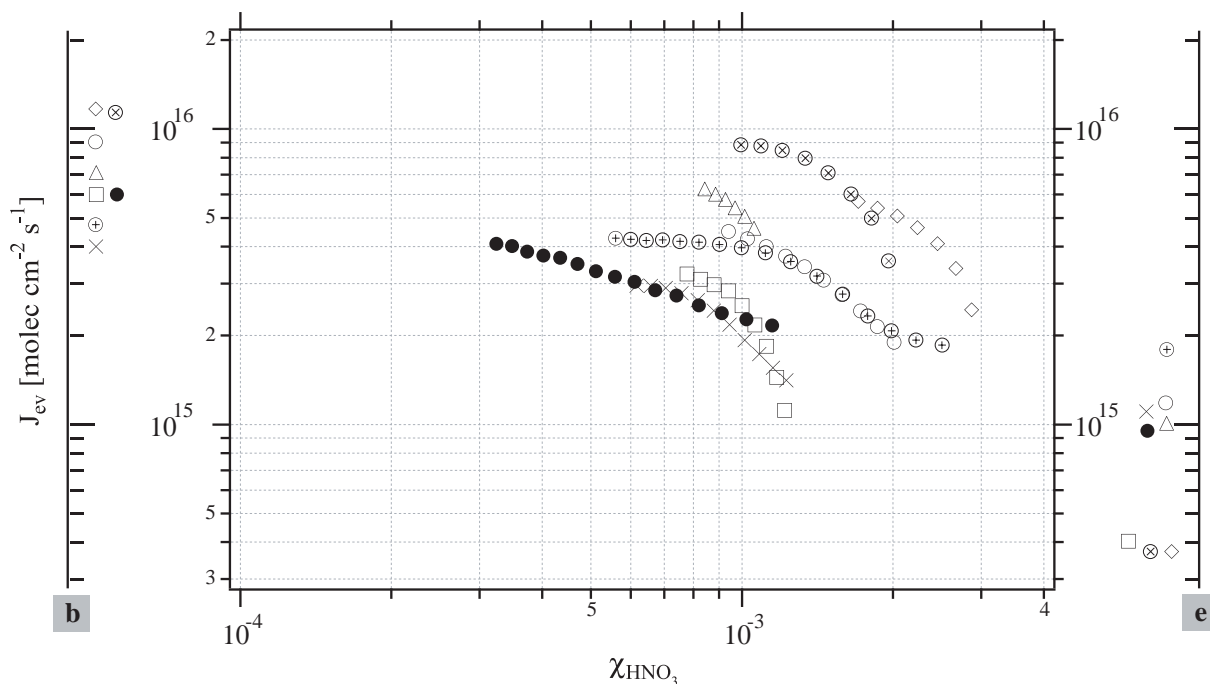


Figure 5.11: Change of evaporative flux, J_{ev} , of H_2O with the average relative concentration, χ_{HNO_3} , for different protocols of HNO_3 deposition on ice in the temperature range $179 < T < 185$ K. Information concerning each experimental set (symbol, rate of deposition and quantity of HNO_3 adsorbed) is listed in Table 5.2. Significance of axes labelled "b" and "e" is given in the text.

between $3.1 \cdot 10^{12}$ to $3.1 \cdot 10^{13}$ molec s^{-1} . Figure 5.10 displays the change of J_{ev} of H_2O during ice film evaporation as a function of increasing average χ_{HNO_3} for the different cases presented in Table 5.2 under **range 1**. The values of $J_{\text{ev}}^{\text{b}}(\text{H}_2\text{O})$ and $J_{\text{ev}}^{\text{e}}(\text{H}_2\text{O})$ are plotted on the left axis labelled "b" and on the right axis labelled "e", respectively. The common trend in the cases presented in Figure 5.10 is a continuous albeit non-linear decrease of J_{ev} starting at J_{ev}^{e} to J_{ev}^{b} during ice film evaporation regardless of the deposition protocol. In most cases J_{ev} first decreases "slowly" before coming to a "fast" decrease with increasing χ_{HNO_3} . In order to identify the nature of the adsorbed HNO_3 on ice we have calculated the equivalent partial pressure of HNO_3 , P_{HNO_3} , required to maintain the measured rate of HNO_3 deposition listed in Table 5.2. Owing to the fact that HNO_3 dosing tubes (see Figure 5.1) oriented towards the

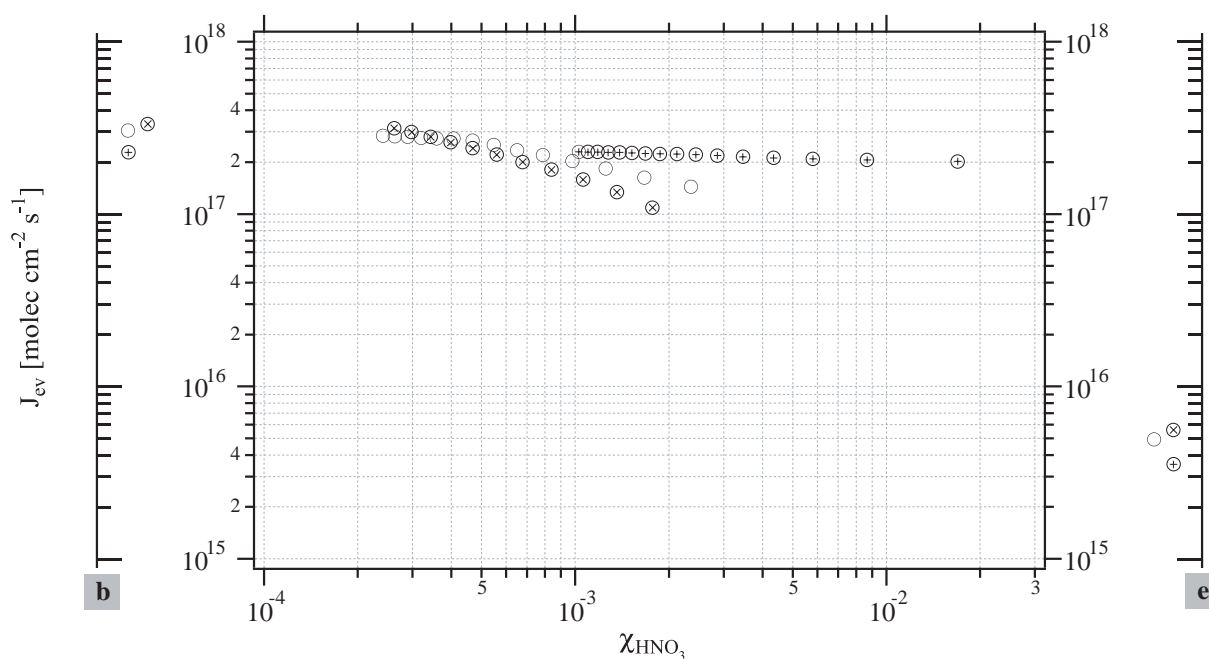


Figure 5.12: Change of evaporative flux, J_{ev} , of H_2O with the average relative concentration, χ_{HNO_3} , for different protocols of HNO_3 deposition on ice in the temperature range $205 < T < 208$ K. Information concerning each experimental set (symbol, rate of deposition and quantity of HNO_3 adsorbed) is listed in Table 5.2. Significance of axes labelled "b" and "e" is given in the text.

ice-film clad QCM sensor have been used, the partial pressure of HNO_3 within the dosing tubes giving rise to the measured rate of uptake of HNO_3 , R_{HNO_3} , was not directly measured. The calculation of the HNO_3 partial pressure resulting in the same rate of adsorption of HNO_3 on ice for each chosen temperature was made using the data published by Aguzzi and Rossi [28] for the uptake coefficient γ of HNO_3 on ice in the range 180-211 K. The resulting pressures are listed in Table 5.3.

The main conclusion from Table 5.3 is that for all the cases presented in this work the predominant HNO_3 species that was formed during deposition on ice is nitric acid trihydrate (NAT, $\text{HNO}_3 \cdot 3\text{H}_2\text{O}$) in agreement with the published $\text{HNO}_3/\text{H}_2\text{O}$ phase diagram [29]. This prediction is confirmed by spectroscopic studies that have been performed using the same deposition protocols and the FTIR window as support (Si) presented in Section 2.7. These FTIR spectra in

Table 5.3: Partial pressure of HNO₃ required to result in the measured rate of HNO₃ deposition, R_{HNO₃}, listed in column 4 and also given in column 5 in Table 5.2.

T range [K]	Experiment number	T _{ice} [K]	R _{HNO₃} [molec s ⁻¹]	γ [28]	P _{HNO₃} [Torr]	Predicted surface species [29]
189-195	5	195	3.1·10 ¹²	0.22	1.1·10 ⁻⁷	NAT
	7	189	3.1·10 ¹³	0.26	9.7·10 ⁻⁷	NAT
179-185	12	180	5.5·10 ¹²	0.30	1.5·10 ⁻⁷	NAT
	18	185	2.2·10 ¹³	0.29	6.0·10 ⁻⁷	NAT
205-208	22	207	5.6·10 ¹²	0.11	4.1·10 ⁻⁷	NAT
	21	207	3.0·10 ¹³	0.11	2.2·10 ⁻⁶	NAT

transmission shown in Figure 5.8 will be used as supporting evidence below. We claim that the systematic formation of nitric acid trihydrate NAT in all experiments performed in this work is due to the deposition of HNO₃ under slightly undersaturated conditions relative to H₂O vapor in agreement with results reported in reference [29]. A comparison of experiment **15** (symbol ⊗) in Figure 5.11) presented in Table 5.2 with the work published by Zondlo et al. [24] leads to the same conclusion that undersaturation in water vapor may be the key to the formation of crystalline NAT. As a case in point, Zondlo et al. show in their study that the deposition of HNO₃ on an ice film leads to an FTIR spectrum characteristic of a supercooled H₂O/HNO₃ liquid at P_{HNO₃}=5.0·10⁻⁷ Torr. It just so happens that the calculated rate of HNO₃ deposition in that work at 185 K based on the uptake coefficient γ=0.29 of Aguzzi and Rossi [28] closely corresponds to experiment **15** listed in Table 5.2. In contrast to Zondlo et al. [24] we observe the formation of NAT that is identified using FTIR absorption to be discussed below. The main difference between the work of Zondlo et al. and the present one is that in the former case the deposition of HNO₃ is performed under equilibrium conditions of H₂O vapor P_{H₂O}^{eq}, whereas the latter occurred under conditions of subsaturation of H₂O vapor at stirred flow, that is at slow pumping conditions leading to P_{H₂O}^{ss}<P_{H₂O}^{eq}. Moreover, as P_{H₂O} or relative humidity was decreased below 100 % in the study of Zondlo et al. the FTIR spectrum indicated a change towards the formation of NAT. They claimed that this change was due to the preferential evaporation of H₂O rather than HNO₃ when the relative humidity decreased. This led to an increased

concentration of HNO_3 in the ice film and reportedly to NAT formation. We confirm that the undersaturation in H_2O vapor may be key to direct crystallisation of NAT during HNO_3 deposition. In support of these conclusions Middlebrook et al. describe the direct nucleation of NAT for conditions of undersaturation of $P_{\text{H}_2\text{O}}$ [30]. Further to our observation that the deposition of HNO_3 systematically leads to the formation of NAT we have chosen to focus our study on the influence of the dose and the rate of deposition of HNO_3 on ice as well as the temperature of deposition as far as $J_{\text{ev}}(\text{H}_2\text{O})$ from HNO_3 -contaminated ice is concerned.

Similar to the data displayed in Figure 5.7 we have plotted the values of $r^{b/e}$ representing the extent of the decrease of J_{ev} for each experiment presented in Figures 5.10, 5.11 and 5.12. The resulting $r^{b/e}$ are displayed in Figures 5.13 and 5.14 as a function of R_{HNO_3} and of the dose of HNO_3 , N_{HNO_3} , respectively. Although it is difficult to duplicate both dose, N_{HNO_3} , and rate of deposition of HNO_3 , R_{HNO_3} , exactly, experiments **15** and **18** performed at 185 K and displayed in Figure 5.11 (symbols \otimes and \diamond in Table 5.2) may be selected to evaluate the reproducibility of the present experiments. Although both dose and rate are approximately 10 % larger in experiment **18** (\diamond) compared to **15** (\otimes) the resulting value for $r^{b/e}$ is identical to within the uncertainty limit as may be seen in Figures 5.13 and 5.14 which thus points to a satisfactory reproducibility.

In search of the experimental parameters controlling the average concentration (χ_{HNO_3}) dependence displayed in Figures 5.10, 5.11 and 5.12 the parameter $r^{b/e}$ bracketing the beginning and the end of a thin film evaporation experiment has been plotted as a function of the logarithm of R_{HNO_3} and $N_{\text{HNO}_3}^{\text{dep}}(t_{\text{dyn}})$ in Figures 5.13 and 5.14. Owing to the fact that the distribution of the $r^{b/e}$ values is practically identical in both figures to within experimental accuracy we come to the conclusion that R_{HNO_3} and $N_{\text{HNO}_3}^{\text{dep}}(t_{\text{dyn}})$ are not independent parameters controlling the observable $r^{b/e}$. Both R_{HNO_3} and $N_{\text{HNO}_3}^{\text{dep}}(t_{\text{dyn}})$ are interconnected by the deposition time t_{dep} through $R_{\text{HNO}_3} \times t_{\text{dep}} = N_{\text{HNO}_3}^{\text{dep}}(t_{\text{dyn}})$ or the time integral of R_{HNO_3} in case it is not constant. This means that a plot of $r^{b/e}$ as a function of t_{dep} would look the same with respect to Figures 5.13 and 5.14 with the exception of points **14** and **16** which are inverted in both figures.

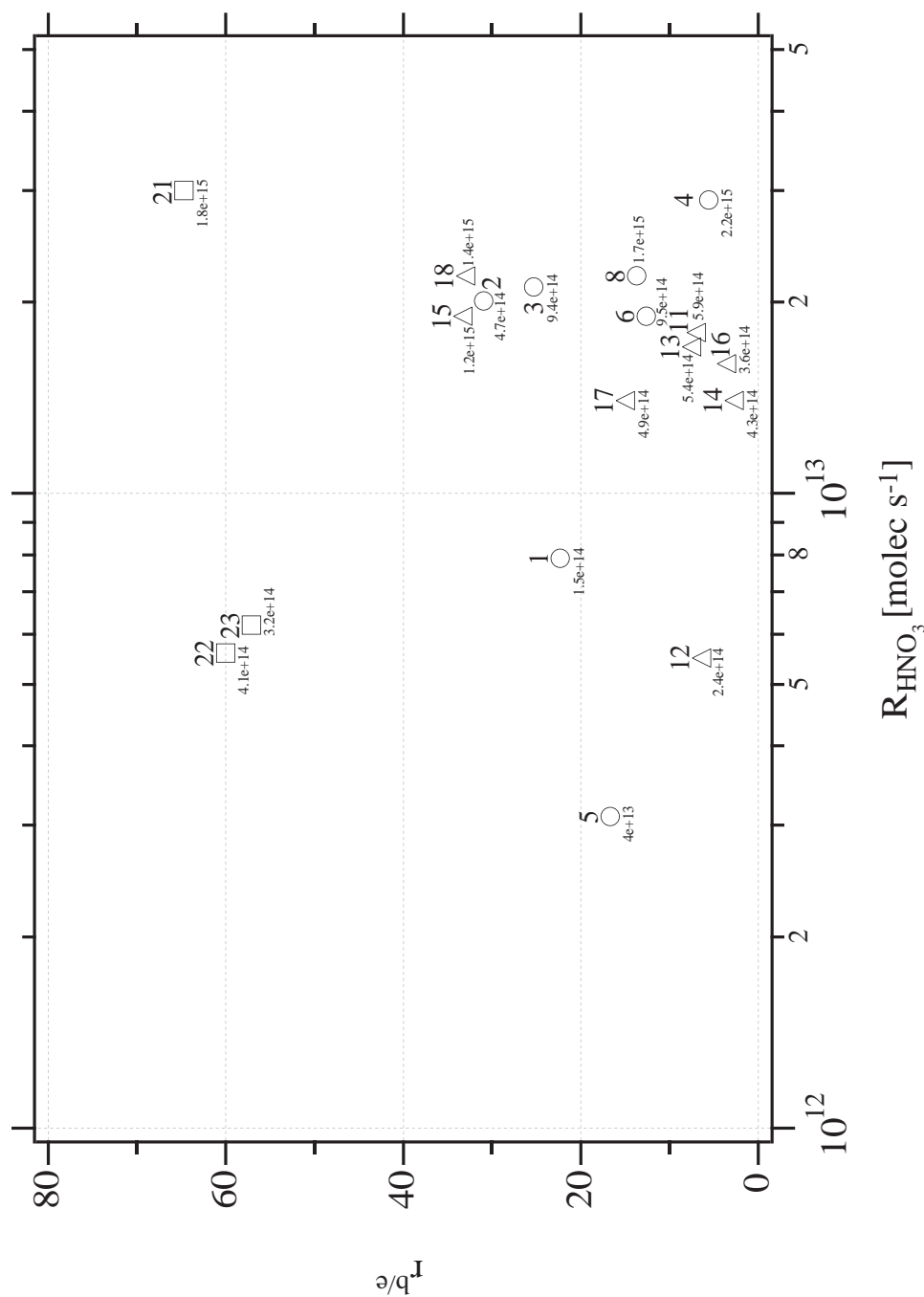


Figure 5.13: Synopsis of the dependence of $r^{b/e}$ on the rate of deposition R_{HNO_3} of HNO_3 for temperatures between 179 and 208 K. Data (o) apply to 189-195 K, (Δ) to 179-185 K, (\square) to 205-208 K. Each point is marked with the total number of HNO_3 molecules deposited on the ice film and with a number referring to each experiment listed in Table 5.2.

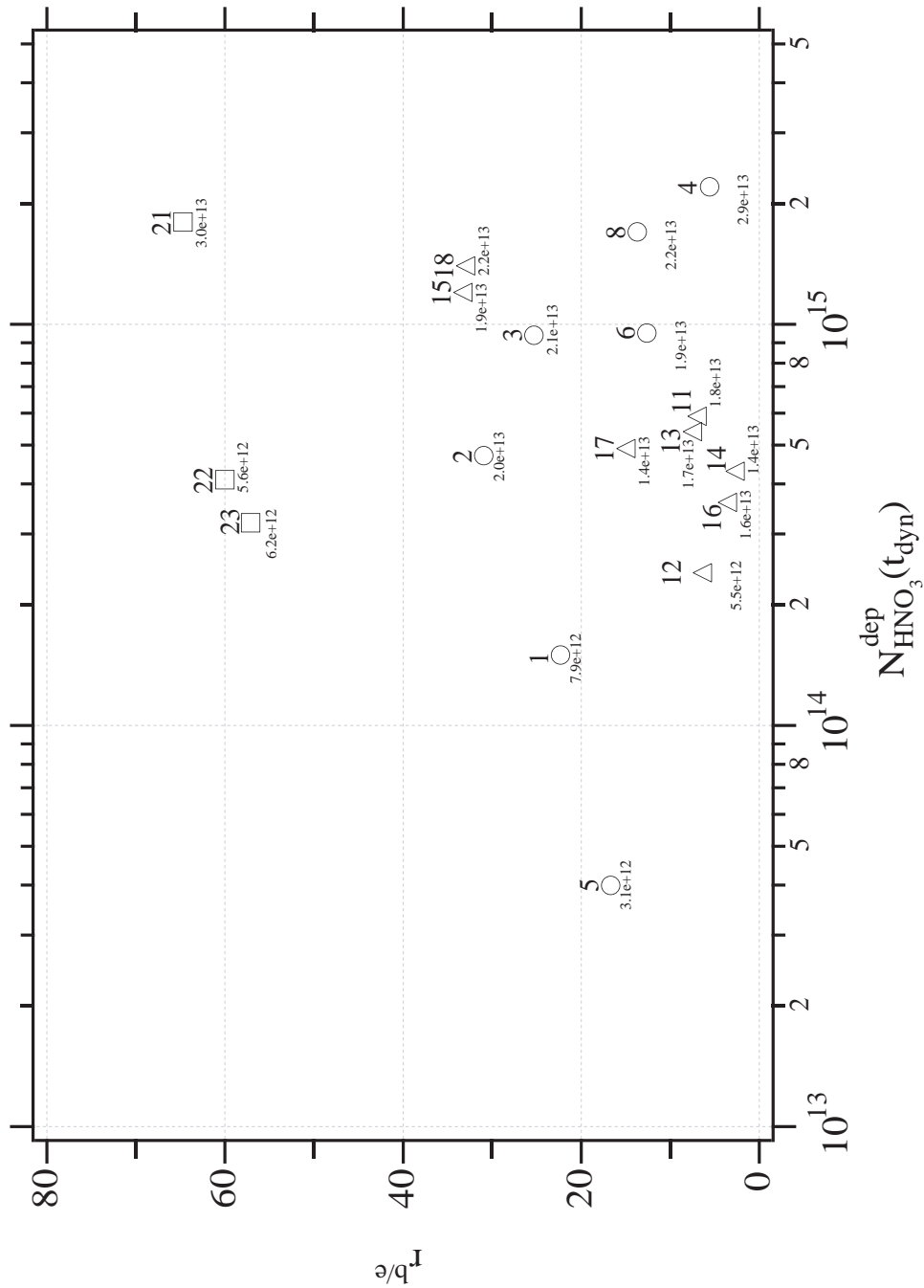


Figure 5.14: Synopsis of the dependence of $r^{b/e}$ on the adsorbed of HNO_3 , $N_{\text{HNO}_3}^{\text{dep}}(t_{\text{dyn}})$, dispensed on ice for temperatures between 179 and 208 K. Data (○) applies to 189-195 K, (△) to 179-185 K, (□) to 205-208 K. Each point is marked with the deposition rate of HNO_3 molecules in molec s^{-1} on the ice film and with a number referring to each experiment information listed in Table 5.2.

To a first approximation temperature seems to be the most important controlling parameter for $r^{b/e}$ with which it scales in some fashion. The $r^{b/e}$ values for **range 3** (205-208 K) are approximately 60 whereas they are between 3 and 15 for **range 2** (179-185 K) with the values for **range 1** lying in-between. There are two apparent exceptions, namely $r^{b/e}$ values for experiments **15** and **18** as well as for experiment **4**. The latter value seems too low for **range 1**, whereas the former values pertaining to **range 2** seem too high although the temperature of 185 K is close to 189 K, the lower bound of **range 1**. Even within a given range the increase of temperature affects $r^{b/e}$ in a significant way which may be seen when considering the increase of $r^{b/e}$ of experiment **6** (189 K) and **3** (193 K). It seems that the details of the concentration dependence of J_{ev} depend in a complex way on several parameters, and the effect of t_{dep} and R_{HNO_3} on $r^{b/e}$ would seem to be an excellent starting point for a systematic study that we have not undertaken in this work. Specifically, the "outlier" experiment **4** leading to low values of $r^{b/e}$ discussed above is also the one performed at the highest value of R_{HNO_3} suggesting an inverse dependence of $r^{b/e}$ on R_{HNO_3} . In fact, experiments **3**, **6**, **8** and **4** of **range 1** displayed in Figure 5.14 lead to lower values of $r^{b/e}$ compared to the maximum for experiment **2**. It is also this group of experiments that has been performed at distinctly higher values of R_{HNO_3} compared to experiments **5** and **1** to the left of the maximum, experiment **2**, small temperature differences within **range 1** notwithstanding. In summary, temperature undoubtedly seems to be an important parameter as well as R_{HNO_3} , $N_{HNO_3}^{dep}(t_{dyn})$ and t_{dep} or a combination thereof. However, the exact functional dependence of $r^{b/e}$ on these three parameters will have to be studied in more detail in the future.

These conclusions have helped us understand the results of Zondlo et al. [24] concerning the decrease of the rate of evaporation of H₂O from ice in the presence of HNO₃. They claimed to have measured a small decrease in J_{ev} of 40 % relative to pure ice. Indeed, we read off a J_{ev} value from their data that is a factor of 1.7 smaller than for pure ice at 0 % relative humidity which approximately corresponds to the previously claimed decrease of 40 %. Using their conditions for deposition of HNO₃ on ice, namely $1.0 \cdot 10^{-5}$ Torr of HNO₃ at dynamic equilibrium and $T=192$

K in conjunction with the uptake coefficient from Aguzzi and Rossi [28] ($T=192$ K, $\gamma=0.23$) we arrive at $N_{\text{HNO}_3}(t_{\text{dyn}})=2.8 \cdot 10^{15}$ molec and $R_{\text{HNO}_3}=2.8 \cdot 10^{14}$ molec s^{-1} . Owing to the trend observed in the present study where increasing values of R_{HNO_3} lead to a decrease of $r^{b/e}$ we would expect a decrease of $r^{b/e}$ to a value lower than 5.6 which is measured in experiment 4. Thus, the low observed value of $r^{b/e}=1.7$ observed by Zondlo et al. would confirm the trend of a decrease of $r^{b/e}$ with increasing R_{HNO_3} given the fact that R_{HNO_3} used in experiment 4 is just a factor of ten lower than the data of Zondlo et al. used for the sake of comparison, whereas $N_{\text{HNO}_3}^{\text{dep}}$ is approximately the same in both cases.

In addition to these kinetic considerations we have investigated the trend in the dependence of the thickness of ice affected by the presence of HNO_3 which should be of prime interest in atmospheric science. We have therefore investigated the influence of both $N_{\text{HNO}_3}(t_{\text{dyn}})$ and R_{HNO_3} on d_{D} defined as the thickness of the remaining ice beyond which J_{ev} is smaller than that for pure ice. Values for d_{D} are given in Table 5.2, and Figures 5.15 and 5.16 show the dependence of d_{D} on R_{HNO_3} and $N_{\text{HNO}_3}(t_{\text{dyn}})$, respectively.

Similar to the effort of searching for the significant parameters controlling $r^{b/e}$ discussed above we have plotted d_{D} as a function of R_{HNO_3} and $N_{\text{HNO}_3}(t_{\text{dyn}})$ in Figures 5.15 and 5.16. Despite the considerable scatter in the plots the temperature seems to group the d_{D} values into broad categories where high and low temperatures correlate with low and high values of d_{D} , respectively, in an inverse relationship. On the other hand, no clear trend of d_{D} with R_{HNO_3} and $N_{\text{HNO}_3}(t_{\text{dyn}})$ can be discerned. However, if one takes the data of **range 1** from Table 5.2, or simply the two limiting experiments 5 and 4 one may be left with the suggestion that a large HNO_3 deposition rate or dose may lead to a large value of d_{D} which would indicate an increasing resistance of an ice film to HNO_3 penetration into the bulk owing to kinetic limits imposed by diffusion of HNO_3 in ice. This will have to be confirmed in further experiments.

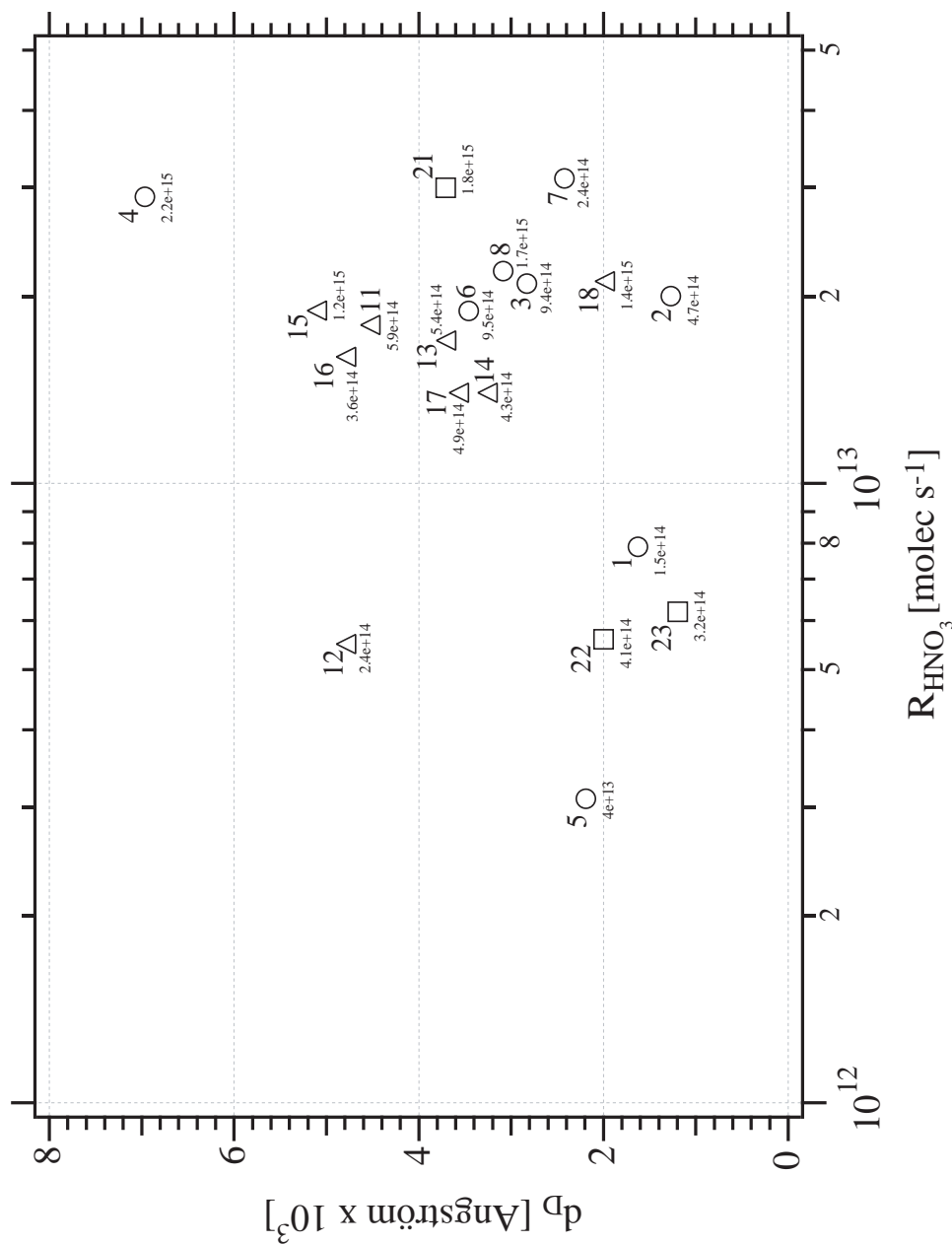


Figure 5.15: Synopsis of the dependence of d_D on the rate of deposition R_{HNO_3} of HNO_3 for temperatures between 179 and 208 K. Data (○) applies to 189-195 K, (△) to 179-185 K, (□) to 205-208 K. Each point is marked with the total number of HNO_3 molecules, $N_{\text{HNO}_3}^{\text{dep}}$, deposited on the ice film and with a number referring to each experiment listed in Table 5.2.

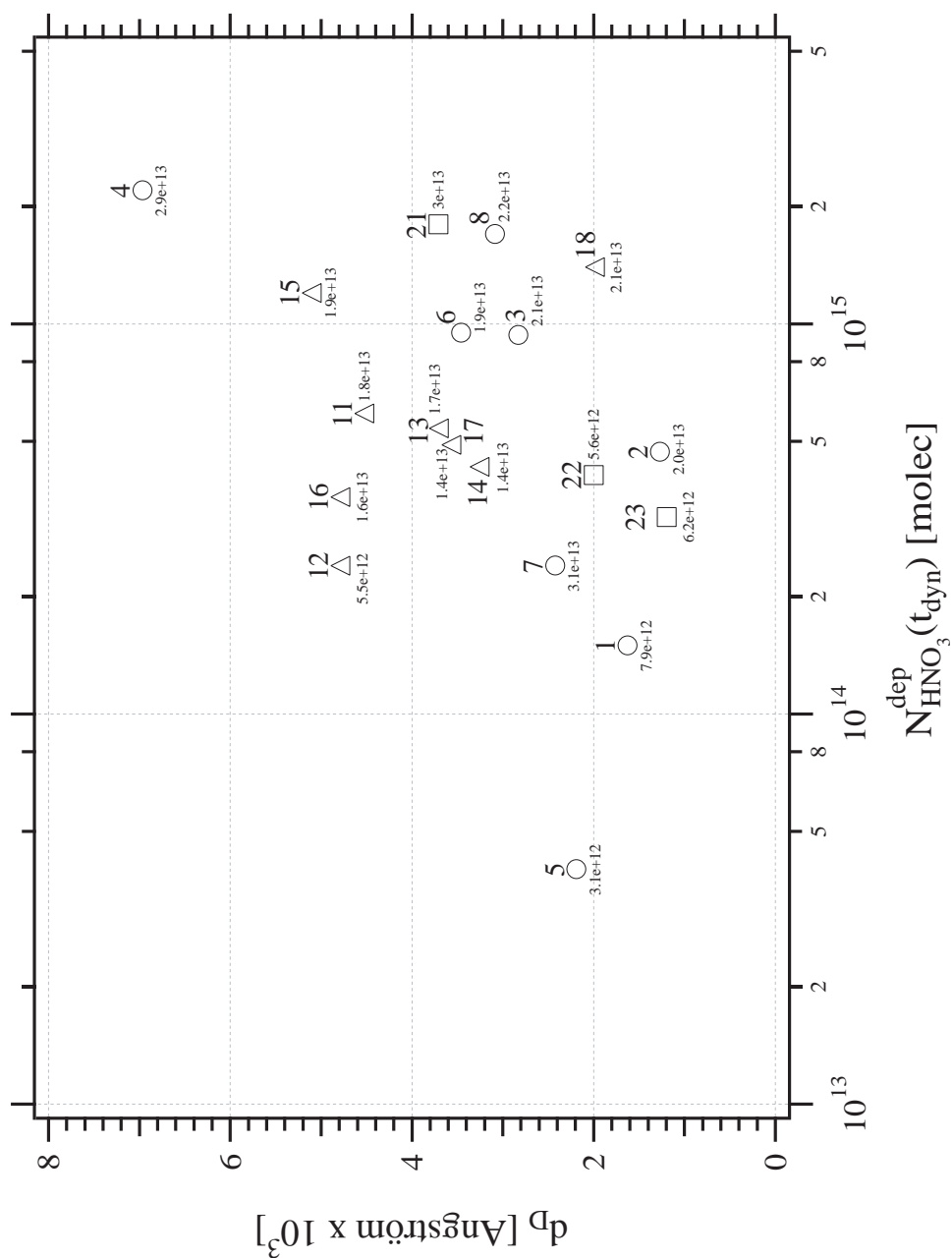


Figure 5.16: Synopsis of the dependence of d_p on the adsorbed number of HNO_3 , $N_{\text{HNO}_3}^{\text{dep}}(t_{\text{dyn}})$, dispensed on ice for temperatures between 179 and 208 K. Data (○) apply to 189-195 K, (△) to 179-185 K, (□) to 205-208 K. Each point is marked with the deposition rate of HNO_3 in molec s^{-1} , R_{HNO_3} , on the ice film and with a number referring to each experiment listed in Table 5.2.

Fahey et al. [2] report the detection of large HNO₃-containing particles in the winter Arctic stratosphere at altitudes between 16 and 21 km. Based on their experimental conditions of 16-21 km altitude, H₂O and HNO₃ mixing ratios of 5 ppmv and 9 ppbv, respectively, a temperature of 192 K and on the measured uptake coefficient for HNO₃ on ice [28] of $\gamma=0.23$ at 192 K we have calculated an equivalent rate of deposition of HNO₃, R_{HNO_3} , of $1.5 \cdot 10^{13}$ molec s⁻¹ in our experimental chamber which closely corresponds to experiment **2** in Table 5.2 that is labelled with the Δ symbol in Figure 5.10. Notwithstanding the fact that experiment **2** has been performed at a slightly larger value of R_{HNO_3} , and lower temperature (190 instead of 192 K) compared to the field experiment reported by Fahey et al. we claim that the relevant laboratory experiment displayed in Figure 5.10 comes quite close to explaining the existence of NAT-”coated” ice particles in the atmosphere. The kinetic results suggest a significantly lower value for J_{ev} of H₂O with increasing χ_{HNO_3} . It will eventually decrease to the limiting low value of J_{ev} in agreement with $r^{\text{b/e}}=30.9$. This low value of J_{ev} will lead to a small but persistent NAT-coated ice particle that will rapidly grow under conditions of H₂O supersaturation.

We have performed several sets of evaporation experiments using the spectroscopic silicon window in order to check whether NAT is the HNO₃ species when deposited on the ice film. The signature of the deposit on the Si-window was monitored using FTIR absorption spectroscopy in transmission. Using the same protocol for ice growth and doping with HNO₃ as the one for deposition on the QCM sensor we have been able to confirm that in all cases the formation of NAT occurred when HNO₃ was deposited on ice under stirred flow conditions. The typical absorption at 1384 cm⁻¹ of NAT and more generally FTIR spectra between 700 and 4000 cm⁻¹ were in good agreement with previously published spectroscopic results [31, 32, 33, 34, 35, 36, 37, 38] for NAT, so called α -NAT. Figure 5.8 presents a typical FTIR spectrum that perfectly agrees with the literature spectra but was recorded in the final stage of evaporation of an investigation of $P_{\text{H}_2\text{O}}^{\text{eq}}$ of a HNO₃-doped ice film.

In Figure 5.8 the black trace corresponds to the FTIR spectrum of the pure ice film before doping with HNO₃. Subsequently, the film is doped with roughly 200 monolayers of HNO₃

at a rate of $7.0 \cdot 10^{14}$ molec s^{-1} and the temperature is increased under static conditions as explained previously. First, the FTIR spectrum of the doped ice exhibits the characteristic band of absorption of so called α -NAT (dark grey trace in Figure 5.8). The decrease of the absorbance in the OH-stretch region (3236 cm^{-1}) is mainly due to the decrease of the thickness of the doped ice film in order to maintain $P_{\text{H}_2\text{O}}^{\text{eq}}$ in the reactor when the temperature increases. When the ice film containing 200 monolayers of HNO_3 reached the temperature of 205 K at point **A** the pressure change started to lag behind the temperature increase of the film up to point **B** at 210 K before increasing again. The light grey trace in Figure 5.8 showing 3 peaks at 1380 , 1331 and 1202 cm^{-1} is representative of the FTIR spectrum of β -NAT just after point **A** was reached. This spectrum has been attributed to other species of NAT in previous studies [34]. The conversion of crystalline NAT from the metastable α - to the stable β - form may be responsible for the change of the FTIR spectrum during the temperature increase as identified in previous studies [30, 39, 40]. This observation may be correlated with the data of Koehler [27] who also report a rapid conversion from α - to β -NAT during TPD experiments, albeit at lower temperatures. It seems that under our experimental conditions the metastable α -NAT is formed on the ascending portion of the total pressure change before reaching point **A** in Figure 5.9, whereas the conversion from α - to the stable β -NAT takes place just after point **A** on the flat portion of the $P_{\text{H}_2\text{O}}^{\text{eq}}$ curve.

Using the parameters given in Table 5.1 for the optical cryostat such as the surface of the silicon window of 0.78 cm^2 , the optical density of ice of 1.08 corresponding to a thickness of 10000 \AA and data published by Middlebrook et al. [36] on the ability for HNO_3 inclusions to hinder ice evaporation, we have calculated the average relative concentration χ_{HNO_3} at point **A** in Figure 5.9. Middlebrook et al. have calibrated the optical density, OD, at 1384 cm^{-1} of α -NAT in order to measure the thickness of NAT films and found $\frac{\text{OD}_{1384}}{\text{thickness}} = 0.728 \mu\text{m}^{-1}$. Using this result we have calculated the thickness of α -NAT given by the dark grey trace displayed in Figure 5.8 to be 8600 \AA . In 1952, Luzzati [41] measured the density of NAT as 1.65 g cm^{-3} based on crystallographic measurements. This value combined with the previously calculated thickness

of 8600 Å gives a total number of $5.7 \cdot 10^{17}$ formula units of NAT in the examined sample. If all adsorbed HNO₃ molecules are implied in NAT formation, the FTIR spectrum would correspond to $5.7 \cdot 10^{17}$ molecules of HNO₃ present on the ice film. This value is larger by approximately 20 % than the one we obtained using the standard method for the determination of the number of HNO₃ molecules deposited onto ice, namely $4.1 \cdot 10^{17}$ molecules, given previously. Using data for pure ice presented in Chapter 3, we have calculated that the dark grey spectrum representing HNO₃-doped ice (α -NAT) in Figure 5.8 corresponds to $3.3 \cdot 10^{18}$ molecules of H₂O if we use the optical density of 1.4 units at the peak of α -NAT of 3236 cm^{-1} . This leads to $\chi_{\text{HNO}_3} = 0.17$ which seems to be necessary to induce a phase change going from a HNO₃/H₂O mixture towards NAT including its associated change of $P_{\text{H}_2\text{O}}^{\text{eq}}$ from point **A** to higher temperatures (Figure 5.9).

This last result is of importance because the case whose spectrum is presented in Figure 5.8 is far more concentrated in HNO₃ compared to all other experiments presented in this study.

To summarize, owing to the sets of experiments presented in this chapter we have been able to observe that the protocol used for the deposition of HNO₃ onto pure ice, namely the rate of deposition, R_{HNO_3} , and the number of HNO₃ molecules deposited, $N_{\text{HNO}_3}^{\text{dep}}$, controls the evaporative flux of H₂O, J_{ev} , from the doped ice film. As was the case in the presence of HCl described in Chapter 3 we have been able to distinguish three different kinds of H₂O molecules in the doped ice film. First, right after the end of the doping process a certain number of H₂O molecules, depending on the doping protocol, evaporate at a rate that is characteristic of pure ice and are apparently not influenced by the presence of HNO₃. Second, remaining H₂O molecules are "trapped" in the ice film and lead to an evaporative flux, J_{ev} that decreases continuously as the number of H₂O molecules in the ice film becomes smaller and smaller, concomitantly with the increasing value of χ_{HNO_3} , the average molar fraction of HNO₃. The evaporation of all these remaining H₂O molecules is influenced by the presence of HNO₃, even if they are not directly involved in the α -NAT structure that is revealed by FTIR spectroscopy. Of utmost importance, the evaporation/condensation of most of these "trapped" H₂O molecules leads to an equilibrium vapor pressure in the presence of a HNO₃-doped ice film that is that of pure ice. This result

implies that the rate of condensation of H_2O onto the doped ice film should decrease to the same extent as J_{ev} in order to achieve thermochemical closure. Finally, as χ_{HNO_3} increases to values higher than 0.17 ± 0.09 we have observed that the equilibrium vapor pressure of H_2O over the doped ice film no longer is the one of pure ice but leads to a lower value.

Bibliography

- [1] C. Voigt, J. Schreiner, A. Kohlmann, P. Zink, K. Mauersberger, N. Larsen, T. Deshler, C. Kroger, J. Rosen, A. Adriani, F. Cairo, G. Di Donfrancesco, M. Viterbini, J. Ovarlez, H. Ovarlez, C. David, and A. Dornbrack, *Science*, 2000, **290**(5497), 1756–1758.
- [2] D. W. Fahey, R. S. Gao, K. S. Carslaw, J. Kettleborough, P. J. Popp, M. J. Northway, J. C. Holecek, S. C. Ciciora, R. J. McLaughlin, T. L. Thompson, R. H. Winkler, D. G. Baumgardner, B. Gandrud, P. O. Wennberg, S. Dhaniyala, K. McKinney, T. Peter, R. J. Salawitch, T. P. Bui, J. W. Elkins, C. R. Webster, E. L. Atlas, H. Jost, J. C. Wilson, R. L. Herman, A. Kleinbohl, and M. von Konig, *Science*, 2001, **291**(5506), 1026–1031.
- [3] U. M. Biermann, J. N. Crowley, T. Huthwelker, G. K. Moortgat, P. J. Crutzen, and T. Peter, *Geophysical Research Letters*, 1998, **25**(21), 3939–3942.
- [4] T. Peter, R. Muller, P. J. Crutzen, and T. Deshler, *Geophysical Research Letters*, 1994, **21**(13), 1331–1334.
- [5] S. C. Wofsy, R. J. Salawitch, J. H. Yatteau, M. B. McElroy, B. W. Gandrud, J. E. Dye, and D. Baumgardner, *Geophysical Research Letters*, 1990, **17**(4), 449–452.
- [6] R. S. Gao, P. J. Popp, D. W. Fahey, T. P. Marcy, R. L. Herman, E. M. Weinstock, D. G. Baumgardner, T. J. Garrett, K. H. Rosenlof, T. L. Thompson, P. T. Bui, B. A. Ridley, S. C. Wofsy, O. B. Toon, M. A. Tolbert, B. Karcher, T. Peter, P. K. Hudson, A. J. Weinheimer, and A. J. Heymsfield, *Science*, 2004, **303**(5657), 516–520.
- [7] S. A. Stern, J. T. Mullhaupt, and W. B. Kay, *Chemical Reviews*, 1960, **60**(2), 185–207.
- [8] P. K. Hudson, J. E. Shilling, M. A. Tolbert, and O. B. Toon, *Journal of Physical Chemistry A*, 2002, **106**(42), 9874–9882.
- [9] F. F. Fenter, F. Caloz, and M. J. Rossi, *Journal of Physical Chemistry*, 1994, **98**(39), 9801–9810.
- [10] A. Aguzzi *Atmospheric heterogeneous reactions of chlorine and bromine containing molecules: a laboratory study. (Thesis number 2403)* PhD thesis, Ecole Polytechnique Fédérale de Lausanne, Suisse, 2001.
- [11] J. Hessinger and R. O. Pohl, *Journal of Non-Crystalline Solids*, 1996, **208**(1-2), 151–161.
- [12] J. Hessinger, B. E. White, and R. O. Pohl, *Planetary and Space Science*, 1996, **44**(9), 937–944.
- [13] A. A. Elvin, J. J. Connor, and D. H. Choi, *Journal of Engineering Mechanics-Asce*, 1998, **124**(1), 54–60.
- [14] B. S. Berland, D. E. Brown, M. A. Tolbert, and S. M. George, *Geophysical Research Letters*, 1995, **22**(24), 3493–3496.

-
- [15] M. Kumai, *Journal of Glaciology*, 1968, **7**, 95–108.
- [16] M. S. Bergren, D. Schuh, M. G. Sceats, and S. A. Rice, *Journal of Chemical Physics*, 1978, **69**(8), 3477–3482.
- [17] C. Delval, B. Fluckiger, and M. J. Rossi, *Atmospheric Chemistry and Physics*, 2003, **3**, 1131–1145.
- [18] C. S. Lu and O. Lewis, *Journal of Applied Physics*, 1972, **43**(11), 4385–4390.
- [19] C. Delval and M. J. Rossi, *Physical Chemistry Chemical Physics*, 2004, **6**, 4665–4676.
- [20] P. Pratte and M. J. Rossi, *Submitted*, (2004).
- [21] J. A. Smith, F. E. Livingston, and S. M. George, *Journal of Physical Chemistry B*, 2003, **107**(16), 3871–3877.
- [22] E. Thibert and F. Domine, *Journal of Physical Chemistry B*, 1998, **102**(22), 4432–4439.
- [23] M. A. Zondlo, S. B. Barone, and M. A. Tolbert, *Journal of Physical Chemistry A*, 1998, **102**(29), 5735–5748.
- [24] M. A. Zondlo, P. K. Hudson, A. J. Prenni, and M. A. Tolbert, *Annual Review of Physical Chemistry*, 2000, **51**, 473–499.
- [25] M. S. Warshawsky, M. A. Zondlo, and M. A. Tolbert, *Geophysical Research Letters*, 1999, **26**(7), 823–826.
- [26] J. Marti and K. Mauersberger, *Geophysical Research Letters*, 1993, **20**(5), 363–366.
- [27] B. G. Koehler, *International Journal of Chemical Kinetics*, 2001, **33**(5), 295–309.
- [28] A. Aguzzi and M. J. Rossi, *Physical Chemistry Chemical Physics*, 2001, **3**(17), 3707–3716.
- [29] D. R. Worsnop, L. E. Fox, M. S. Zahniser, and S. C. Wofsy, *Science*, 1993, **259**(5091), 71–74.
- [30] A. M. Middlebrook, B. S. Berland, S. M. George, M. A. Tolbert, and O. B. Toon, *Journal of Geophysical Research-Atmospheres*, 1994, **99**(D12), 25655–25666.
- [31] J. Roziere and J. Potier, *Journal of Inorganic and Nuclear Chemistry*, 1973, **35**(4), 1179–1183.
- [32] M. A. Tolbert and A. M. Middlebrook, *Journal of Geophysical Research-Atmospheres*, 1990, **95**(D13), 22423–22431.
- [33] R. H. Smith, M. T. Leu, and L. F. Keyser, *Journal of Physical Chemistry*, 1991, **95**(15), 5924–5930.
- [34] G. Ritzhaupt and J. P. Devlin, *Journal of Physical Chemistry*, 1991, **95**(1), 90–95.

Chapter 5. The influence of monolayer amounts of HNO₃ on the evaporation rates of H₂O over ice in the range 179 to 208 K: a QCM study.

- [35] N. Barton, B. Rowland, and J. P. Devlin, *Journal of Physical Chemistry*, 1993, **97**(22), 5848–5851.
- [36] A. M. Middlebrook, M. A. Tolbert, and K. Drdla, *Geophysical Research Letters*, 1996, **23**(16), 2145–2148.
- [37] R. T. Tisdale, A. J. Prenni, L. T. Iraci, M. A. Tolbert, and O. B. Toon, *Geophysical Research Letters*, 1999, **26**(6), 707–710.
- [38] R. Escribano, M. Couceiro, P. C. Gomez, E. Carrasco, M. A. Moreno, and V. J. Herrero, *Journal of Physical Chemistry A*, 2003, **107**(5), 651–661.
- [39] M. A. Tolbert, B. G. Koehler, and A. M. Middlebrook, *Spectrochimica Acta Part a-Molecular and Biomolecular Spectroscopy*, 1992, **48**(9), 1303–1313.
- [40] S. Peil, S. Seisel, and O. Schrems, *Journal of Molecular Structure*, 1995, **348**, 449–452.
- [41] V. Luzzati, *Acta Crystallographica*, 1953, **6**(2), 152–157.

Chapter 6

The influence of monolayer amounts of HCl on the evaporation rates of H₂O over ice in the range 188 to 210 K: a QCM study.

Chapter 3 ended by stressing the significant effect of the presence of submonolayer to quantities of several monolayers of HCl on the kinetics of evaporation and condensation of H₂O in the presence of ice. The HCl doping apparently leads to the decrease of both the evaporative flux, J_{ev} , and the rate of condensation, k_{cond} , of H₂O onto ice as presented in Figures 3.4 and 3.5 (on pages 75 and 76, respectively) without, essentially, perturbing the equilibrium vapor pressure of H₂O, $P_{\text{H}_2\text{O}}^{\text{eq}}$, in the presence of ice. It was also shown that the way J_{ev} decreases with time depends on the rate of deposition and the number of deposited HCl molecules as reported for a few typical examples in Table 3.3 on page 82. On the basis of the data presented in this table it is clear that the different HCl species on ice, namely amorphous HCl·H₂O and crystalline HCl·6H₂O slow down the evaporative flux in a different manner. Moreover, Table 3.4 on page 85,

summarized the limiting conditions on the rate of deposition of HCl on ice, namely $1 \cdot 10^{13}$ to $5 \cdot 10^{13}$ molec s⁻¹ on the 0.78 cm² ice surface area, that lead to the formation of crystalline HCl·6H₂O whereas all rates of deposition outside this window of opportunity seemed to favor formation of amorphous HCl·H₂O. It therefore becomes clear that crystallization seems to occur only under very specific conditions of doping. It also follows from this conclusion that the way J_{ev} decreases as a function of time depends on the rate of deposition of HCl, R_{HCl} , on ice by combining the results presented in Tables 3.3 and 3.4. In addition, the previous chapter reported the fact that in the case of the controlled contamination of ice by HNO₃ the way J_{ev} decreases is governed by a complex interplay between parameters such as the rate of deposition of HNO₃ on ice, R_{HNO_3} , the number of deposited HNO₃ molecules, $N_{\text{HNO}_3}^{\text{dep}}$, the time of deposition, t_{dep} , and the temperature of deposition of HNO₃, T_{ice} , as reported in Figures 5.13 to 5.16 (pages 190 to 195) despite the fact that NAT is always observed under the chosen doping conditions.

The consideration of all these results has led us to perform a few experiments using the QCM technique to investigate the impact of HCl doping on the temporal change of $J_{\text{ev}}(\text{H}_2\text{O})$. The main goal of this work is to determine to what extent the protocol used for HCl deposition on ice, namely R_{HCl} and N_{HCl} , may be responsible for the scatter of the data concerning J_{ev} and γ presented in Figures 3.4 and 3.5 for HCl-doped ice.

6.1 Experiments and Results

The apparatus has been described in the previous chapters. The experimental conditions are nearly the same and the corresponding experimental parameters are summarized in Table 6.1.

The only significant difference between the study of HNO₃-doped ice in Chapter 5 and the present condensed phase investigation of HCl-doped ice is in the mode of the trace gas injection. Whereas HNO₃ was deposited by directed injection on ice films as described in Figure 5.1 displayed on page 162, HCl was deposited by backfilling of the reactor under stirred

Table 6.1: Hardware parameters of both cryogenic sample supports for the kinetic study of HCl-doped ice.

	Si Optical Window	QCM
Reactor temperature T_r [K]	320	
Reactor volume V_r [K]	2350	
Conversion factor (1/RT) Conv [molec cm ⁻³ Torr ⁻¹]	$3.0 \cdot 10^{16}$	
Sample surface area [cm ²]	0.78	0.50
H ₂ O collision frequency with ice sample ω_{H_2O} [s ⁻¹]	5.08	3.26
H ₂ O effusion rate constant of calibrated leak $k_{esc}(H_2O)$ [s ⁻¹]	0.064	
MS calibration factor for H ₂ O (m/z=18, <i>Stirred Flow</i>) C_{18}^{s-flow} [molec s ⁻¹ A ⁻¹]	$2.4 \cdot 10^{24}$	
MS calibration factor for H ₂ O (m/z=18, <i>Dynamic</i>) C_{18}^{dyn} [molec s ⁻¹ A ⁻¹]	$1.7 \cdot 10^{25}$	
HCl collision frequency with ice sample ω_{HCl} [s ⁻¹]	3.59	2.31
HCl effusion rate constant of calibrated leak $k_{esc}(HCl)$ [s ⁻¹]	0.047	
MS calibration factor for HCl (m/z=36, <i>Stirred Flow</i>) C_{36}^{s-flow} [molec s ⁻¹ A ⁻¹]	$3.9 \cdot 10^{24}$	
MS calibration factor for HCl (m/z=36, <i>Dynamic</i>) C_{36}^{dyn} [molec s ⁻¹ A ⁻¹]	$6.3 \cdot 10^{24}$	
Calculated escape orifice area A_{esc} [mm ²]	1.0	
Thickness for		
FTIR O.D. = 1.08 [Å] ^a		
10000		
		calibration factor
	Temperature [K]	C_f [a.u.]
	170	9.0
	180	8.0
	190	7.8
	193	6.0
	205	2.0
	208	1.9

^asee Equation 2.23, page 50

flow conditions with the inlet tubing used for trace gas injection oriented towards the Si-window of the cryostat in position DT_{HX}^{Si} in the absence of an ice film in analogy to $DT_{HNO_3}^{Si}$ described in Section 5.1 page 161. This choice was imposed by the transformation of the cryostat from IR transmission to a geometry that accommodates a grazing incidence experiment to be discussed in detail in Chapter 7. This represents the next step in the evolution of this multiple diagnostics experiment, however, it temporarily prevented the directed injection onto the QCM sensor.

Evaporation experiments have been performed in the temperature range 188-210 K. The rate of deposition of HCl, R_{HCl} , as well as the number of HCl molecules, N_{HCl} , deposited on ice have been evaluated using the method described in Section 2.5, on page 40. Typically, R_{HCl} ranges between $8.0 \cdot 10^{11}$ and $4.2 \cdot 10^{13}$ molec s⁻¹ and N_{HCl} between $1.0 \cdot 10^{14}$ and $5.4 \cdot 10^{15}$ molecules. The experimental conditions of HCl-doping as well as some representative results are reported in Table 6.2.

One may note that as was the case for HNO₃ the mass balance under dynamic conditions (see Section 5.1) between HCl deposited, N_{HCl}^{dep} , and HCl recovered in the process of ice evaporation, N_{HCl}^{evap} , agrees to within better than a factor of 2 which corresponds to the worst case. In the following N_{HCl} will always refer N_{HCl}^{dep} .

The data have been treated like the ones dealing with HNO₃-doped ice in Section 5.2 through Equations 5.8 to 5.13 (pages 175 to 178).

The experimental data reported in Table 6.2 on the change of the evaporative flux, J_{ev} , of H₂O as a function of the average relative concentration of HCl, χ_{HCl} , in the remaining ice film during the evaporation process under dynamic conditions (GV open) are presented in Figure 6.1. The axes labelled "b" and "e" correspond to the values of J_{ev} of H₂O at the beginning of the ice evaporation and after desorption of most of the adsorbed HCl, respectively. Two different trends in the change of J_{ev} with χ_{HCl} may be distinguished in Figure 6.1. The first corresponds to the curves describing J_{ev} in the case of experiments **1**, **2**, **9** and **11** and defined as **set A**

Table 6.2: Representative experimental results for the kinetics of H₂O evaporation in the presence of HCl for different temperatures, rates of deposition and doses of HCl. In the first column the number refers to the corresponding experiment and identifies the data in Figures 6.1 to 6.5.

Experiment number	T _{ice}	R _{HCl}	t _{dep}	N _{HCl} ^{dep}	N _{HCl} ^{evap}	d _D	J _{ev} ^b	J _{ev} ^e	r ^{b/e}
	[K]	[molec s ⁻¹]	[s]	[molec]	[molec]	[Å]	[molec cm ⁻² s ⁻¹]	[molec cm ⁻² s ⁻¹]	
1	192	3.1·10 ¹²	36	1.0·10 ¹⁴	1.8·10 ¹⁴	2823	2.9·10 ¹⁶	7.1·10 ¹⁴	40.8
2	192	8.0·10 ¹¹	356	2.6·10 ¹⁴	1.6·10 ¹⁴	6817	3.2·10 ¹⁶	6.5·10 ¹⁴	49.2
3	193	3.5·10 ¹²	220	7.0·10 ¹⁴	8.1·10 ¹⁴	5659	4.9·10 ¹⁶	1.8·10 ¹⁵	27.2
4	190	4.2·10 ¹³	126	5.4·10 ¹⁵	3.6·10 ¹⁵	6360	2.9·10 ¹⁶	1.4·10 ¹⁵	20.7
5	188	1.3·10 ¹³	66	8.7·10 ¹⁴	8.9·10 ¹⁴	4540	1.2·10 ¹⁶	3.9·10 ¹⁵	3.1
6	190	3.9·10 ¹³	56	2.2·10 ¹⁵	1.8·10 ¹⁵	12861	3.4·10 ¹⁶	1.7·10 ¹⁶	2.0
7	195	4.3·10 ¹²	45	1.9·10 ¹⁴	1.8·10 ¹⁴	5325	4.6·10 ¹⁶	2.0·10 ¹⁵	23.0
8	205	1.6·10 ¹³	36	5.9·10 ¹⁴	3.0·10 ¹⁴	4607	2.0·10 ¹⁷	1.0·10 ¹⁶	20.0
9	210	3.5·10 ¹²	84	3.0·10 ¹⁴	1.9·10 ¹⁴	12136	3.0·10 ¹⁷	1.8·10 ¹⁶	16.7
10	174	6.4·10 ¹²	94	6.0·10 ¹⁴	4.7·10 ¹⁴	2733	1.9·10 ¹⁵	4.4·10 ¹⁴	4.3
11	192	5.4·10 ¹²	108	5.4·10 ¹⁴	6.8·10 ¹⁴	7717	4.0·10 ¹⁶	7.9·10 ¹⁴	50.6

of the data. These traces present a slow continuous decrease of J_{ev} as χ_{HCl} increases during H₂O evaporation. The corresponding values of R_{HCl} range from $8.0 \cdot 10^{11}$ to $5.4 \cdot 10^{12}$ molec s⁻¹. The second trend is characterized by an initial plateau of J_{ev} with increasing χ_{HCl} starting from pure ice evaporation followed by a sudden decrease of J_{ev} . This behavior corresponds to the evolution of J_{ev} for experiments **3**, **4**, **7** and **8** and is called **set B** of the data. For these experiments the corresponding R_{HCl} ranges from $3.5 \cdot 10^{12}$ to $4.2 \cdot 10^{13}$ molec s⁻¹ which is larger than for **set A**.

As was the case for the HNO₃ study presented in the previous chapter, we have evaluated the impact of the doping protocol on the ratio, $r^{\text{b/e}}$, between the evaporative flux at the beginning of ice evaporation, J_{ev}^{b} , that is reported on the left axis in Figure 6.1, and the evaporative flux nearly at the end after desorption of HCl into the gas phase, J_{ev}^{e} , that is reported on the right axis in Figure 6.1. Further explanations are given in Section 5.2 on page 181. The impact of both the rate of deposition of HCl on ice, R_{HCl} , and the dose of deposited HCl, N_{HCl} , are presented in Figures 6.2 and 6.3, respectively. It appears from these figures that the data may be classified along the separation into two cases presented previously, namely data **sets A** and **B**. Indeed, considering data **set A** it seems that $r^{\text{b/e}}$ depends on a complex combination of R_{HCl} , N_{HCl} and the temperature of deposition as was the case in the HNO₃ study. One may take note for instance of the low value of $r^{\text{b/e}}$ at 210 K for experiment **9** where the conditions of deposition are not very different from the ones of experiments **1** and **2**, and yet, their respective values of $r^{\text{b/e}}$ differ significantly. As opposed to the case of HNO₃ it seems that $r^{\text{b/e}}$ is inversely dependent on T_{ice} in the case of HCl. Considering experiments **1**, **2** and **11**, it seems that $r^{\text{b/e}}$ increases with N_{HCl} and decreases with R_{HCl} . Interestingly, for data **set B** the $r^{\text{b/e}}$ values are nearly the same for all the cases between 20 and 27.2 and, moreover, seem independent of R_{HCl} and N_{HCl} . In contrast, the $r^{\text{b/e}}$ values for **set A** seem widely scattered over the parameter space.

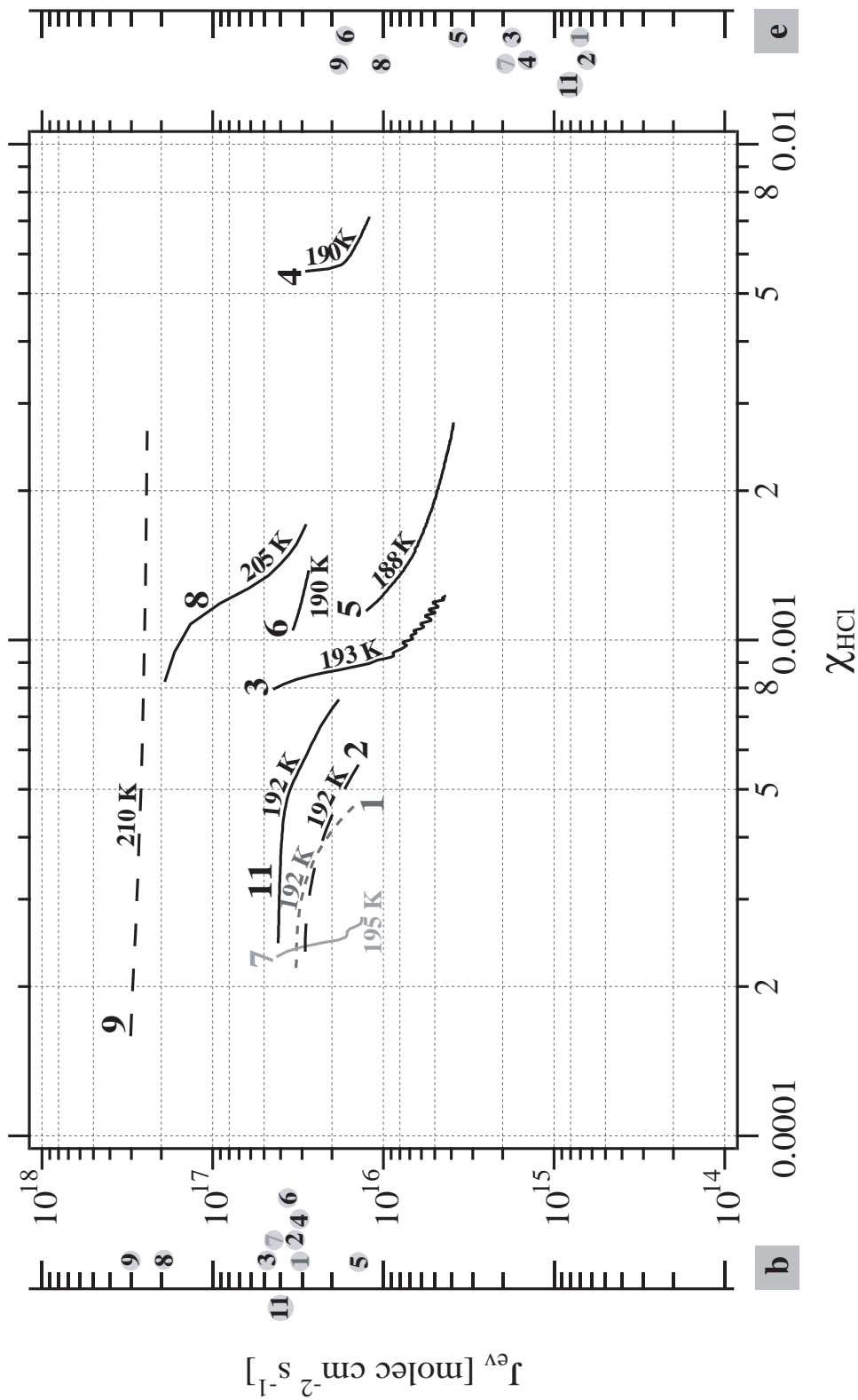


Figure 6.1: Change of the evaporative flux J_{ev} of H_2O with the average relative concentration, χ_{HCl} , for the cases presented in Table 6.2. The significance of the axes with the second label "b" and "e" is explained in the text.

In addition, we have also investigated the impact of the protocol used for deposition on d_D , which is the thickness of ice that is affected by the presence of HCl, namely the remaining thickness of ice that corresponds to a change of J_{ev} of H₂O in the presence of ice (see Section 5.2). The results are presented in Figures 6.4 and 6.5.

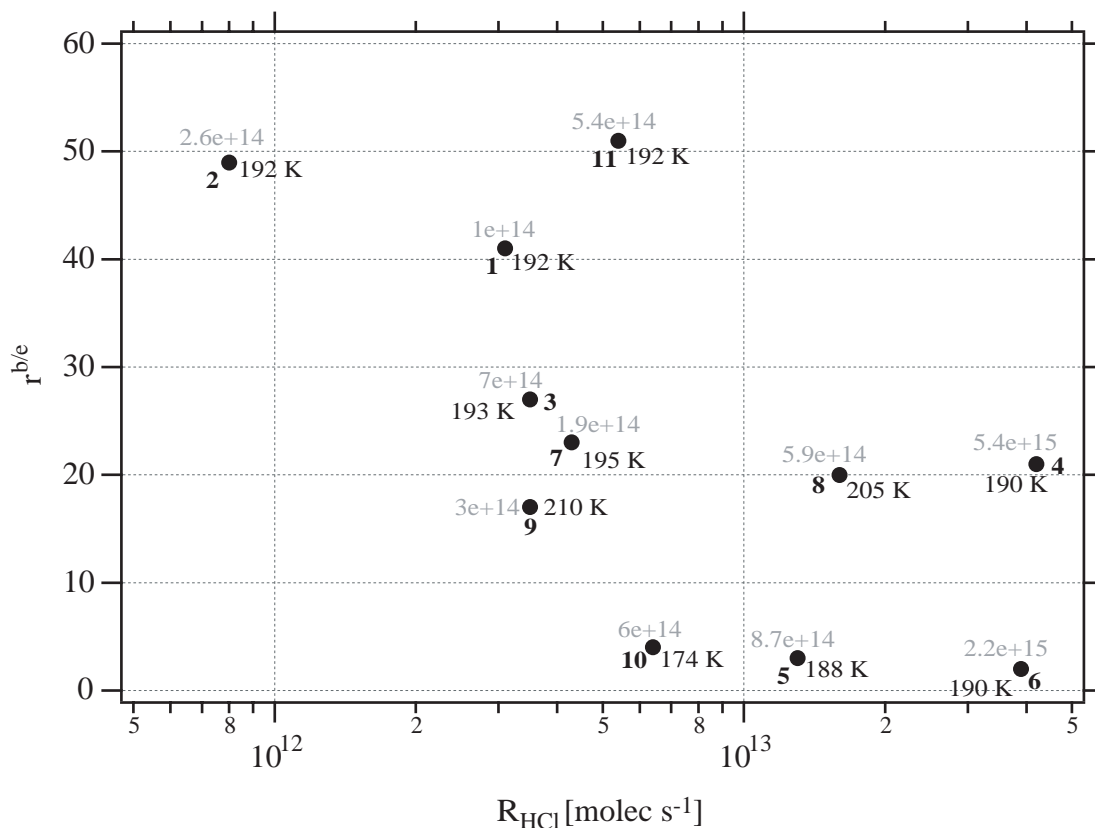


Figure 6.2: Synopsis of the dependence of $r^{b/e}$ on the rate of deposition R_{HCl} of HCl for temperatures between 188 and 210 K. Each point is marked with the total number of HCl molecules deposited on the ice film (gray), the temperature of the ice film (black) and the experiment number (bold) referring to Table 6.2.

Once more the data corresponding to experiments of **set A** seems to present a complex dependence of d_D on the parameters T_{ice} , R_{HCl} and N_{HCl} . The data show a tendency of an increase of d_D with T_{ice} and N_{HCl} whereas d_D seems to decrease with R_{HCl} . Data **set B** is more consistent as d_D is nearly the same in all cases similar to behavior of $r^{b/e}$ and ranges

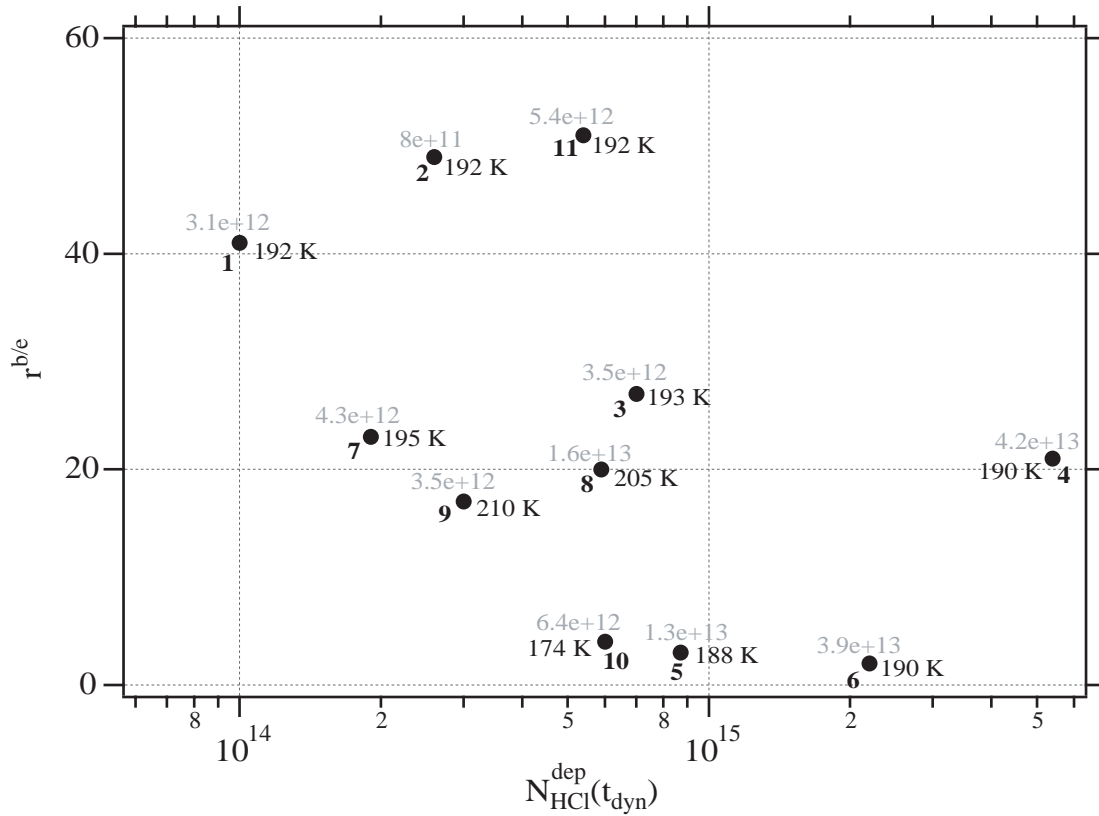


Figure 6.3: Synopsis of the dependence of $r^{b/e}$ on the number of adsorbed HCl, $N_{\text{HCl}}^{\text{dep}}(t_{\text{dyn}})$, adsorbed on ice for temperatures between 188 and 210 K. Each point is marked with the deposition rate of HCl molecules in molec s^{-1} on the ice film (gray), the temperature of the ice film (black) and the experiment number (bold) referring to Table 6.2.

between 4607 and 6360 Å.

6.2 Discussion

As in the case of HNO_3 -doped ice it seems that there is a large impact of the doping protocol of HCl on ice defined by the temperature of deposition, T_{ice} , the rate of HCl deposition, R_{HCl} , and the total number of HCl molecules deposited on ice, N_{HCl} , on $r^{b/e}$ and d_{D} which depend on an interplay between these three parameters that we cannot at present disentangle based on these experiments. Nevertheless, the case of the data corresponding to **set B** of experiments

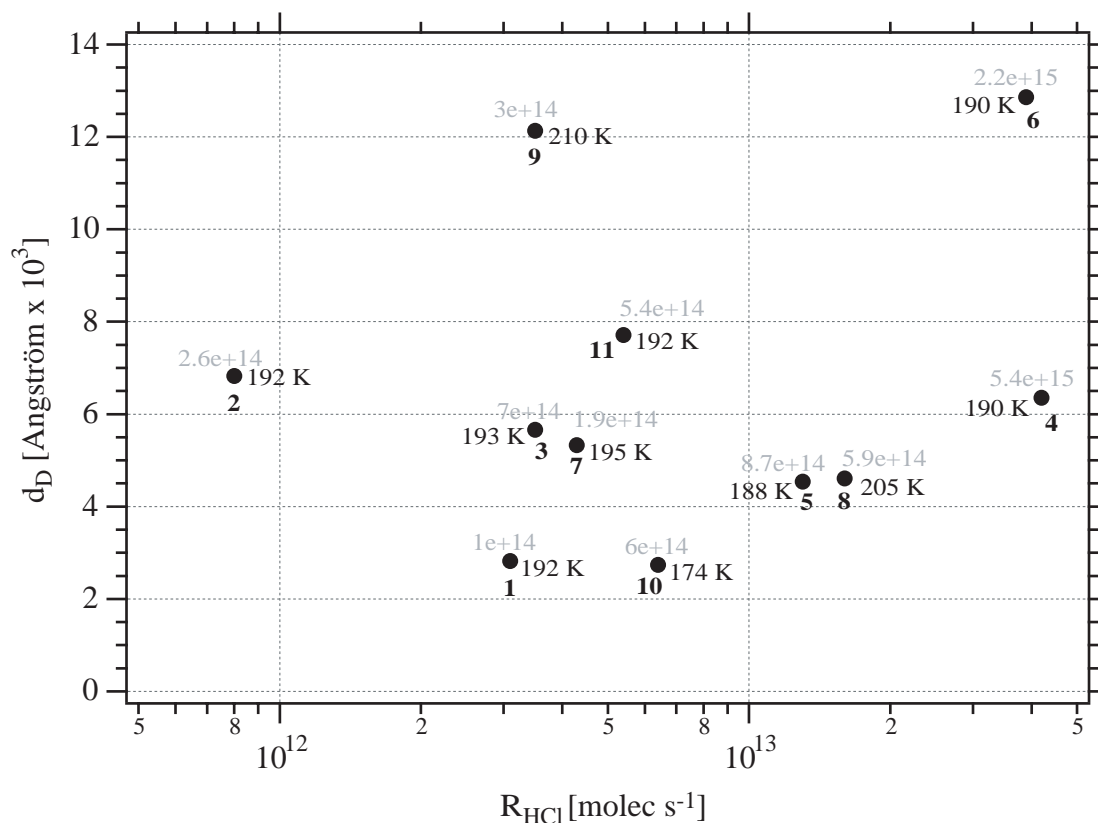


Figure 6.4: Synopsis of the dependence of d_D on the rate of deposition R_{HCl} of HCl for temperatures between 188 and 210 K. Each point is marked with the total number of HCl molecules deposited on the ice film (gray), the temperature of the ice film (black) and the experiment number (bold) referring to Table 6.2.

is interesting. Indeed, Figure 6.1 shows that whereas N_{HCl} is ten times larger in the case of experiment 4 compared to experiment 11, J_{ev} begins to decrease for experiment 4 when the average mole fraction χ_{HCl} in the ice film reaches a value that is a little larger than ten times compared to experiment 11 for a comparable decrease of J_{ev} . This observation also holds for the comparison between experiment 4 and experiments 3 or 8. The number of molecules of H₂O that are influenced or "trapped" by HCl under the particular conditions of deposition proper to data set B must be nearly the same because they give rise to similar values of $r^{b/e}$. This assertion is confirmed by the fact that d_D seems to be independent of T_{ice} , R_{HCl} and N_{HCl}

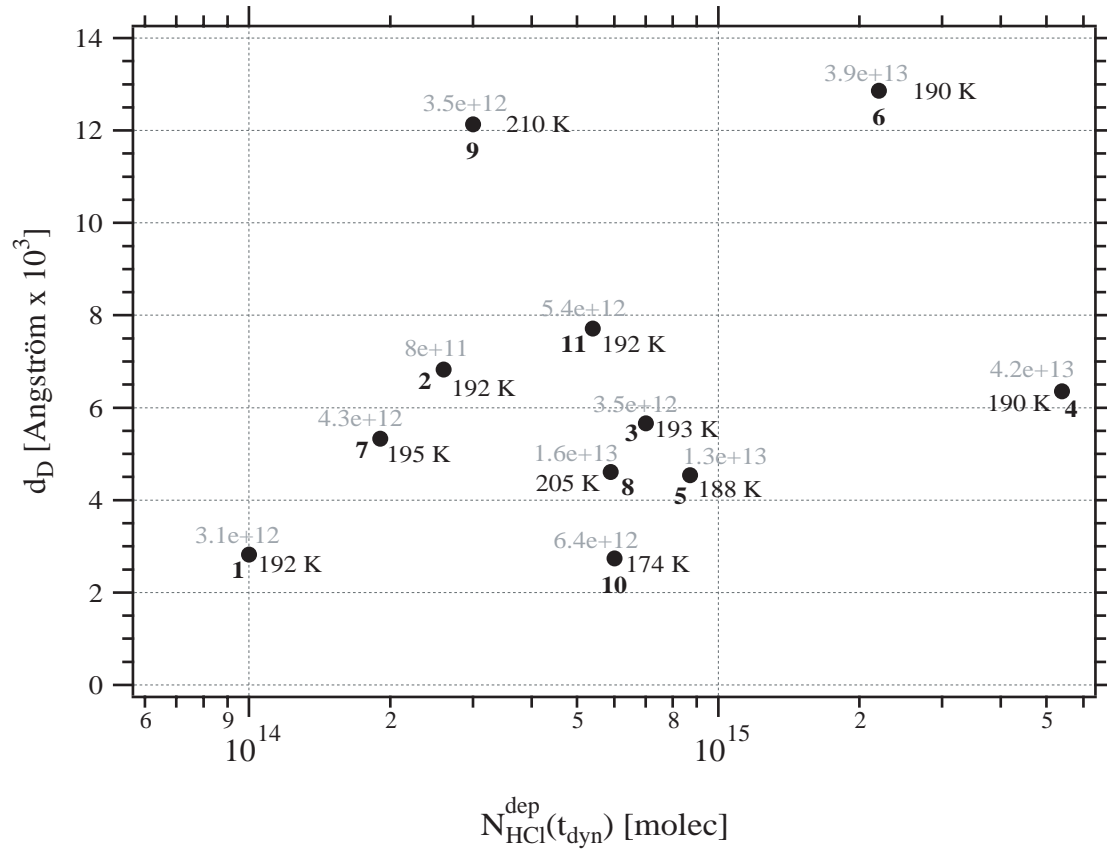


Figure 6.5: Synopsis of the dependence of d_D on the number of adsorbed HCl, $N_{\text{HCl}}^{\text{dep}}(t_{\text{dyn}})$, dispensed on ice for temperatures between 188 and 210 K. Each point is marked with the deposition rate of HCl in molec s^{-1} on the ice film (gray), the temperature of the ice film (black) and the experiment number (bold) referring Table 6.2.

when looking at Figures 6.4 and 6.5. If we consider the mean value of d_D , $\overline{d_D}$, for data **set B** we find that $\overline{d_D} = 5490 \text{ \AA}$ which corresponds to $8.5 \cdot 10^{17}$ molecules of H_2O "trapped" on the ice film. Regarding the results presented in Chapter 3 in Table 3.4, on page 85, it appears that the rates of deposition of HCl in the case of experiments **3**, **4**, **7** and **8** are close to the range between $1.0 \cdot 10^{13}$ and $5.0 \cdot 10^{13} \text{ molec s}^{-1}$ when taking into account the different surface areas for the Si-window, $A_{\text{Si}} = 0.78 \text{ cm}^2$, and the QCM, $A_{\text{QCM}} = 0.5 \text{ cm}^2$. This range defines the necessary R_{HCl} for the observation of crystalline $\text{HCl} \cdot 6\text{H}_2\text{O}$ hydrate. When we consider the results presented in Table 3.3, on page 82, for cases (b) and (b') we conclude that the number of H_2O molecules that

are "trapped", or are affected, by the presence of HCl, which is equivalent to d_D dealt with in the present chapter, is on the order of $1.2 \cdot 10^{18}$ molecules for the formation of crystalline HCl·6H₂O. We need to add that HeNe interferometry is only a crude means to evaluate the thickness of the remaining ice film as a function of the change of J_{ev} . The results obtained using the QCM suggest that on the 0.5 cm² surface area of the QCM quartz sensor $7.7 \cdot 10^{17}$ molecules of H₂O are "trapped" which is in good agreement with the $8.5 \cdot 10^{17}$ molecules of H₂O calculated from $\overline{d_D}$. We may conclude that when formation of HCl·6H₂O occurs at the appropriate experimental conditions it seems that the hexahydrate traps or immobilizes a number of H₂O molecules that depends on the surface area of the ice film based on a comparison involving the surface area of the ice sample.

In contrast, in the case of data **set A**, it seems that the interplay between the parameters is too difficult to disentangle on the basis of the existing experiments. The low rate of deposition of HCl resembles the one given in Table 3.4, column (c), for the formation of amorphous HCl·H₂O. The larger values for d_D displayed in Figures 6.4 and 6.5 for data **set A** compared to **set B** are in good agreement with the results presented in Table 3.3 where the formation of the amorphous HCl·H₂O mixture has an impact of at least twice the number of H₂O molecules making up the ice film compared to HCl·6H₂O.

Regarding experiments **3**, **6** and **11** we may remind the reader that the limiting values for R_{HCl} that were chosen in Table 3.4 are arbitrary to a certain extent and not definitive as a systematic study has not yet been undertaken in order to precisely define these limiting values of R_{HCl} leading to the formation of hexahydrate.

Finally, the results may help explain the observed scatter of the data for J_{ev} and γ of H₂O in the presence of doped-ice presented in Figures 3.4 and 3.5 as pointed out in Chapter 3.

The defining moment of the crystallisation of the HCl·6H₂O has not been accessible from the experiments presented here. Does the sudden decrease of J_{ev} observed in the case of HCl-doping for data **set B** correspond to a structural change of adsorbed HCl in the ice film as opposed to the continuous slow decrease of J_{ev} in the case of what appears to be an amorphous phase?

The answer to this question will have to await further experiments in the future.

Chapter 7

Outlook: Fourier transform infrared reflection-absorption spectroscopy of pure and doped ice films condensed on a QCM sensor

The previous chapters have shown the advantage of a multiple diagnostic experiment in which the different investigation techniques are fully complementary.

Chapter 3 illustrated how the combination of concentration or pressure measurements, using mass spectrometry or an absolute pressure gauge, with He-Ne interferometry and simultaneous FTIR measurements permits to obtain the kinetics of condensation and evaporation of H₂O from pure and doped ice whose structure may be identified using FTIR spectroscopy in transmission. In Chapters 4 and 5 the addition of the quartz crystal microbalance whose piezoelectric sensor is used as a substrate for ice deposition was combined with the previously cited measurement techniques. This has enabled an increased precision on the kinetic measurements in order to afford a close look at mechanistic details. In Chapters 5 and 6 we have used the capabilities of

both cryogenic supports, namely the cryostat/FTIR as well as the temperature controlled QCM. We have been able to observe the impact of the doping protocol of HNO_3 and HCl on the time evolution of the evaporative flux of H_2O from ice. Moreover, we have been able to determine to some extent the identity of the structures of the contaminants on ice that led to certain trends of the change of J_{ev} . As pointed out in the text numerous times exactly reproducing identical conditions for deposition is not easy from an experimental point of view, especially when low flow rates or low doses of contaminants are involved. Considering Table 3.4, on page 85 or Figure 6.1, on page 209, it is clear that we need to obtain structural information, using FTIR, preferably together with the kinetics. To that end it would be highly desirable to merge both the spectroscopic (FTIR) as well as the kinetic support (QCM) into one device in order to take advantage of a spatially and temporally merged unified support. This implies that the further development of the apparatus should focus on the spectroscopic investigation of the ice deposited on the QCM sensor using Fourier transform spectroscopy in a reflection-absorption configuration as opposed to transmission.

Several reflection-absorption studies of pure [1] or doped [2] ice have already been performed at small angles of incidence. Some work has been performed using the so-called grazing incidence RAIR technique that uses a large angle of incidence on the investigated substrate, be it pure ice [3, 4, 5, 6] or doped ice [7]. The grazing incidence technique was first proposed as a result of the theoretical study of Greenler [8, 9] and affords an enhancement of the sensitivity to surface species for thin ice films [3] which may be of interest in future work performed using the present apparatus. Moreover, the lack of space in the present reactor naturally encourages the embodiment of such a configuration in order to keep all other elements of the setup working at the same time.

Adopting the same constraint as for the development of the other cryostats, namely the absence of cold spots except on the substrate used for deposition which is the piezoelectric sensor, we have developed a new QCM-based support for ice growth, housed in a well-fitted Delrin assembly, that was placed in the reactor and is adapted for grazing-incidence measurements of

FTIR spectroscopy.

Figure 7.1 presents an overview of the new QCM and its Delrin insulation. The left panel presents a first test of insulation that was not really satisfying due to the presence of cold zones near the crystal stainless steel holder. This problem occurred within a few minutes of operation. We nevertheless present this configuration as it allows to see the path followed by the FTIR beam and the angle of 68° between the surface normal of the QCM sensor element and the beam. At present, the last development of the Delrin insulation looks more massive and is pierced with two apertures thus allowing access of the FTIR beam as well as the trace gases towards the sensor surface. Regarding the optical beam the present Delrin insulation affords the advantage to act as a diaphragm and it also prevents the appearance of cold spots near the sensor as far as we have measured.

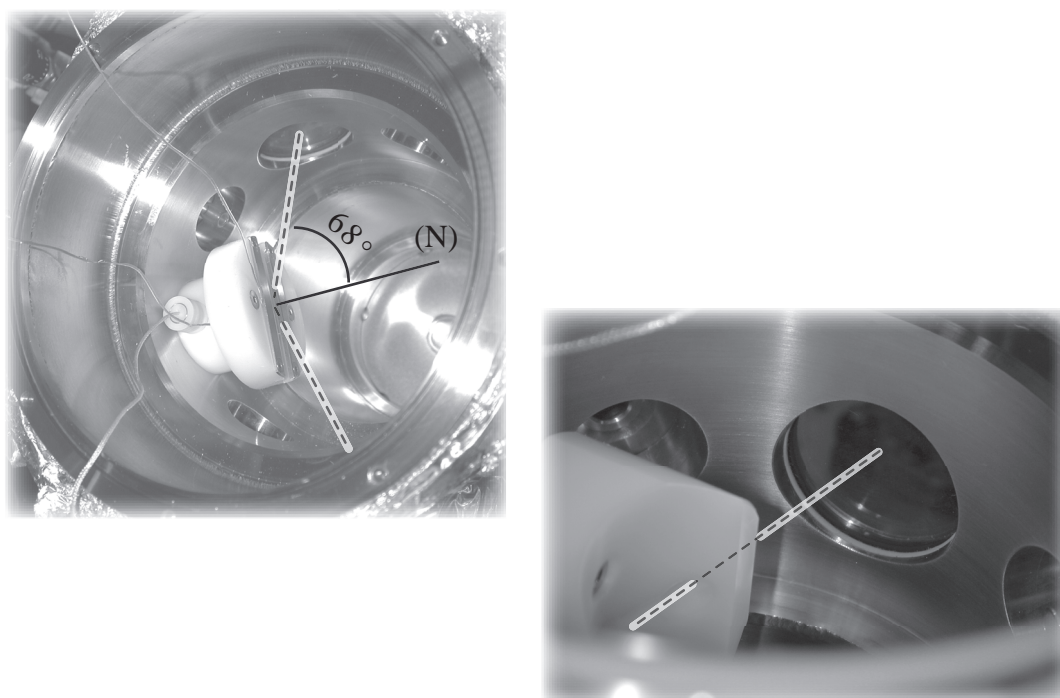


Figure 7.1: Overview of the grazing incidence QCM. The large white and black-dashed lines show the path followed by the FTIR beam. (N) symbolizes the surface normal of the QCM sensor. The left panel was a first test of the performance of the QCM insulation. The right panel corresponds to the actual design of the Delrin insulated QCM.

Figure 7.2 shows one of the first spectra acquired at the surface of the gold-coated piezoelectric sensor for a $1\ \mu\text{m}$ thick ice deposit whose thickness was measured using the QCM technique described in Chapter 4. This spectrum is in excellent agreement with the results of Horn et al. [3] and Zondlo et al. [5] for the spectrum of the grazing incidence RAIR FTIR study of crystalline ice even though the beam of our FTIR is not polarised for the moment.

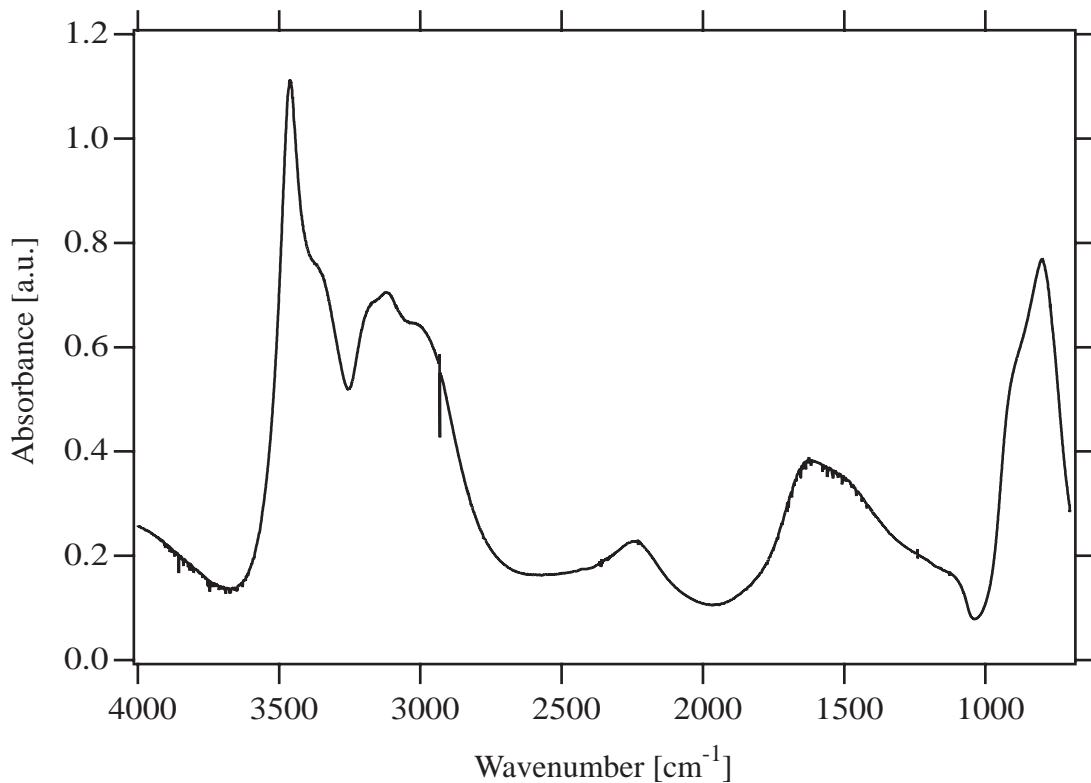


Figure 7.2: FTIR RAIR spectrum under grazing incidence of 68° of pure ice deposited on a QCM gold-coated piezoelectric sensor.

The IR-beam polarization should be implemented in the long term in order to obtain spectra that are easier to interpret [3]. Maté et al. [6] are using an angle that is approximately the same as we use and is comprised between 68 and 72° from the surface normal with respect to the sensor. They present RAIR spectra that are identical to ours. Finally, the advantage of using such a technique combined with the precision afforded by the QCM is that data for the comparison

of the experimental results with models exist for pure ice and nitric acid contaminated ice [10] as well as some experimental measurement concerning doped ice [7]. This may be useful in the pioneering and validation phase of the present experimental setup.

Last but not least it is clear considering Figure 4.16, on page 149, that we have to find a way to modify the morphology of the gold coating of the QCM sensor in order to enable experiments under grazing incidence that will be able to be interpreted in a straightforward way.

Bibliography

- [1] L. Schriver-Mazzuoli, A. Schriver, and A. Hallou, *Journal of Molecular Structure*, 2000, **554**, 289–300.
- [2] H. Chaabouni, L. Schriver-Mazzuoli, and A. Schriver, *Journal of Physical Chemistry A*, 2000, **104**(30), 6962–6969.
- [3] A. B. Horn, S. F. Banham, and M. R. S. McCoustra, *Journal of the Chemical Society-Faraday Transactions*, 1995, **91**(21), 4005–4008.
- [4] F. Bensebaa and T. H. Ellis, *Progress in Surface Science*, 1995, **50**(1-4), 173–185.
- [5] M. A. Zondlo, T. B. Onasch, M. S. Warshawsky, M. A. Tolbert, G. Mallick, P. Arentz, and M. S. Robinson, *Journal of Physical Chemistry B*, 1997, **101**(50), 10887–10895.
- [6] B. Mate, A. Medialdea, M. A. Moreno, R. Escibano, and V. J. Herrero, *Journal of Physical Chemistry B*, 2003, **107**(40), 11098–11108.
- [7] M. Sato, O. Setokuchi, K. M. T. Yamada, and T. Ibusuki, *Vibrational Spectroscopy*, 2003, **31**(2), 167–172.
- [8] R. G. Greenler, *Journal of Chemical Physics*, 1966, **44**(1), 310.
- [9] R. G. Greenler, *Journal of the Optical Society of America*, 1966, **56**(10), 1453.
- [10] O. B. Toon, M. A. Tolbert, B. G. Koehler, A. M. Middlebrook, and J. Jordan, *Journal of Geophysical Research*, 1994, **99**(12), 25631–25654.

Chapter 8

General Appendix

8.1 Ideal Gas Law: numerical values and justification

Equation 2.2, page 22 and subsequently 2.3 are based on the kinetic theory of gases. Several definitions exist to express what an ideal gas is, depending on the chosen point of view: thermodynamic, gas kinetics or statistical thermodynamics. In a preliminary way, the thermodynamic "definition" of the ideal gas [1] follows from the law of Boyle-Mariotte combined with the one of Charles and Gay-Lussac. The former may be expressed as follows:

$$PV = C_2(T, n) \quad (8.1)$$

where P , V , T and n are the pressure, the volume, the temperature and the number of moles of the gas, respectively. C_2 is a "constant" that depends on T and n . The latter implies the following relation:

$$C_2(T, n) = C(n) \times T \quad (8.2)$$

where C is a "constant" that depends on n .

The combination of these relations naturally leads to the definition:

”An ideal gas simultaneously obeys the Boyle-Mariotte and Charles and Gay-Lussac’s laws and consequently leads to the equality $\frac{PV}{T} = C(n)$.”

This simple definition is at the origin of Equation 2.1. Nevertheless, the law of Boyle-Mariotte implies that the intermolecular forces in an ideal gas must be negligible [1, 2] when applied to the gas kinetics theory for an ideal gas.

The kinetic theory of ideal gases gives the following definition of an ideal gas:

”An ideal gas is a system of particles without interactions which follows the Maxwell-Boltzmann distribution of molecular velocities.”

The first assertion exactly corresponds to the previously cited statement. The second part implies that at equilibrium the function for the velocity distribution for an ideal gas in the velocity space must follow the following expressions:

$$d^3n = f^{[0]}(\vec{v})d_3v \quad (8.3)$$

$$f^{[0]}(\vec{v}) = Ane^{-\frac{mv^2}{2k_B T}} \quad (8.4)$$

$$A = \left(\frac{2\pi k_B T}{m}\right)^{-\frac{3}{2}} \quad (8.5)$$

where d^3n is the average number of particles that have a velocity vector in the range $[\vec{v}, d_3v]$ per unit volume with the elemental volume $d_3v = dv_x dv_y dv_z$ centered on \vec{v} , n the number of molecules per unit volume, m the mass of one particle, T the temperature of the wall, and $k_B = \frac{\mathcal{R}}{\mathcal{N}_A} = 1.38 \cdot 10^{-23} \text{ J K}^{-1}$ the Boltzmann constant. This leads to the ideal gas constant $\mathcal{R} = 8.31 \text{ J mol}^{-1} \text{ K}^{-1}$ and to Avogadro’s number $\mathcal{N}_A = 6.02 \cdot 10^{23}$ molecules. Finally, the mean particular speed \bar{c} in such a gas follows the relation:

$$\bar{c} = \sqrt{\frac{8k_B T}{\pi m}} \quad (8.6)$$

Let us now consider a molecular gas. We can write \bar{c} , the mean molecular speed, in the form:

$$\bar{c} = 100 \times \sqrt{\frac{8\mathcal{R}T}{\pi M}} \quad (8.7)$$

with $\mathcal{R}=8.31 \text{ J mol}^{-1} \text{ K}^{-1}$ being the ideal gas constant, T the temperature in K, and M the molar mass in kg mol^{-1} . The factor of 100 directly yields \bar{c} in cm s^{-1} . In the same vein the density of the molecular flux Φ across unit surface area anywhere in the gas is

$$\Phi = \frac{n\bar{c}}{4} = \frac{N\bar{c}}{4V} \quad (8.8)$$

with Φ in $\text{molec cm}^{-2} \text{ s}^{-1}$, n the molecular density in molec cm^{-3} , N the total number of molecules in V, the volume of gas considered in cm^3 . Naturally, the average gas-wall collision frequency for a given molecule and per cm^2 of surface, commonly referred to as Z_1 , is given by Equation 8.9 if we consider all the molecules to be indistinguishable:

$$Z_1 = \frac{\Phi}{N} = \frac{\bar{c}}{4V} = 100 \times \sqrt{\frac{8\mathcal{R}T}{\pi M}} \times \frac{1}{4V} \quad (8.9)$$

which is identical to Equation 2.2, page 22. If we now consider the gas contained in a vessel of volume V_r , and of internal surface S_r at temperature T_r we obtain for the gas-wall collision frequency ω_c at the inner surface of the vessel the following expression:

$$\omega_c = \frac{\Phi S_r}{N} = \frac{\bar{c} S_r}{4V} = 100 \times \sqrt{\frac{8\mathcal{R}T}{\pi M}} \times \frac{S_r}{4V} \quad (8.10)$$

For the reactor we present in this work the internal surface of the reactor is $S_r=1288 \text{ cm}^2$ and its volume is $V_r=2812 \text{ cm}^3$ using the data given in Figure 2.2, page 21. We consider the wall at 320 K which is the standard case in this work. The total number of collisions per molecule and unit time for water vapor is

$$\omega_c = 100 \times \sqrt{\frac{8 \times 8.31 \times 320}{\pi \times 18 \cdot 10^{-3}}} \times \frac{1288}{4 \times 2812} = 7025 \text{ collisions molec}^{-1} \text{ s}^{-1}$$

We may compare ω_c with the gas-gas collision frequency in order to determine the limiting pressure in the reactor allowing us to consider that H₂O vapor consists of a gas of particles without interactions as previously cited and thus may be considered an ideal gas.

First, we must evaluate a cross-section for gas-gas collisions. In a simple model considering the molecules as spheres we can determine their diameter from the parameters a and b of the Van der Waals model for real gases. We gather from reference [3] that $a=5.464 \text{ l}^2 \text{ atm mol}^{-2}$ and $b=0.03049 \text{ l mol}^{-1}$ for H₂O vapor. For one mole of gas the Van der Waals equation assumes the form

$$\left(P + \frac{a}{V^2}\right)(v - b) = \mathcal{R}T \quad (8.11)$$

with P in atm, a in l² atm mol⁻², V in l, b in l mol⁻¹, \mathcal{R} in l atm mol⁻¹ K⁻¹ and T in K. In the Van der Waals equation b corresponds to the excluded volume of the total number of molecules of diameter δ . If we consider that each molecule excludes a volume $\frac{4\pi\delta^3}{3}$ for other molecules and that half of the molecules in one mole of the gas do the same for the other half, we obtain the following definition for b:

$$\frac{\mathcal{N}_A}{2} \times \frac{4\pi\delta^3}{3} = b \quad (8.12)$$

leading to

$$\delta = 10 \times \sqrt[3]{\frac{3b}{2\pi\mathcal{N}_A}} \quad (8.13)$$

with δ in cm.

In the case of H₂O one may calculate that $\delta=2.9 \cdot 10^{-8}$ cm. Using an elastic collision approximation of gas-gas collisions we may evaluate the cross-section for collisions \mathcal{Q} as follows:

$$\mathcal{Q} = \pi\delta^2 \quad (8.14)$$

which yields $Q=2.6 \cdot 10^{-15} \text{ cm}^2$ for water.

If we are interested in the collision frequency of one particular molecule with its neighbours that are considered to be fixed the gas-gas collision frequency ω_g has the following form:

$$\omega_g = nQ\bar{c}\sqrt{2} \quad (8.15)$$

with n in molec cm^{-3} , Q in cm^2 , \bar{c} in cm s^{-1} and ω_g in $\text{collisions molec}^{-1} \text{ s}^{-1}$. In the case of ideal gases the concentration n can be deduced from the pressure following the relation

$$n = \text{Conv} \times P \quad (8.16)$$

with n in molec cm^{-3} , Conv the conversion factor derived from the ideal gas law in $\text{molec Torr}^{-1} \text{ cm}^{-3}$ and P the pressure in Torr. At 320 K, the temperature of the wall of the reactor, one may calculate $\text{Conv}=3.0 \cdot 10^{16} \text{ molec Torr}^{-1} \text{ cm}^{-3}$. Taken together in Equation 8.15 we obtain:

$$\omega_g = 6.8 \cdot 10^6 \times P_{[\text{Torr}]} \text{ collisions molec}^{-1} \text{ s}^{-1}$$

If we compare ω_g with ω_c for H_2O molecules one can easily find that the gas-wall collisions are predominant only for pressures lower than approximately $1.0 \cdot 10^{-3} \text{ Torr}$. We find here the commonly admitted upper limit of the high vacuum region, $P=7.5 \cdot 10^{-4} \text{ Torr}$, at which the ideal gas law unambiguously applies [2]. This pressure corresponds to the vapor pressure of H_2O over a pure ice film at T_{ice} at approximately 200 K [4].

In order to verify whether or not the H_2O vapor over an ice film at temperatures higher than 200 K which imply vapor pressures of H_2O higher than $1.0 \cdot 10^{-3} \text{ Torr}$, can be considered an ideal gas we may look at the changes introduced by the Van der Waals equation which fits well the behavior of real gases. As a simple example let us first consider that H_2O is an ideal gas within a reactor of volume $V_r=2812 \text{ cm}^3$ whose walls are at $T_r=320 \text{ K}$. An ice film on a cold substrate at $T_{\text{ice}}=240 \text{ K}$ in the reactor under static conditions (GV and LV closed)

supports an equilibrium vapor pressure on the film of approximately $200 \cdot 10^{-3}$ Torr [3]. Following Equation 8.16 such a pressure corresponds to a total number of molecules of $N=1.7 \cdot 10^{19}$ molec equivalent to $\mathcal{N}=2.8 \cdot 10^{-5}$ mol. For \mathcal{N} moles of gas the Van der Waals law assumes the following form:

$$\left(P + \frac{\mathcal{N}^2 a}{V^2} \right) (v - \mathcal{N}b) = \mathcal{N} \mathcal{R} T \quad (8.17)$$

with P in atm, \mathcal{N} in mole, $\mathcal{R}=0.008205$ l atm mol⁻¹ K⁻¹ and T in K. At the given value of $\mathcal{N}=2.8 \cdot 10^{-5}$ mol previously calculated using the ideal gases law we calculate the corresponding pressure using Equation 8.17 and find $P=199 \cdot 10^{-3}$ Torr that may be compared to the $200 \cdot 10^{-3}$ Torr that have been introduced in the ideal gas law to determinate $\mathcal{N}=2.8 \cdot 10^{-5}$ mol. We conclude that even at the highest pressures used in this work, the corrections introduced by the Van der Waals law are negligible. It therefore seems that the use of ideal gas law is appropriate for the kind of experiments we have performed. If we come back to the last definition of an ideal gas that is given previously, "an ideal gas is a system of particles without interactions...", we can compare the range of the intermolecular force σ with the intermolecular distance d and with the thermal wavelength λ_{th} [5]. Using a simple cubic model for the arrangement of the H₂O molecules in the reactor it follows that a rough evaluation of d is given by:

$$d = \sqrt[3]{\frac{V}{N}} \quad (8.18)$$

with d in cm, V in cm³ and N the total number of molecules. In the present experiments we have $d=5.5 \cdot 10^{-6}$ cm for N_{H_2O} corresponding to the equilibrium vapor pressure over ice at 240 K. For the range of the intermolecular forces, commonly referred to as σ , we may take either the diameter of the molecules cited above, $\delta=2.9 \cdot 10^{-8}$ cm, or the constant $\sigma_0=2.6 \cdot 10^{-8}$ cm of the Lennard-Jones intermolecular potential [6, 7, 8]. Let us take $\sigma=3.0 \cdot 10^{-8}$ cm as a first order approximation for the intermolecular distance. The thermal wavelength is a parameter that is derived from statistical thermodynamics in the theory on the systems of identical particles

without interactions [5]. When this theory is extended to the classical limit both Fermi-Dirac and Bose-Einstein statistics tends to Maxwell-Boltzmann statistics which is relevant for ideal gases. The thermal wavelength represents the validation parameter of the classical theory. It is defined as

$$\lambda_{\text{th}} = 100 \times \sqrt{\frac{h^2}{2\pi m k_B T}} \quad (8.19)$$

with λ in cm leading to the factor of 100, $h=6.62 \cdot 10^{-34}$ J s (Planck's constant), m the mass of one molecule in kg, $k_B=1.38 \cdot 10^{-23}$ J K⁻¹ (Boltzmann's constant) and T the temperature in K. At the experimental conditions in the reactor we have cited above we calculate $\lambda_{\text{th}}(\text{H}_2\text{O})=2.3 \cdot 10^{-9}$ cm.

To summarize, we have

- $d=5.5 \cdot 10^{-6}$ cm
- $\sigma=3.0 \cdot 10^{-8}$ cm
- $\lambda_{\text{th}}(\text{H}_2\text{O})=2.3 \cdot 10^{-9}$ cm

which means that the intermolecular distance is more than ten times larger than the range of the intermolecular forces and the thermal wavelength. These two conditions are defined in reference [5] as the validity criterion for a gas to be considered as ideal.

In conclusion, we claim that, regarding these results even if not exhaustive, the use of the ideal gas law is entirely justified in the data treatment of the experiments we have performed.

Bibliography

- [1] B. H. Mahan and R. J. Myers, *University chemistry*, Benjamin/Cummings Pub. Co., Menlo Park, Calif., 4th ed., 1987.
- [2] J. M. Lafferty, *Foundations of vacuum science and technology*, Wiley, New York, 1998.
- [3] R. C. Weast, *CRC Handbook of Chemistry and Physics*, CRC Press, Boca Raton, FL, 1st student ed., 1988.
- [4] J. Marti and K. Mauersberger, *Geophysical Research Letters*, 1993, **20**(5), 363–366.
- [5] C. Coulon and S. Moreau, *Physique statistique et thermodynamique cours et exercices corrigés 2ème cycle*, Dunod, Paris, 2000.
- [6] R. W. Bickes, G. O. Este, G. Scoles, and K. M. Smith, *Journal of Physics B-Atomic Molecular and Optical Physics*, 1974, **7**(1), L19–L21.
- [7] R. W. Bickes, *Journal of Physics B-Atomic Molecular and Optical Physics*, 1974, **7**(12), 1609–1609.
- [8] R. W. Bickes, G. Duquette, C. J. Vandenmeijdenberg, A. M. Rulis, G. Scoles, and K. M. Smith, *Journal of Physics B-Atomic Molecular and Optical Physics*, 1975, **8**(18), 3034–3043.

Acknowledgements

ou plutôt **remerciements**...Les plus sincères à toutes celles et tous ceux qui les méritent, pour leur soutien, leur aide, leurs conseils, leur simple présence...leur patience...avec là, une petite mention spéciale pour **Louise et Delphine**...plus généralement à celles et ceux qui tâchent de ne jamais nuire à personne...à Jean-Claude, le père-mère (merci Jodorowsky!)...à Flavio Comino, pour avoir toujours répondu *présent*...à Michel J. Rossi, pour la compétence et parce que cela s'achève **ici...et maintenant!**

EPFL, Lausanne, SUISSE, le 06 janvier 2005

Curriculum Vitae and Publications

Delval Christophe

Born on July 19th 1973 (Mt St Aignan)

Father of Louise

French citizenship

Address:

chemin du creux au loup, 3

1197 PRANGINS (SWITZERLAND)

12, lieu dit Combe Benoit

25650 VILLE DU PONT (FRANCE)

Education

2000-2004: Ph.D. student in the Laboratory of Air and Soil Pollution Study of the Swiss Federal Institute of Technology (**EPFL**), under supervision of Dr. Michel J. Rossi.

Research on the kinetics of condensation and evaporation of atmospheric ices.

Development of a multiple diagnostic apparatus.

1998-1999 : **DEA** AOEMS (Acousto-Opto-Électronique et Mécanique des Structures)

specialty **optics** at P.M. DUFFIEUX Optics Laboratory, University of FRANCHE-COMTÉ,

BESANÇON. Diploma subject: "Conception d'un télémètre optique pour l'aide à la mobilité des aveugles : étude préliminaire".

1993-1996 : Undergraduate Studies of Physics at University of **Rouen** (FRANCE).

1991-1993 : Classes Préparatoires aux **Grandes Écoles**, **Montbéliard** (FRANCE).

1990-1991 : **Baccalauréat** technologique **F5, Physique**, June 1991.

Publications

- C. Delval, B. Flückiger and M. J. Rossi: The rate of water vapor evaporation from ice substrate in the presence of HCl and HBr: implications for the lifetime of atmospheric ice particles, *Atmospheric Chemistry and Physics*, 3, 2003, 1131-1145.
- C. Delval and M. J. Rossi: The kinetics of condensation and evaporation of H₂O from pure ice in the range 173-223 K: a quartz crystal microbalance study, *Physical Chemistry Chemical Physics*, 6, 2004, 4665-4676.
- C. Delval and M. J. Rossi: The influence of monolayer amounts of HNO₃ on the evaporation rates of H₂O over ice in the range 179 to 208 K: a quartz crystal microbalance study, *Journal of Physical Chemistry*, Submitted.
- C. Delval and M. J. Rossi: The influence of monolayer amounts of HCl on the evaporation rates of H₂O over ice in the range 188 to 210 K: a quartz crystal microbalance study. Determination of the infrared absorption cross-section in the range 700-4000 cm⁻¹ of crystalline HCl·6H₂O hexahydrate, *Atmospheric Chemistry and Physics*, In preparation.
- C. Delval and M. J. Rossi: A novel multiple diagnostics apparatus for kinetic and spectroscopic studies of multiphase systems: ice in the temperature range of 150-240 K, *Review of Scientific Instruments*, In preparation.